Technische Universität München

TUM School of Engineering and Design

Value-based design of wind turbines

Helena Canet Tarrés

Vollständiger Abdruck der von der TUM School of Engineering and Design der Technischen Universität München zur Erlangung des akademischen Grades einer

Doktorin der Ingenieurwissenschaften (Dr.-Ing.)

genehmigten Dissertation.

Vorsitz: Prof. Dr. Rafael Macián-Juan
Prüfer*innen der Dissertation: 1. Prof. Dr. Carlo L. Bottasso
                                     2. Dr. Katherine Dykes

Die Dissertation wurde am 26.04.2022 bei der Technischen Universität München eingereicht und durch die TUM School of Engineering and Design am 06.09.2022 angenommen.

ABSTRACT

This dissertation explores the design of a wind turbine from different points of view. A wind turbine is here defined beyond the common notion of a machine whose only goal is to produce low-carbon energy at a minimum cost. Indeed, a wind turbine has multiple inherent values –i.e. worth for different groups of users–, which can be enhanced through its design. For instance, a wind turbine is of great scientific value for researchers, as it is also a tool to understand better wind energy science – and thus help with its further development; it is of economic value for investors, who might see a wind turbine as an asset to obtain economic benefits, but also for customers, who want to pay as little as possible for the energy consumed daily; and it is also of societal value for society, who find in a wind turbine an opportunity to generate low-carbon energy and decarbonize the electricity sector, thus contributing to a cleaner environment. While several topics can be explored to increase these values, this thesis focuses on four topics: design and performance of scaled rotors, methods for uncertainty quantification, integration of lidar-assisted control in wind turbine design and eco-conscious design.

First, the thesis formulates laws for scaling wind turbine rotors. The analysis reveals the changes to physical characteristics induced by a generic change of scale, and indicates which characteristics can be matched faithfully by a subscaled model, and states the conditions that must be fulfilled for desired matchings to hold. Based on the scaling laws formulated, two alternative design strategies are defined. Practical illustrations are given to better demonstrate the challenges implicit in scaling and the necessary trade-offs and approximations.

Next, the thesis focuses on methods for uncertainty quantification and the effect of uncertain inputs in design drivers. The performance of two non-intrusive uncertainty quantification methods is benchmarked against a brute-force extensive Monte Carlo sampling. The solution space is also analyzed to identify the effect of uncertainties and their couplings in design drivers.

Third, the thesis investigates the potential benefits brought by the integration of lidar-assisted control in the design of a wind turbine. The study identifies which design drivers can be relaxed by LAC, as well as by how much these drivers could be reduced before other conditions become the driver. A generic LAC load-reduction model is applied to redesign the rotor and tower of three representative turbines, differing in terms of wind class, size and power reductions. The load reductions enabled by LAC are exploited to save mass, increase hub height or extend lifetime.

Finally, the thesis focuses on the definition of novel eco-conscious metrics, that capture the environmental effect produced by a wind turbine over its entire life cycle, expressed in terms of CO_2-equivalent emissions. Future societal savings are also derived, based on the environmental savings obtained through the deployment of a wind turbine. A new approach to design is proposed, whereby Pareto fronts of solutions are computed to define optimal trade-offs between economic and environmental goals. The proposed methodology is demonstrated on the redesign of a baseline 3 MW wind turbine at two locations in Germany, different for typical wind speeds.

Back in October 2015, as an exchange master student in Munich, I enrolled in the course *Modeling, Control and Design of Wind Turbines*, organized by the Wind Energy Institute and lectured by Prof. Bottasso. I remember being very motivated by the multi-disciplinarity of wind turbine design, and it was not long before I decided to also carry out my master thesis on the topic. I did not know at the time that that would be the first step towards several years of research in wind energy and the dissertation here presented. During these years I have had the fortune of working with many different people, who have very positively impacted my work and my experience. I would like to acknowledge and thank them here.

My deepest gratitude is for Prof. Carlo L. Bottasso, who not only gave me the opportunity to pursue this doctoral degree, but also offered his wise guidance, support and patience along the journey. Thank you Carlo, for your kindness and for the trust you gave me so many times.

I also thank Pietro Bortolotti, who was my mentor during the first years. You deserve all my gratitude for all the times you sat next to me and helped solving any problem I was having and for all the pieces of advice you gave me: time proved how valuable they were.

My experience would not have been the same without the collaboration and wonderful times inside and outside the office with my colleagues/friends at the Wind Energy Institute: the laughs with Abhinav and Anik about *The Office*, the barista lessons with Bastian, the *Settlers of Catan* battles with Chengyu and Johannes, the delicious foods brought by Doruk, benchsurfing with Filippo, the Weleda conversations with Franz, the Wordle discussions with Robert, the admin skills learnt from Robin, the karaoke nights with Stefan and the Mensa fridays with Andi, Hadi and Simone.
A special acknowledgment is for Adrien and Samuel with whom I have closely collaborated during the last years on the work on societal value here presented. I am very proud of the great supportive team we built together, and I am certain that the piece of work here included would not have been possible without our almost daily conversations. Additionally, Elli and Martina deserve here a special mention for their patience and all the bureaucratic support they offered.
Last but not least, the uncountable discussions and theories about basically anything, the trips, the pizza fridays and gossips with Carlo R., Marta and Manos have been the backbone of these wonderful years.

During these years, I have also collaborated with different researchers through different project networks. The Winsent project has accompanied me from the very first day, and it is thanks to its great leadership team, especially Andreas Rettenmeier and Florian Haizmann, that the project has gone forward. Additionally, I would like to thank Fiona Lüdecke, Giorgia Guma, Philipp Bucher and Tim Hagemann, doctoral students from University of Stuttgart and Technical University of Munich, for the great collaborative environment we built and maintained throughout the whole project and for the fun times we spent together.

Finally, my gratitude is also for Andreas Manjock from DNV, with whom I worked within the Farmconners project, the WindForS community and the IEA Wind Task 37 leadership team, who gave me the opportunity to join the team and learn from their work.

I had heard that one only truly understands something when able to teach it, and I now know that this is true. Indeed, during these years I had the opportunity of collaborating with highly motivated

*The world belongs to those who set out to conquer it armed
with self-confidence and good humor*

CHARLES DICKENS

Contents

Introduction

Even though climate change can be caused by natural factors – such as variations in the solar radiation received by the Earth, plate tectonics or volcanic eruptions – it is extremely likely that the warming observed since the mid-20th century has been influenced by human activity [1].
Indeed, the United Nations Framework Convention on Climate Change (UNFCCC) defines climate change as the variation of climate directly attributed to human activity, which adds to the natural climate variability [2, 3]. Climate change affects all regions around the world for both natural and human systems. In fact, it is likely that anthropogenic warming has already had a discernible influence on many physical and biological systems. Impacts in these systems are expected to continue and further increase in the next decades because of the altered frequencies and intensities of extreme weather, climate and sea-level events [4]. Even though adaptation measures are already necessary to address the impacts brought by the unavoidable warming caused by past emissions; it is still possible to avoid, reduce or delay future impacts – if proper actions are taken early enough. Indeed, the International Panel on Climate Change reports that adopting a portfolio of adaptation and mitigation measures can diminish the risks associated with climate change [4]. Clearly, action is urgent and these measures must be taken early enough to avoid the worst. As a response to this imminent threat, 195 countries signed the Paris Agreement on 2015, recognizing the need for an effective and progressive response to climate change, and agreeing to keep the temperature increase below 2° Celsius compared to pre-industrial level [5].

The European Energy Agency estimates that, from the globally emitted greenhouse gases (GHG) – i.e. those gases that contribute to the greenhouse effect by absorbing infrared radiation in the atmosphere –, about two thirds are linked to burning fossil fuels for energy to be used for heating, electricity, transport and industry [6]. A clear and simple solution to reduce emissions is therefore to employ cleaner energy sources and/or reduce the overall consumption of energy.

Wind turbines are an energy-generating technology with a very low environmental impact, a so-called low-carbon technology. Indeed, a wind turbine is an eco-friendly machine by definition as it captures kinetic energy from the wind to produce electricity without directly releasing pollutant emissions. Even though GHG are emitted during multiple processes involved at different stages of the life-cycle of a wind turbine, the overall environmental impact of wind energy – expressed as equivalent grams of CO_2 per unit of energy produced – is in average 70 times lower than the environmental impact of a coal-fired power generation plant [7].

Wind power is as well one of the fastest-growing renewable energy technologies. For instance, the cumulative capacity of onshore wind experienced almost a fourfold increase worldwide in the past decade, while offshore wind increased more than eleven-fold in the same time, as its development started later [8]. This growth is partially powered by technological improvements, a growing maturity of the sector and increased competitiveness. Indeed, the development of larger and more reliable turbines, with higher towers and lower specific power – i.e. rated power divided by rotor swept area – has led to an increase of 81% in capacity factor since 1983 [8]. The installation, operation and maintenance (O&M) costs per unit of energy generated also benefit from the larger size of the turbine and have decreased over the last decades [8, 9]. This trend can be spotted in Fig. 1.1, which displays the
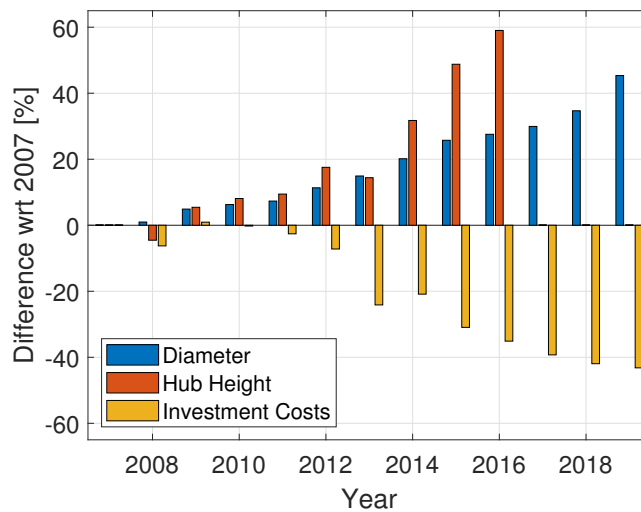
Figure 1.1: Average rotor diameter, hub height and investment costs of onshore wind turbines of 1 MW or larger connected to the grid in a specific year in the European Union, expressed as relative difference to 2007. Data collected from [10], own illustration. No data is available for hub height for 2017, 2018 and 2019.

evolution of the average rotor diameter and hub height, as well as investment costs of onshore wind turbines installed in the European Union over the last decade.

In consequence, the levelized cost of energy (LCOE) of wind turbines – defined as the average net present cost of electricity generation (considering both capital and operating cost) over its lifetime [11] – has experienced a reduction of 87% over the last three decades [8] – and is expected to decrease even further in the next decades, with experts predicting further decreases of up to 50% by 2050 with respect to costs in 2015 [12].

Due to its low cost and almost negligible environmental impact, it is no surprise that wind energy is posed to play a leading role in the energy transition [13]. In fact, current studies estimate that one third of the worldwide energy production in 2050 should come from wind to meet the targets set by the Paris agreement. Clearly, the wind energy market will have to experience a significant growth over the next three decades to meet this target. IRENA estimates that the global cumulative installed capacity of onshore wind power needs to increase more than three-fold by 2030 and nine-fold by 2050, with an even larger growth expected for offshore wind power [13].

Such an increase of cumulative capacity will require the installation of wind turbines in less-attractive wind sites, as well as the reblading or replacement of already existing turbines [9, 12]. The research community and industry are already devoting significant efforts to the development of even larger machines, that capture more energy and provide even further economies of scale [9]. The development of these enlarged machines is clearly not trivial, as the larger dimensions increase the complexity of the wind turbine dynamic behavior and increasingly push the boundaries of assumptions and models used so far. [9]. Subscale testing – i.e. employing subscaled replicas of larger machines – offers an opportunity to further understand different aspects of the dynamics of these enlarged machines at a much lower cost than full-scale testing.

The next generation of wind turbines can also highly benefit from technological advances in separate areas – such as material science or control. However, caution should be exercised when assessing these new technologies, as any new benefit will be accompanied by a penalty in another figure. It is therefore necessary to carefully assess which technologies have the potential to decrease LCOE and to which extent. For instance the development of lidar-assisted control (LAC) – control

systems augmented with preview information obtained from turbine-mounted light detection and ranging (lidar) sensors – provides an opportunity for load mitigation. However, adopting these systems will as well increase the investment cost, as well as the annual operating expenses. A reduction in LCOE will therefore only be reached if the gains brought by the new technology outweigh the costs.

The energy production and structural safety of a wind turbine are also subject to several uncertainties. Indeed, as the wind resource is highly stochastic and uncertain, the power production and lifetime of a wind turbine are also relatively uncertain. Additional uncertainties are certainly also present and can be introduced, for example, due to manufacturing tolerances or weathering and erosion. The further understanding and consideration of these uncertainties for operating and maintenance activities, or even within the design of the machine, can eventually lead to a higher energy production, reduction in costs due to better maintenance or even further extensions of the lifetime of the machine – among other benefits.

However, there are also barriers at economic, socio-political and environmental levels that must be mitigated to enable the full development of wind power [12, 13, 17]. Indeed, the future of wind energy will not only be shaped by technological developments and its economic competitiveness, but also by the value that can be provided to different groups of users [15, 16]. For instance, as wind energy becomes more competitive and its dependency on subsidies slowly reduces, it is necessary to bring the economic value of wind energy given by energy markets into the spotlight [12]. Additionally, enhancing the inherent societal value of wind energy and economic benefits associated with it– for instance through the displacement of GHG emissions – is also extremely important and can play a role not only in accelerating the decarbonization of the power sector, but also in enhancing the societal perception of this low-carbon energy source [18].

1.1   Research topics and innovative content

Modern wind turbines are multi-disciplinary machines. Designing these machines is not straightforward and typically demands the identification of trade-offs between different aspects. For instance, designing a wind turbine blade generally requires the identification of an external shape that is slender enough to bring a good aerodynamic performance, yet not too slender so that very thick (and therefore expensive) internal structural components are required to ensure its structural safety throughout its lifetime. Additionally, the blade generally must be transportable (leading to additional constraints in the external shape, and even structural properties), manufacturable and might have to be designed to operate without exceeding a noise emission threshold, among other considerations.

LCOE, a figure that quantifies the competitiveness of a generating technology in the energy market, is typically the metric driving these trade-offs in industrial wind turbine design. While design for LCOE has clearly proved to be beneficial, as it has driven wind energy to achieve cost parity with conventional sources in a broad range of conditions and locations, this figure only captures one of the several inherent values of a wind turbine. Indeed, a wind turbine is much more than a machine that can be used to generate low-carbon energy at a minimum cost. A wind turbine has multiple inherent values – here understood as *the worth of a wind turbine for a certain group of users* [19]–, which can be enhanced through its design. For instance, a wind turbine is of great scientific value for researchers, as it is also a tool to understand better wind energy science – and thus help with its further development; it is of economic value for investors, who might see a wind turbine as an asset to obtain economic benefits, but also for customers, who want to pay as little as possible for the energy consumed daily; and it is also of societal value for society, who find in a wind turbine an opportunity to generate low-carbon energy and decarbonize the electricity sector, thus contributing to a cleaner environment.

While the multi-disciplinarity of a wind turbine increases the complexity of wind turbine design, it is also what makes the design of these machines such an interesting and promising activity, where
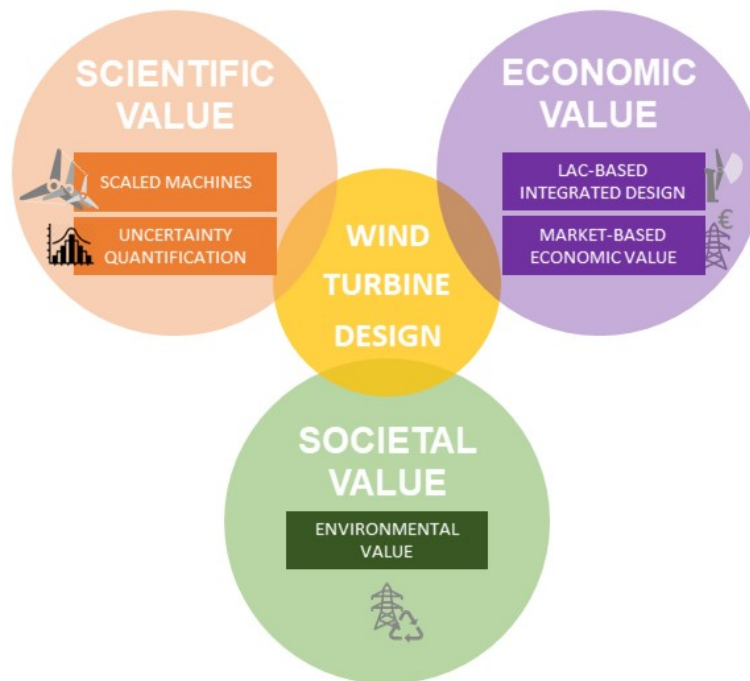
Figure 1.2: Overview of the topics included in this thesis

different trade-offs are certainly possible and can be achieved to enhance different inherent values. This thesis explores how wind turbine design can be employed to enhance the inherent scientific, economic and societal value of wind turbines.

These are certainly very broad areas, which can contain multiple topics. This thesis focuses on five topics relevant for current wind turbine development: design and performance of scaled machines, methods for uncertainty quantification, LAC-based integrated design, market-based economic value and environmental value. Fig. 1.2 gives an overview of the topics included in this thesis which are thoroughly described in the next section. The topics are introduced in the next section, where the innovative content of this thesis is also described. Additionally, Sect. 1.1.4 summarizes the innovative content of this thesis in 4 core research questions. Finally, Sect. 1.2.1 lists the publications included in this thesis.

1.1.1   Design for scientific value

DESIGN AND PERFORMANCE OF SCALED MACHINES

Background. Scaled wind turbines are machines that have been specifically designed to mimic one or more aspects of a wind turbine at a different scale. Both up- and subscaling are possible: On the one side, upscaling is useful to understand the required changes that can be expected in the turbine response as the result of an increase in size. On the other side, subscaling is useful as a research tool that can help validate simulations tools, explore ideas, compare alternative solutions and deepen the knowledge and understanding of complex physical phenomena. Subscaled testing is usually much cheaper and less risky than full-scale testing.

Subscaled testing has already contributed in the past to the further advancement of wind energy science. For instance, studies carried out within the Unsteady Aerodynamics Experiment [20] with a

10 m-diameter, stall-regulated 20 kW turbine were, among others, key to uncover the importance of specific flow phenomena, such as dynamic stall, 3D rotational effects and tower-wake interactions. Later, multiple aerodynamic models, ranging from blade element momentum (BEM) to computational fluid dynamics (CFD) were validated within the Model rotor EXperiments In controlled COnditions (MEXICO) project thanks to the use of 4.5-m-diameter scaled models, designed to replicate as accurately as possible the aerodynamic behavior of full-scale machines [21]. More recently, the inclusion of closed loop controls [22–24] and aeroservoelastic considerations [25, 26] in the scaling process expanded the scope of wind tunnel testing beyond aerodynamics. Subscaled models are expected to continue playing a significant role in the further development of wind energy, for instance in promising areas such as wind farm flow control [27].

Indeed, it is generally necessary to choose which characteristics of the aeroservoelastic response of the full-scale machine should be replicated by the subscaled rotor, as the exact matching of all relevant physical processes between full-scale and subscaled models is generally not possible. This mismatch increases with the scale ratio, and it becomes especially problematic when large wind turbines are scaled to very small size wind tunnel models. This issue can be relaxed by testing in the field with small-size wind turbines, instead of using very small models in a wind tunnel. Even though some of the limitations typically present in wind tunnel testing are overcome, some of the advantages are also lost. Indeed, measurements are more difficult, costs are higher and the range of testing conditions cannot be controlled. Research in this area has so far focused on steady-state aerodynamic and wake effects. For instance, within the National Rotor Testbed project, a subscaled rotor was designed to replicate the wake of a commercial 1.5MW rotor [28].

The complexity of designing a subscaled machine also depends on the characteristics of the full-scale machine. For instance, one might not be able to neglect the effect of gravity in a scaled wind turbine designed as a replica of a very large wind turbines (with rotors of the order of magnitude of 10^2 m), due to its importance in its loads, stability and performance. Clearly, ensuring that gravitational loads are properly captured by subscaled models require specific conditions in the scaling of time, which increases the complexity of its design. Even though subscaled wind turbines have been designed to mirror different aspects of the full-scale response for decades [26, 33–35], the increasing complexity of their applications [22, 23, 23–25, 29–32] leads to ever more challenging design requirements. Indeed, the full potential of subscaled testing can only be reached with subscaled models that capture the target aeroservoelastic response of a full-machine as faithfully as possible. It is therefore necessary to further understand to which extent a scaled model can replicate the behavior of a full-scale counterpart, and how design choices (i.e. trade-offs between quantities to be matched or choice of subscaled size) play a role in the performance of subscaled models.

Core research question. *To which extent can a subscaled model replicate the aeroservoelastic response of a full-scale counterpart?*

Innovative content. The three publications on the topic of design and performance of scaled machines included in this thesis explore the limitations, design requirements and performance of subscaled models of different sizes, specifically designed to replicate the aeroservoelastic response of very large modern wind turbines.

First, **Paper I** offers one of the most comprehensive analysis of the problems of scaling wind turbines presented thus far – to the author's knowledge. The paper analyzes the scaling conditions that should be met by a subscaled model to match the full aeroservoelastic response of a full-scale reference machine. The analysis shows that many relevant key aspects of the steady and unsteady response of a machine, considered as flexible, can indeed be matched. This analysis can also be applied to understand expected changes due to upscaling, useful for the design of larger rotors. **Paper I** also describes and formulates two alternative ways of designing a scaled rotor. The first is based on the idea

of exactly zooming down the full-scale reference to obtain the subscaled model. An alternative strategy is to completely redesign the rotor, from both an aerodynamic and a structural point of view. This strategy leads to a scaled blade that, although possibly very different from the full-scale one, matches some of its key characteristics as closely as possible. These two alternative strategies are analyzed in **Paper I**, and applied to gravo-aeroservoelastically scale the rotor of a conceptual 10 MW turbine to three different subscaled sizes: two utility-scale sizes that represent small-size turbines tested in the field, and a very small size, typical of wind tunnel models. The faithfulness of the designed subscaled models is measured in their capacity to match several key performance indicators, as well as relevant trends.

The detailed design of a wind tunnel model, capable of mimicking the dynamic behavior of a conceptual 10 MW design is examined in **Paper II**, based on the alternative design approach described in **Paper I**. Finally, **Paper III** further investigates the accuracy of subscaled models. This work extends the analysis presented in **Paper I**, by also looking at the effects of scaling on wake behavior. Additionally, the alternative redesign approach described in **Paper I** is applied to design different full-scale turbine models that match specific quantities of an existing subscaled machine.

METHODS FOR UNCERTAINTY QUANTIFICATION

Background. Wind turbines and the environment in which they operate are profoundly affected by uncertainties. Clearly, including these uncertainties in the design process would be extremely valuable, as robust solutions are often more interesting than very sharp optima, where minor changes in the conditions or parameters might significantly drop important quantities.

Uncertainty quantification – the science of quantifying, characterizing, tracing and managing uncertainty in computational and real word systems – has indeed been a topic of interest of the mathematical community for decades and several methods and techniques have been developed to capture and propagate uncertainties efficiently. While these methods have already been successfully applied to engineering problems of different fields [121, 123], the application of uncertainty quantification techniques in wind energy is still in early stages, in part due to the complexity of the topic and the high computational power required. Indeed, comprehensive wind turbine simulation requires multiphysics models, which are inherently complex and generally present a high computational cost.

Some of the existing studies analyzing the performace of uncertainty quantification methods in wind energy include Witteveen et al. [36], which applies an intrusive formulation of polynomial chaos expansion to analyze the effects of uncertainties affecting the ONERA dynamic stall model; or Petrone et al. [37], where a simplex stochastic collocation (SSC) method was applied to propagate uncertainties on the levels of contamination of the airfoil polars along the span of the blade. Some initial studies on robust design optimization can also be found, for instance Campobasso et al. [38] presented a simple robust design optimization of wind turbine rotor blade, considering uncertainties in the chord and twist distributions and prescribed pitch angle. More recent publications revolve around non-intrusive methods, which are decoupled from the aeroelastic solvers [39, 40].

Clearly, a first step towards the overarching goal of robust design consists in further understanding which uncertainties affect typical design drivers, and to which extent. Due to the high computational cost of the problem, it is also necessary to further investigate which mathematical models can be applied to efficiently propagate these uncertainties.

Core research question. *How are typical design drivers affected by uncertainties in the inputs?*

Innovative content. From the several uncertainty quantification methods available in the literature, **Paper IV** focuses on non-intrusive polynomial chaos expansion (NIPCE) and Kriging. These were identified by a previous work [40] as two promising methods for uncertainty quantification for wind energy. Both methods are applied to propagate a set of uncertain inputs into output quantities of

interest, which are typically related to design drivers. The convergence performance of these methods is benchmarked against a classic Monte Carlo approach. Additionally, the accuracy of the methods to reconstruct the main statistics of key quantities is assessed. Results shown in **Paper IV** are also analyzed to assess the impact of these uncertainties into typical design drivers and the suitability of the safety factors prescribed by international design standards.

1.1.2 Design for economic value

LAC-BASED INTEGRATED DESIGN

Background. Traditional wind turbine controllers rely on feedback measurements to drive blade pitch, generator torque and yaw. Since they operate based on the response of the system as expressed by live measurements, these controllers are only capable of reacting to wind disturbances that have already impacted the wind turbine. This is an intrinsic limitation of all feedback-based mechanisms, which can only see the past but know nothing about the future. To improve on this situation, control systems can be augmented with preview information, which informs the controller about the wind that will affect the turbine in the immediate future. Wind preview can be obtained from turbine-mounted *light detection and ranging* (lidar) sensors, which are capable of measuring various properties of the incoming flow field up to several hundred meters in front of the rotor. Clearly different LAC formulations are certainly possible, with their performance in terms of power capture and load mitigation generally reported in the literature. For instance, studies with a standard feedback controller enhanced by a feedforward blade pitch branch enabled by lidar wind preview indicate promising reductions in blade flap and tower fore-aft fatigue damage, without any appreciable loss in power production [41–43]. Benefits have also been confirmed in the field [44], albeit to the present date only on a small research wind turbine. Feedforward torque control strategies have also been investigated; results indicate marginal increments in mean power capture at the expense of high power and torque variations [41, 45, 46]. More advanced formulations, such as nonlinear model-predictive controllers [47] or flatness-based controllers [48], have also been enhanced with lidar wind preview information. Promising results were reported in terms of load reductions and power increase, at the expense of a much higher computational cost, which makes real-time execution more challenging to achieve and test in the field [49]. Even though the potential of LAC is widely recognized, the system-level benefits that LAC may possibly bring to LCOE are still not fully understood. In general two strategies have been suggested for reducing LCOE by LAC [50]: On one side, a *retrofit strategy* consists in employing lidars to extend the lifetime of a wind turbine that has already been designed and installed [50]. On the other side, an *integrated approach* considers LAC as part of the system from its very inception. The idea in this second case is that, by considering LAC within the design process, its full potential can be realized by translating the benefits of load reductions directly into an improved turbine. Indeed, while the research community widely agrees on the potential benefits of adopting LAC [51, 52], the actual cost-benefit trade-offs among turbine, lidar and control system are still not fully understood.

Core research question. *Can the LCOE of a wind turbine be further reduced through the adoption of a LAC system?*

Innovative content. Paper V and **Paper VI** explore an *integrated approach*. As a first step, the focus is given to the identification of the potential exploitable margins of the three machines analyzed– i.e. to which extent design driving quantities can be affected by LAC to produce a beneficial effect. A further increase would not be interesting, as some other effect beyond the reach of LAC would become the driver. Understanding these boundaries is extremely valuable, as it provides a target maximum margin of improvement that this technology can bring.
The rotor blade and tower of the three reference turbines are redesigned in **Paper V** and **Paper VI**

considering the load reductions brought by LAC. Clearly, direct redesign is not the only strategy to exploit the benefits introduced by an average LAC system. Indeed, **Paper VI** explores two additional pathways to exploit the reduction in tower loads brought by LAC: designing a tower that can reach higher above ground, where the rotor is exposed to faster wind speeds (and thus AEP is higher); or designing a tower for a longer lifetime. The strategies are also assessed in terms of costs.

MARKET-BASED ECONOMIC VALUE

Background. The market price of electricity can widely oscillate due to supply and demand variability, as well as transmission and storage constraints. Indeed, the economic value of a electricity is time- and location-specific [53]. Clearly, if wind turbines are independent from subsidies and directly participate in the energy market, the revenue obtained for selling the energy will depend on the time- and location-dependent economic value of electricity.

In this context, LCOE – the metric generally employed to capture the economic competitiveness of an energy source – is a flawed metric, as it is unable to capture the time-specific economic value of wind energy [54].

It is therefore necessary to define alternative metrics that offer a more complete picture of the value of a wind turbine.

The importance of economic value has additionally not gone unnoticed to the recent literature, and a range of options for increasing the economic value of wind energy has been explored. For instance, several metrics that capture the economic value of a wind turbinee have been proposed [15, 55]. Different strategies to increase the economic value of a wind turbine have been investigated, for instance their geographic location of wind plants – and, more in general, of variable renewable energy plants – and the diversification of the energy mix [56]. Additionally, even the design characteristics of wind-generating assets can change when considering value, rather than simply cost. In fact, some wind turbine design parameters – in particular hub height and specific power (i.e. rated power divided by rotor swept area) – can have a significant effect on economic value [56–58]. It is therefore necessary, not only to define metrics that capture the economic value of wind turbines, but also to further understand which design choices can increase the economic value of a wind turbine.

Core research question. *Can short-term economic and long-term societal benefits brought by a wind turbine be enhanced through its design?*

Innovative content. Paper VII explores how the choice of rotor diameter and hub height can impact the economic value of a wind turbine. Market-based metrics available in the literature are here coupled with a framework to find the optimum hub height and rotor diameter of an average wind turbine in Germany. The paper not only explores the trade-offs between economic value and economic cost, but also juxtaposes these short-term economic needs with long-term sustainable development goals, here represented by environmental impacts.

1.1.3 Design for societal value

ENVIRONMENTAL VALUE

Background. A wind turbine is an eco-friendly machine by definition, as it captures kinetic energy from the wind to produce electricity without directly releasing pollutants into the environment. Additionally, the deployment of each new wind turbine displaces a certain amount of GHG emissions, because other more polluting energy sources are not required anymore. However, even wind turbines have an environmental impact, as non-negligible amounts of GHGs are emitted throughout the different stages of their life. For example, the production of the large amount of steel needed for the tower, or the

extraction of raw materials – such as the rare-earth elements present in the generator –, have significant environmental impacts. Clearly, all stages of the life-cycle of a wind turbine –from the extraction of raw materials to the eventual disposal/recycling/repurposing of its components–, generate impacts that can be quantified in terms of equivalent CO_2 emissions.

Recent studies [59–63] have evaluated the environmental impact of a wind turbine, while other sources [64, 65] have also analyzed the GHG displacement of wind energy. However, formal definitions of metrics that capture these quantities – and the societal benefits associated – are still missing. Additionally, the effect that the design of a wind turbine can have on these environmental quantities is still not understood.

Core research question. *Can short-term economic and long-term societal benefits brought by a wind turbine be enhanced through its design?*

Innovative content. Paper VII introduces novel metrics to quantify the environmental cost and value of a wind turbine. These metrics are defined exploiting the parallelism with familiar economic concepts: environmental cost can be understood as the GHG emitted during the lifetime of a wind turbine – similarly to economic cost; and environmental value can be defined as the environmental benefits of deploying a wind turbine – i.e. GHG displaced. Additionally, the social cost of carbon (SCC) – an estimate of the net present value of monetized social damages occurring from the emission of an additional metric ton of CO_2 [66, 67] is applied to transform actual environmental value into future societal savings. **Paper VII** also employs these metrics for the preliminary design of an average reference wind turbine in two locations of Germany.

1.1.4   Overview: core research questions

The main high-level core questions discussed in this thesis are listed as follows:

- To which extent can a subscaled model replicate the aeroservoelastic response of a full-scale counterpart?

- How are typical design drivers affected by uncertainties in the inputs?

- Can the LCOE of a wind turbine be further reduced through the adoption of a LAC system?

- Can short-term economic and long-term societal benefits brought by a wind turbine be enhanced through its design?

1.2   List of publications

This publication-based dissertation collects seven publications, which are referred to in the text as **Papers I-VII**. Fig. 1.3 shows an overview of the different publications, while the publications included in this thesis are listed in Sect. 1.2.1. **Papers I-III** focus on the design and performance of scaled rotors. Indeed, **Paper I** offers a general analysis on the requirements and limitations of scaling, as well as the description of two different approaches to design a scaled rotor. Three scaled wind turbines of different sizes are here designed and their performance is assessed. The design of a wind tunnel model following gravo-aeroservoelastic scaling laws is detailed in **Paper II**, while **Paper III** focuses on the accuracy of wakes of scaled models.

Paper IV includes a study on the convergence of different methods to propagate the uncertainties of selected inputs into key quantities of interest related to design drivers.

Paper V and **Paper VI** look into the potential benefits of considering lidar-assisted control (LAC) within

the design of two key components of a wind turbine: the tower and the blade. Additionally, **Paper VI** analyzes the potential exploitable margins of the design drivers of three different reference machines and three pathways to exploit the benefits introduced by LAC in the design of these two components. Finally, **Paper VII** introduces eco-conscious metrics that quantify the environmental impact and value of wind energy. The parallelism between economic and eco-conscious metrics is here detailed and the metrics are applied to guide the preliminary sizing of a wind turbine.
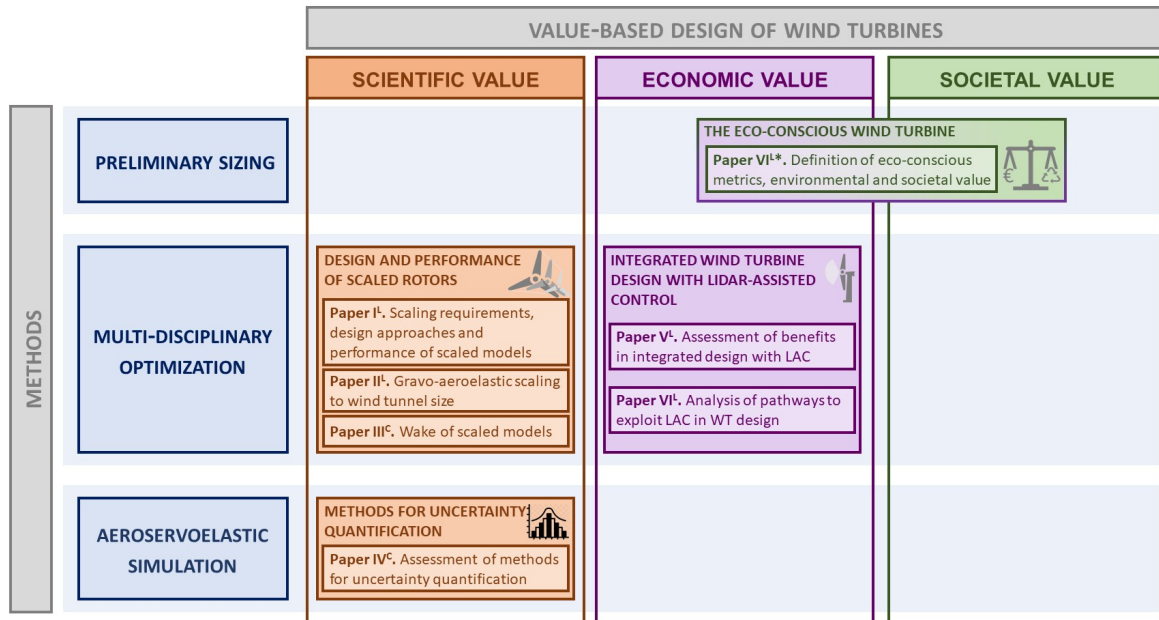
Figure 1.3: Schematic overview of the thesis structure in terms of publications, content and methods; *: paper in review; ^{L}: leading author; ^{C}:co-author

1.2.1 List of publications

This section lists the publications collected in this dissertation. While most have already been published on peer-reviewed journals, **Paper VII** is still in the review process. The summary of each paper and description of the contribution of each author is described in Chapters 3, 4 and 5.

Publications led by the author:

- **Paper I**: H. Canet, P. Bortolotti, and C. L. Bottasso, "On the scaling of wind turbine rotors," *Wind Energy Science*, vol. 6, no. 3, pp. 601–626, 2021. doi: 10.5194/wes-6-601-2021

- **Paper II**: H. Canet, P. Bortolotti, and C. L. Bottasso, "Gravo-aeroelastic scaling of very large wind turbines to wind tunnel size," *Journal of Physics: Conference Series*, vol. 1037, no. 042006, 2018. doi: 10.1088/1742-6596/1037/4/042006

- **Paper V**: H. Canet, S. Loew, and C. L. Bottasso, "Lidar-assisted control in wind turbine design: Where are the potential benefits?" vol. 1618, no. 042020, 2020. doi: 10.1088/1742-6596/1618/4/042020

- **Paper VI**: H. Canet, S. Loew, and C. L. Bottasso, "What are the benefits of lidar-assisted control in the design of a wind turbine?" *Wind Energy Science*, vol. 6, no. 5, pp. 1325–1340, 2021. doi: 10.5194/wes-6-1325-2021

- **Paper VII**: H. Canet, A. Guilloré, and C. L. Bottasso, "The eco-conscious wind turbine: bringing societal value to design," *Wind Energy Science Discussions*, 2022

Publications with significant scientific contribution by the author:

- **Paper III**: C. Wang, F. Campagnolo, H. Canet, D. J. Barreiro, and C. L. Bottasso, "How realistic are the wakes of scaled wind turbine models?" *Wind Energy Science*, vol. 6, no. 3, pp. 961–981, 2021. doi: 10.5194/wes-6-961-2021

- **Paper IV**: P. Bortolotti, H. Canet, C. L. Bottasso, and J. Loganathan, "Performance of non-intrusive uncertainty quantification in the aeroservoelastic simulation of wind turbines," *Wind Energy Science*, vol. 4, no. 3, pp. 397–406, 2019. doi: 10.5194/wes-4-397-2019

Methods

This chapter describes the existing and novel methods that have been developed and integrated to conduct the work presented in this thesis. Three main methods are therefore here presented: the framework for preliminary sizing applied in **Paper VII**, the multi-disciplinary optimization framework `Cp-Max`, which is modified and implemented for **Papers I-III** and **Papers VI-V**, and the uncertainty quantification methods applied in **Paper IV**.

Fig. 2.1 provides an overview of the architecture of the three methods here presented. While each of these methods is independent and has been developed for a specific purpose, several of the underlying models and tools – such as the aeroelastic solver or the pitch-torque controller – are common. These models are colored blue in Fig. 2.1, while the models and algorithms specifically formulated for a method are colored differently. It should be noted that these illustrations are simplifications of the real architecture of each method, which is more complex – as described in the next sections.

This chapter is divided in four sections: First, Sect. 2.1 introduces the underlying models and tools
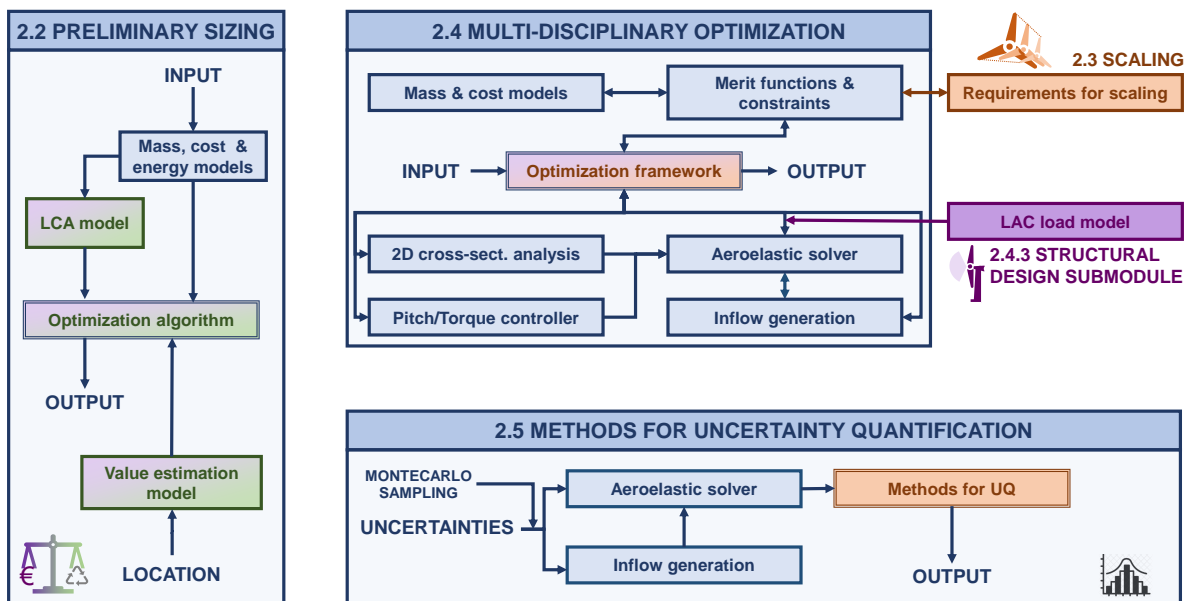
Figure 2.1: Overview of the methods, models and tools applied for the work presented in this thesis. The architecture of each method has been simplified for illustration purposes.

presented in Fig. 2.1. Sect. 2.2 briefly describes the tools and methods defined for the preliminary sizing based on economic and environmental metrics presented in this thesis. Next, Sect. 2.3 derives design requirements for scaled rotors, and formulates two alternative design approaches. Sect. 2.4 formulates the multi-disciplinary optimization tool `Cp-Max`, and its application for the design of scaled models. Sect. 2.4.3 describes the blade and tower structural optimization algorithm, and introduces

the LAC load-reduction model. Finally, Sect. 2.5 reports the methods for uncertainty quantification applied in the study presented in this thesis.

2.1 Models and tools

2.1.1 Aeroelastic solver

The aeroelastic solver used in this thesis is `Cp-Lambda` [105]. The code is based on a multibody formulation for flexible systems with general topologies described in Cartesian coordinates. A complete library of elements, including rigid bodies, nonlinear flexible elements, joints, actuators and aerodynamic models is available, as well as sensor and control elements. The aerodynamic characteristics of the blades are described through lifting lines, including spanwise chord and twist distribution and aerodynamic coefficients. The code is coupled with aerodynamic models based on a BEM model, formulated according to stream-tube theory with annular and azimuthally-variable axial and swirl inductions, unsteady corrections, root and blade tip losses as well as a dynamic stall model. The tower and rotor blades are modeled by nonlinear geometrically-exact beams of arbitrary initially undeformed shapes, which are bending, shear, axial and torsion deformable.

2.1.2 Pitch-torque controller

A wind turbine is governed by controllers interfaced by external dynamic libraries. A supervisory unit manages the dynamic behavior by switching among different operating states and handling emergencies. The blade pitch and torque are governed by two controllers that operate in closed-loop with the machine, based on data supplied by sensor models. The work in this thesis employs two different collective-pitch/torque controllers:

The controller employed within the studies presented in **Papers I-III**, requires a look-up table for torque to operate at rated TSR in region II, and a proportional-integral-derivative (PID) pitch loop to maintain constant rated power in region III. The scaled models designed and analyzed in these studies considered scaled PID gains, which are obtained by applying the scaling laws to the PID gains of the full-scale machine. The regulation trajectory of each model is adapted to account for differences in the C_P-TSR curves.

The work presented in **Papers IV-VI** considers a linear quadratic regulator (LQR) controller, described in [75]. This formulation has been shown to be useful in a design context, as a new sets of gains that work in combination with the new design are automatically produced. Indeed, in each iteration the underlying reduced order model is updated as the wind turbine parameters change.

2.1.3 Inflow generation

A numerical inflow turbulence tool provides numerical simulations of full-field flows containing coherent turbulent structures that a wind turbine can encounter during its lifetime. The tool here employed is `TurbSim` [76], an stochastic, full-field, turbulent wind simulator. This tool generates wind grids based on different turbulent models – such as Kaimal or von Karman – based on a list of inputs, including grid characteristics (height, width, number of points), and meteorological boundary conditions (turbulence model, turbulence characteristics, mean wind speed or wind profile type). These wind grids serve as input for the aeroservoelastic simulator `Cp-Lambda`. `TurbSim` generates the wind grids for the studies presented in **Papers I-VI**. However **Paper I** and **Paper IV** combine this inflow generator with other tools.

Indeed, **Paper I** analyzes the performance of scaled models, which require the scaling of all inputs

– including wind conditions. Therefore, for this work, the wind grid files created with `TurbSim` are correspondingly scaled, following the scaling laws defined for each scaled model. Additionally, this work also analyzes the performance of the scaled models under waked conditions. The wake is here modeled by the superposition of a turbulent wind grid generated with `TurbSim` and the first order solution of the deficit of the Larsen model (EWTSII model) [77].

Paper IV analyzes the propagation of several uncertainties in the inputs, including wind characteristics. Therefore, the inputs of `TurbSim` are not deterministically predefined, but stochastically defined following a Monte Carlo strategy.

2.1.4 2D cross-sectional analysis

The finite element cross sectional analysis code `ANBA` (<u>AN</u>isotropic <u>B</u>eam <u>A</u>nalysis), based on the theory of Giavotto et al. [78], is here employed. `ANBA` produces the six-by-six stiffness matrix defining the sectional characteristics at a specific spanwise location of the blade. Additionally, `ANBA` computes the sectional moments of inertia, as well as the coordinates of the mass center and shear center. `ANBA` also computes the unit stress and unit deformation of each panel modeling, in turn enabling the computation of internal states of stress and strain for each blade structural component.

2.1.5 Cost model

Cost models estimate the cost of the different components of a wind turbine, as well as balance-of-station costs and maintenance costs. These costs usually scale with the mass of the component, or with turbine macroparameters such as rotor diameter, rated power or hub height [80].

The work here presented is based on the combination of three cost models, which are generally used for academic projects. The 2015 NREL cost model [79] – an updated version of the 2006 cost model [80] – is applied for onshore wind turbines. The cost of the components of offshore wind turbines is estimated with the INNWIND cost model [81], which was specifically designed to capture the cost trends of very large turbines.

While the estimation of blade cost is performed with the NREL cost model in **Paper VII**, a more sophisticated model is applied for **Papers V** and **VI**. Indeed, here the blade cost is estimated with the highly detailed SANDIA blade cost model [82], which also considers material, labor and equipment costs.

The output of these models are expressed in 2017 € for **Paper VII**, and in 2020 € for **Papers V** and **VI**, correspondingly inflated by the consumer price index and exchange rate.

2.1.6 Mass model

The optimization exercises in this thesis focus on the design of the blade and tower (**Papers I-III**, **Papers V-VI**). The mass of these components is therefore an output of these optimization activities. However, a mass model is required to estimate the mass of other components – such as generator, hub or drive train. **Papers I-VI** employ the NREL mass model 2017 [79], an updated version of the 2006 cost and scaling model [80] for onshore turbines, while the INNWIND mass model [81] is applied for offshore turbines. Generally, these mass models scale with turbine macro parameters, such as rotor diameter or hub height.

The mass model is extended with two additional submodels for **Paper VII**. Indeed, for the work there presented, the mass of all components is further broken down into a detailed bill of materials, based on a set of assumptions [59, 61–63, 83, 84]. The material breakdown model provides the requirements of 15 different materials: glass fibers, carbon fibers, Epoxy resin, sandwich foam, alloyed steel, un-alloyed steel, galvanized steel, copper, aluminium, PVC and other plasts, rubber, paint and coating,

Neodymium permanent magnet (NdFeB), electronics and concrete.

Finally, a waste factor model computes the quantity of materials wasted during the different life-cycles. Waste factors for fiberglass, epoxy resin, foam, rubber, paint and coating are modeled according to the NREL 2019 Detailed Wind Turbine Blade Cost Model [85], while a factor of 5% is considered for the other materials.

2.1.7 Energy model

The energy production of the machines considered in **Papers I-VI** is quantified through aeroelastic simulations. An energy model is however employed in **Paper VII** to estimate the energy produced by the wind turbine in a specific location during a specific year y. E_y is here estimated as T_y AF PF WF $\int_{U_{in}}^{U_{out}} P(U) W_y(U) dU$, where T_y is the year in hours, $P(U)$ represents the power curve of the wind turbine, $W_y(U)$ is the Weibull probability of the site in the year y and U_{in} and U_{out} are the cut-in and cut-out wind speed respectively.

The model considers three correction coefficients: availability factor (AF), performance factor (PF) and wind factor (WF). AF considers failure, maintenance and curtailment time. A standard coefficient of 98% is considered [61–63, 86]. PF considers different sources of losses such as turbulence and gust losses or wake losses and usually take values between 65% and 75% [57]. A value of 65% is considered here. Finally, WF describes possible deviations of the wind resource from the normalized design Weibull distribution for yearly performance variance [57]. A WF of 100% is considered as $W_y(U)$ will be defined based on real data, and therefore already contains this variability.

2.2 Preliminary sizing

2.2.1 LCA model

An attributional literature-sourced Life-Cycle Assessment (LCA) model is defined and applied in **Paper VII** to estimate the GHG emitted during the life-cycle of a wind turbine. LCA is a normed scientific methodology to exhaustively assess the environmental impacts of a product or a service, over its whole lifetime from cradle to grave. Here LCA is performed by an in-house-developed literature-sourced model that follows the environmental management standards of the International Organization for Standardization (ISO), according to ISO 14040 and ISO 14044 [87,88]. Sect. 2.2.1 describes the different life-stage cycles considered, as well as the assumptions taken. The objective of the LCA model is to assess the complete life-cycle GHG emissions associated with the production of one functional unit, which in this case is 1 kWh of electricity. Emissions are broken down in terms of life-cycle stages, components and materials. Only climate-change-related environmental impacts are considered, and other effects such as human toxicity, eco-toxicity, acidification or resource depletion are excluded.

The model is formulated in a parametric way, i.e it is not specific to a given wind turbine model, and it is generally applicable to contemporary onshore variable-speed horizontal-axis technology. It is assumed that the turbine is installed in Europe between 2015 and 2025, and has a lifetime of 20 years. The machine is composed by rotor, nacelle, drivetrain, tower and foundation, and the elements within these components, i.e. generator or shaft; connection to the grid, storage or other equipment and devices are outside of the scope of this model.

The processes involved in each one of the life-cycle stages are modeled based on typical scenarios from several sources [59, 61–63, 83, 84, 89], among others. Emission factors are based on Ecoinvent IPCC 2013 [90–92].

This LCA method considers the atmospheric emissions of all gases that are recognized to have a greenhouse effect, including CO_2, CH_4, N_2O and fluorinated gases. For each one of these gases,

the mass of CO_2 that would have the same greenhouse effect is defined and used as a measure of impact [90, 92].

Life-cycle stages

This section briefly defines the life-stages considered, and the assumptions taken in each of them, which are further detailed in **Paper VII**.

- **Life-cycle stage 1: Raw material extraction and processing.** This stage accounts for the environmental impact upstream of the purchasing of a unit of ready-to-use material for manufacturing. The impact of each unit of raw material extracted and processed is modelled according to the databank *Ecoinvent* [91].

- **Life-cycle stage 2: Transportation of raw materials to manufacturing sites.** This stage considers both direct emissions caused by the burning of transportation fuel, and indirect emissions produced in the life-cycle of the fuel from well to tank. Indirect emissions from the production of the transportation technology itself are also included. Assumptions on transportation distances are based on [61–63], while transportation emissions are considered from [91], assuming that materials are transported by freight and lorry [93].

- **Life-cycle stage 3: Wind turbine component manufacturing.** This stage considers the environmental impact of the energy consumed for the transformation of the materials into wind turbine components. The upstream environmental impact of the energy consumed – which is generally electricity from the grid and whose impact depends on the specific electricity mix – is also considered. Manufacturing emissions are obtained from several sources [91, 94, 95].

- **Life-cycle stage 4: Transportation of the components to the wind plant site.** The same assumptions on transportation vehicles of the life-cycle stage 2 are taken, adding ship transport. Assumptions on transportation distances are modeled from [61–63].

- **Life-cycle stage 5: Assembly and installation of the wind turbine.** This life-cycle stage considers the direct and indirect emissions from the assembly and installation of the different components. Assumptions on utilization of heavy machinery per turbine are defined according to [59, 89].

- **Life-cycle stage 6: Operation and maintenance (O&M).** This stage considers different impacts related to operation and maintenance, and is defined according to [59, 61–63, 83, 84, 89]. The GHG emitted during O&M are determined as the sum of emissions related to lubricant oil change, the use of inspection van and maintenance crane, and related to the replacement of components, as detailed next.

  - **Lubricant Oil.** The oil employed for the regular change of gearbox oil and lubricant is here considered. Assumptions are taken according to [59, 84, 89].

  - **Inspection van.** It is here assumed that a roundtrip from the maintenance base is required every 6 months [59] with a diesel passenger car of emission category EURO4 [93].

  - **Maintenance Crane.** It is considered that heavy crane machinery is required for a total of 8 hours over the turbine lifetime [59].

  - **Components replacements.** All components may be subjected to failures, and generally several parts need to be replaced over the lifetime of a wind turbine. Failure rates are here modeled according to [59, 83, 84, 96]. Life-cycle stages 1 to 5 are used to estimate the emissions resulting from the spare components that need to be replaced. Additionally, the impact of the transport of the replacement components to the site is doubled, to account for the trip back with the defect replaced components.

- **Life-cycle stage 7: Decommission and transportation of parts.** This life-cycle stage considers 16 hours of crane work, as described in [59, 89]. The same assumptions taken for the life-cycle stage 4 are used also here to estimate the emissions caused by the transportation of the parts to their End-of-life (EOL) treatment centers.

- **Life-cycle stage 8: End-of-life treatment** The End-of-life (EOL) scenario is a key stage in the life of a wind turbine. Three treatments are here considered: recycling, incineration and landfilling. In accordance with ISO 14044 [87, 88], the approach of closed-loop material cycle is considered, where full credit is given to the emissions of life-cycle stage 1 linked to the recycled materials. Recycled materials are considered to have a negative impact and thus represent environmental benefits. Metals – steel, copper and aluminium – currently present high recyclability rates, as shown in Fig. 2.2 [61–63, 84, 96, 97]. On the other hand, there is no wide-spread mature technology yet for the recycling of the thermoset glass-fiber reinforced polymers (GFRP), which are currently incinerated or landfilled [97, 98], depending on the legislation of the country. A representative scenario of 50% incineration and 50% landfilling is here assumed, as described in [61–63]. The overall EOL impact is the sum of the recycling, incineration and landfilling environmental impacts. This quantity can either be positive or negative, depending on whether the recycling benefits outweigh the incineration and landfilling environmental impact.
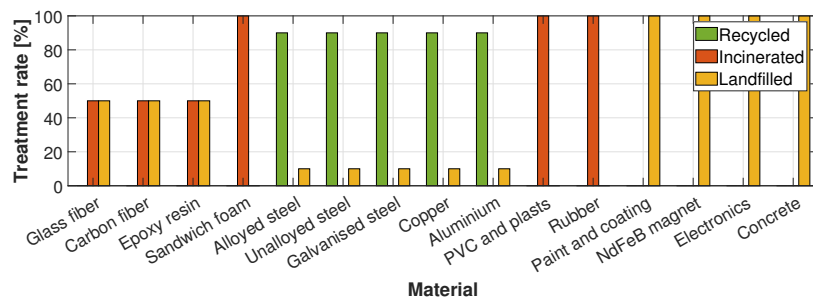
Figure 2.2: EOL treatment rates (by mass) for various materials types.

Validation of the LCA model

The LCA model was validated against results presented in [59–63, 96, 99], as shown in Fig. 2.3. In
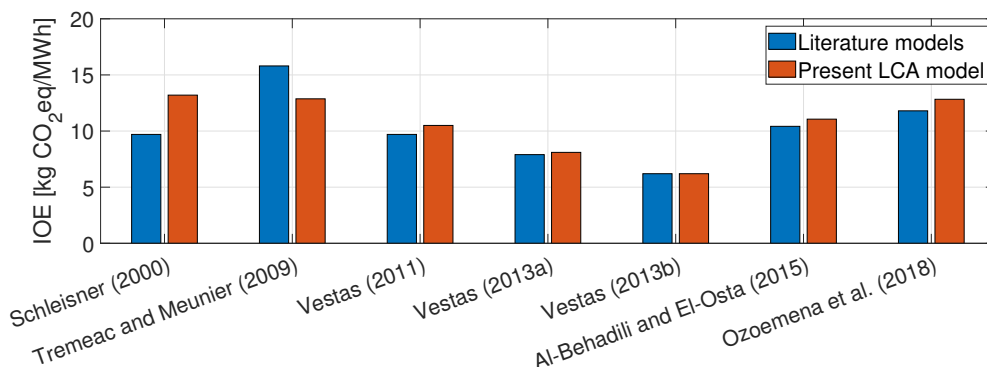

Figure 2.3: Comparison of the environmental impact obtained with the present LCA model and with results sourced from the literature.

general, there is a good match between previous studies and the present model. Differences arise due

to non identical hypotheses and assumptions, for instance in life-cycle scenarios, bill of materials, or energy production. Indeed, several publications do not thoroughly detail the assumptions taken, or the processes considered in the different life-stage cycles, which hinders an exact comparison.

2.2.2 Value estimation model

The studies presented in **Paper VII** require the implementation of a value estimation model to quantify the economic and environmental value of the analyzed wind turbine, for a specific location and a specific time frame, as illustrated in Fig. 2.4.
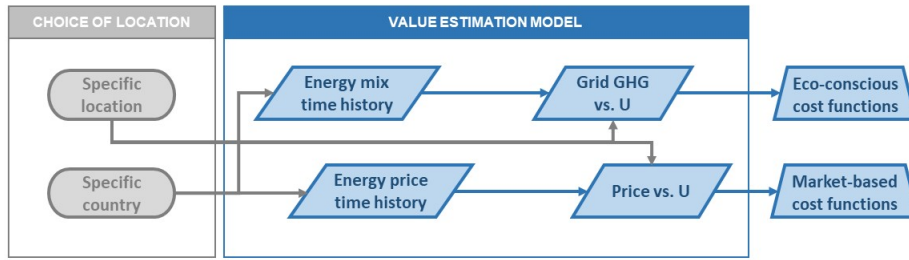
Figure 2.4: Workflow of the value estimation model of Fig. 2.1. Rounded squares represent variables, squares are models, rhombuses are data, and trapezoids are merit functions.

The estimation of economic value is based on historical data. The time series of the spot market price were correlated with the time series of wind speed at a specific location and hub height, resulting in the price-wind model $p_y(U)$. The economic value V_y is therefore estimated as

$$V_y = T_y \int_{U_{\text{in}}}^{U_{\text{out}}} p_y(U) P(U) W_y(U) \, dU, \tag{2.1}$$

where T_y is year y in hours, $P(U)$ is the power produced by the wind turbine at a specific wind speed, $w_y(U)$ is the Weibull probability of the specific location in the year y.

Similarly, the environmental value was estimated based on the energy mix time history of the country (or region where the turbine is located. Therefore V_y^{env} is estimated as

$$V_y^{env} = T_y \int_{U_{\text{in}}}^{U_{\text{out}}} f_{grid,y}(U) P(U) W_y(U) dU, \tag{2.2}$$

where $f_{grid,y}$ is the emission factor of the grid which depends on the wind speed seen by the wind turbine. The average emission factor of each generation technology in the mix was obtained from the database `Ecoinvent` [91] and only considers operational emissions [65, 100]. The wind speed time history used to estimate the Weibull distribution $W(U)$, as well as to correlate the spot market price and the grid average emission factor was adjusted to the hub height of the turbine based on the mean shear of the specific location, also computed based on the historic data considered.

2.2.3 Constrained optimization

Two different design problems are considered, based on either a single- or a two-objective constrained optimization. In both cases, the problem is formulated as:

$$\min_{\mathbf{p}} \quad J(\mathbf{p}), \tag{2.3a}$$

$$\text{such that:} \quad \mathbf{c}(\mathbf{p}) \leq 0, \tag{2.3b}$$

where J is the cost function to be minimized, $\mathbf{p} = (D, H)$ are the design variables, with D the rotor diameter and H the hub height. Finally, $\mathbf{c}$ are inequality constraints that enforce desired design conditions. The single-objective optimization problem is solved with a sequential quadratic programming algorithm, in which gradients are computed by means of finite differences [101]. The multi-objective optimization problem is solved with a non-dominating sorting genetic algorithm (NSGA-II) [102].

2.3 Aerostructural design of scaled rotors

This section defines scaling laws and applies these laws to design a scale rotor. The section is divided into two parts. First, Sect. 2.3.1 describes the theoretical background of scaling. Here, the choice of nondimensional parameters is discussed. Sect. 2.3.2 describes two different approaches to design a scaled model that satisfies the desired matching conditions.

2.3.1 Theoretical background: requirements for scaled rotors

The Buckingham's Π Theorem [103] states that a scaled model – here labeled $(\cdot)_M$ – has the same behavior as a full-scale physical system – here labeled $(\cdot)_P$ – if all the m relevant nondimensional variables π_i are matched between the two systems. In other words, when the governing equations are written as

$$\phi(\pi_{1P}, \ldots, \pi_{mP}) = 0, \tag{2.4a}$$

$$\phi(\pi_{1M}, \ldots, \pi_{mM}) = 0, \tag{2.4b}$$

then the two systems are similar if

$$\pi_{iP} = \pi_{iM}, \quad i = (1, m). \tag{2.5}$$

The length (geometric) scale factor between scaled and full-scale systems is defined as

$$n_l = \frac{l_M}{l_P}, \tag{2.6}$$

where l is a characteristic length (for example the rotor radius R), whereas the scale factor for time t is defined as

$$n_t = \frac{t_M}{t_P}. \tag{2.7}$$

As a consequence of the definition of the time and length scale factor, one can determine the angular velocity and wind speed scaling factors, which respectively write $n_\Omega = \Omega_M/\Omega_P = 1/n_t$ and $n_v = V_M/V_P = n_l/n_t$. Nondimensional time can be defined as $\tau = t\Omega_r$, where Ω_r is a reference rotor speed; for example, the rated one. It is readily verified that, by the previous expressions, nondimensional time is matched between the model and physical system, i.e. $\tau_M = \tau_P$. These two factors condition, to a large extent, the characteristics of a scaled model. No matter what choice is made for these parameters, the exact matching of some nondimensional parameters can always be guaranteed; while others cannot be simultaneously matched, and one has to make a choice. The next sections describe the requirements to match rotor and wake aerodynamics, gravitational and elastic forces. Table 2.1 gives an overview into the main scaling relationships, described in the next sections.

Rotor and wake aerodynamics

- The matching of the scaled and full-scale TSR is readily verified by any combination of n_l and n_t. Therefore, it is always possible to match the scaled and full-scale TSR and ensure the same velocity triangle at the blade sections and the same wake helix pitch.

Table 2.1: Main scaling relationships relevant to a wind turbine. Additional scaling effects are discussed in the text. The analysis considers that testing is performed in air, either in a wind tunnel or in the field, neglecting hydrodynamics.

Quantity	Scaling ratio	Coefficient	Comment
Length	l_M/l_P	n_l	
Time	t_M/t_P	n_t	
Nondimensional time	τ_M/τ_P	1	
TSR λ	λ_M/λ_P	1	
Rotor speed	Ω_M/Ω_P	$1/n_t$	Due to nondimensional time matching
Wind speed	U_M/U_P	n_l/n_t	Due to nondimensional time & TSR matching
Mach number	$\mathrm{Ma}_M/\mathrm{Ma}_P$	n_l/n_t	
Reynolds number	$\mathrm{Re}_M/\mathrm{Re}_P$	n_l^2/n_t	
Froude number	$\mathrm{Fr}_M/\mathrm{Fr}_P$	n_l/n_t^2	
Strouhal number	$\mathrm{St}_M/\mathrm{St}_P$	1	Due to TSR matching
Rossby number	$\mathrm{Ro}_M/\mathrm{Ro}_P$	1	Due to TSR matching
Lock number	$\mathrm{Lo}_M/\mathrm{Lo}_P$	1	Requires $\rho_{mM} = \rho_{mP}$
Nondimensional nat. freq.	$\widetilde{\omega}_{iM}^n/\widetilde{\omega}_{iP}^n$	1	Requires $K_M = K_P n_l^6/n_t^2$
Deflections due to aero. loads	$\widetilde{s}_M/\widetilde{s}_P$	1	Due to Lock & nondim. freq. matching
Reduced frequency	κ_{jM}/κ_{jP}	1	Requires $(\widetilde{\omega}_{m_j})_M/(\widetilde{\omega}_{m_j})_P$ due to inflow, pitch and vibrations
Nondim. TSR rate of change	λ'_M/λ'_P	1	Requires $(Q_e + Q_m)_M = (Q_e + Q_m)_P n_l^5/n_t^2$, $\rho_{mM} = \rho_{mP}$ and $(U'/U)_M = (U'/U)_P$

- Ideally, a scaled model should match the full-scale C_P and C_T coefficients over a range of conditions. These coefficients – as shown by BEM theory – depend on the steady-state aerodynamic characteristics of the airfoils. In turn, the lift C_L and drag C_D coefficients of the aerodynamic profiles depend on the angle of attack and on the Mach and Reynolds numbers:

  - The local Mach number accounts for compressibility effects. Because of typical tip speeds, compressibility does not play a significant role in wind turbines and the matching of the Mach number can be usually neglected for current wind turbines.

  - The Reynolds number represents the ratio of inertial to viscous forces and has a strong effect on the characteristics and behavior of the boundary layer that develops over the blade surface, which in turn, through the airfoil polars, affects the performance and loading of the rotor. The effects due to a chord-based Reynolds mismatch can be mitigated by replacing the airfoils of the full-scale system with others better suited for the typical Reynolds conditions of the scaled model. Another approach is to increase the chord of the scaled model, which will however increase rotor solidity and might have additional consequences.

- Additionally, chord c and lift C_L are further constrained by the circulation $\Gamma = 1/2cC_LW$, which plays an important role in the aerodynamics for the rotor and its wake. Indeed, desiging a blade that matches the spanwise distribution of Γ ensures that the scaled rotor sheds the same trailed vorticity. It also ensures a matched thrust, which is largely responsible for the speed deficit in the wake and for its deflection in misaligned conditions.

- The Rossby number represents the ratio of inertia to Coriolis forces. This number is therefore always matched for any choice of n_l and n_t.

- The Strouhal number is associated with vortex shedding, relevant in tower and rotor wake behavior. This number is always exactly matched when TSR is matched.

Gravity

- The Froude number represents the ratio of aerodynamic to gravitational forces. Enforcing Froude results in the time scaling factor being set to $n_t = \sqrt{n_l}$. This scaling is used when gravity plays an important role, for example in the loading of very large rotors or for floating offshore applications where weight and buoyancy forces should be in equilibrium.

Elasticity

- Nondimensional deflections can be matched, provided that the stiffness can be adjusted as $(EJ)_M = (EJ)_P n_l^6 / n_t^2$, where EJ is the bending stiffness, E is Young's modulus, and J is the cross-sectional moment of inertia.

- The same conclusion is reached, when looking at the matching of nondimensional natural frequencies. Indeed, the system ith nondimensional natural frequency is defined as $\tilde{\omega}_i = \omega_i / \Omega$, where $\tilde{\omega}_i$ is the ith dimensional natural frequency. Matching the lowest N nondimensional frequencies means that the corresponding eigenfrequencies in the scaled and full-scale system have the same relative placement among themselves and with respect to the harmonic excitations at the multiple of the rotor harmonics. By matching nondimensional frequencies, the ratio of elastic to inertial forces is correctly scaled.

- Considering the blade flapping, the Lock number Lo is defined as:

$$Lo = \frac{C_{L,\alpha} \rho c R^4}{I_b} \tag{2.8}$$

where I_b is the blade flapping inertia. Matching the Lock number ensures the same ratio of aerodynamic to inertial forces. Considering that the flapping inertia is dimensionally proportional to $[\rho_m][l]^5$, where ρ_m is the material density and l a characteristic length, matching the Lock number can be obtained by simply matching the material density of the blade, i.e., $\rho_{mM} = \rho_{mP}$.

Subscaling criteria: choice of length and time scaling factors

As previously discussed, scaling is essentially governed by two parameters: the geometric scaling factor n_l and the time scaling factor n_t, whose definition is highly problem dependent. On the one side, n_l is usually set by the size of the scaled replica – which is usually predefined –, given a full-scale reference. For instance, the two utility-size scale blades introduced in **Paper I** are designed as a reblading of an existing turbine. The n_l factor is therefore defined after the given full-scale replica and the size of the already existing turbine. On the other side, the n_l factor of the wind tunnel rotor designed in **Paper I** and **Paper II** is chosen to limit blockage. The choice of n_t is often not straightforward and implies trade-offs among quantities that cannot be simultaneously matched. **Papers I** and **II** focus on the design of subscale rotors that mimic a 10 MW machine, where gravity plays a large role. For this reason, n_t is defined as $n_t = \sqrt{n_l}$, ensuring the matching of aerodynamic to gravitational forces. **Paper III** deals with the upscaling of a rigid scale rotor, neglecting all gravo-aeroelastic effects, and setting n_t to minimize the error in the Reynolds number and the acceleration of scaled time – selected to relax the requirements on closed-loop control sampling time.

2.3.2 Design strategies

Two different strategies are here described to design a scaled blade that satisfies the conditions aforementioned.

Straightforward zooming-down

This strategy is based on the exact geometric zooming of the blade, including both its external and internal shape [104]. The geometric zooming of the external blade shape implies that the same airfoils are used for both the scaled and the full-scale models. The mismatch of the Reynolds number may imply a different behavior of the polars, especially for large values of n_l. On the other hand, as shown earlier, a geometric scaling ensures the near matching (up to the effects due to changes in the polars) of various characteristics, such as optimum TSR, nondimensional circulation, rotational augmentation and vorticity shedding.

This strategy is found in **Paper I** to be the most simple for the design of the two utility-size models. Indeed, the airfoil polars at the sub-scale Reynolds still showed a good performance. Even though a redesign approach with alternative airfoils was not attempted, it would most likely lead only to marginal improvements of the aerodynamic performance. A different conclusion was reached for the design of the wind tunnel model in **Paper I** and **Paper II**, because of the small geometric scaling factor. Indeed, for this application, the original airfoils presented a large reduction in aerodynamic efficiency at the sub-scale Reynolds.

Regarding the internal blade shape, the skin, shear webs and spar caps are also geometrically scaled down when using straightforward zooming. It should be noted that, for large geometric scaling factors n_l, the thickness of elements such as the skin or the shear webs may become very thin, possibly less than typical composite plies. The zoomed scaling has to satisfy two constraints on the properties of the materials used for its realization.

A first constraint is enforced in the density of the materials used ($\rho_{mM} = \rho_{mP}$), which is necessary to ensure the same Lock number. It should be remarked that the overall material density of the blade includes not only the density of the main structural elements, but also contributions from coatings, adhesive and lightning protection. These components may not be simply scaled down, so this problem may deserve some additional attention.

A second constraint is enforced in the scaling of the stiffness, which is necessary to ensure the matching of nondimensional natural frequencies. For Froude scaling, stiffness changes as $K_M = K_P n_l^5$. Considering bending, the stiffness can be simplified as $K = EJ$. Since the sectional moment of inertia J is dimensionally proportional to l^4, – l being a characteristic length of the blade cross section —, this constraint requires the Young's modulus to change according to $E_M = E_P n_l$. This implies that all materials in the scaled blade, including the core, should have a lower stiffness (and the same density) than the materials used at full scale, a constraint not easily met.

The application of this approach to design the structure of the utility-size models in **Paper I** is found to be challenging. Indeed, the identification of suitable materials and consideration of manufacturability constraints is found to increase the complexity of the approach. Additionally, this approach can not be used for the wind tunnel models of **Paper I** and **Paper II** due to the differences in external shape.

Aerostructural redesign

An alternative approach to design scaled model consists in identifying an external shape and an internal structure that match, as closely as possible, the aeroelastic behavior of the full-scale blade. This approach offers more degrees of freedom at the cost of an increased design complexity; indeed, one designs a new blade that, although completely different from the full-scale one, matches some of its characteristics. In this second approach, the first step consists in defining a blade shape that can mimic the aerodynamic behavior of the full-scale system.

First, an alternative set of airfoils is selected to match as closely as possible the polar coefficients of the airfoils of the full-scale blade – despite the different Reynolds of operation. Second, the two rotors should have similarly shaped power coefficient curves, which is relevant for performance on and off the design point. Finally, the blades should have the same spanwise circulation distribution, which is

relevant for a similar aerodynamic loading of the blade and wake behavior. The resulting scaled blade shape (both in terms of cross sections, because of the changed airfoils, and in terms of chord and twist distributions) will be different from the full-scale rotor. However, this is clearly irrelevant, as the goal is to match some quantities of interest between the two rotors, not their shape. Other criteria is certainly possible, depending on the specific characteristics to be matched. As already discussed, this approach is implemented for the design of the wind tunnel models described in **Paper I** and **Paper II**.

Once the new aerodynamic shape is identified, the second step consists in the design of an internal blade structure that can mimic the full-scale aeroelastic behavior while ensuring integrity and satisfying manufacturing and realizability constraints. This approach allows for more freedom than the zooming-down approach; for example, one can use different materials than the ones used for the full-scale design, and nonstructural masses can be added without affecting the matching characteristics of the scaled blade. This approach was implemented for the design of the utility-size scaled models and wind tunnel model described in **Paper I** and **Paper II**.

The redesign approach was implemented within the design framework `Cp-Max`, described in Section 2.4.

2.4 Multi-disciplinary optimization

The design tool `Cp-Max` is a multi-disciplinary framework which implements optimization algorithms that can perform the coupled aerostructural design optimization of the blades and the tower, but also individual mono-objective component design. This section describes the main characteristics and formulation of the main loops, and further details can be found in [105–107]. The framework architecture is presented in Fig. 2.5 and described in the next sections.

2.4.1 Macrooptimization

The framework can perform the aerostructural optimization to minimize a merit figure, typically defined as cost of energy. The goal of the macrooptimization is to find the optimal global vector $\boldsymbol{p}_g^*$, and the associated aerodynamic vector $\boldsymbol{p}_a^*$ and structural vector $\boldsymbol{p}_s^*$ that leads to a minimum cost of energy, LCOE* (or another merit figure). The global vector is defined as $\boldsymbol{p}_g^* = \left[R, H, \gamma, \phi, \sigma_c, \tau_c, \sigma_t, \tau_t \right]$, where R is the rotor radius, H is the hub height, γ is the rotor cone angle, ϕ is the nacelle uptilt angle and $\sigma_c, \tau_c, \sigma_t$ and τ_t are the aerostructural parameters solidity and tapering, defined for both chord and thickness respectively.

The procedure follows Algorithm 2.1, which conducts an aerodynamic optimization and a structural

---

Algorithm 2.1: Macrooptimization

1 Function$\left(\boldsymbol{p}_a^*, \boldsymbol{p}_s^*, \boldsymbol{p}_g, \text{LCOE}\right)$=ComputeLCOE$\left(\boldsymbol{p}_a, \boldsymbol{p}_s, \boldsymbol{p}_g, \text{D}, \boldsymbol{\Gamma}_s\right)$
2 $\left[\boldsymbol{p}_a^*, \text{AEP}^*\right]$=MaxAEP$\left(\boldsymbol{p}_a, \boldsymbol{p}_s, \boldsymbol{p}_g, \text{D}\right)$
3 $\left[\boldsymbol{p}_s^*, \text{ICC}^*\right]$=MinICC$\left(\boldsymbol{p}_a^*, \boldsymbol{p}_s, \boldsymbol{p}_g, \text{D}, \boldsymbol{\Gamma}_s\right)$
4 AEP^*=ComputeAEP$\left(\boldsymbol{p}_a^*, \boldsymbol{p}_s^*, \boldsymbol{p}_g, \text{D}\right)$
5 LCOE^*=LCOEmod$\left(\text{AEP}^*, \text{ICC}^*, \boldsymbol{p}_a^*, \boldsymbol{p}_s^*, \boldsymbol{p}_g, \text{D}\right)$

---

optimization in sequence. Afterwards, AEP* and LCOE* are computed based on the updated $\boldsymbol{p}_a^*$, and $\boldsymbol{p}_s^*$ vectors. These algorithms are linked through the choice of four aerostructural parameters $\sigma_c, \tau_c, \sigma_t$ and τ_t, which allow for an interaction between the aerodynamic and the structural loop. Additionally, the variable D contains all those quantities that are given as input such as rated power P_r, class C, cut-in and cut-out wind speeds U_{in}, U_{out}, blade airfoil family AF, maximum allowed tip speed U_{tip} and the list of dynamic load cases (DLC) $\mathbf{L}_{DLC}$, as defined in the standards [108]. A selection of the
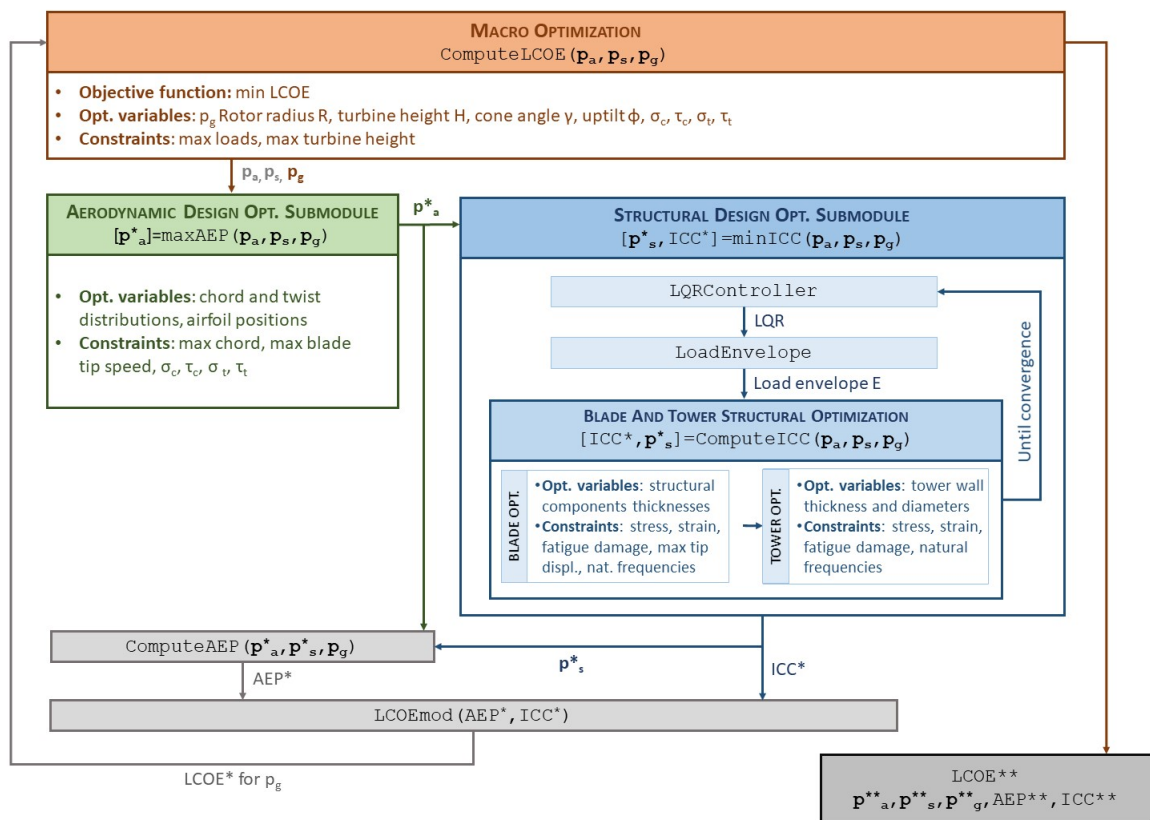
Figure 2.5: Overview of the architecture of the multi-disciplinary framework `Cp-Max`

DLCs included in $\mathbf{L}_{\text{DLC}}$ is listed in Table 2.2, where NTM is normal turbulence model, ETM is extreme turbulence model, ECD is extreme coherent gust with direction change, EWS is extreme wind shear, EOG is extreme operating gust and EWM is extreme wind speed model.

For each $\boldsymbol{p}_g$, an optimal $\boldsymbol{p}_a^*$ and $\boldsymbol{p}_s^*$ is found, with their corresponding AEP* and LCOE*. The optimal

Table 2.2: Selection of DLC cases prescribed by the standards and considered in $\mathbf{L}_{\text{DLC}}$

DLC	Design situation	Wind speed	Wind profile	Other condition
1.1	Power production	U_{in}:U_{out}	NTM	
1.2	Power production	U_{in}:U_{out}	NTM	
1.3	Power production	U_{in}:U_{out}	ETM	
1.4	Power production	$U_{\text{rated}} \pm 2\,\text{ms}^{-1}$	ECD	
1.5	Power production	U_{in}:U_{out}	EWS	
2.1	Power production	U_{in}:U_{out}	NTM	Grid loss
2.3	Power production	$U_{\text{out}}, U_{\text{rated}} \pm 2\,\text{ms}^{-1}$	EOG	Grid loss
6.1	Parked	U_{ref}	EWM 50 year	Yaw mis. ±8 deg
6.2	Parked	U_{ref}	EWM 50 year	Grid loss
6.3	Parked	U_{ref}	EWM 1 year	Ext. yaw mis. ±20 deg

solution is the turbine with the global vector $\boldsymbol{p}_g^{**}$, and associated aerodynamic $\boldsymbol{p}_a^{**}$ and structural vector $\boldsymbol{p}_s^{**}$ that lead to the overall minimium LCOE**.

As shown in Fig. 2.5, the architecture of `Cp-Max` enables the implementation of each standalone loop for the detailed design of system components – for example the tower structural design or the blade aerodynamic shape. Indeed, **Papers I-III** required the implementation of both the aerodynamic and the structural submodules, while **Papers V-VI** focused on the structural design of the blade and the tower, and therefore only the structural submodule was run. The following formulate the aerodynamic `MaxAEP` and structural `MinICC` design optimization submodules.

2.4.2 Aerodynamic design optimization submodule

The goal of the blade aerodynamic design optimization submodules is to identify the aerodynamic vector $\boldsymbol{p}_a^*$ which maximizes AEP, while satisfying a list of constraints. The vector $\boldsymbol{p}_a$ contains the aerodynamic variables of the optimization problem: chord distribution $\boldsymbol{p}_c$, twist distribution $\boldsymbol{p}_{a_\theta}$ and position of airfoils $\boldsymbol{p}_g$. Additionally, a set of constraints $\boldsymbol{g}_a \le 0$ introduces additional requirements and can be tailored for specific needs. Generally it may include values for transportability – for instance boundaries on the chord –, geometric constraints to ensure smoothness, or specific requirements on the blade shape.

The formulation of the algorithm is described in Algorithm 2.2. The constrained optimization included

---

Algorithm 2.2: Aerodynamic design optimization submodule

1   Function$\left(\boldsymbol{p}_a^*, \text{AEP}^*\right)$=`MaxAEP`$\left(\boldsymbol{p}_a, \boldsymbol{p}_s, \boldsymbol{p}_g\right)$

2   $\boldsymbol{p}_a = \boldsymbol{p}_{a_c} \cup \boldsymbol{p}_{a_\theta} \cup \boldsymbol{p}_{a_t}$

3   AEP^*=$\max_{\boldsymbol{p}_a}\left(\texttt{ComputeAEP}\left(\boldsymbol{p}_a, \boldsymbol{p}_s, \boldsymbol{p}_g, \text{D}\right)\right)$

4   $\boldsymbol{p}_a^*$=$\arg\left(\max_{\boldsymbol{p}_a}\left(\texttt{ComputeAEP}\right)\right)$

5   $\boldsymbol{g}_a(\boldsymbol{p}_a) \le 0$

---

in `MaxAEP` is solved by means of a sequential quadratic programming (SQP) algorithm [101], where gradients are computed by means of forward finite differences. The aerodynamic design optimization loop can be tailored to support other applications beyond the maximization of AEP. For instance, the

algorithm is applied in **Paper I**, **II** and **III** to design the external shape of aeroelastically and aerodynamically scaled models. The goal of this submodule is in this context no longer to achieve maximum AEP, but to define the external shape of a subscaled model that mimicks a target full-scale model. While different options are certainly possible depending on the specific quantities to be matched, the merit function considered for **Papers I-III**, as formulated in Eq. [**?**], drives the C_p of the designed model towards the power coefficient of the target full-scale model $\widehat{C}_P$ at N_{C_p} control stations. The goal here is to ensure that the subscaled model —whose airfoils generally present a reduced efficiency due to the lower chord-based Reynolds— has a C_P that is as close as possible to the full-scale model. Using $N_{C_p} = 1$, leads to a design with a best C_P at the TSR λ_1.

$$J_a = \sum_i^{N_{C_p}} \left(\frac{C_P(\lambda_i) - \widehat{C}_P(\lambda_i)}{\widehat{C}_P(\lambda_i)} \right)^2 . \tag{2.9}$$

Within the vector of matching equality constraints, the matching of the spanwise distribution of the circulation $\widehat{\Gamma}$ at N_Γ control stations is also enforced:

$$\frac{\Gamma(\eta_i) - \widehat{\Gamma}(\eta_i)}{\widehat{\Gamma}(\eta_i)} = 0, \quad i = (1, N_\Gamma), \tag{2.10}$$

where $\widehat{(\cdot)}$ indicates in general a to-be-matched scaled quantity of the target full-scale model. Another constraint may be added to prescribe the maximum power coefficient to take place at the same design TSR, i.e. $\lambda_{\max(C_P)} = \lambda_{\max(\widehat{C}_P)}$.

2.4.3 Structural design optimization submodule

The structural design optimization submodule generally aims at obtaining the lightest structure that satisfies a set of requirements – for a given external shape. The submodule can size the rotor for a given tower, the tower for a given rotor, or it can also consider the more general problem of simultaneously sizing rotor and tower.

The submodule aims at identifying the set of parameters $\boldsymbol{p}_s^*$ that minimize ICC, or another merit function. The vector $\boldsymbol{p}_s$ includes the blade optimization variables of the blade and the tower. The blade optimization variables include can be chosen among the thickness of external shell, spar caps, shear webs, as well as leading and trailing edge reinforcements at different sections; while the tower optimization variables include the diameter and thickness of different sections. The full geometry is then obtained through interpolation. The structural optimization, described in Algorithm 2.3, is an

---

Algorithm 2.3: Structural design optimization submodule

1   Function$\left(\boldsymbol{p}_s^*, \text{ICC}^*\right)$=MinICC$\left(\boldsymbol{p}_a, \boldsymbol{p}_s, \boldsymbol{p}_g, \text{D}, \boldsymbol{\Gamma}_s\right)$
2   LQR=LQRController$\left(\boldsymbol{p}_a, \boldsymbol{p}_s, \boldsymbol{p}_g, \text{D}\right)$
3   $\mathbf{E}$=LoadEnvelope$\left(\boldsymbol{p}_a, \boldsymbol{p}_s, \boldsymbol{p}_g, \text{D}, \text{LQR}\right)$
4   ICC*=min$_{\boldsymbol{p}_s}\left(\text{ComputeICC}\left(\boldsymbol{p}_a, \boldsymbol{p}_s, \boldsymbol{p}_g, \text{D}, \boldsymbol{E}, \boldsymbol{\Gamma}_s\right)\right)$
5   $\boldsymbol{p}_s^*$=arg$\left(\text{min}_{\boldsymbol{p}_s}\left(\text{ComputeICC}\right)\right)$
6   $\boldsymbol{\Gamma}_s^*$=3DFEAnalysis$\left(\boldsymbol{p}_a, \boldsymbol{p}_s^*, \boldsymbol{p}_g, \text{D}, \boldsymbol{E}, \boldsymbol{\Gamma}_s\right)$
7   $\Delta\boldsymbol{p}_s$= $|\boldsymbol{p}_s^* - \boldsymbol{p}_s|$, ΔICC= $|$ ICC*-ICC $|$
8   $\Delta\boldsymbol{\Gamma}_s^*$= $|\boldsymbol{\Gamma}_s^* - \boldsymbol{\Gamma}_s|$
9   $\boldsymbol{p}_s$=$\boldsymbol{p}_s^*$, $\boldsymbol{\Gamma}_s$=$\boldsymbol{\Gamma}_s^*$
10   while $(\Delta p_s \geq tol_{p_s}, \Delta\text{ICC} \geq tol_{\text{ICC}}, \Delta\Gamma_s \geq tol_{\Gamma_s})$

---

iterative loop, which stops when convergence is reached. The algorithm starts with the calculation of

the regulation trajectory and the synthesis of the LQR controller gains in `LQRController`, updated based on the current wind turbine design, as described in [109]. Next, the design load cases from the list $\mathbf{L}_{DLC}$ are run with the aeroservoelastic simulator `Cp-Lambda` [105]. The postprocessing of this set of load cases returns the vector $\mathbf{E}$, which contains the load envelope vector at different positions of the blade and the tower. The rainflow counting is also performed in this step. The structural sizing is solved within `MinICC` by means of a SQP optimization [101]. Here again, gradients are computed by means of forward finite differences. The optimization loop is constrained based on the list of parameters $\mathbf{\Gamma}_s$, which imposes the desired design requirements. As defined in [106], this includes a list of constraints to guarantee the structural integrity of the blade, as well as its manufacturability:

- Manufacturing, technological and and geometrical constraints. For instance to limit the cone angle of the tower segments, or the span-wise ply tapering rates.

- Frequency placement constraints to avoid resonance conditions. For example, to ensure that the first flap blade eigenfrequency lies above the three-per-revolution at rated rotor speed, or that a suitable gap exists between two consecutive blade frequencies. If the tower is considered, the first fore-aft and side-side frequencies could be located above (for a stiff design) or below (for a soft design) the one-per-revolution at rated rotor speed.

- Bounds on stress and strain components at a number of points on selected verification cross-sections, therefore ensuring that sufficient structural strength is obtained by the blade. Von Mises stresses are considered for the tower.

- Bounds on fatigue damage according to [108]. First, a fatigue damage index d_{σ_r} due to a single stress component is computed at preselected points on verification sections. The multi-axial damage index is defined as:

$$d_b = d_{\sigma 1}^{2/m} + d_{\sigma 1}^{2/m} - (d_{\sigma 1} d_{\sigma 2})^{1/m} + d_{\sigma 6}^{2/m},\tag{2.11}$$

where m is the inverse slope of the Wöhler curve and the longitudinal, transverse and shear stress components are identified by indices 1, 2 and 6, respectively. For the tower, the fatigue constraint implies the computation of the d_t index as indicated in

$$d_t = \left(\frac{\gamma_{Ff}\Delta\sigma_{E,2}}{\Delta\sigma_c/\gamma_{Mf}}\right)^3 + \left(\frac{\gamma_{Ff}\Delta\tau_{E,2}}{\Delta\tau_c/\gamma_{Mf}}\right)^5\tag{2.12}$$

where $\Delta\sigma_c$ and $\Delta\tau_c$ are reference values of fatigue strength, $\Delta\sigma_{E,2}$ and $\Delta\tau_{E,2}$ are equivalent constant amplitude stress ranges related to 2 million cycles, while γ_{Ff} and γ_{Mf} are safety factors. The damage indices for all verification points are stacked in vectors $\mathbf{d}_b$ and $\mathbf{d}_t$, and they are then bounded to unity.

- Constraint to ensure blade-tower clearance for strike-free operation for all considered DLCs.

Finally, the fulfillment of all the structural constraints is validated at a finer description level through a higher fidelity 3D analysis Overall, the structural loop converges when $\mathbf{p}_s$, ICC and $\mathbf{\Gamma}_s$ are within a tolerance.

LAC-based redesign

In **Paper V-VI**, the structural design optimization submodule is augmented with a literature-sourced lidar-assisted control (LAC) load-reduction model. Table 2.3 describes the reduction coefficient for each component and load case, in terms of percent changes with respect to a non-LAC controller. In the table, F and M respectively indicate force and moment components, expressed in the (x, y, z)

righthanded triad, where x points downstream, y is in the crossflow direction, and z is vertical pointing upwards. Components not reported in the table experience either null or negligible reductions. For simplicity, this model does not include lidar faults and assumes a lidar availability of 100%. This load-reduction model is derived from the work presented in [41], which was chosen as reference because it presents a comprehensive list of effects of LAC for several key quantities of several components and uses a fairly plain implementation, which might be representative of an initial conservative deployment on production machines. This work used a simple feedforward collective pitch LAC combined with a conventional feedback controller, applied to a 5 MW turbine. On the other hand, power capture —and hence Annual Energy Production (AEP)— is largely unaffected by this LAC implementation.

The load-reduction model reported in Table 2.3 only considers a selected set of load cases that can

Table 2.3: Load-reduction coefficients based on [41], expressed as percentages with respect to a non-LAC controller.

		BLADE					
	Key quantity	Fx	Fy	Fz	Mx	My	Mz
DLC 1.2	DEL	-3.8%	-0.1%	-0.25%	-0.4%	-3.8%	-3.5%
DLC 1.X	Extreme loads					-2.0%	
	Tip deflection					-2.0%	
		MAIN BEARING					
	Key quantity	Fx	Fy	Fz	Mx	My	Mz
DLC 1.2	DEL	-10.0%			-1.2%	-0.4%	-1.0%
DLC 1.X	Extreme loads						
		TOWER TOP (YAW BEARING)					
	Key quantity	Fx	Fy	Fz	Mx	My	Mz
DLC 1.2	DEL	-12.0%	-0.1%	-2.1%	-2.0%	-1.8%	-0.2%
DLC 1.X	Extreme loads						
		TOWER BOTTOM					
	Key quantity	Fx	Fy	Fz	Mx	My	Mz
DLC 1.2	DEL	-3.0%	0.2%	-2.2%	-0.1%	-12.0%	-0.2%
DLC 1.X	Extreme loads					-5.0%	

be modified by the adoption of a lidar-assisted control. Specifically, only DLC 1.1, 1.2 and 1.3 are considered, cases which include power production. In reality, these are not the only DLCs that are modifiable —in the sense that they can be affected by a change in the controller—, and for instance, also DLC 1.4 (power production with extreme wind direction), 1.5 (power production with extreme wind shear), 2.1 (power production with control system fault or grid disconnection under normal turbulence conditions) and 2.3 (power production with control system fault or grid disconnection under extreme operating gusts) are modifiable DLCs. The first two of these DLCs are not considered in the LAC load-reduction model, because they do not typically generate design driving loads. The case of DLC 2.1 and 2.3 is however different: here, maximum loads are typically generated during a shutdown, triggered by an extreme ambient condition change, a fault or a grid disconnection. When this happens, the entity of the generated loads will be largely dictated by the behavior of the shutdown procedure, which here is assumed not to be assisted by a lidar for safety reasons. On the other hand, loads generated during a shutdown might also depend to some extent on the state of the turbine at the time the shutdown was triggered, which does depend on the behavior of the LAC controller. A precise quantification of the effects of LAC on these DLCs would therefore require simulations with LAC in the loop, which are outside of the scope of the present preliminary work. It is therefore assumed that LAC-enabled reductions are negligible for these DLCs.

A distinction must be made between the application of load-reduction coefficients to ultimate loads

and deflections, which is straightforward, and to fatigue loads. The former simply consists in the correction of the key quantities obtained by a non-LAC controller with the corresponding coefficients of the load-reduction model. Combined loads —for example at tower base or at the main and blade pitch bearings— are computed from the corrected individual load components.

For fatigue damage, the following procedure is used. Site-weighted DELs are computed as

$$\text{DEL} = \sum_{U_{\text{in}}}^{U_{\text{out}}} W(U) L_{eq}(U),\tag{2.13}$$

where $W(U)$ is the Weibull probability density function at a wind speed U, while the damage equivalent load at that same wind speed is expressed as

$$L_{eq} = \left(\frac{\sum_{i=1}^{n} S_{r,i}^m}{N_{eq}} \right)^{1/m},\tag{2.14}$$

where m is the Wöhler coefficient, $S_{r,i}$ is the load range of a cycle i, n is the total number of cycles and N_{eq} the equivalent number of cycles [110].

Next, it is assumed that load reductions are independent of wind speed and load range. This way, the Weibull-weighted DEL reductions reported in the literature can be applied directly to the load time histories obtained here with a non-LAC controller by aeroelastic simulations. Clearly this is an approximation, as LAC-enabled reductions generally depend on the wind speed, as reported by several studies [46, 50, 111]. This approximation holds true when the reduction coefficients are small, as those reported in Table 2.3. Next, transient combined loads are computed from the relevant components (for example, combining fore-aft and side-side components at tower base, and similarly combining the associated components at the main and pitch bearings), and then processed by rainflow counting to obtain DELs, finally searching for the point in the cross section of interest with the maximum damage. The computation of fatigue margin constraints for the steel tower is performed following the European regulations [112].

Structural design for scaled rotors

The structural design optimization submodule is modified in **Papers I** and **II** to design the internal blade structure of scaled rotors that can mimic the full-scale aeroelastic behavior while ensuring their integrity and satisfying manufacturing constraints. In this context, the merit figure driving the structural optimization algorithm, and the list of constraints are correspondingly adapted.

Indeed, assuming the blade to be modeled as a beam, the structural optimization cost can be formulated as

$$J_s = \sum_{i}^{N_s} \left(\frac{M_p(\eta_i) - \widehat{M}_p(\eta_i)}{\widehat{M}_p(\eta_i)} \right)^2 + w_s \sum_{i}^{N_s} \left(\frac{K_q(\eta_i) - \widehat{K}_q(\eta_i)}{\widehat{K}_q(\eta_i)} \right)^2, \qquad p \in \mathscr{S}_M, q \in \mathscr{S}_K,\tag{2.15}$$

where w_s is a tuning weight, M_p and K_q are elements of the mass and stiffness matrices, and the sets $\mathscr{S}_M$ and $\mathscr{S}_K$ identify the elements that should be considered within the generally fully populated symmetric mass and stiffness matrices. The first term in the cost aims at the matching of the scaled target mass distribution, while the second at the stiffness distribution. Constraints are also adapted and include the matching of a desired number of natural frequencies $\omega_i = \widehat{\omega}_i$, and the matching of a desired number of mode shapes and/or static deflections $\mathbf{u}_j(\eta_i) = \widehat{\mathbf{u}}_j(\eta_i)$ at a given number of spanwise stations η_i. Finally, additional design inequality constraints consider all other necessary and desired conditions that must be satisfied in order for the structural design to be viable, and in general include maximum stresses and strains for integrity, maximum tip deflection for safety, buckling, manufacturing and technological conditions.

2.5 Methods for uncertainty quantification

Finally, the third method here presented is defined with the purpose of propagating a selected set of uncertainties found in inputs into a selected set of key output quantities. Even though the method here presented is applied to uncertainties found in the wind characteristics and the blade state, the method is general and can be applied for a different set of uncertainties.

The application of these methods is carried out in **Paper VI** through the toolbox `Dakota`, released by the SANDIA National Laboratories [113]. However, this section includes a brief overview of the formulation of these methods.

2.5.1 Sources of uncertainty

Uncertainties are generally classified into two families: epistemic and aleatory. Epistemic uncertainties are those that originate from a lack of knowledge and data, while aleatory uncertainties are those related to the intrinsic variability of a process or physical system. A wind turbine is largely affected by uncertainty because of the inherently stochastic nature of the wind resource. Additionally, uncertainties can also be found in the aerodynamic and structural characteristics of the machine, for instance in the mechanical properties of the materials. Uncertainties are also introduced by manufacturing processes or the status of wear and tear of each individual component. Aleatory uncertainties can generally be represented through a probability distribution function, while modeling epistemic uncertainties is challenging, as there are usually not enough elements to choose a specific probability distribution function and different methods need to be used [114]. **Paper IV** considers two main sources of uncertainties: Uncertainties affecting the wind inflow and the aerodynamics of the blades. Three uncertainties are here considered: Uncertainty in the turbulence intensity of the wind, which is propagated to the shear exponent; Uncertainty in the surface degradation along the span due to erosion by sand and rain; and uncertainty in the airfoil performance – measured in terms of aerodynamic coefficients of lift, drag and moment. The three uncertainties are modeled as beta probability distributions.

2.5.2 Methods for UQ

Two uncertainty quantification methods are here presented, and applied in **Paper IV**: Polynomial Chaos Expansion and Kriging. The performance of these two methods is benchmarked against a Montecarlo approach in **Paper IV**.

Polynomial Chaos Expansion

Based on the Cameron-Martin theorem [115], the chaos expansion for a response R can be written as a series of orthogonal polynomials, comparable to a Fourier series:

$$R = \sum_{j=0}^{\infty} \alpha_j \Psi_j(\xi) \tag{2.16}$$

where $\xi : \Omega \rightarrow \mathbb{R}^d$ is a multi-dimensional random variable with d mutually independent entries and Ψ_j are the multivariate polynomials involving products of the one-dimensional polynomials, and α_j are real coefficients, with $j \in \mathbb{N}$. The infinite expansion described in Eq. 2.16 is generally truncated at a finite number of random variables d and a finite expansion order p, and writes

$$R \approx \sum_{j=0}^{N_t} \alpha_j \Psi_i(\xi). \tag{2.17}$$

It is common practice to fix a polynomial order N_t and use all multivariate basis functions up to that order, which leads to

$$N_t = \frac{(d+p)!}{d!p!} - 1. \tag{2.18}$$

The coefficients α_j are generally estimated using either spectral projection or linear regression [116]. In the spectral projection approach, the response is projected onto each basis function Ψ_j. The polynomial orthogonality properties are employed to extract each coefficient α_j, according to

$$\alpha_j = \frac{\langle R, \Psi_j \rangle}{\langle \Psi_j^2 \rangle} = \frac{1}{\langle \Psi_j^2 \rangle} \int_{\mathbb{R}^d} R \Psi_j \rho(\xi) d\xi, \tag{2.19}$$

where $\rho(\xi) = \prod i = 1^d \rho_i(\xi_i)$ of the joint probability density weight function. The denominator can be analytically readily computed using the product of univariate norms squared [117, 118].

In the linear regression approach, the linear system $\Psi \alpha = R$ is solved for a set of coefficients α that reproduce a set of response values R. The set of response values can be defined based on point collocation – i.e. an unstructured grid obtained from sampling within the density function of Ψ, or probabilistic collocation – a structured grid defined from uniform random sampling on the multi-index of a tensor-product quadrature grid [116]. Various methods can be employed to solve the linear system, the most frequently used being least squares regression. Compressed sensing methods attempt to only identify the elements of the coefficient vector with the largest magnitude and enforce as many elements as possible to zero [119, 120].

A linear regression approach based on least squares regression is applied in **Paper IV**.

Kriging

Kriging (or Gaussian process regression) is a generalized linear regression model that accounts for the correlation in the residuals between the regression model and the observations. Considering the design points $\mathbf{X} = (\mathbf{x}_1, \mathbf{x}_2, ..., \mathbf{x}_m)^\top$, and the corresponding design outputs $\mathbf{Y} = (\mathbf{y}_1, \mathbf{y}_2, ..., \mathbf{y}_m)^\top$, the mathematical form of a Kriging model can be written as:

$$\widehat{y}(\mathbf{x}) = \sum_{j=1}^{n} \beta_j f_j(\mathbf{x}) + \epsilon(\mathbf{x}) = \mathbf{f}^\top(\mathbf{x})\beta + \epsilon(\mathbf{x}). \tag{2.20}$$

The equation has two parts: the first part is a linear regression where $\mathbf{f}$ represents the the n regressors modeling the drift of the process mean and writes $\mathbf{f} = [f_1, f_2, ..., f_n]^\top$. The second part, $\epsilon(\mathbf{x})$ is a stationary Gaussian random process with zero mean and covariance:

$$\text{Cov}[\epsilon(\mathbf{x}_i), \epsilon(\mathbf{x}_j)] = \sigma^2 \mathcal{R}(\mathbf{x}_i, \mathbf{x}_j), \tag{2.21}$$

where σ^2 is the process variance and $\mathcal{R}(\mathbf{x}_i, \mathbf{x}_j)$ is the spatial correlation function that controls the smoothness of the resulting Kriging model and the influence of nearby points [121–124]. The Kriging model applied in **Paper VI** is formulated as Universal Kriging and assumes a best linear unbiased predictor (BLUP) at a new input location $\mathbf{x}^*$. Therefore

$$\widehat{y}(\mathbf{x}^*) = \mathbf{f}^\top(\mathbf{x}^*)\widehat{\beta} + \mathbf{r}^\top(\mathbf{x}^*)\mathbf{R}^{-1}(y - \mathbf{F}\widehat{\beta}), \tag{2.22}$$

where $\mathbf{r}$ is the correlation of $\mathbf{x}^*$ with the design points $\mathbf{X}$, written as $\mathbf{r}(\mathbf{x}^*) = [\mathcal{R}(\mathbf{x}^*, \mathbf{x}_1), \mathcal{R}(\mathbf{x}^*, \mathbf{x}_2), ..., \mathcal{R}(\mathbf{x}^*, \mathbf{x}_m)]$, $\mathbf{F}$ is the set of regression functions evaluated at m known design points,

$$\mathbf{F} = [\mathbf{f}(\mathbf{x}_1), \mathbf{f}(\mathbf{x}_2), ..., \mathbf{f}(\mathbf{x}_m)] = \begin{bmatrix} f_1(\mathbf{x}_1) & f_2(\mathbf{x}_1) & ... & f_n(\mathbf{x}_1) \\ f_1(\mathbf{x}_2) & f_2(\mathbf{x}_2) & ... & f_n(\mathbf{x}_2) \\ \vdots & \vdots & \ddots & \vdots \\ f_1(\mathbf{x}_m) & f_2(\mathbf{x}_m) & ... & f_n(\mathbf{x}_m) \end{bmatrix}, \tag{2.23}$$

$\mathbf{R}$ is the correlation matrix of design points $\mathbf{X}$, defined as

$$\mathbf{R} = \begin{bmatrix} \mathscr{R}(\mathbf{x}_1,\mathbf{x}_1) & \mathscr{R}(\mathbf{x}_1,\mathbf{x}_2) & \dots & \mathscr{R}(\mathbf{x}_1,\mathbf{x}_m) \\ \mathscr{R}(\mathbf{x}_2,\mathbf{x}_1) & \mathscr{R}(\mathbf{x}_2,\mathbf{x}_2) & \dots & \mathscr{R}(\mathbf{x}_2,\mathbf{x}_m) \\ \vdots & \vdots & \ddots & \vdots \\ \mathscr{R}(\mathbf{x}_m,\mathbf{x}_1) & \mathscr{R}(\mathbf{x}_m,\mathbf{x}_2) & \dots & \mathscr{R}(\mathbf{x}_m,\mathbf{x}_m) \end{bmatrix}, \tag{2.24}$$

and $\widehat{\beta}$ is the least squares estimate of β and writes

$$\widehat{\beta} = \left(\mathbf{F}^{\mathsf{T}}\mathbf{R}^{-1}\mathbf{F}\right)^{-1}\mathbf{F}^{\mathsf{T}}\mathbf{R}^{-1}\mathbf{y}. \tag{2.25}$$

The MSE or variance of the estimate $\widehat{y}(\mathbf{x}^*)$ is

$$MSE\left[\widehat{y}(\mathbf{x}^*)\right] = \sigma^2\left\{1 - \mathbf{r}^{\mathsf{T}}(\mathbf{x}^*)\mathbf{R}^{-1}\mathbf{r}(\mathbf{x}^*) + \left(\mathbf{r}^{\mathsf{T}}(\mathbf{x}^*)\mathbf{R}^{-1}\mathbf{F} - \mathbf{f}^{\mathsf{T}}(\mathbf{x}^*)\right)^{\mathsf{T}}\left(\mathbf{F}^{\mathsf{T}}\mathbf{R}^{-1}\mathbf{F}\right)^{-1}\left(\mathbf{r}^{\mathsf{T}}(\mathbf{x}^*)\mathbf{R}^{-1}\mathbf{F} - \mathbf{f}^{\mathsf{T}}(\mathbf{x}^*)\right)\right\} \tag{2.26}$$

.

Design for scientific value

3.1 Paper I: On the scaling of wind turbine rotors

3.1.1 Summary

This work investigates several aspects regarding the scaling of wind turbine rotors. Specifically, the work tries to answer the following questions:

- What are the effects of a change of scale (i.e., both in the case of up- and subscaling) on the steady and transient response of a wind turbine?

- What steady and transient characteristics of the response of a full-scale wind turbine can be matched by a subscaled model?

- What are the most suitable ways to design the aerodynamic and structural characteristics of a subscaled model?

The paper first considers the general problem of scaling a wind turbine rotor to a different size. The study analyzes the main steady and transient characteristics of a rotor in terms of performance, aeroservoelasticity and wake shedding, as well as determining the effects caused by a generic change of scale. The analysis reveals that, in principle, most of the response features can be faithfully represented by a subscaled model. An exact matching of all features is generally impossible because of chord-based Reynolds effects, which lead to changes in the aerodynamic behavior of the system. An additional limitation is found in the wind conditions. Indeed, the wind field is not subscaled when using utility-size models in the field, and wind tunnel flows can only partially match the characteristics of the atmospheric boundary layer. The analysis also indicates that scaling is essentially governed by two parameters: the geometric and time scaling factor. All matched and unmatched quantities can be fully characterized by these factors.

Next, the work describes and compares two different approaches to design a subscaled rotor – that however must fulfill the same criteria derived from the previously defined scaling laws. The first approach consists in the exact geometric zooming of the blade, including both its external and internal shape. Alternatively, a second approach based on an aerostructural redesign is presented. This approach consists in the redesign of both the external shape and the internal structure to match as closely as possible the aeroelastic behavior of a full-scale blade. This approach offers more degrees of freedom at the expense of a higher complexity.

Next, the applicability of the two design strategies is investigated through the subscaling of a conceptual 10 MW machine to three different sizes: two utility-size models, with rotors 70% and 85% smaller than the full-scale rotor, and a wind tunnel model of 2.8 m diameter, 98.88% smaller than the full-scale rotor. The application of the two design strategies highlights the different limitations of each approach. The choice of strategy for the design of the aerodynamic shape is shown to be driven by the performance of the polars at the sub-scale Reynolds. Indeed, the application of a straightforward zooming down approach requires the adoption of the full-scale airfoils, even though the performance

of the polars can be compromised at subscale Reynolds. The zooming down approach is chosen for the design of the utility-size models, as the airfoils are still performing well at their corresponding typical Reynolds number. For the wind tunnel model, however, an aerodynamic redesign with efficient profiles specifically developed for low-Reynolds-number applications is necessary.

Several hurdles are also identified for the implementation of a zooming down approach to design the internal structure of both utility-size models. First, the thicknesses of some components are unrealistically low; the subscaled structure requires materials characterized by very peculiar mechanical properties and nonstructural masses cannot be exactly zoomed down by geometric scaling. A structural redesign is found to be the simplest approach, despite the higher complexity of the approach. Indeed, the adoption of such approach gives more freedom for the choice of materials, and more careful attention can also be paid to the distributions of nonstructural masses. Given the redesigned aerodynamic shape of the wind tunnel model, a structural redesign is required. For this application, a full cross section obtained by machining a foamy material is considered.

The aeroelastic response of the models are compared to the full-scale machine both in terms of relevant key characteristics and load trends for a power production state at different turbulent wind speeds. The utility-size subscaled models are found to match the key indicators of the full-scale target reasonably well, considering both Reynolds effects and redesigned structure. The wind tunnel model also shows a satisfactory faithfulness for most key indicators, notwithstanding the very different Reynolds numbers. The largest mismatch is, as expected, found for the maximum edgewise tip displacement due to the larger chord.

Finally, the accuracy of the three models in capturing trends instead of absolute values is also assessed. The three models and full-scale machine are simulated considering a turbulent inflow with several differently superposed wake deficits. The lateral distance between the wake center and the downwind turbine is varied from right to left realizing different degrees of wake-rotor overlap. The subscaled models are simulated by velocity-scaling the full-scale waked inflows. Overall, the utility-size subscaled models follow the trends very well. The wind tunnel model captures the trends reasonably well, with the exception of flapwise bending root moment, because of a different stalling point of the airfoils used for this subscaled machine.

3.1.2 Contribution

This paper is the result of the common effort of different authors. Canet led the modifications of the design tool `Cp-Max` to support the subscaled matching optimization, designed the subscale models, performed the simulations and analyzed and postprocessed the results, in cooperation with Bortolotti. Bottasso supervised the work and led the formulation of the theoretical scaling analysis. Canet and Bottasso wrote the paper, with contributions from Bortolotti.

3.1.3 Reference

H. Canet, P. Bortolotti, and C. L. Bottasso, "On the scaling of wind turbine rotors," *Wind Energy Science*, vol. 6, no. 3, pp. 601–626, 2021. doi: 10.5194/wes-6-601-2021

3.2 Paper II: Gravo-aeroelastic scaling of very large wind turbines to wind tunnel size

3.2.1 Summary

The paper proposes an aeroelastic scaling methodology that includes gravitational effects and applies the methodology for the design of a wind tunnel subscaled model that mimics the gravo-aeroelastic response of a 10 MW wind turbine as faithfully as possible.

First, suitable scaling laws are defined. As gravitational loads play a significant role in modern very large wind turbines, the scaling laws are defined to enforce the matching of the Froude number – i.e. the ratio between aerodynamic and gravitational forces. Matching this quantity implies a mismatch of the Reynolds and Mach numbers, as these quantities can generally not be simultaneously guaranteed. Additionally, TSR, nondimensional time, nondimensional natural frequencies and Lock number must be simultaneously matched. Enforcing these conditions allows the derivation of the scaling ratios, which dictate the required characteristics in the subscaled model.

A wind tunnel model that mimics a 10 MW wind turbine is here designed through an aero-structural redesign approach. This approach requires the identification of suitable airfoils – airfoils with polars as similar as possible at lower operating Reynolds, and suitable materials – as mass and stiffness distributions must be properly scaled. The resulting wind tunnel subscaled model has a very different aerodynamic shape and blade topology, but presents a gravo-aeroelastic response close to the full-scale 10 MW machine. This work highlights the challenges posed by representing a gravo-aerolastic system at a much reduced scale.

3.2.2 Contribution

Canet led the modifications of the design tool `Cp-Max` to support the subscaled matching optimization and designed the subscale model, with the support of Bortolotti. Bottasso supervised the work. Canet and Bottasso wrote the paper, with contributions from Bortolotti.

3.2.3 Reference

H. Canet, P. Bortolotti, and C. L. Bottasso, "Gravo-aeroelastic scaling of very large wind turbines to wind tunnel size," *Journal of Physics: Conference Series*, vol. 1037, no. 042006, 2018. doi: 10.1088/1742-6596/1037/4/042006

3.3   Paper III: How realistic are the wakes of scaled wind turbine models?

3.3.1   Summary

This work is concerned with the research question *how faithful are the wakes of scaled wind turbine models with respect to the actual ones in the field?*

The main factors driving wake behavior are first analyzed through a dimensional analysis and wake physics. The goal is here to identify the physical aspects of the full-scale wakes that cannot be matched at a reduced scale and with the considered experimental setup. The analysis reveals that it is relatively easy to match the main processes taking place in the outer shell of the near wake, as well as those that drive its breakdown and the characteristics of the far wake, but that several mismatched effects exist in the central core of the near wake.

Based on the results of this analysis, different full-scale models are designed to match some of the characteristics of the subscaled wind tunnel model G1. These models range from realistic full-scale turbines, with a large number of mismatched effects, to less realistic ones that however match a larger set of quantities of the subscaled model.

Next, an LES-ALM code is employed to simulate the wind tunnel experiments run with the subscaled wind tunnel model G1. Key quantities of interest such as power and thrust coefficient and wake profiles are compared against the wind tunnel measurements to validate the code. The designed full-scale models are then simulated with the same LEA-ALM code, considering the same numerical methods and algorithmic parameters employed for the subscaled simulations. These wind turbine models are exposed to the same ambient turbulent inflow considered in the subscaled simulations – yet correspondingly upscaled. Finally, the numerically simulated subscaled and full-scale wakes are compared under a different set of conditions, including wind-aligned and misaligned conditions.

3.3.2   Contribution

The simulations and analyses were performed by Wang. Bottasso devised the original idea of this research, performed the scaling analysis, interpreted the results and supervised the work. Campagnolo was responsible for the wind tunnel experiments and co-supervised the work. Canet designed the full-scale wind turbine models and Barreiro validated the full-scale turbine models with BEM and CFD codes. Wang and Bottasso wrote the manuscript. All authors provided important input to this research work through discussions, feedback and by improving the manuscript.

3.3.3   Reference

C. Wang, F. Campagnolo, H. Canet, D. J. Barreiro, and C. L. Bottasso, "How realistic are the wakes of scaled wind turbine models?" *Wind Energy Science*, vol. 6, no. 3, pp. 961–981, 2021. doi: 10.5194/wes-6-961-2021

3.4 Paper IV: Performance of non-intrusive uncertainty quantification in the aeroservoelastic simulation of wind turbines

3.4.1 Summary

This study characterizes the performance of non-intrusive uncertainty quantification methods for aeroservoelastic wind turbine analysis. Specifically, the study deals with two main research questions:

- What are the most suitable methods for the propagation of uncertainties throughout aeroservoelastic wind turbine models?

- How are design drivers and other quantities of interest affected by uncertain inputs?

Due to its preliminary character, the study only focuses on two sources of aleatory uncertainties – i.e. uncertainties emerging from the underlying randomness of a process. Precisely, among the many uncertain variables in the wind inflow, the study focuses on turbulence intensity (TI). Additionally, the study considers uncertainties in the aerodynamics of the blades: surface degradation along the span due to erosion by sand and rain and uncertainties in the airfoil performance – measured in terms of aerodynamic coefficients of lift, drag and moment.

Propagation methods are chosen based on results from previous work [125], which identified regression-based third-order Non-intrusive polynomial chaos expansion (NIPCE) and Universal Kriging (UK) as promising methods for uncertainty propagation throughout aeroservoelastic wind turbine models. The previously described uncertainties are propagated throughout the aeroservoelastic model of a conceptual very large offshore machine, which is simulated in power production state at different wind speeds from cut-in to cut-out considering six seeds. A set of different outputs of interests typically related to design drivers is analyzed– including maximum tip deflection, AEP and maximum loads and its damage equivalent loads.

Both UK and NIPCE are benchmarked against an exhaustive brute-force Monte Carlo strategy. Both methods are found to require at least one order of magnitude less simulations than Monte Carlo, with UK converging faster than NIPCE. Finally, the UK solution space is analyzed to investigate the effects of uncertainties in design drivers and the potential shortcomings of current mostly deterministic approaches based on safety factors. For instance, the value of maximum tip deflection obtained in the deterministic condition prescribed by the standards is found to be associated with very low probabilities, implying an overestimation of the safety factor. Further comprehensive studies might lead to a revision of typical safety factors to achieve more cost-competitive yet fully safe designs.

3.4.2 Contribution

Bortolotti led the study and set up the framework for the Monte Carlo study. Bortolotti and Canet run the Monte Carlo simulations, performed the convergence study with the framework `Dakota` and postprocessed the outputs. Loganathan set up the initial framework and defined the input data. Bottasso supervised the work. The paper was written by Bortolotti and Bottasso, with contributions from Canet.

3.4.3 Reference

P. Bortolotti, H. Canet, C. L. Bottasso, and J. Loganathan, "Performance of non-intrusive uncertainty quantification in the aeroservoelastic simulation of wind turbines," *Wind Energy Science*, vol. 4, no. 3, pp. 397–406, 2019. doi: 10.5194/wes-4-397-2019

Design for economic value

4.1 Paper V: Lidar-assisted control in wind turbine design: Where are the potential benefits?

4.1.1 Summary

This paper explores the potential benefits of considering Lidar-assisted control (LAC) in the design of a wind turbine. The study deals with two main research questions:

- Which key quantities can be reduced by a basic LAC implementation?

- Which LCOE reduction can be expected from a LAC-based redesigned turbine?

The study, performed on three machines of different class and specific power, identifies a significant potential reduction margin in the blade tip displacement, a quantity that typically drives the design of the spar caps. Additionally, fatigue-based towers are also found to have great potential since fatigue is not blocked by other DLCs and can be directly reduced by LAC.

However, the potential identified cannot always be fully exploited. Indeed, the potential margin identified for tip displacement can only be partially exploited by LAC and only modest reductions in blade mass are achieved. However, the redesign of the towers shows a more significant potential: While the design of buckling-driven towers can generally not be modified by LAC, fatigue-based towers enjoy significant benefits from LAC and achieve a mass reduction up to 17%, leading to a decrease of ICC of up to 3%.

The impact in LCOE is found to be different for offshore and onshore machines. The annual expenses created by the maintenance of the lidar system do not significantly increase the already high annual operating expenses (AOE) for offshore machines. However, they play a larger role in onshore machines and increase AOE by approximately 2%. Overall, LCOE increases for all onshore machines and slightly decreases for the offshore machine.

4.1.2 Contribution

Canet made the necessary modifications in the `Cp-Max` framework, performed the analysis of design drivers and redesigned the blade and the tower of the three reference machines, Loew defined the literature-based LAC and assisted Canet in the implementation of this model within the design framework. Bottasso supervised the work. The paper was written by Canet and Bottasso. All authors provided important input to this research work through discussions, feedback and by improving the manuscript.

4.1.3 Reference

H. Canet, S. Loew, and C. L. Bottasso, "Lidar-assisted control in wind turbine design: Where are the potential benefits?" vol. 1618, no. 042020, 2020. doi: 10.1088/1742-6596/1618/4/042020

4.2   Paper VI: What are the benefits of lidar-assisted control in the design of a wind turbine?

4.2.1   Summary

This paper further explores the potential benefits of considering lidar-assisted control in the design of a wind turbine, and investigates different pathways to fully reap these benefits. The study deals with three main research questions:

- To which extent can design-driving constraints be relaxed by LAC?

- What is the best way of reaping the benefits brought by LAC in the design of rotor and tower?

- To make LAC beneficial at system level, is it necessary to improve its performance or reduce its costs?

The study expands and further refines the analysis presented in **Paper V**, focusing on the potentially exploitable margins of the design-driving key quantities, and the extent to which these are actually exploited by average LAC formulations.
As discussed in **Paper V**, the study identifies fatigue-based towers as the components that can benefit the most from the introduction of LAC. The work here presented analyzes three different pathways to exploit these benefits in the design of fatigue-driven towers:

- **Tower redesign:** LAC-based load reductions are directly exploited to decrease the tower mass. Results show that this approach leads to a mass reductions of up to 17%. The impact in LCOE is larger for offshore machines than for onshore machines as purchase and maintenance costs of LAC do not significantly increase the already high AOE.

- **Taller tower redesign:** The LAC-based load reductions are here exploited to design taller towers that reach higher above the ground, where higher AEP can be captured. Significant potential is identified for the tower of the offshore machine, where both tower mass and ICC are decreased. However, due to the purchase and maintenance costs of LAC, a decrease in LCOE of only about 1.5% is achieved. The fatigue-driven tower of the onshore turbine presents only marginal benefits in terms of costs.

- **Tower redesign for longer lifetime:** The LAC-based load reductions are here exploited to design a tower with a longer lifetime. This approach is found to be promising, as a LAC-based designed tower with doubled lifetime requires the same or less mass as the original non-LAC baseline. These are however only preliminary rough trends, due to the different assumptions taken.

Only rather modest mass reductions are achieved for the blades of the three models analyzed, due to the moderate influence of LAC in design-driving quantities. The reductions are too modest to create a significant impact in LCOE.

4.2.2   Contribution

Canet led the research work, made the necessary modifications in the `Cp-Max` framework, performed the studies to define the potentially exploitable margins and conducted the design studies. Loew defined the literature-based LAC load-reduction model and assisted Canet in the implementation of this model within the design framework. Bottasso supervised the work. The paper was written by Canet and Bottasso. All authors provided important input to this research work through discussions, feedback and by improving the manuscript.

4.2.3 Reference

H. Canet, S. Loew, and C. L. Bottasso, "What are the benefits of lidar-assisted control in the design of a wind turbine?" *Wind Energy Science*, vol. 6, no. 5, pp. 1325–1340, 2021. doi: 10.5194/wes-6-1325-2021

Design for societal value

5.1 Paper VII: The eco-conscious wind turbine: bringing societal value to design

5.1.1 Summary

This work is concerned with the inherent societal value of wind turbines, and how this value can be enhanced through their design. While societal value is clearly a very broad concept that includes several important topics for society; the focus is here given to the societal benefits brought by the displacement of environmental emissions.

The paper first defines metrics that quantify the societal value of a wind turbine based on two concepts: environmental cost and environmental value. The former refers to the greenhouse gases (GHG) emitted in several life-cycle stages of the wind turbine, and the latter refers to the displacement of GHG in the grid enabled by the deployment of a wind turbine. These metrics are defined mirroring the familiar economic concepts of economic cost and economic value, here defined as the revenue received for selling the energy produced in the energy market.

These metrics are first employed to analyze the environmental cost of an average modern wind turbine, focusing on the contribution of the life-cycle of each component. Next, the defined eco-conscious metrics, as well as the economic metrics are used within a multi-objective design framework, which sizes two macroscopic parameters – Rotor diameter and hub height – of a wind turbine to find optimal trade-offs between economic and environmental parameters.

Finally, the environmental value is translated into future societal savings through the application of the social cost of carbon (SCC) – an estimate of the net present value of monetized social damages occurring from the emission of an additional metric ton of CO_2. The application of these metrics for two turbines in different locations in Germany shows that the environmental value is one order of magnitude higher than the environmental cost. Two locations with different wind profiles are found to have similar environmental values, implying that environmental value is not as dependent on the location as economic value. Additionally, the study points out the benefits of low specific-power machines, which are implied to present a higher economic and environmental value.

5.1.2 Contribution

The paper is the common effort of three authors. Canet led the development of this work and performed the results here presented, in close collaboration with Guilloré and Bottasso. Guilloré developed and validated the LCA model. The paper was written by Canet and Bottasso, with contributions from Guilloré. All authors provided important input to this research hwork through discussions, feedback and by writing the paper.

5.1.3 Reference

H. Canet, A. Guilloré, and C. L. Bottasso, "The eco-conscious wind turbine: bringing societal value to design," *Wind Energy Science Discussions*, 2022

Discussion and conclusions

This dissertation has explored the design of wind turbines from different points of view. Indeed, a wind turbine is here defined beyond the common notion of a machine whose goal is to produce low-carbon energy at a minimum cost. A wind turbine is here understood as a machine that has different purposes for different groups of users, and has therefore different inherent values. Three main values are here explored: scientific value, economic value and societal value. Within each value, several specific topics were investigated, and four high-level questions, which shape the core of this thesis, were introduced. These questions are first introduced in Sect. 1.1, and discussed in Sect. 6.1, based on the findings included in this thesis. The section also discusses the limitations of the work presented, and suggests future steps to further explore these topics.

Sect. 6.2 describes the novel contributions of the work contained in this thesis to the existing literature and Sect. 6.3 offers a perspective beyond the topics and values considered in this thesis.

6.1   Core research questions

This section discusses the four core research questions of this thesis, based on the results included in the papers. Limitations and additional work are also included.

> ***To which extent can a subscaled model replicate the aeroservoelastic response of a full-scale counterpart?***

The faithfulness of the response of a subscaled machine is shaped based on the chosen scaling laws – including the choice of subscale size – and the choice of the realization procedures selected, and its limitations.

- **Scaling laws.** Scaling is essentially governed by two parameters: the geometric and the time scaling factor. The former depends on the full- and subscale sizes, while the latter results from the choice of quantities to be matched. Indeed, it is not possible to fully capture the aeroservoelastic response of a full-scale wind turbine and when defining the scaling laws, one has to carefully define which characteristics of the response of the target full-scale machine should be fully captured, which trade-offs should be made, and which quantities should be disregarded. For some applications it is also necessary to include realization constraints, such as requirements on closed-loop control sampling time.

  - **Aerodynamic response.** Rotor aerodynamics can typically only be approximately matched, because of its dependency on the Reynolds and Mach number. Indeed, a mismatch of the chord-based Reynolds, which accounts for the ratio of inertial to viscous forces, is unavoidable because of the difference in size. The Mach number can be neglected for wind turbines, as compressibility does not typically play a significant role. Additionally, if gravitational effects are to be mimicked – for instance when targeting the loading of very large rotors or for floating offshore applications – the Froude number should be enforced.

Enforcing the Froude number, which represents the ratio of aerodynamic to gravitational forces implies that the time scaling factor is defined.

- **Elastic and inertial response.** If the subscaled model is designed beyond aerodynamics to also include aeroelastic effects, two additional conditions must be guaranteed: the Lock number and the placement of non-dimensional frequencies. Indeed, matching the Lock number enforces the same ratio of aerodynamic to inertial forces. This condition is ensured by simply matching the material density of the blade. The same nondimensional frequencies placement sets the ratio of elastic and inertial forces and additionally requires adjusting the stiffness of the subscaled model to meet specific requirements – defined by the full-scale stiffness characteristics and the scaling laws. If both conditions on Lock number and nondimensional natural frequencies are fulfilled, structural deflections caused by aerodynamic loads are also correctly scaled.

- **Design strategy.** Two different approaches to design the external shape and internal structure of a scaled rotor can be identified: a straightforward zooming down approach and a redesign approach. The former consists in the geometrically scaling all characteristics of the blade, while the latter consists in fully redesigning the blade external shape to mimic the aeroelastic response of the full-scale. In this case, one designs a new blade that, although completely different from the full-scale one, matches some of its characteristics. The choice of design strategy is highly dependent on the scaling laws.

  - **Straightforward geometric scaling.** For the aerodynamic shape, the approach requires the adoption of the airfoils from the full-scale blade. The faithfulness of the aerodynamic response of the subscaled model will therefore be subject to the effect of the Reynolds (and Mach) mismatch.

    The application of this approach to the internal structure of the blade also presents some challenges. Indeed, the approach requires the geometric scaling of the internal structure, which is not always feasible due to manufacturing constraints. Additionally, the blade elastic and inertial properties must also be correspondingly scaled, which might prove to be challenging. As mass and stiffness properties follow different scaling ratios, finding suitable materials can be challenging, specially for small geometric scaling ratios. Additional issues are identified because of requirements in nonstructural masses, which do not follow the same scaling ratios as structural masses. Additionally, the approach can only be applied if the external shape has also been zoomed down. If these issues are overcome, a full matching of the Lock number and the proper placement of non-dimensional frequencies could be achieved.

  - **Redesign approach.** This approach offers more degrees of freedom, at the expense of a higher level of complexity. Indeed, the blade aerodynamic shape is here redesigned to match specific characteristics of the full-scale response. However, it is not guaranteed that an aerodynamically redesigned blade will be able to replicate the response of the full-scale machine more faithfully than a zoomed down blade. Indeed, this approach requires the identification of a set of suitable airfoils at the sub-scale Reynolds, which might not be straightforward. Trade-offs must generally be made: for instance, only specific characteristics of the full-scale aerodynamic response can be targeted and/or the operating range is limited. These challenges generally increase for smaller geometric scaling ratios, due to the increased difficulty of finding suitable airfoils at low Reynolds numbers. The faithfulness of the aerodynamic response of the subscaled blade will therefore depend on the choice and availability of suitable airfoils, and the design conditions (characteristics

of the aerodynamic response to be matched and operating range) considered within the design of the blade.

The internal structure of the blade can also be redesigned considering alternative materials, as well as manufacturing constraints or realistic nonstructural masses. While fully matching the targeted inertial and elastic properties is certainly possible, the success of the approach depends here as well on the identification of suitable materials, and limitations (manufacturing constraints or requirements of nonstructural masses – such as glues and adhesives) associated. These challenges typically increase for smaller geometric scaling ratios or particular combinations of geometric and time scaling ratios. Here again, trade-offs or relaxations are required, for instance in the number of nondimensional frequencies properly placed, or the matching threshold of these conditions. The faithfulness of the subscaled model will therefore depend on the extent to which the Lock number and nondimensional frequencies have been matched.

The choice of design strategy depends on the problem at hand. Generally, a zooming down strategy appears to be the most straightforward approach to design the aerodynamic shape of a subscaled blade, as long as the Reynolds mismatch is still acceptable. For very small geometric scaling ratios, a redesign approach with alternative airfoils is generally more suitable, even if only part of the aerodynamic response can be faithfully captured. The simplest way of designing the internal structure of a subscaled blade appears to be a redesign approach, thanks to the additional degrees of freedom brought by the choice of materials. The design of the internal structure might, however, prove to be challenging for particular combinations of geometric and time scaling ratios, due to the requirements in blade mass and stiffness brought.

The design of subscaled rotors is a very complex procedure, in which many factors play a driving role. Overall, the work included in this thesis highlights the fact that the faithfulness of the response of subscaled models is limited by several factors – such as the identification of suitable airfoils and materials. Some of these can be relaxed or even solved by technological advances. For instance, improvements in measurement technology can relax requirements on the scaling of time, allowing for a better match of other quantities. Advances in material and manufacturing may ease the application of unconventional materials, relax sizing constraints, and lead to more accurate, simpler, faster-to-develop and cheaper models. Nonetheless, as shown by the models designed within this thesis, if scaling laws and design procedures are carefully selected, subscaled models can replicate very well the full (or partial) aeroservoelastic response of a full-scale machine. Indeed, the scaled models here designed were found not only to match reasonably well several key performance indicators of the full-scale machine, but also to follow the same trends fairly accurately.

The discussion here presented only considers testing performed in air and neglects hydrodynamics. However, the faithfulness of aero-hydroservoelastic subscaled machines should be further explored. Indeed, as floating wind energy is expected to significantly grow in the coming years, it is becoming increasingly important to better understand which aspects of the aero-hydroservoelastic response of these machines can be matched and how to best design subscaled models.

Additionally, perfectly scaled inflow conditions were here assumed, which are not always the case. Further research efforts should also focus on better understanding how to replicate the inflow conditions that full-scale machines face in various types of atmospheric and terrain conditions. This is a challenging task, since it requires a deep understanding of atmospheric flows, their interaction with the terrain orography and the vegetation, and technology to replicate these flows at scale.

How are typical design drivers affected by uncertainties in the inputs?

The design of a wind turbine is generally based on deterministic inputs. However, a wind turbine is subject to several uncertainties, not only because of the stochastic nature of the wind, but also because of several processes at different life-stages of its lifetime, for instance manufacturing processes, or wear and tear, among others. Clearly, identifying and modeling all uncertainties is highly challenging. Indeed, while aleatory uncertainties can be generally represented through a probability distribution, modeling epistemic uncertainties can be more complex as there are usually not enough elements to choose a specific probability distribution function.

Even though the study included in this thesis only focused on a few sources of uncertainties, the propagation of these uncertainties into outputs of interest typically related to design drivers – including extreme loads, fatigue damage – exemplified the importance of going towards a probabilistic approach. Indeed, the preliminary results obtained pointed out that the maximum values of loads and power production obtained with the deterministic conditions prescribed by international design standards are not always associated with high probabilities of occurrence. While the results obtained in this study were not comprehensive enough to draw significant conclusions, it is implied that the use of formal mathematical methods of uncertainty propagation may lead to a revision of typical safety factors in the interest of more cost-competitive but still fully safe designs. Further studies should analyze the impact of a broader set of uncertainties present in a wind turbine, as well as their couplings. Additionally, a ranking of uncertainties and a deeper understanding of their effects is a very worthwhile endeavor, and might have a significant role in the future design of wind energy systems.

Sampling strategies and methods for uncertainty quantification. Due to the large number of uncertain inputs, and the complexity and computational expense of aeroservoelastic simulators, another critical point is the choice of suitable sampling strategies and methods for uncertainty quantification that capture the output space with a minimum number of samples. The most simple approach is a Monte Carlo strategy where random inputs are selected from the probability distributions over the domain, and used as input for deterministic simulations. This method, however, requires a large number of samples – i.e. executions of the aeroservoelastic simulator – and cannot fully capture the computation of extreme states, which populate the tails of the probability distributions and often act as design drivers. Ad hoc sampling strategies have been developed by the research community, and could be applied to the problem at hand. Other sophisticated sampling methods, such as Latin hypercube sampling or Hammersley sampling, have been described in the literature and should be the topic of future studies.

Additionally, the large number of samples required is further challenged by the problem of turbulent realizations. Here the number of turbulent seeds typically recommended by design standards was used, but appeared not to be always sufficient for guaranteeing convergence of the statistics. If the number of seeds needs to be increased in a substantial manner to ensure convergence, a change in the methodological approach might be required, as the computational cost might become prohibitive. In this sense, the use of surrogate models, instead of the high fidelity ones considered in the studies of this thesis, might become attractive. Clearly, methods for uncertainty quantification offer a more efficient approach, as the methods are capable of modeling different performance indicators with a much lower number of samples. The work included in this thesis benchmarks the performance of two uncertainty quantification methods, non-intrusive polynomial chaos expansion (NIPCE) and universal Kriging (UK) against a brute-force Monte Carlo approach. Comparisons indicate a good performance in terms of quality at a significantly lower computational cost. Of the two, UK appears to consistently converge faster than NIPCE. Clearly, other methods are certainly available and further studies should also analyze their performance.

Can the LCOE of a wind turbine be further reduced through the adoption of a LAC system?

In general, two different strategies to reduce LCOE with the adoption of a LAC system can be pursued: a *retrofit strategy*, in which lidars are employed to extend the lifetime of a wind turbine which has already been designed and installed; and an *integrated approach*, in which LAC is considered as part of the system from its very inception. This discussion focuses on the latter. The impact on LCOE brought by LAC through an integrated approach will depend on several factors: the design drivers of the wind turbine, the characteristics of the specific LAC system and the integration strategy followed.

- **Wind turbine design drivers.** Design-driving quantities are those key indicators that define active constraints (design drivers), thereby affecting the design solution. Design-driving quantities include, for instance, elastic deflections and ultimate and fatigue loads resulting from the aeroservoelastic simulation of a comprehensive set of design load cases, as established by the standards. Even though design-driving quantities are specific for each machine – as they depend on multiple design choices –, generalizations can be made. They can be modified by LAC only to some extent, past which some other effect beyond the reach of the technology becomes the driver, preventing further improvements. For instance, the improvement potential of the design of fatigue-driven towers is a priori promising, as the design is driven by a quantity generally modifiable. The design of the rotor blade is generally driven by tip deflection – a modifiable quantity–, but also by requirements on the blade flap frequencies, which are not modifiable and might limit the blade improvement potential.

- **Characteristics of the LAC system.** Characteristics of the LAC system includes its performance – i.e. the extent in which key quantities are affected by LAC; its reliability and its cost and lifetime.

  - **Performance.** The performance of a LAC system will define the extent in which the design-driving quantities are actually reduced. Indeed, the LAC system should aim at reducing the design-driving quantities that present the largest exploitable margins. For instance, fatigue damage is generally reduced by LAC, as this is generated in power production in turbulent wind conditions, where the lidar preview information leads to a general reduction of load fluctuations. On the other hand, LAC can not always modify ultimate conditions (such as maximum stresses, strains, or blade tip deflection), leading to very limited improvement potential for design-driving quantities based on ultimate conditions. Additionally, even when LAC plays a role, other factors may have an even larger effect; for example, this is the case of shutdowns, where the pitch-to-feather policy may have a dominant role in dictating the peak response.

  - **Reliability.** LAC systems might not always be available or produce reliable information, as faults, inaccuracies, misses or unavailabilities might be present during its lifetime. This means that, even when LAC does improve design-driving ultimate conditions, an even more general question still remains: shall one design a component based on an ultimate condition that was reduced by LAC? If so, what are the extra precautions that should be taken in order to hedge against faults, inaccuracies, misses, or unavailability of the lidar? A solution could be the adoption of a redundant system with multiple lidars, which would, however, increase the costs.

  - **Cost and lifetime.** The impact on LCOE will also depend on the lifetime of a LAC system, and therefore the number of systems required for the lifetime of the wind turbine and the different costs – for instance purchase and maintenance costs – associated.

- **Integration strategy.** Finally, the benefits brought by LAC can be exploited with different strategies. The studies presented in this thesis focus on two of the main components of a wind turbine: the rotor and the tower. The load reductions brought by LAC can be exploited

to design lighter (and generally cheaper) components, to design a taller tower that reaches higher above ground or a larger rotor that has a larger swept area, or to design components with a longer lifetime. LAC can therefore be integrated to reduce the cost of a component (and therefore the overall initial capital costs), or/and indirectly increasing AEP. A decrease in component cost or/and increase in AEP is certainly not enough to ensure a decrease in LCOE. Indeed, the purchase cost of LAC, which depends on the lifetime of a LAC system, and the annual operating expenses must be outweighed by the gains brought by LAC.

Understanding the impact of lidar-assisted control in LCOE is clearly not straightforward. The studies conducted within this thesis highlight that, even when significant mass reductions are achieved, an improvement of LCOE is not guaranteed. Indeed, the increase in annual operating expenses is found to play a significant role, especially for onshore wind turbines. The largest LCOE reduction is found for offshore wind turbines, where reductions of LCOE of about 2% are estimated. Additionally, the design of towers for extended lifetime is found to be promising and should be the focus of further studies.

These conclusions are based on a number of assumptions, and further work should be performed. First, only three turbines were considered; although these machines are reasonable approximations of contemporary products, it is clear that design drivers are typically turbine specific, and a more ample range of cases should be investigated. Additionally, only the conventional configuration of thin-walled steel towers with circular tubular tapered sections was considered. This configuration presents important geometric constraints that impact the benefits of LAC. Second, there was no attempt here to consider lidar availability, faults, and possible redundancy; an analysis of these aspects would help in clarifying whether LAC-enabled reductions in ultimate conditions can indeed be exploited in the structural redesign of the blade and the tower or not. Finally, it should be remarked that the use of a generic load model implies some significant approximations. Although this was done here on purpose with the goal of making the study more general, it is also clear that the performance of different LAC systems can be very different, depending on the lidar characteristics and on the controller formulation and tuning. Therefore, here again, more specific studies based on fully coupled simulations should be performed to further explore the trends reported here and find additional niches of applicability of LAC missed by the present general analysis.

Can short-term economic and long-term societal benefits brought by a wind turbine be enhanced through its design?

LCOE has been traditionally employed to measure the economic competitiveness of energy sources. This metric, however, only captures a partial view of a situation that is much more complex that what appears through cost alone. Indeed, a wind turbine has an *economic cost*, but also an *economic value*, as the energy generated is sold in the spot market for a variable price and therefore produces a revenue. However, the benefits of a wind turbine should not only be measured in economic terms. Indeed, the focus should also be widened to include broader long-term sustainable development goals. As long as these impacts are quantifiable through some appropriate metric, they can be considered in a design procedure. However, while several publications propose metrics that capture the economic profitability of a wind turbine [15, 55, 56], no metrics are yet available to quantify the societal benefits of a wind turbine.

How can long-term societal benefits be quantified? While there are undoubtedly several different options to quantify long-term societal effects in the design of wind turbines, the work presented in this thesis focuses on the impact exerted by wind technology on the environment in terms of greenhouse gas (GHG) emissions. While GHG emissions clearly do not capture all effects of wind energy, they provide for a major and quantifiable impact with long-term consequences. Clearly, a parallelism can be established between an environmental perspective – which represents the point of view of society; and an economic perspective – which can be defined from the point of view of a consumer that wants to get energy at minimum cost. Indeed, a wind turbine has an *environmental cost*, as GHG emissions are emitted during the different life-cycle stages, but more importantly, but also has an *environmental value*, as GHG emissions are displaced through the deployment of wind energy. This parallelism can be exploited to define eco-conscious metrics that mimic existing economic ones. Furthermore, GHG emissions can also be quantified as economic savings by applying the social cost of carbon (SCC), which estimates the net present value of monetized social damages occurring from the emission of an additional metric ton of CO_2.

How would a wind turbine with enhanced economic and societal value look like? The work presented in this thesis explores how the choice of rotor diameter (and therefore specific power – i.e. rated power divided by rotor swept area) and hub height can enhance the economic and societal value of a wind turbine. The eco-conscious metrics defined are applied to resize an average wind turbine for two different locations in Germany. Low-specific-power machines are found to present a higher economic and environmental value, as they operate longer at low wind speeds when there is less renewable energy in the grid. These benefits come at the expense of a higher LCOE, as the larger energy captured does not generally compensate the costs of a larger rotor. However, current research points out that the benefits of low specific power turbines go beyond what is quantified through costs. Indeed, studies have shown that low-specific-power turbines also better utilize the transmission system, lower forecast error and could lead to cheaper financing.

The trends shown here are only valid for Germany in the years considered in the study. Clearly, both economic and environmental value depend on the time-specific composition of the energy mix, whose behavior is very complex and depends on more variables than just wind speed, as it was assumed here for simplicity. The assumptions taken in this work are clearly oversimplifications that try to produce initial rough preliminary trends. Future work should couple the present models with more sophisticated descriptions of the energy mix, able to capture their present and future composition. In fact, understanding how the economic and environmental value of wind energy will develop in the next years is yet another crucial element that deserves further work. Indeed, as wind penetration is set to increase, the economic value of wind energy is expected to decrease, an effect called "self-

cannibalization". However, predicting the impact of an increase in wind energy is not straightforward, as the final effects depend on the emission factors of the generating technologies in the energy mix. The impact on displaced GHG is even more complex to estimate, as it depends on the emission factors of the generating technologies operating on the margin, which are not only strongly country-specific, but also time-dependent. Here again, these effects can only be properly captured by using more sophisticated models, including an electricity market model.

6.2 Contribution to the existing literature

The novelty of the work presented in this thesis with respect to the existing literature is described in this section.

DESIGN AND PERFORMANCE OF SCALED ROTORS

Multiple studies in the literature describe the definition of scaling laws to design subscaled models that target different characteristics of a full-scale machine [25, 28, 33] and apply these scaling laws through different design procedures [26, 104]. The contribution to the literature of **Paper I** is three-fold: first, a comprehensive analysis of the effect of the change of scale on the steady and transient response of a wind turbine is presented to understand which quantities can be captured. To the author's knowledge, this is the most comprehensive analysis available so far. Second, two different approaches to design subscaled rotors are described and challenges and advantages of each approach are highlighted. While some of the advantages and challenges of each approach are widely understood, this is the first work that presents a comprehensive analysis of the feasibility and restrictions of each approach for three sizes from utility to wind tunnel size. Third, three models of different sizes are designed with the most suitable approach and their performance is analyzed. While studies in the literature show the performance of specific subscaled models, the novelty of the work here presented lies in the comparison of the faithfulness of three models of different sizes not only to capture absolute quantities, but also to follow relative trends.

In **Paper II**, the aerodynamic and structural shape of a wind tunnel model is designed for the first time following gravo-aeroservoelastic scaling laws. Finally, **Paper III** focuses on the wakes of scaled models. The study presents a comprehensive review of the main factors driving wake behavior to analyze which physical aspects of full-scale wakes cannot be matched at the reduced scale. Only partial analysis of the effect of scale in wakes was available in the literature so far [126].

METHODS FOR UNCERTAINTY QUANTIFICATION

Studies in the literature describe and analyze the application of several methods for uncertainty quantification to wind energy [36–40]. **Paper IV** investigates the performance and convergence properties of two different methods for uncertainty quantification. The novelty of this work lies not only in the assessment of these two methods, but also in the choice of quantities for the assessment. Indeed, the two considered uncertainty propagation methods are compared in terms of their ability to reconstruct the main statistics of key performance indicators related to design drivers, including maximum blade tip deflection, ultimate and fatigue loads and AEP.

LAC-BASED INTEGRATED DESIGN

Several studies in the literature describe the benefits of LAC systems in terms of load reductions, power production and fatigue loads [42–44, 46–48]. Literature also presents a first approach to estimate the benefits of LAC through a retrofit strategy [50], and describes the potential pathways to exploit the benefits brought by LAC with an integrated approach [49, 52]. To the author's knowledge, **Paper V** and **Paper VI** are the first articles in the literature where the rotor and tower of several reference models are actually redesigned considering benefits brought by LAC. Additionally, these articles quantify the potentially exploitable margins by LAC, thus defining the requirements for LAC systems to increase their impact within the design of a wind turbine.

MARKET-BASED ECONOMIC VALUE

Studies in the literature about market-based economic value describe alternative merit functions that go beyond LCOE and capture the market-based value of wind energy [15, 55, 56]. Additionally, literature

also analyzes the impact of advanced wind turbine design in the market-based value [53,56,58]. For the first time, **Paper VII** couples a selection of already existing market-based metrics with an optimization framework, based on cost and mass models, that sizes two macroparameters of the wind turbine. The turbines designed in this paper are similar to the advanced wind turbine designs explored in the literature.

ENVIRONMENTAL VALUE

Studies in the literature assess the environmental impact [59–63] and environmental value of a wind turbine [64, 65]. To the author's knowledge, **Paper VII** is as well the first work that formally defines metrics based on environmental quantities to drive the design of a wind turbine. This work also defines metrics that quantify the societal value of wind energy estimating the future savings through the displacement of GHG. Additionally, for the first time, this work couples these metrics with an optimization framework and analyzes how the design of a wind turbine can enhance its environmental and societal value.

6.3 Outlook

The work here presented should not only be extended in scope, but also in depth. Indeed, the work included in this thesis mainly focuses on the rotor and tower design, with drivetrain and nacelle components being neglected. These components, however, play a very important role not only from an economic perspective, but also from an environmental and scientific point of view. Further work should introduce physics-based models of all wind turbine components within the design framework, to ensure that truly holistic design procedures are achieved.

Additionally, the topics considered in this thesis are certainly not the only pathways to enhance scientific, economic and societal value. Other promising topics not considered here include, for instance, control co-design, which consists in designing the control algorithm parallelly to the wind turbine [127]; or the exploration of technological solutions that present a lower environmental impact, such as towers made of wood, or wind turbine blades made of fully recyclable composites [128] to enhance its environmental and societal value.

Additional values can also be identified: for instance, a wind turbine also has a (positive and negative) value for ecosystems. Indeed, the operation of wind turbines has been linked to an increased probability of collision for birds and bats [129]. Recent publications imply that a simple design choice such as the color of the blades can lead to a reduction in avian fatalities [130]. Positive impacts that can be enhanced by design can also be found. For instance, the scour protection for offshore wind turbines often consists of rocks that are positioned on the seabed to prevent erosion and may resemble a marine rocky reef, which can have important ecosystem functions. This scour protection can, for instance, be tailored to support the abundance and diversity of marine species [131].

A wind turbine can also be simply understood as a piece of a larger system. Indeed, a wind turbine can also be a generation technology within a wind farm, wind-based hybrid generation system, a power-to-x system or a larger electricity grid. Indeed, a wind turbine can be designed as an altruistic machine, whose value is to serve a larger system. For instance, designing a wind turbine as part of a wind farm might imply tailoring the characteristics of each machine to minimize wakes between wind turbines, thus maximizing the overall power production – at the expense of their own individual production [132]; the design of a wind turbine for a wind-based hybrid generation system connected to a battery might aim at maximizing power quality and reliability to ensure a good battery performance [133]; or designing a wind turbine as a generation technology within a larger electricity grid system might also require looking beyond its own power production, with other quantities such as reactive power and voltages coming into focus [134].

While wind turbine design can certainly play a significant role to enhance the different inherent values of a wind turbine, the true holistic value of wind energy can only be achieved when value is considered at all levels. For instance, it is through the planning and development of a wind farm that additional societal benefits such as job creation and local economic development impacts can be enhanced; or it is through the control of a wind turbine that short-term economic trends can be captured, or selected ecological impacts minimized.

Even though this thesis has considered the values here described to be independent, couplings are certainly possible. For instance, any choice that impacts the environmental or the ecological value of a wind turbine will have as well an economic impact – and viceversa. Enhancing the holistic value of a wind turbine might therefore require to establish trade-offs between different aspects. The full benefits of wind energy can only be achieved when these trade-offs are not only driven by short-term needs, but also by long-term sustainable development goals.

[1] I. P. on Climate Change, "Summary for policymakers," in *Climate Change 2013: The Physical Science Basis. Contribution of Working Group I to the Fifth Assessment Report of the Intergovernmental Panel on Climate Change*, T. Stocker, D. Qin, G. Plattner, M. Tignor, S. Allen, J. Boschung, A. Nauels, Y. Xia, V. Bex, and P. Midgley, Eds. Cambridge, United Kingdom and New Yor, NY, USA: Cambridge University Press, 2013. [Online]. Available: http://www.climatechange2013.org/ images/report/WG1AR5_SPM_FINAL.pdf

[2] U. N. F. C. on Climate Change, "Article 1: Definitions." [Online]. Available: https://unfccc.int/ resource/ccsites/zimbab/conven/text/art01.htm

[3] I. P. on Climate Change, "Annex i: Glossary," in *Global Warming of 1.5°C. An IPCC Special Report on the impacts of global warming of 1.5°C above pre-industrial levels and related global greenhouse gas emission pathwys, in the context of strengthening the global response to the threat of climate change, sustainable development, and efforts to erradicate poverty*, V. Masson-Delmotte, P. Zhai, H. Pörtner, D. Roberts, J. Skea, P. Shukla, A. Pirani, W. Moufouma-Okia, C. Péan, R. Pidcock, S. Connors, J. Matthews, Y. Chen, X. Zhou, M. Gomis, E. Lonnoy, T. Maycock, M. Tignor, and T. Waterfield, Eds. Cambridge, United Kingdom and New Yor, NY, USA: Cambridge University Press, 2018. [Online]. Available: https://www.ipcc.ch/sr15/chapter/glossary/

[4] M. Parry, O. Canziani, J. Palutikof, P. van der Linden, and C. Hanson, "Climate change 2007: Impacts, adaptation and vulnerability. contribution of working group ii to the fourth assessment report of the intergovernmental panel on climate change," Cambridge, UK, 2007. [Online]. Available: https://www.ipcc.ch/site/assets/uploads/2018/03/ar4_wg2_full_report.pdf

[5] U. Nations, "Paris agreement." [Online]. Available: https://treaties.un.org/pages/ViewDetails. aspx?src=TREATY&mtdsg_no=XXVII-7-d&chapter=27&clang=_en

[6] E. E. Agency, "Energy and climate change," 2017. [Online]. Available: https://www.eea.europa. eu/signals/signals-2017/articles/energy-and-climate-change

[7] S. Schlömer, T. Bruckner, L. Fulton, E. Hertwich, A. McKinnon, D. Perczyk, J. Roy, R. Schaeffer, R. Sims, P. Smith, and R. Wiser, "Annex iii: Technology-specific cost and performance parameters," in *Climate Change 2014: Mitigation of Climate Change. Contribution of Working Group III to the Fifth Assessment Report of the Intergovernmental Panel on Climate Change*, O. Edenhofer, R. Pichs-Madruga, Y. Sokona, E. Farahani, S. Kadner, K. Seyboth, A. Adler, I. Baum, S. Brunner, P. Eickemeier, B. Kriemann, J. Savolainen, S. Schlömer, C. von Stechow, T. Zwickel, and J. Minx, Eds. Cambridge, United Kingdom and New Yor, NY, USA: Cambridge University Press, 2014. [Online]. Available: https://www.ipcc.ch/site/assets/uploads/2018/02/ipcc_wg3_ar5_annex-iii. pdf

[8] IRENA, "Renewable power generation costs in 2020," Abu Dhabi, 2021.

[9] P. Veers, K. Dykes, E. Lantz, S. Barth, C. L. Bottasso, O. Carlson, A. Clifton, J. Green, P. Green, H. Holttinen, D. Laird, V. Lehtomäki, J. Lundquist, J. Manwell, M. Marquis, C. Meneveau, P. Moriarty, X. Munduate, M. Muskulus, J. Naughton, L. Pao, J. Paquette, J. Peinke, A. Robertson, J. Sanz Rodrigo, A. Sempreviva, J. Smith, A. Tuohy, and R. Wiser, "Grand challenges in the science of wind energy," *Science*, 2019. doi: dx.doi.org/10.1126/science.aau2027

[10] T. 26, "Data viewer." [Online]. Available: https://iea-wind.org/task26/data-viewer/

[11] J. Aldersey-Williams and T. Rubert, "Levelised cost of energy - a theoretical justification and critical assessment," *Energy Policy*, pp. 169–179, 2019. [Online]. Available: https://doi.org/10.1016/j.enpol.2018.10.004

[12] R. Wiser, J. Rand, J. Seel, P. Beiter, E. Baker, E. Lantz, and Gilman.P, "Expert elicitation survey predicts 37by 2050," *Nature Energy*, vol. 6, p. 555–565, 2021. doi: https://doi.org/10.1038/s41560-021-00810-z

[13] IRENA, "Future of wind: Deployment, investment, technology, grid integration and socio-economic aspects (a global energy transformation paper)," Abu Dhabi, 2019. [Online]. Available: https://www.irena.org/-/media/files/irena/agency/publication/2019/oct/irena_future_of_wind_2019.pdf

[14] E. Lantz, R. Wiser, and M. Hand, "Iea wind task 26 - the past and future cost of wind energy," Golden, Colorado, 2012.

[15] M. T. M. M. and K. Eurek, "Competitiveness metrics for electricity system technologies," NREL, Golden, CO, USA, Tech. Rep. NREL/TP-6A20-72549, 2021. [Online]. Available: https://www.osti.gov/biblio/1765599

[16] P. Beiter, A. Cooperman, E. Lantz, T. Stehly, M. Shields, R. Wiser, T. Telsnig, L. Kitzing, V. Berkhout, and Y. Kikuchi, "Wind power costs driven by innovation and experience with further reductions on the horizon," *WIREs Energy and Environment*, vol. 5.

[17] G. A. M. van Kuik, J. Peinke, R. Nijssen, D. Lekou, J. Mann, J. N. Sørensen, C. Ferreira, J. W. van Wingerden, D. Schlipf, P. Gebraad, H. Polinder, A. Abrahamsen, G. J. W. van Bussel, J. D. Sørensen, P. Tavner, C. L. Bottasso, M. Muskulus, D. Matha, H. J. Lindeboom, S. Degraer, O. Kramer, S. Lehnhoff, M. Sonnenschein, P. E. Sørensen, R. W. Künneke, P. E. Morthorst, and K. Skytte, "Long-term research challenges in wind energy: a research agenda by the european academy wind energy," *Wind Energy Science*, vol. 1, no. 1, pp. 1–39, 2016. [Online]. Available: https://wes.copernicus.org/articles/1/1/2016/. doi: 10.5194/wes-1-1-2016

[18] G. Ellis and G. Ferraro, "The social acceptance of wind energy: Where we stand and the path ahead," Luxembourg (Luxembourg), Scientific analysis or review LC-NA-28182-EN-N, 2016.

[19] C. E. Dictionary. Value. Cambridge University. [Online]. Available: https://dictionary.cambridge.org/dictionary/english/value

[20] D. Simms, S. Schreck, M. Hand, and L. Fingersh, "Nrel unsteady aerodynamics experiment in the nasa-ames wind tunnel: A comparison of predictions to measurements," 2001. [Online]. Available: http://citeseerx.ist.psu.edu/viewdoc/download?doi=10.1.1.452.974&rep=rep1&type=pdf

[21] H. Snel, J. Schepers, and N. Siccama, "Mexico project: The database and results of data processing and interpretation," *47th AIAA Aerospace Sciences Meeting Including The New Horizons Forum and Aerospace Exposition Orlando, Florida*, 2009. [Online]. Available: https://doi.org/10.2514/6.2009-1217

[22] F. Campagnolo, V. Petrović, J. Schreiber, E. M. Nanos, A. Croce, and C. L. Bottasso, "Wind tunnel testing of a closed-loop wake deflection controller for wind farm power maximization," *Journal of Physics: Conference Series*, vol. 753, no. 032006, 2016. doi: 10.1088/1742-6596/753/3/032006

[23] F. Campagnolo, R. Weber, J. Schreiber, and C. L. Bottasso, "Wind tunnel testing of wake steering with dynamic wind direction changes," *Wind Energy Science*, vol. 5, no. 4, pp. 1273–1295, 2020. doi: 10.5194/wes-5-1273-2020

[24] M. Bastankhah and F. Porté-Agel, "Experimental and theoretical study of wind turbine wakes in yawed conditions," *Journal of Fluid Mechanics*, vol. 806, p. 506–541, 2016. doi: 10.1017/jfm.2016.595

[25] C. Bottasso, F. Campagnolo, and V. Petrovic, "Wind tunnel testing of scaled wind turbine models: Beyond aerodynamics," *J. Wind Eng. Ind. Aerodyn.*, pp. 11–28, 2014. [Online]. Available: https://doi.org/10.1016/j.jweia.2014.01.009

[26] F. Campagnolo, C. L. Bottasso, and P. Bettini, "Design, manufacturing and characterization of aero-elastically scaled wind turbine blades for testing active and passive load alleviation techniques within a abl wind tunnel," *J. Phys: Conf. Ser.*, 2014. [Online]. Available: http://doi.org/10.1088/1742-6596/524/1/012061

[27] J. Meyers, C. Bottasso, K. Dykes, P. Fleming, P. Gebraad, G. Giebel, T. Göçmen, and J.-W. van Wingerden, "Wind farm flow control: prospects and challenges," *Wind Energy Science Discussions*, vol. 2022, pp. 1–56, 2022. doi: 10.5194/wes-2022-24

[28] B. R. Resor and D. C. Maniaci, "Definition of the national rotor testbed: An aeroelastically relevant research-scale wind turbine rotor," 32nd ASME Wind Energy Symposium, AIAA SciTech Forum National Harbor, Maryland, Tech. Rep., 2013.

[29] L. P. Chamorro and F. Porté-Agel, "A wind-tunnel investigation of wind-turbine wakes: Boundary-layer turbulence effects," *Boundary-Layer Meteorology*, vol. 132, pp. 129–149, 2009. doi: 10.1007/s10546-009-9380-8

[30] L. P. Chamorro and F. Porté-Agel, "Effects of thermal stability and incoming boundary-layer flow characteristics on wind-turbine wakes: A wind-tunnel study," *Boundary-Layer Meteorology*, vol. 136, pp. 515–533, 2010. doi: 10.1007/s10546-010-9512-1

[31] H. Hu, Z. Yang, and P. Sarkar, "Dynamic wind loads and wake characteristics of a wind turbine model in an atmospheric boundary layer wind," *Experiments in Fluids*, vol. 52, pp. 1277–1294, 2012. doi: 10.1007/s00348-011-1253-5

[32] G. V. Iungo, F. Viola, S. Camarri, F. Porté-Agel, and F. Gallaire, "Linear stability analysis of wind turbine wakes performed on wind tunnel measurements," *Journal of Fluid Mechanics*, vol. 737, p. 499–526, 2013. doi: 10.1017/jfm.2013.569

[33] E. M. Nanos, C. L. Bottasso, F. Campagnolo, S. Letizia, G. V. Iungo, and M. A. Rotea, "Design, performance and wake characterization of a scaled wind turbine with closed-loop controls," *Wind Energy Science Discussions*, vol. 2021, pp. 1–36, 2021. doi: 10.5194/wes-2021-66

[34] J. Schottler, A. Hölling, J. Peinke, and M. Hölling, "Design and implementation of a controllable model wind turbine for experimental studies," *Journal of Physics: Conference Series*, vol. 753, no. 072030, 2016. doi: 10.1088/1742-6596/753/7/072030

[35] M. Bastankhah and F. Porté-Agel, "A new miniature wind turbine for wind tunnel experiments. part i: Design and performance," *Energies*, vol. 10, no. 7, 2017. doi: 10.3390/en10070908

[36] J. Witteveen, S. Sarkar, and H. Bijl, "Modeling physical uncertainties in dynamic stall induced fluid–structure interaction of turbine blades using arbitrary polynomial chaos," *Computers & Structures*, vol. 85, no. 11, pp. 866–878, 2007. [Online]. Available: https://www.sciencedirect.com/science/article/pii/S0045794907000168. doi: https://doi.org/10.1016/j.compstruc.2007.01.004

[37] G. Petrone, C. de Nicola, D. Quagliarella, J. Witteveen, and G. Iaccarino, *Wind Turbine Performance Analysis Under Uncertainty*. [Online]. Available: https://arc.aiaa.org/doi/abs/10.2514/6.2011-544

[38] M. S. Campobasso, E. Minisci, and M. Caboni, "Aerodynamic design optimization of wind turbine rotors under geometric uncertainty," *Wind Energy*, vol. 19, no. 1, pp. 51–65, 2016. [Online]. Available: https://onlinelibrary.wiley.com/doi/abs/10.1002/we.1820. doi: https://doi.org/10.1002/we.1820

[39] J. P. Murcia, P.-E. Réthoré, N. Dimitrov, A. Natarajan, J. D. Sørensen, P. Graf, and T. Kim, "Uncertainty propagation through an aeroelastic wind turbine model using polynomial surrogates," *Renewable Energy*, vol. 119, pp. 910–922, 2018. [Online]. Available: https://www.sciencedirect.com/science/article/pii/S0960148117306985. doi: https://doi.org/10.1016/j.renene.2017.07.070

[40] D. Matthäus, P. Bortolotti, J. Loganathan, and C. L. Bottasso, *Propagation of Uncertainties Through Wind Turbine Models for Robust Design Optimization*. [Online]. Available: https://arc.aiaa.org/doi/abs/10.2514/6.2017-1849

[41] E. Bossanyi, A. Kumar, and O. Hugues-Salas, "Wind turbine control applications of turbine-mounted lidar," *J. Phys.: Conf. Ser.*, 2014. [Online]. Available: 10.1088/1742-6596/555/1/012011

[42] F. Dunne, L. Pao, A. Wright, B. Jonkman, and N. Kelley, "Adding feedforward blade pitch control to standard feedback controllers for load mitigation in wind turbines, mechatronics," pp. 682–690, 2011. [Online]. Available: 10.1016/j.mechatronics.2011.02.011

[43] F. Dunne, D. Schlipf, L. Pao, A. Wright, B. Jonkman, N. Kelley, and E. Simley, "Comparison of two independent lidar-based pitch control designs," *Proc. AIAA Aerospace Sciences Meeting*, 2012. [Online]. Available: 10.2514/6.2012-1151

[44] D. Schlipf, P. Fleming, F. Haizmann, A. Scholbrock, M. Hofsäß, A. Wright, and P. Cheng, "Field testing of feedforward collective pitch control on the cart2 using a nacelle-based lidar scanner," *J. Physics*, 2013. [Online]. Available: doi.org/10.1088/1742-6596/555/1/012090

[45] N. Wang, K. Johnson, and A. Wright, "Comparison of strategies for enhancing energy capture and reducing loads using lidar and feedforward control," *IEEE Transactions on Control Systems Technology*, pp. 1129–1142, 2013. [Online]. Available: 10.1109/TCST.2013.2258670

[46] D. Schlipf, P. Fleming, S. Kapp, A. Scholbrock, F. Haizmann, F. Belen, A. Wright, and P. Cheng, "Direct speed control using lidar and turbine data," *American Control Conference 2013*, 2013. [Online]. Available: 10.1109/ACC.2013.6580163

[47] D. Schlipf, D. Schlipf, and M. Kühn, "Nonlinear model predictive control of wind turbines using lidar," *Wind Energ.*, vol. 7, pp. 1107–1129, 2013.

[48] D. Schlipf and P. Cheng, "Flatness-based feedforward control of wind turbines using lidar," *IFAC Proceedings Volumes*, vol. 47, pp. 5820–5825, 2014. [Online]. Available: 10.3182/20140824-6-ZA-1003.00443

[49] A. Scholbrock, P. Fleming, A. Wright, N. Wang, D. Schlipf, and K. Johnson, "Lidar-enhanced wind turbine control: Past, present and future," Tech. Rep. NREL/CP-5000-65879, 2016.

[50] D. Schlipf, S. Fürst, H.and Raach, and F. Haizmann, "Systems engineering for lidar-assisted control: A sequential approach," *J. Phys.: Conf. Ser.*, 2018. [Online]. Available: 10.1088/1742-6596/1102/1/012014

[51] E. Simley, H. Fürst, and D. Schlipf, "Optimizing lidars for wind turbine control applications — results from the iea wind task 32 workshop," *Remote Sens.*, vol. 863, 2018. [Online]. Available: 10.3390/rs10060863

[52] E. Simley, P. Bortolotti, A. Scholbrock, D. Schlipf, and K. Dykes, "Iea wind task 32 and task 37: Optimizing wind turbines with lidar-assisted control using systems engineering," *J. Phys.: Conf. Ser.*, 2020. [Online]. Available: 10.1088/1742-6596/1618/4/042029

[53] L. Hirth, "Integration costs and the value of wind power. thoughts on a valuation framework for variable renewable electricity sources," *USAEE Working Paper*, pp. 12–150, 2012. [Online]. Available: doi.org/10.2139/ssrn.2187632

[54] P. Joskow, "Comparing the costs of intermittent and dispatchable electricity generating technologies," *American Economic Review*, vol. 101, no. 3, pp. 238–41, May 2011. [Online]. Available: https://www.aeaweb.org/articles?id=10.1257/aer.101.3.238. doi: 10.1257/aer.101.3.238

[55] J. Simpson, E. Loth, and K. Dykes, "Cost of valued energy for design of renewable energy systems," *Renewable Energy*, 2020. doi: https://doi.org/10.1016/j.renene.2020.01.131

[56] L. Hirth and S. Müller, "System-friendly wind power: How advanced wind turbine design can increase the economic value of electricity generated through wind power," *Energy Economics*, pp. 51–63.

[57] E. Lantz, A. Dalla Riva, J. Hethey, and A. Vitina, "Impacts of wind turbine technology on the system value of wind in europe," NREL, Golden, CO, USA, Tech. Rep. NREL/TP-6A20-70337, 2017. [Online]. Available: nrel.gov/docs/fy18osti/70337.pdf

[58] P. Swisher, J. Murcia Leon, J. Gea Bermudez, M. Koivisto, H. Madsen, and M. Münster, "Competitiveness of a low specific power, low cut-out wind speed wind turbine in north and central europe towards 2050," *Applied Energy*, no. 118043, 2022. [Online]. Available: https://doi.org/10.1016/j.apenergy.2021.118043

[59] M. Ozoemena, W. Cheung, and R. Hasan, "Comparative lca of technology improvement opportunities for a 1.5 mw wind turbine in the context of an onshore wind farm," *Clean Technologies and Environmental Policy*, pp. 173–190, 2018. [Online]. Available: https://doi.org/10.1007/s10098-013-0642-2

[60] S. Al-Behadili and W. El-Osta, "Life cycle assessment of dernah (libya) wind farm," *Ren. Energy*, pp. 1227–1233, 2015. [Online]. Available: https://doi.org/10.1016/j.renene.2015.05.041

[61] Vestas, "Life cycle assessment of electricity production from a v90-2.0 mw gridstreamer wind plant," Aahrus, Denmark, Tech. Rep., 2011.

[62] Vestas, "Life cycle assessment of electricity production from an onshore v90-3.0 mw wind plant," Aahrus, Denmark, Tech. Rep., 2013.

[63] Vestas, "Life cycle assessment of electricity production from an onshore v100-2.6 mw wind plant," Aahrus, Denmark, Tech. Rep., 2013.

[64] A. Hawkes, "Estimating marginal co2 emissions rates for national electricity systems," *Energy Policy*, pp. 5977–5987, 2014. [Online]. Available: https://doi.org/10.1016/j.enpol.2010.05.053

[65] R. Thomson, G. Harrison, and J. Chick, "Marginal greenhouse gas emissions displacement of wind power in great britain," *Energy Policy*, pp. 201–210, 2017. [Online]. Available: https://doi.org/10.1016/j.enpol.2016.11.012

[66] K. Gillingham and J. Stock, "The cost of reducing greenhouse gas emissions," *Journal of Economic Perspectives*, vol. 4, pp. 53–72, 2018. [Online]. Available: doi.org/10.1257/jep.32.4.53

[67] E. National Academies of Sciences and Medicine, "Valuing climate damages: Updating estimation of the social cost of carbon dioxide," *The National Academies Press*, 2017. [Online]. Available: https://doi.org/10.17226/24651

[68] H. Canet, P. Bortolotti, and C. L. Bottasso, "On the scaling of wind turbine rotors," *Wind Energy Science*, vol. 6, no. 3, pp. 601–626, 2021. doi: 10.5194/wes-6-601-2021

[69] H. Canet, P. Bortolotti, and C. L. Bottasso, "Gravo-aeroelastic scaling of very large wind turbines to wind tunnel size," *Journal of Physics: Conference Series*, vol. 1037, no. 042006, 2018. doi: 10.1088/1742-6596/1037/4/042006

[70] H. Canet, S. Loew, and C. L. Bottasso, "Lidar-assisted control in wind turbine design: Where are the potential benefits?" vol. 1618, no. 042020, 2020. doi: 10.1088/1742-6596/1618/4/042020

[71] H. Canet, S. Loew, and C. L. Bottasso, "What are the benefits of lidar-assisted control in the design of a wind turbine?" *Wind Energy Science*, vol. 6, no. 5, pp. 1325–1340, 2021. doi: 10.5194/wes-6-1325-2021

[72] H. Canet, A. Guilloré, and C. L. Bottasso, "The eco-conscious wind turbine: bringing societal value to design," *Wind Energy Science Discussions*, 2022.

[73] C. Wang, F. Campagnolo, H. Canet, D. J. Barreiro, and C. L. Bottasso, "How realistic are the wakes of scaled wind turbine models?" *Wind Energy Science*, vol. 6, no. 3, pp. 961–981, 2021. doi: 10.5194/wes-6-961-2021

[74] P. Bortolotti, H. Canet, C. L. Bottasso, and J. Loganathan, "Performance of non-intrusive uncertainty quantification in the aeroservoelastic simulation of wind turbines," *Wind Energy Science*, vol. 4, no. 3, pp. 397–406, 2019. doi: 10.5194/wes-4-397-2019

[75] C. L. Bottasso, A. Croce, Y. Nam, and C. Riboldi, "Power curve tracking in the presence of a tip speed constraint," *Renewable Energy*, vol. 40, no. 1, pp. 1–12, 2012. [Online]. Available: https://www.sciencedirect.com/science/article/pii/S0960148111004411. doi: https://doi.org/10.1016/j.renene.2011.07.045

[76] N. I. Portal, *TurbSim v1.40*, 2016. [Online]. Available: https://nwtc.nrel.gov/TurbSim

[77] C. L. Bottasso, S. Cacciola, and J. Schreiber, "Local wind speed estimation, with application to wake impingement detection," *Renewable Energy*, pp. 155–168, 2017. [Online]. Available: https://doi.org/10.1016/j.renene.2017.09.044

[78] V. Giavotto, M. Borri, P. Mantegazza, and G. Ghiringhelli, "Anisotropic beam theory and applications," *Computers & Structures*, vol. 16, no. 1, pp. 403 – 413, 1983. [Online]. Available: http://www.sciencedirect.com/science/article/pii/0045794983901797. doi: http://dx.doi.org/10.1016/0045-7949(83)90179-7

[79] NREL, "Wisdem v3.2.0," 2021. [Online]. Available: https://github.com/WISDEM/WISDEM

[80] L. Fingersh, M. Hand, and A. Laxson, "Wind turbine design cost and scaling model," Tech. Rep. NREL/TP-500-40566, 2006. [Online]. Available: https://www.nrel.gov/docs/fy07osti/40566.pdf

[81] P. Chaviaropoulos, I. Karga, C. Harkness, and B. Hendriks, "Deliverable 1.23 pi-based assessment of innovative concepts," INNWIND.EU technical report, Tech. Rep., 2014. [Online]. Available: www.innwind.eu

[82] D. Griffith and W. Johans, "Large blade manufacturing cost studies using the sandia blade manufacturing cost tool and sandia 100-meter blades," Sandia National Laboratories technical report, Albuquerque, NM, Tech. Rep., 2013. [Online]. Available: https://energy.sandia.gov/wp-content/gallery/uploads/dlm_uploads/SAND_SNLLargeBladeManufacturingCostTrendsAnalysis_SAND2013-2734.pdf

[83] N. Demir and A. Taskin, "Life cycle assessment of wind turbines in pinarbasi-kayseri," *Journal of Cleaner Production*, pp. 253–263, 2013. [Online]. Available: doi.org/10.1016/j.jclepro.2013.04.016

[84] K. Haapala and P. Prempreeda, "Comparative life cycle assessment of 2.0 mw wind turbines," *Int. J. of Sustainable Manufacturing*, pp. 170–185, 2014. [Online]. Available: http://dx.doi.org/10.1504/IJSM.2014.062496

[85] P. Bortolotti, D. Berry, R. Murray, E. Gaertner, D. Jenne, R. Damiani, G. Barter, and K. Dykes, "A detailed wind turbine blade cost model," NREL, Golden, CO, USA, Tech. Rep. NREL Report TP-5000-73585, 2019. [Online]. Available: https://dx.doi.org/10.2172/1529217

[86] S. Pfaffel, S. Faulstich, and K. Rohrig, "Performance and reliability of wind turbines: A review," *Energies*, vol. 10, no. 1904, 2017. [Online]. Available: https://doi.org/10.3390/en10111904

[87] M. Wolf, R. Pant, K. Chomkhamsri, S. Sala, and D. Pennington, *The International Reference Life Cycle Data System (ILCD) Handbook - Towards more sustainable production and consumption for a resource-efficient Europe, Technical report, Joint Research Center, European Commission.* Publications Office of the European Union, 2012.

[88] M. Z. Hauschild, R. K. Rosenbaum, and S. I. Olsen, *Life Cycle Assessment, Theory and Practice.* Springer, 2018. [Online]. Available: doi.org/10.1007/978-3-319-56475-3

[89] C. Rydh, M. Jonsson, and P. Lindahl, "Replacement of old wind turbines assessed from energy, environmental and economic perspectives," Kalmar, Sweden, Tech. Rep. NEI-SE-544, 2004. [Online]. Available: https://www.osti.gov/etdeweb/biblio/20534695

[90] G. Myhre, G. Shindell, F. M. Breon, W. Collins, J. Fuglestvedt, F. Huang, D. Koch, J.-F. Lamarque, D. Lee, B. Mendoza, N. T., R. A., S. G., T. T., and H. Zhang, "Anthropogenic and natural radiative forcing," *Cambridge University Press, book section 8*, pp. 659–740, 2013.

[91] S. C. for Life Cycle Inventories, "Ecoinvent version 3.6," Tech. Rep., 2020. [Online]. Available: https://v36.ecoquery.ecoinvent.org

[92] G. Bourgault, "Implementation of impact assessment methods in the ecoinvent database version 3.6," Tech. Rep., 2019.

[93] M. Spielmann, C. Bauer, R. Dones, and M. Tuchschmid, "Transport services in ecoinvent," Swiss Center for Life Cycle Inventories, Tech. Rep. Ecoinvent report No. 14, 2007. [Online]. Available: https://db.ecoinvent.org/reports/14_transport.pdf

[94] Y. Song, J. Youn, and T. Gutowski, "Life-cycle energy analysis of fiber-reinforced composites," *Composites Part A: Applied Science and Manufacturing*, pp. 1257–1265, 2009.

[95] H. C. and N. A., "Lca database of environmental impacts to inform material selection process, damage controlled composite materials (dacomat) deliverable 6.1," Tech. Rep., 2018.

[96] B. Tremeac and F. Meunier, "Life cycle analysis of 4.5mw and 250w wind turbines," *Renewable and Sustainable Energy Reviews*, vol. 13, pp. 2104–2110, 2009. [Online]. Available: https://doi.org/10.1016/j.rser.2009.01.001. doi: /10.1016/j.rser.2009.01.001

[97] M. Schmid, N. Gonzalez Ramon, A. Direckx, and T. Wegman, "Accelerating wind turbine blade circularity," Wind Europe Report, Tech. Rep., 2020. [Online]. Available: https://windeurope.org/intelligence-platform/product/accelerating-wind-turbine-blade-circularity/

[98] J. Beauson, A. Laurent, and J. Pagh Jensen, "The complex end-of-life of wind turbine blades: A review of the european context," *Renewable and Sustainable Energy Reviews*, vol. 155, no. 111847, 2022. [Online]. Available: https://doi.org/10.1016/j.rser.2021.111847

[99] L. Schleisner, "Life cycle assessment of a wind farm and related externalities," *Ren. Energy*, vol. 20, pp. 279–288, 2000. [Online]. Available: https://doi.org/10.1016/S0960-1481(99)00123-8. doi: 10.1016/S0960-1481(99)00123-8

[100] F. Boeing and A. Regett, "Hourly co2 emission factors and marginal costs of energy carriers in future multi-energy systems," *Energies*, no. 2260, 2019. [Online]. Available: https://doi.org/10.3390/en12122260

[101] M. 2019a, "Fmincon," 2019. [Online]. Available: https://www.mathworks.com/help/optim/ug/fmincon.html

[102] A. Seshadri, "Nsga-ii: A multi-objective optimization algorithm," MATLAB Central File Exchange, Tech. Rep., 2020. [Online]. Available: https://www.mathworks.com/matlabcentral/fileexchange/10429-nsga-ii-a-multi-objective-optimization-algorithm

[103] E. Buckingham, "On physically similar systems," *Illustrations of the Use of Dimensional Equations, Phys. Rev.*, pp. 345–376, 1914. doi: https://doi.org/10.1103/PhysRev.4.345

[104] E. Loth, M. Kaminski, C. Qin, L. Fingersh, and D. Griffith, "Gravo-aeroelastic scaling for extreme-scale wind turbines," *35th AIAA Applied Aerodynamics Conference*, 2017. doi: https://doi.org/10.2514/6.2017-4215

[105] C. L. Bottasso, F. Campagnolo, and A. Croce, "Multi-disciplinary constrained optimization of wind turbines," *Multibody System Dynamics*, vol. 27, no. 1, pp. 21–53, 2012. [Online]. Available: http://dx.doi.org/10.1007/s11044-011-9271-x. doi: 10.1007/s11044-011-9271-x

[106] C. L. Bottasso, P. Bortolotti, A. Croce, and F. Gualdoni, "Integrated aero-structural optimization of wind turbines," *Multibody System Dynamics*, vol. 38, no. 4, pp. 317–344, 2016. [Online]. Available: http://dx.doi.org/10.1007/s11044-015-9488-1. doi: 10.1007/s11044-015-9488-1

[107] P. Bortolotti, C. L. Bottasso, and A. Croce, "Combined preliminary–detailed design of wind turbines," *Wind Energy Science*, vol. 1, no. 1, pp. 71–88, 2016. [Online]. Available: http://www.wind-energ-sci.net/1/71/2016/. doi: 10.5194/wes-1-71-2016

[108] I. E. C. I. E. Commission, "Iec 61400-1 ed.3: wind turbines — part 1: Design requirements," Tech. Rep., 2005.

[109] C. L. Bottasso, A. Croce, Y. Nam, and C. E. D. Riboldi, "Power curve tracking in the presence of a tip speed constraint," *1*, pp. 1917–1931, 2015.

[110] H. Hendriks and B. Bulder, "Fatigue equivalent load cycle method: A general method to compare the fatigue loading of different load spectrums," *Energy Research Centre of the Netherlands technical report*, 1995. [Online]. Available: https://publicaties.ecn.nl/PdfFetch.aspx?nr=ECN-C--95-074

[111] C. Bottasso, P. Pizzinelli, C. Riboldi, and L. Tasca, "Lidar-enabled model predictive control of wind turbines with real-time capabilities," *Ren. En.*, pp. 442–452, 2014. [Online]. Available: 10.1016/j.renene.2014.05.041

[112] "Eurocode 3: Design of steel structures - part 1-9: Fatigue," Tech. Rep.

[113] B. Adams, L. Bauman, W. Bohnhoff, K. Dalbey, M. Ebeida, J. Eddy, M. Eldred, P. Hough, K. Hu, J. Jakeman, J. Stephens, L. Swiler, D. Vigil, and T. Wildey, "Dakota, a multilevel parallel object-oriented framework for design optimization, parameter estimation, uncertainty quantification, and sensitivity analysis: Version 6.0 user's manual," Sandia Technical Report SAND2014-4633, Tech. Rep., 2015. [Online]. Available: https://dakota.sandia.gov

[114] M. Caboni, E. Minisci, and A. Riccardi, "Aerodynamic design optimization of wind turbine airfoils under aleatory and epistemic uncertainty," *Journal of Physics: Conference Series*, vol. 1037, p. 042011, jun 2018. [Online]. Available: https://doi.org/10.1088/1742-6596/1037/4/042011. doi: 10.1088/1742-6596/1037/4/042011

[115] R. Cameron and W. Martin, "The orthogonal development of non-linear functionals in series of fourier-hermite functionals." *Annals of Mathematics, Second Series*, vol. 48, pp. 385–392, 1947. doi: http://dx.doi.org/10.2307/1969178

[116] M. Eldred and J. Burkardt, *Comparison of Non-Intrusive Polynomial Chaos and Stochastic Collocation Methods for Uncertainty Quantification*. [Online]. Available: https://arc.aiaa.org/doi/abs/10.2514/6.2009-976

[117] N. Wiener, "The homogeneous chaos," *American Journal of Mathematics*, vol. 60, no. 4, pp. 897–936, 1938. [Online]. Available: http://www.jstor.org/stable/2371268

[118] R. Ghanem and P. Spanos, *Stochastic Finite Elements: A Spectral Approach.* Springer New York Inc., 1991. ISBN 978-1-4612-7795-8

[119] G. Blatman and B. Sudret, "Adaptive sparse polynomial chaos expansion based on least angle regression," *Journal of Computational Physics*, vol. 230, no. 6, pp. 2345–2367, 2011. [Online]. Available: https://ui.adsabs.harvard.edu/abs/2011JCoPh.230.2345B. doi: 10.1016/j.jcp.2010.12.021

[120] A. Doostan and H. Owhadi, "A non-adapted sparse approximation of pdes with stochastic inputs," *Journal of Computational Physics*, vol. 230, no. 8, pp. 3015–3034, 2011. doi: 10.1016/j.jcp.2011.01.002

[121] J. Sacks, W. J. Welch, T. J. Mitchell, and H. P. Wynn, "Design and Analysis of Computer Experiments," *Statistical Science*, vol. 4, no. 4, pp. 409 – 423, 1989. doi: 10.1214/ss/1177012413

[122] X. Wu, C. Wang, and T. Kozlowski, *Kriging-based surrogate models for uncertainty quantification and sensitivity analysis*. [Online]. Available: https://www.kns.org/files/int_paper/paper/MC2017_2017_5/P237S05-07WuX.pdf

[123] J. D. Martin and T. W. Simpson, "Use of kriging models to approximate deterministic computer models," *AIAA Journal*, vol. 43, no. 4, pp. 853–863, 2005. doi: 10.2514/1.8650

[124] M. Stein, *Interpolation of Spatial Data. Some Theory for Kriging.* Springer New York Inc., 1999. ISBN 978-1-4612-1494-6

[125] D. Matthaeus, P. Bortolotti, J. Loganathan, and C. L. Bottasso, "Propagation of uncertainties through wind turbine models for robust design operation," *AIAA SciTech Forum*, 2016. doi: https://doi.org/10.2514/6.2017-1849

[126] L. Chamorro, R. E. A. Arndt, and F. Sotiropoulos, "Reynolds number dependence of turbulence statistics in the wake of wind turbines," *Wind Energy*, pp. 733—742, 2012. doi: https://doi.org/10.1002/we.501

[127] L. Y. Pao, D. S. Zalkind, D. T. Griffith, M. Chetan, M. S. Selig, G. K. Ananda, C. J. Bay, T. Stehly, and E. Loth, "Control co-design of 13 mw downwind two-bladed rotors to achieve 25energy," *Annual Reviews in Control*, vol. 51, pp. 331–343, 2021. [Online]. Available: https://www.sciencedirect.com/science/article/pii/S1367578821000079. doi: https://doi.org/10.1016/j.arcontrol.2021.02.001

[128] A. Guilloré, H. Canet, and C. L. Bottasso, "Life-cycle environmental impact of wind turbines: What are the possible improvement pathways?" *J. of Physics, to appear*, 2022.

[129] A. T. Marques, H. Batalha, S. Rodrigues, H. Costa, M. J. R. Pereira, C. Fonseca, M. Mascarenhas, and J. Bernardino, "Understanding bird collisions at wind farms: An updated review on the causes and possible mitigation strategies," *Biological Conservation*, vol. 179, pp. 40–52, 2014. [Online]. Available: https://www.sciencedirect.com/science/article/pii/S000632071400305X. doi: https://doi.org/10.1016/j.biocon.2014.08.017

[130] R. May, T. Nygard, U. Falkdalen, J. Astrom, O. Hamre, and B. G. Stokke, "Paint it black: Efficacy of increased wind turbine rotor blade visibility to reduce avian fatalities," *Ecology and Evolution*, vol. 10, no. 16, pp. 8927–8935. [Online]. Available: https://onlinelibrary.wiley.com/doi/abs/10.1002/ece3.6592. doi: https://doi.org/10.1002/ece3.6592

[131] M. Glarou, M. Zrust, and J. Svendsen, "Using artificial-reef knowledge to enhance the ecological function of offshore wind turbine foundations: Implications for fish abundance and diversity," *Journal of Marine Science and Engineering*, vol. 8, no. 332, 2020. [Online]. Available: https://doi: 10.3390/jmse8050332

[132] J. Allen, E. Young, P. Bortolotti, R. King, and G. Barter, "Blade planform design optimization to enhance turbine wake control," *Wind Energy*, 2022.

[133] J. Zeng, B. Zhang, C. Mao, and Y. Wang, "Use of battery energy storage system to improve the power quality and stability of wind farms," in *2006 International Conference on Power System Technology*, 2006, pp. 1–6. doi: 10.1109/ICPST.2006.321662

[134] R. Abhinav and N. M. Pindoriya, "Grid integration of wind turbine and battery energy storage system: Review and key challenges," in *2016 IEEE 6th International Conference on Power Systems (ICPS)*, 2016, pp. 1–6. doi: 10.1109/ICPES.2016.7583998

Included publications

A.1 Paper I: On the scaling of wind turbine rotors

On the scaling of wind turbine rotors

Helena Canet[1], Pietro Bortolotti[2], and Carlo L. Bottasso[1]

[1]Wind Energy Institute, Technische Universität München, 85748 Garching b. München, Germany
[2]National Renewable Energy Laboratory, Golden, CO 80401, USA

Correspondence: Carlo L. Bottasso (carlo.bottasso@tum.de)

Abstract. This paper formulates laws for scaling wind turbine rotors. Although the analysis is general, the article primarily focuses on the subscaling problem, i.e., on the design of a smaller-sized model that mimics a full-scale machine. The present study considers both the steady-state and transient response cases, including the effects of aerodynamic, elastic, inertial, and gravitational forces. The analysis reveals the changes to physical characteristics induced by a generic change of scale, indicates which characteristics can be matched faithfully by a subscaled model, and states the conditions that must be fulfilled for desired matchings to hold.

Based on the scaling laws formulated here, the article continues by considering the problem of designing scaled rotors that match desired indicators of a full-scale reference. To better illustrate the challenges implicit in scaling and the necessary tradeoffs and approximations, two different approaches are contrasted. The first consists in a straightforward geometric zooming. An analysis of the consequences of zooming reveals that, although apparently simple, this method is often not applicable in practice, because of physical and manufacturing limitations. This motivates the formulation of scaling as a constrained optimal aerodynamic and structural matching problem of wide applicability.

Practical illustrations are given considering the scaling of a large reference 10 MW wind turbine of about 180 m in diameter down to three different sizes of 54, 27, and 2.8 m. Results indicate that, with the proper choices, even models characterized by very significant scaling factors can accurately match several key performance indicators. Additionally, when an exact match is not possible, relevant trends can at least be captured.

1 Introduction

This article is concerned with the aeroservoelastic scaling of wind turbine rotors. The general scaling problem includes both up- and subscaling (or downscaling). This work primarily focuses on the latter aspect – i.e., on the design of subscaled models – but also briefly touches upon the former. Specifically, this work tries to answer the following scientific questions:

– What are the effects of a change of scale (i.e., both in the case of up- and subscaling) on the steady and transient response of a wind turbine?

– What steady and transient characteristics of the response of a full-scale wind turbine can be matched by a subscaled model?

– What are the most suitable ways to design the aerodynamic and structural characteristics of a subscaled model?

The understanding of both up- and subscaling is relevant to contemporary wind energy technology.

Regarding upscaling, wind turbines have experienced a continuous growth in size in the past decades. This trend has been mostly driven by a desire for increased capacity factors, which can be obtained essentially through two main design parameters: by lowering the specific power – which, for a given power rating, means a larger rotor-swept area – and by designing taller towers, which reach higher above ground, where wind blows faster. In turn, improved capacity factors have a positive effect on the cost of energy, which has helped propel the penetration of wind in the energy mix. The design of the next-generation wind turbines, especially for offshore

applications, is expected to follow this same path, with rotor diameters of present and future products already exceeding 200 m (IRENA, 2019; GE, 2019; Siemens Gamesa, 2020). Unfortunately, larger blades cannot be obtained by simply scaling up existing smaller blades but must be designed to beat the cubic law of growth. In fact, weight (and hence cost) grows with volume – i.e., with the cube of size – whereas power capture only grows with rotor swept area, i.e., with the square of size (Sieros et al., 2012). Against this background, it is clearly useful to understand the changes that can be expected in a turbine response as the result of an increase in size.

Subscaling, on the other hand, is useful as a research tool: by designing and testing smaller-scale versions of full-scale references, one can validate simulation tools, explore ideas, compare alternative solutions, and deepen the knowledge and understanding of complex physical phenomena. Among other advantages, scaled testing is usually much cheaper and less risky than full-scale testing. In addition, full-scale testing is typically performed on prototypes or even commercial products, which raises often unsurmountable issues because of intellectual property rights and trade secrecy. In turn, this limits opportunities for publication, data sharing, and full exploitation of the results from the scientific community. With commercial turbine sizes expected to grow even further in the future, it is becoming more important than ever to fully understand how to best employ subscaling as a research tool.

Two subscaled testing activities are possible: wind tunnel testing with small-scale models and field testing with small turbines. In both cases, the goal is to match at least some of the characteristics of the original full-scale problem. Clearly, this requires a complete understanding of the effects of a change (in this case, a reduction) of scale on the response of a wind turbine.

Wind tunnel testing of subscaled wind turbine models offers some unique opportunities. First, the operating conditions in a wind tunnel are to a large extent controllable and typically highly repeatable. Second, measurements – especially of flow quantities – that are possible in the lab environment are generally more difficult, are less precise, and have a lower resolution at full scale. Third, costs and risks are much more limited than in the case of field testing, and the time for the conduction of the experiments is shorter (not only because of the reduced challenges but also because of time acceleration, as explained later). Fourth, since a small-scale model cannot exactly match a full-scale product, property right issues are typically much less of a constraint.

The first wind tunnel experiments on wind turbine aerodynamics were conducted in the last decades of the 20th century, as summarized in Vermeer et al. (2003). Studies carried out during the Unsteady Aerodynamics Experiment (Simms et al., 2001) with a stall-regulated 10 m diameter, 20 kW turbine were, among others, key to uncovering the importance of specific flow phenomena, such as dynamic stall, 3D rotational effects, and tower–wake inter-

actions. Later, the 4.5 m diameter scaled models designed for the Model rotor EXperiments In controlled COnditions (MEXICO) project enabled the validation of multiple aerodynamic models, ranging from blade element momentum (BEM) to computational fluid dynamics (CFD) (Snel et al., 2009). These wind turbine models were designed following a set of scaling laws aimed at replicating as accurately as possible the aerodynamic behavior of full-scale machines. More recently, the inclusion of closed-loop controls and aeroservoelastic considerations in the scaling process expanded the scope of wind tunnel testing beyond aerodynamics (Campagnolo et al., 2014). Nowadays, wind tunnel tests are extensively used to gain a better understanding of wake effects, to validate simulation tools, and to help develop novel control strategies (Bottasso and Campagnolo, 2020). The recent study of Wang et al. (2020) tries to quantify the level of realism of wakes generated by small-scale models tested in a boundary layer wind tunnel.

Unfortunately, the exact matching of all relevant physical processes between full-scale and subscale models is typically not possible. This mismatch increases with the scale ratio, and it becomes especially problematic when large wind turbines (with rotor sizes on the order of 10^2 m and power ratings on the order of 10^6–10^7 W) are scaled to very small size wind tunnel models (characterized by rotors on the order of 10^{-1}–10^0 m and power ratings on the order of 10^0–10^2 W). To limit the scale factor, instead of using very small models in a wind tunnel, testing can be conducted in the field with small-size wind turbines (with a rotor on the order of 10^1 m and power ratings on the order of 10^5 W).

Examples of state-of-the-art experimental test sites realized with small-size wind turbines are the Scaled Wind Farm Technology (SWiFT) facility in Lubbock, Texas (Berg et al., 2014), which uses three 27 m diameter Vestas V27 225 kW turbines, or the soon-to-be-ready WINSENT complex-terrain facility in the German Swabian Alps (ZSW, 2016), which uses two 54 m diameter S&G 750 kW turbines.

Reducing the scaling ratios and moving to the field offers the opportunity to overcome some of the constraints typically present in wind tunnel testing, although some of the advantages of wind tunnels are clearly lost. Indeed, the range of testing conditions cannot be controlled at will, measurements are more difficult, and costs are higher. Here research has so far mainly focused on steady-state aerodynamics and wake metrics. For example, within the National Rotor Testbed project (Resor and Maniaci, 2014), teams at the University of Virginia, Sandia National Laboratories, and National Renewable Energy Laboratory have designed a blade for the SWiFT experimental facility, replacing the original Vestas V27 blade. The scaling laws were specifically chosen to replicate the wake of a commercial 1.5 MW rotor at the subscale size of the V27 turbine. To capture the dynamic behavior of very large wind turbines, additional effects must, however, be considered in the scaling laws. For example, Loth et al. (2017) have recently proposed a methodology to

include gravity in the scaling process, and they have demonstrated their approach to scale a 100 m blade down to a 25 m size. Gravity is also crucially important in floating offshore applications (Azcona et al., 2016) to balance buoyancy and correctly represent flotation dynamics, with its effects on loads, stability, and performance and with implications for control design.

This paper considers the general problem of scaling a wind turbine rotor to a different size, including the effects caused by aerodynamic, elastic, inertial, and gravitational forces. The study is structured in two main parts.

Initially, an analysis of the problem of scaling is presented. The main steady and transient characteristics of a rotor in terms of performance, aeroservoelasticity, and wake shedding are considered, and the effects caused by a generic change of scale are determined. The analysis reveals that, in principle, most of the response features can be faithfully represented by a subscaled model. However, an exact matching of all features is typically impossible because of chord-based Reynolds effects, which lead to changes in the aerodynamic behavior of the system. Another limit comes from wind conditions: the wind field is not scaled when using utility-size models in the field, and wind tunnel flows can only partially match the characteristics of the atmospheric boundary layer. The analysis also shows that scaling is essentially governed by two parameters: the geometric (length) scaling factor and the time scaling factor. Based on these two parameters, all matched and unmatched quantities can be fully characterized.

In the second part, the paper continues by looking at the problem of designing a subscaled model. Two different approaches are considered. The first is a straightforward zooming down of all blade characteristics based on a pure geometrical scaling (Loth et al., 2017), which is appealing for its apparent simplicity. The second is based on a complete aerostructural redesign, which is formulated here in terms of two constrained optimizations: the aerodynamic one defines the external shape of the blade, whereas the structural optimization sizes the structural components. Both strategies aim at replicating the dynamic behavior (including gravitational effects) of a full-scale wind turbine at a smaller scale, and they are therefore based on the same scaling laws. Clearly, the complete redesign is a more complicated process than the pure geometric zooming-down approach. However, the main goal of scaling is that of designing a rotor that matches at scale the behavior of a target full-scale machine as closely as possible. From this point of view, the simplicity of design – which is a one-off activity – is less of a concern, especially today, when sophisticated automated rotor design tools are available (Bortolotti et al., 2016). Apart from simplicity, zooming is very often simply not possible for large scale factors because of unrealistically small sizes (especially the thickness of shell structures), non-achievable material characteristics, or impossible-to-duplicate manufacturing processes (Wan and Cesnik, 2014; Ricciardi et al., 2016).

In all those cases, a different aerodynamic shape, a different structural configuration, and different materials are used to obtain the desired behavior, as shown, for example, in the design of a small-size aeroelastically scaled rotor by Bottasso et al. (2014), or as customarily done in the design of scaled flutter models for aeronautical applications (Busan, 1998).

Although the intrinsic limits of the straightforward zooming-down approach are probably well understood, these two alternative methodologies are compared here in order to give a better appreciation of the complexities that one has to face in the design of scaled models. To give practical and concrete examples, a very large rotor is scaled down to three different model sizes, including two different utility wind turbines and a small-scale wind tunnel model. For each model, the zooming-down approach is adopted when possible for its simplicity and then replaced by the redesign method when fidelity or physical limits make it impractical or impossible.

Furthermore, the paper analyzes the accuracy with which the subscale models successfully mirror relevant key characteristics of the full-scale reference, in terms both of absolute values and of trends. This is indeed an important aspect of scaling: even if the exact matching of certain quantities is sometimes not possible, scaled models can still be highly valuable if they are able to at least capture trends. As an example of such a trend analysis, the subscale models are used here to explore changes in loading between unwaked and waked inflow conditions, which are then validated against the corresponding loading changes of the full-scale machine. Results indicate that even the smallest model is capable of capturing complex details of wake interaction, including an interesting lack of symmetry for left/right wake impingements caused by rotor uptilt.

A final section completes the paper, listing the main conclusions that can be drawn from the results and highlighting their limits.

2 Scaling

Buckingham's Π theorem (Buckingham, 1914) states that a scaled model (labeled $(\cdot)_M$) has the same behavior as a full-scale physical system (labeled $(\cdot)_P$) if all the m relevant nondimensional variables π_i are matched between the two systems. In other words, when the governing equations are written as

$$\boldsymbol{\phi}(\pi_{1P}, \ldots, \pi_{mP}) = 0, \tag{1a}$$
$$\boldsymbol{\phi}(\pi_{1M}, \ldots, \pi_{mM}) = 0, \tag{1b}$$

the two systems are similar if

$$\pi_{iP} = \pi_{iM}, \quad i = (1, m). \tag{2}$$

Depending on the scaled testing conditions, not all dimensional quantities can usually be matched. In the present case,

we consider testing performed in air, either in a wind tunnel or in the field, neglecting hydrodynamics.

The length (geometric) scale factor between scaled and full-scale systems is defined as

$$n_{\mathrm{l}} = \frac{l_{\mathrm{M}}}{l_{\mathrm{P}}}, \tag{3}$$

where l is a characteristic length (for example the rotor radius R), whereas the scale factor for time t is defined as

$$n_{\mathrm{t}} = \frac{t_{\mathrm{M}}}{t_{\mathrm{P}}}. \tag{4}$$

As a consequence of these two definitions, one can determine the angular velocity and wind speed scaling factors, which are respectively written as $n_\Omega = \Omega_{\mathrm{M}}/\Omega_{\mathrm{P}} = 1/n_{\mathrm{t}}$ and $n_{\mathrm{v}} = V_{\mathrm{M}}/V_{\mathrm{P}} = n_{\mathrm{l}}/n_{\mathrm{t}}$. A nondimensional time can be defined as $\tau = t\Omega_{\mathrm{r}}$, where Ω_{r} is a reference rotor speed, for example the rated one. It is readily verified that, by the previous expressions, nondimensional time is matched between the model and physical system; i.e., $\tau_{\mathrm{M}} = \tau_{\mathrm{P}}$. The two factors n_{l} and n_{t} condition, to a large extent, the characteristics of a scaled model.

The following Sects. 2.1 and 2.2 analyze the main steady and transient characteristics of a rotor in terms of performance, aeroservoelasticity, and wake shedding. The analysis discusses which of these characteristics can be matched by a scaled model and which conditions are required for the matchings to hold. Next, Sect. 2.3 offers an overview on the main scaling relationships and discusses the choice of scaling parameters.

2.1 Steady state

2.1.1 Rotor aerodynamics

The power coefficient characterizes the steady-state performance of a rotor, and it is defined as $C_{\mathrm{P}} = P/(1/2\rho A V^3)$, where P is the aerodynamic power, ρ the density of air, $A = \pi R^2$ the rotor disk area, and V the ambient wind speed. The thrust coefficient characterizes the wake deficit and the rotor loading and is defined as $C_{\mathrm{T}} = T/(1/2\rho A V^2)$, where T is the thrust force. For a given rotor, the power and thrust coefficients depend on tip-speed ratio (TSR) $\lambda = \Omega R/V$ and blade pitch β, i.e., $C_{\mathrm{P}} = C_{\mathrm{P}}(\lambda, \beta)$ and $C_{\mathrm{T}} = C_{\mathrm{T}}(\lambda, \beta)$.

It is readily verified that $\lambda_{\mathrm{M}} = \lambda_{\mathrm{P}}$ for any n_{l} and n_{t}, which means that it is always possible to match the scaled and full-scale TSR. This ensures the same velocity triangle at the blade sections and the same wake helix pitch.

Ideally, a scaled model should match the C_{P} and C_{T} coefficients of a given full-scale target; it is clearly desirable for the match not to hold at a single operating point but over a range of conditions. BEM theory (Manwell et al., 2002) shows that both rotor coefficients depend on the steady-state aerodynamic characteristics of the airfoils. In turn, the lift C_{L} and drag C_{D} coefficients of the aerodynamic profiles depend

on the angle of attack and on the Mach and Reynolds numbers.

The local Mach number accounts for compressibility effects and is defined as $Ma = W/a_{\mathrm{s}}$, where W is the flow speed relative to a blade section, and a_{s} is the speed of sound. Using the previous expressions, the Mach number of the scaled model is $Ma_{\mathrm{M}} = Ma_{\mathrm{P}} n_{\mathrm{l}}/n_{\mathrm{t}}^2$. Because of typical tip speeds, compressibility does not play a significant role in wind turbines. Hence, the matching of the Mach number can be usually neglected for current wind turbines. The situation might change for future offshore applications, where, without the constraints imposed by noise emissions, higher tip-speed and TSR rotors may have interesting advantages.

The Reynolds number represents the ratio of inertial to viscous forces and is defined as $Re = \rho l u/\mu$, where l is a characteristic length, u a characteristic speed, and μ the dynamic viscosity. In the present context, the most relevant definition of the Reynolds number is the one based on the blade sections, where $l = c$ is the chord length, and $u = W$ is the flow speed relative to the blade section. In fact, the Reynolds number has a strong effect on the characteristics and behavior of the boundary layer that develops over the blade surface, which in turn, through the airfoil polars, affects the performance and loading of the rotor. Testing in air in a wind tunnel or in the field (hence with similar ρ and μ but with a reduced chord c) leads to a mismatch between the scaled and full-scale chord-based Reynolds numbers, as $Re_{\mathrm{M}} = Re_{\mathrm{P}} n_{\mathrm{l}}^2/n_{\mathrm{t}}$.

The effects due to a chord-based Reynolds mismatch can be mitigated by replacing the airfoils of the full-scale system with others better suited for the typical Reynolds conditions of the scaled model (Bottasso et al., 2014). A second approach is to increase the chord of the scaled model. This, however, has the effect of increasing the rotor solidity – defined as $\Sigma = B A_{\mathrm{b}}/A$, where B is the number of blades and A_{b} the blade planform area – which may have additional consequences. In fact, the TSR of the maximum power coefficient is directly related to rotor solidity. This can be shown by using classical BEM theory with wake swirl, which gives the optimal blade design conditions by maximizing power at a given design TSR λ_{d}. By neglecting drag, the optimal design problem can be solved analytically to give the chord distribution of the optimal blade along the spanwise coordinate r (Manwell et al., 2002):

$$\frac{c(r)}{R} = \frac{16\pi}{9 B C_{\mathrm{L}} \lambda_{\mathrm{d}}^2 r/R}. \tag{5}$$

Although based on a simplified model that neglects some effects, this expression shows that chord distribution and design TSR are linked. This means that, if one increases solidity (and hence chord) to contrast the Reynolds mismatch while keeping C_{L} fixed, the resulting rotor will have a lower TSR for the maximum power coefficient. Therefore, this technique of correcting the Reynolds number moves the optimal TSR away from the one of the full-scale reference, which may or may not be acceptable, depending on the goals of

the model. For example, if one wants to match the behavior of the C_P–λ curves over a range of TSRs, such an approach would not be suitable. As shown by Eq. (5), this effect can be eliminated or mitigated by changing the design C_L accordingly; however, if this moves the operating condition of the airfoil away from its point of maximum efficiency, a lower maximum power coefficient will be obtained.

In addition, chord c and lift C_L are further constrained by the circulation $\Gamma = 1/2cC_L W$ (Burton et al., 2001), which plays an important role in the aerodynamics of the rotor and its wake.

Considering first the rotor, the lift and drag generated by the airfoils located close to the blade root are modified by the combined effects of centrifugal and Coriolis forces. In fact, the former causes a radial pumping of the flow that, as a result, moves outboard in the spanwise direction. This radial motion over a rotating body generates chordwise Coriolis forces that alleviate the adverse pressure gradient on the airfoils and, in turn, delay stall. As shown by the dimensional analysis developed by Dowler and Schmitz (2015), rotational augmentation causes multiplicative corrections, denoted g_{C_L} and g_{C_D}, to the nonrotating lift and drag coefficients, which can be written, respectively, as

$$g_{C_L} = \left(\frac{c}{r}\right)^2 \left(\frac{\Gamma}{RW}\right)^{1/2} \left(\frac{\Omega r}{2W}\right)^{-2}, \tag{6a}$$

$$g_{C_D} = \frac{1}{3}\left(\frac{r}{R}\right)\left(\frac{c}{r}\right)^{-1}\left(\frac{\mathrm{d}\theta}{\mathrm{d}r}\frac{R}{\Delta\theta}\right)\left(\frac{\Omega r}{2W}\right), \tag{6b}$$

where $\Delta\theta$ is the total blade twist from root to tip. Equations (6a) and (6b) show that, in order to match the effects of rotational augmentation, the model and full-scale system should have the same blade nondimensional chord and twist distributions; the same nondimensional circulation $\Gamma/(RW)$; and the same Rossby number $Ro = \Omega r/(2W)$, which represents the ratio of inertia to Coriolis forces. Matching nondimensional circulation between the two systems implies matching either both the planform shape c/R and the lift coefficient C_L or the product of the two. As previously noted, some of these options may lead to a different TSR of optimal C_P. On the other hand, it is readily verified that the Rossby number is always matched for any choice of n_l and n_t.

2.1.2 Wake aerodynamics

The circulation is relevant not only for rotational augmentation but also for wake behavior. In fact, each blade sheds trailing vorticity that is proportional to the spanwise gradient $\mathrm{d}\Gamma/\mathrm{d}r$ (Schmitz, 2020). Therefore, designing a blade that matches the spanwise distribution of Γ (and, hence, also its spanwise gradient) ensures that the scaled rotor sheds the same trailed vorticity. Additionally, a matched circulation ensures also a matched thrust, which is largely responsible for the speed deficit in the wake and for its deflection in misaligned conditions (Jiménez et al., 2010).

The Reynolds mismatch derived earlier applies also to its rotor-based definition, which is relevant to wake behavior and is obtained by using $l = 2R$ and $u = V$. However, Chamorro et al. (2012) showed that the wake is largely unaffected by this parameter as long as $Re > 10^5$, which is typically the case unless extremely small model turbines are used. The same is true for the terrain-height-based Reynolds number definition that applies to flows over complex terrains, where Reynolds-independent results are obtained when $Re > 10^4$ (McAuliffe and Larose, 2012).

The detailed characterization of the behavior of scaled wakes is considered as out of the scope of the present investigation, and the interested reader is referred to Wang et al. (2020) for a specific study on this important topic.

2.1.3 Gravity

The Froude number represents the ratio of aerodynamic to gravitational forces and is written as $Fr = V^2/gR$, where g is the acceleration of gravity. The Froude number of the scaled model is readily found to be $Fr_M = Fr_P n_l/n_t^2$. Enforcing Froude ($Fr_M = Fr_P$) results in the time scaling factor being set to $n_t = \sqrt{n_l}$. This condition determines the only remaining unknown in the scaling laws, so that the scalings of all nondimensional parameters can now be expressed in terms of the sole geometric scaling factor n_l. Froude scaling is used when gravity plays an important role, for example in the loading of very large rotors or for floating offshore applications where weight and buoyancy forces should be in equilibrium.

2.1.4 Elasticity

The steady deflections due to aerodynamic loading of the scaled and full-scale wind turbines can be matched by adjusting the stiffness of the scaled model. In fact, consider the very simplified model of a blade represented by a clamped beam of length R under a uniformly distributed aerodynamic load per unit span, denoted $q = 1/2\rho W^2 cC_L$. The beam nondimensional tip deflection is $s/R = qR^3/(8EJ)$, where EJ is the bending stiffness, E is Young's modulus, and J is the cross-sectional moment of inertia. By the previous definitions of length scale and timescale, one gets $(s/R)_M = (s/R)_P$ if $(EJ)_M = (EJ)_P n_l^6/n_t^2$. Hence, nondimensional deflections can be matched, provided that the stiffness can be adjusted as shown. Matching this requirement may imply changing the material and/or the configuration of the structure, because of technological, manufacturing, and material property constraints (Busan, 1998; Ricciardi et al., 2016), as discussed more in detail later on.

2.2 Transient response

A scaled model should obey some additional conditions in order for the transient response of the full-scale system to be matched.

2.2.1 Rotor aerodynamics and inflow

As mentioned earlier, any aerodynamically scaled model can always be designed to enforce the TSR without additional conditions. To extend the similitude to dynamics, the nondimensional time derivative of the TSR should also be matched, i.e., $\lambda'_M = \lambda'_P$, where a nondimensional time derivative is denoted as $(\cdot)' = \mathrm{d} \cdot /\mathrm{d}\tau$. By using the definition of λ, one gets

$$\lambda' = \frac{\Omega' R}{V} - \lambda \frac{V'}{V}. \tag{7}$$

The rotor dynamic torque balance equilibrium is written as $I\dot{\Omega} = Q$. In this expression, I is the rotor polar moment of inertia, $(\dot{\cdot}) = \mathrm{d} \cdot /\mathrm{d}t$ indicates a derivative with respect to time, and $Q = Q_a - (Q_e + Q_m)$ is the shaft torque. The aerodynamic torque is denoted as $Q_a = 1/2\rho ARC_P/\lambda$, while Q_e is the electrical torque provided by the generator and Q_m the mechanical losses. The aerodynamic torque scales as $Q_{a_M} = Q_{a_P} n_l^5/n_t^2$, and clearly $Q_e + Q_m$ must scale accordingly. Since the mechanical losses depend on friction, it might be difficult to always match Q_m, especially in a small-scale model. This problem, however, can be eliminated by simply providing the necessary electrical torque to generate the correct term, $Q_e + Q_m$. Considering that the dimensions of I are $[I] = [\rho_m][l]^5$, where ρ_m is the material density and l a characteristic length, the first term $\Omega' R/V$ in Eq. (7) is matched between the two models if the material density is matched, i.e., if $\rho_{m_M} = \rho_{m_P}$.

The second term, $\lambda V'/V$, in Eq. (7) is matched if the two systems operate at the same TSR and if the wind speed has the same spectrum of the wind in the field. The matching of wind fluctuations (clearly, only in a statistical sense) induces not only the same variations in the TSR, and hence in the rotor response, but also the same recovery of the wake, which is primarily dictated by the ambient turbulence intensity (Vermeer et al., 2003).

Matching of the wind spectrum is in principle possible in a boundary layer wind tunnel if a flow of the desired characteristics can be generated. Turbulent flows can be obtained by active (Hideharu, 1991; Mydlarski, 2017) or passive means (Armitt and Counihan, 1968; Counihan, 1969). Active solutions are more complex and expensive but also more flexible and capable of generating a wider range of conditions. When testing in the field, the flow is invariably not scaled. This will have various effects on the scaled model response, which might be beneficial or not depending on the goals of scaled testing. In fact, the acceleration of time ($t_M = t_P n_t$) implies a shift in the wind frequency spectrum. Among other

effects, this means that low-probability (extreme) events happen more frequently than at full scale. Similarly, the scaling of speed ($V_M = V_P n_l/n_t$) implies higher amplitudes of turbulent fluctuations and gusts than at full scale.

Magnitude and phase of the aerodynamic response of an airfoil (as for example modeled by Theodorsen's theory (Bisplinghoff and Ashley, 2002)) are governed by the reduced frequency $\kappa = \omega_m c/(2W)$, where ω_m is the circular frequency of motion. Harmonic changes in angle of attack take place at various frequencies ω_{m_j} and are caused by the inhomogeneities of the flow (shears, misalignment between rotor axis and wind vector), blade pitching, and structural vibrations in bending and twisting. The reduced frequency can be written as $\kappa_j = \widetilde{\omega}_{m_j} \Omega c/(2W)$, where $\widetilde{\omega}_{m_j} = \omega_{m_j}/\Omega$ indicates a nondimensional frequency. This expressions shows that, once the nondimensional frequencies $\widetilde{\omega}_{m_j}$ (due to inflow, pitch, and vibrations) are matched, the corresponding reduced frequencies are also matched, as the term $\Omega c/(2W)$ is always automatically preserved between scaled and full-scale systems for any n_l and n_t.

Dynamic stall effects depend on reduced frequency κ and chord-based Reynolds number. Typical dynamic stall models depend on the lift, drag, and moment static characteristics of an airfoil and various time constants that describe its unsteady inviscid and viscous response (Hansen et al., 2004). As previously argued, κ can be matched, and all time constants are also automatically matched by the matching of nondimensional time. However, a mismatch of the chord-based Reynolds number is typically unavoidable and will imply differences in the dynamic stall behavior of the scaled and full-scale models, which will have to be quantified on a case-by-case basis.

2.2.2 Wake aerodynamics

The Strouhal number is associated with vortex shedding, which has relevance in tower and rotor wake behavior; the Strouhal number has also been recently used to describe the enhanced wake recovery obtained by dynamic induction control (Frederik et al., 2019). A rotor–wake-relevant definition of this nondimensional parameter is $St = f2R/V$, where f is a characteristic frequency. Using the previous relationships, it is readily shown that $St_M = St_P n_l/(n_t n_v) = 1$; i.e., the Strouhal number is always exactly matched between scaled and full-scale models for any n_l and n_t when TSR is matched.

During transients, spanwise vorticity is shed that is proportional to its temporal gradient. Using BEM theory (Manwell et al., 2002, p. 175), the nondimensional spanwise circulation distribution is computed as

$$\frac{\Gamma}{RW} = \frac{1}{2}\frac{c}{R}C_{L,\alpha}\left(\frac{U_P}{U_T} - \theta\right). \tag{8}$$

In this expression, $C_{L,\alpha}$ is the slope of the lift curve, θ is the sectional pitch angle, and U_P and U_T are the flow velocity

components at the blade section, respectively perpendicular and tangent to the rotor disk plane, such that $W^2 = U_P^2 + U_T^2$. The flow speed component tangential to the rotor disk is $U_T = \Omega r + u_T$, where u_T contains terms due to wake swirl and yaw misalignment. The flow speed component perpendicular to the rotor disk is $U_P = (1-a)V + \dot{d} + u_P$, where a is the axial induction factor, $\dot{d}$ the out-of-plane blade section flapping speed, and u_P the contribution due to yaw misalignment and vertical shear. Neglecting u_P and u_T and using Eq. (8), the nondimensional time rate of change of the circulation becomes

$$\frac{d}{d\tau}\left(\frac{\Gamma}{RW}\right) = \frac{1}{2}\frac{c}{R}C_{L,\alpha}\frac{d}{d\tau}\left(\frac{1-a+\dot{d}/V}{\lambda}\left(\frac{R}{r}\right) - \theta\right). \quad (9)$$

For a correct similitude between scaled and full-scale systems, the nondimensional derivatives λ', a', θ', and $(\dot{d}/V)'$ should be matched.

The matching of λ' has already been addressed. The term a' accounts for dynamic changes in the induction, which are due to the speed of actuation (of torque and blade pitch) and the intrinsic dynamics of the wake. The speed of actuation is matched if the actuators of the scaled model are capable of realizing the same rates of change of the full-scale system, i.e., if θ' is matched. The intrinsic dynamics of the wake are typically modeled by a first-order differential equation (Pitt and Peters, 1981):

$$\dot{a} + \mathbf{A}a = b, \quad (10)$$

where a represents inflow states and $\mathbf{A}$ is a matrix of coefficients proportional to V/R. It is readily verified that the matching of nondimensional time results in the matching of a'. Finally, the term $(\dot{d}/V)'$ is due to the elastic deformation of the blade, which is addressed next.

2.2.3 Elasticity

Considering blade flapping, the Lock number Lo is defined as

$$Lo = \frac{C_{L,\alpha}\rho c R^4}{I_b}, \quad (11)$$

where I_b is the blade flapping inertia. Matching the Lock number ensures the same ratio of aerodynamic to inertial forces. Considering that the flapping inertia is dimensionally proportional to $[\rho_m][l]^5$, where ρ_m is the material density and l a characteristic length, matching the Lock number can be obtained by simply matching the material density of the blade, i.e., $\rho_{mM} = \rho_{mP}$. A similar definition of the Lock number can be developed for the fore–aft motion of the rotor due to the flexibility of the tower, leading to the same conclusion.

The system ith nondimensional natural frequency is defined as $\widetilde{\omega}_i = \omega_i/\Omega$, where ω_i is the ith dimensional natural frequency. Matching the lowest N nondimensional frequencies means that the corresponding eigenfrequencies in the

scaled and full-scale system have the same relative placement among themselves and with respect to the harmonic excitations at the multiple of the rotor harmonics. In other words, the two systems have the same Campbell diagram (Eggleston and Stoddard, 1987). In addition, by matching nondimensional frequencies, the ratio of elastic to inertial forces is correctly scaled. Considering that the bending natural frequency of a blade is dimensionally proportional to $\sqrt{EJ/\rho_m l^6}$, the matching of nondimensional natural frequencies implies $(EJ)_M = (EJ)_P n_l^6/n_t^2$, which is the same result obtained in the steady case for the matching of static deflections under aerodynamic loading. The same conclusions are obtained when considering deformation modes other than bending, so that in general one can write $K_M = K_P n_l^6/n_t^2$, where K is stiffness. Here again, it can be concluded that, for each given n_l and n_t, one can match the frequencies by adjusting the stiffness of the scaled model.

It should be remarked that this condition only defines the stiffnesses that should be realized in the scaled model, not how these are actually obtained. As noted earlier, it is typically difficult if not impossible to simply zoom down a complex realistic structure, and the model design may require a different configuration and choice of materials (Busan, 1998). An optimization-based approach to the structural matching problem is described later in this work.

It is worth noting that matching both the Lock number and the placement of nondimensional natural frequencies implies that structural deflections caused by aerodynamic loads are correctly scaled. In fact, the Lock number is the ratio of aerodynamic to inertial forces, while $\widetilde{\omega}_i^2$ is proportional to the ratio of elastic to inertial forces. Therefore, if both ratios are preserved, then $Lo/\widetilde{\omega}_i^2$, being the ratio of aerodynamic to elastic forces, is also preserved. In symbols, this ratio is written as

$$\frac{Lo}{\widetilde{\omega}_i^2} = \frac{qL^3}{EJ}, \quad (12)$$

where the right-hand side is indeed proportional to the nondimensional tip deflection $\widetilde{s} = s/R$ of a clamped beam subjected to a distributed load $q = C_{L,\alpha}\rho c(R\Omega)^2$.

The matching of frequencies is also relevant to the matching of transient vorticity shedding in the wake, as mentioned earlier. In fact, assume that the blade flapping motion can be expressed as the single mode $d = d_0 e^{\omega_f t}$, where d is the flapping displacement and ω_f the flapping eigenfrequency. Then, the term $(\dot{d}/V)'$ of Eq. (9) becomes

$$\frac{d}{d\tau}\left(\frac{\dot{d}}{V}\right) = \frac{d_0}{R}\lambda\widetilde{\omega}_f^2 e^{\widetilde{\omega}_f\tau}, \quad (13)$$

where $\widetilde{\omega}_f = \omega_f/\Omega$ is the nondimensional flapping frequency. This term is matched between the scaled and full-scale models if the nondimensional flapping frequency is matched.

Table 1. Main scaling relationships relevant to a wind turbine. Additional scaling effects are discussed in the text.

Quantity	Scaling ratio	Coefficient	Comment
Length	l_M/l_P	n_l	
Time	t_M/t_P	n_t	
Nondimensional time	τ_M/τ_P	1	
TSR λ	λ_M/λ_P	1	
Rotor speed	Ω_M/Ω_P	$1/n_t$	Due to nondimensional time matching
Wind speed	V_M/V_P	n_l/n_t	Due to nondimensional time and TSR matching
Mach number	Ma_M/Ma_P	n_l/n_t^2	
Reynolds number	Re_M/Re_P	n_l^2/n_t	
Froude number	Fr_M/Fr_P	n_l/n_t^2	
Strouhal number	St_M/St_P	1	Due to TSR matching
Rossby number	Ro_M/Ro_P	1	Due to TSR matching
Lock number	Lo_M/Lo_P	1	Requires $\rho_{mM} = \rho_{mP}$
Nondimensional nat. freq.	$\widetilde{\omega}_{iM}^n/\widetilde{\omega}_{iP}^n$	1	Requires $K_M = K_P n_l^6/n_t^2$
Deflections due to aero. loads	$\widetilde{s}_M/\widetilde{s}_P$	1	Due to Lock and nondim. freq. matching
Reduced frequency	κ_{jM}/κ_{jP}	1	Requires $(\widetilde{\omega}_{m_j})_M/(\widetilde{\omega}_{m_j})_P$ due to inflow, pitch and vibrations
Nondim. TSR rate of change	λ'_M/λ'_P	1	Requires $(Q_e + Q_m)_M = (Q_e + Q_m)_P n_l^5/n_t^2$, $\rho_{mM} = \rho_{mP}$, and $(V'/V)_M = (V'/V)_P$

2.3 Subscaling criteria

As shown earlier, scaling is essentially governed by two parameters: the geometric scaling factor n_l and the time scaling factor n_t. No matter what choice is made for these parameters, the exact matching of some nondimensional parameters can always be guaranteed; these include nondimensional time, TSR, and Strouhal and Rossby numbers. In addition, the matching of other nondimensional quantities can be obtained by properly scaling some model parameters, again independently from the choice of n_l and n_t. For example, selecting the material density as $\rho_{mM} = \rho_{mP}$ enforces the matching of the Lock number, whereas scaling the stiffness as $K_M = K_P n_l^6/n_t^2$ ensures the proper scaling of the system nondimensional natural frequencies. This way, several steady and unsteady characteristics of the full-scale system can be replicated by the scaled system. Other quantities, however, cannot be simultaneously matched, and one has to make a choice.

Table 1 summarizes the main scaling relationships described earlier. The reader is referred to the text for a more comprehensive overview of all relevant scalings.

The choice of the scaling parameters n_l and n_t is highly problem dependent. Indeed, given a full-scale reference, n_l is set by the size of its scaled replica, which is usually predefined to a large extent. For instance, the choice of the subscale size for a wind tunnel model depends on the characteristics of the target tunnel, to limit blockage (Barlow et al., 1999). When scaling down to a utility size, one typically chooses to reblade an existing turbine (Berg et al., 2014; Resor and Maniaci, 2014), thereby setting the scaling factor. The choice of n_t is often not straightforward and typically implies tradeoffs among quantities that cannot all be simultaneously matched.

For example, when the effects of gravity have to be correctly represented by the scaled model, the matching of the Froude number must be enforced. By setting $Fr_M = Fr_P$, one obtains the condition for the time scaling factor $n_t = \sqrt{n_l}$. Having set n_t, the scalings of all nondimensional parameters can now be expressed in terms of the sole geometric scaling factor n_l.

Another example is given by the design of small-scale wind turbine models for wind tunnel testing, which typically leads to small geometric scaling factors n_l. Bottasso et al. (2014) defined an optimal scaling by minimizing the error in the Reynolds number and the acceleration of scaled time. The latter criterion was selected to relax the requirements on closed-loop control sampling time: since $Re_M = Re_P n_l^2/n_t$, small geometric scaling factors might require very fast scaled times and hence high sampling rates, which could be difficult to achieve in practice for closed-loop control models. Bottasso and Campagnolo (2020) used a different criterion, where a best compromise between the Reynolds mismatch and power density is sought. In fact, power density (defined as power P over volume or, in symbols, $\rho_P = P/R^3$) scales as $\rho_{P_M}/\rho_{P_P} = n_l^2/n_t^3$ and, hence, increases rapidly for small n_t. For small n_l it becomes increasingly difficult, if not altogether impossible, to equip the scaled models with functional components (e.g., drivetrain, generator, actuation systems, sensors) that fit in the dimensions prescribed by the scaling factors. The adoption of larger components can be acceptable or not, depending on the nonphysical effects that are generated by their bigger dimensions and the goals of the model.

Yet another example of how delicate these choices can be is found in the experiments described by Kress et al. (2015). In this work, a scaled rotor was designed for ex-

periments in a water tank, with the goal of comparing upwind and downwind turbine configurations. The rotor of the model was scaled geometrically from a full-scale reference; however, the same scaling ratio could not be used for the nacelle because of the need to house the necessary mechanical components. As a result, the model was equipped with an unrealistically large nacelle that, combined with the lower Reynolds number (which causes a thicker boundary layer), likely increased the redirection of the flow towards the outer-blade portions in the downwind configuration. In turn, this led to the conclusion that nacelle blockage improves power production in downwind rotors. Although this may be true for the scaled experiment, there is little evidence that the same conclusion holds for a full-scale machine (Anderson et al., 2020). Because of miniaturization constraints, a larger nacelle is also used in the TUM G1 scaled turbine (Bottasso and Campagnolo, 2020), a machine designed to support wake studies and wind farm control research. The effects of the out-of-scale nacelle on the wake have, however, been verified and appear in this case to be very modest (Wang et al., 2020).

Additionally, particular combinations of n_l and n_t can make it difficult to find suitable designs. A clear example is found in the structural redesign of an aeroelastically subscaled blade. Indeed, as previously discussed, the scaled blade should have stiffnesses that scale as $K_M = K_P n_l^6 / n_t^2$ and a mass density that scales as $\rho_{mH} = \rho_{mP}$ to ensure the same nondimensional frequencies and Lock number. Depending on the values of the scaling parameters chosen, these scaling relationships might lead to unconventional combinations of stiffness and mass properties, which can be challenging to fulfill as shown in the next section.

3   Design strategies

Upscaling is a design effort driven by different criteria, including, among others, annual energy production (AEP), cost of material and manufacturing, logistics, and transportation. The situation is different for subscaling. In fact, the previous section has clarified the scaling relationships that exist between a full-scale system and its scaled model. The analysis has revealed that in general several steady and unsteady characteristics of the original system can be preserved in the scaled one. The question is now how to design such a scaled model in order to satisfy the desired matching conditions. This problem is discussed in this section.

3.1   Straightforward zooming down

This approach is based on the exact geometric zooming of the blade, including both its external and internal shape, and it has been advocated by Loth et al. (2017).

Regarding the external blade shape, geometric zooming implies that the same airfoils are used for both the scaled and the full-scale models. The mismatch of the Reynolds num-

ber (which is $Re_M = Re_P n_l^{3/2}$ for Froude scaling) may imply a different behavior of the polars, especially for large values of n_l. On the other hand, as shown earlier, a geometric scaling ensures the near matching (up to the effects due to changes in the polars) of various characteristics, such as optimum TSR, nondimensional circulation, rotational augmentation, and vorticity shedding.

Regarding the internal blade shape, the skin, shear webs, and spar caps are also geometrically scaled down when using straightforward zooming. It should be noted that, for large geometric scaling factors n_l, the thickness of elements such as the skin or the shear webs may become very thin, possibly less than typical composite plies.

The zoomed scaling has to satisfy two constraints on the properties of the materials used for its realization.

The first constraint is represented by the matching of material density ($\rho_{mM} = \rho_{mP}$), which is necessary to ensure the same Lock number. It should be remarked that the overall material density of the blade includes not only the density of the main structural elements but also contributions from coatings, adhesive, and lightning protection. These components of the blade may not be simply scaled down, so this problem may deserve some attention.

The second constraint is represented by the scaling of the stiffness, which is necessary for ensuring the matching of nondimensional natural frequencies. For Froude scaling, stiffness changes as $K_M = K_P n_l^5$. Considering bending, the stiffness is $K = EJ$. For a blade made of layered composite materials, the bending stiffness is more complicated than the simple expression EJ, and it will typically need to be computed with an ad hoc methodology, for example using the anisotropic beam theory of Giavotto et al. (1983). However, the simple expression EJ is sufficient for the dimensional analysis required to understand the effects of scaling. Since the sectional moment of inertia J is dimensionally proportional to l^4, with l being a characteristic length of the blade cross section, this constraint requires Young's modulus to change according to $E_M = E_P n_l$. This implies that all materials used for the scaled blade, including the core, should have a lower level of stiffness than (and the same density as) the materials used at full scale; as shown later, this constraint is not easily met.

Since strain ϵ is defined as the ratio of a displacement and a reference length, it follows that $\epsilon_M = \epsilon_P$. Therefore, given that $E_M = E_P n_l$, it follows that $\sigma_M = \sigma_P n_l$, and the stresses in the scaled model are reduced compared to the ones in the full-scale model. Still, one would have to verify that the admissible stresses and strains of the material chosen for the scaled blade are sufficient to ensure integrity.

The critical buckling stress of a curved rectangular plate is

$$\sigma_{cr} = k_c \frac{\pi^2 E}{12(1 - \nu^2)} \left(\frac{d}{b} \right)^2, \tag{14}$$

where k_c is a coefficient that depends on the aspect ratio of the panel, its curvature, and its boundary conditions; ν is Poisson's ratio; d is the panel thickness; and b is the length of the loaded edges of the plate (Jones, 2006). Here again, the expression of the critical stress of a layered anisotropic composite plate would be more complex than the one reported in Eq. (14), but this is enough for the present dimensional analysis. By using the scaling relationships for length and for E, Eq. (14) readily leads to $\sigma_{cr_M} = \sigma_{cr_P} n_l$. This means that if the full-scale blade is buckling free, so is the scaled one, as both the critical buckling stress and the stresses themselves scale in the same manner.

3.2 Aerostructural redesign

An alternative approach to the design of a subscale model is to identify an external shape and an internal structure that match, as closely as possible, the aeroelastic behavior of the full-scale blade. This approach offers more degrees of freedom, at the cost of an increased design complexity; indeed, one designs a new blade that, although completely different from the full-scale one, matches some of its characteristics.

In this second approach, the first step consists of defining a blade shape that can mimic the aerodynamic behavior of the full-scale system. As previously discussed, this can be obtained according to different criteria. Here, the following three conditions are considered. First, a new set of airfoils is selected to match as closely as possible, despite the different Reynolds number of operation, the polar coefficients of the airfoils of the full-scale blade; this is relevant for the matching of the performance and loading of the rotor. Second, the two rotors should have similarly shaped power coefficient curves, which is relevant for performance on and off the design point. Finally, the blades should have the same spanwise circulation distribution, which is relevant for a similar aerodynamic loading of the blade and wake behavior. The resulting scaled blade shape (both in terms of cross sections, because of the changed airfoils, and in terms of chord and twist distributions) will be different from the full-scale rotor. However, this is clearly irrelevant, as the goal is to match some quantities of interest between the two rotors, not their shape.

The aerodynamic design problem can be formally expressed as

$$\min_{\boldsymbol{p}_a} J_a(\boldsymbol{p}_a), \tag{15a}$$

$$\text{subject to} \quad \boldsymbol{m}_a(\boldsymbol{p}_a) = 0, \tag{15b}$$

$$\boldsymbol{c}_a(\boldsymbol{p}_a) \leq 0. \tag{15c}$$

Vector $\boldsymbol{p}_a$ indicates the aerodynamic design variables, which include the chord and twist distributions $c(\eta)$ and $\theta(\eta)$, appropriately discretized in the spanwise direction, while J_a is a design figure of merit, $\boldsymbol{m}_a$ are matching constraints, and finally $\boldsymbol{c}_a$ are additional design conditions. This formulation of

the aerodynamic design problem is very general, and different choices of the figure of merit and of the constraints are possible, depending on the goals of the scaled model.

In the present work, the aerodynamic optimization cost function is formulated as

$$J_a = \sum_i^{N_{C_P}} \left(\frac{C_P(\lambda_i) - \widehat{C}_P(\lambda_i)}{\widehat{C}_P(\lambda_i)} \right)^2. \tag{16}$$

This cost drives the design towards the power coefficient of the target full-scale model $\widehat{C}_P$ at N_{C_P} control stations. This cost function ensures that the subscale model – whose airfoils generally present a reduced efficiency due to the lower chord-based Reynolds number – has a C_P that is as close as possible to the full-scale model. Using $N_{C_P} = 1$ leads to a design with the best C_P at the TSR λ_1.

Within the vector of matching equality constraints, one set of conditions enforces the matching of the spanwise distribution of the circulation $\widehat{\Gamma}$ at N_Γ control stations:

$$\frac{\Gamma(\eta_i) - \widehat{\Gamma}(\eta_i)}{\widehat{\Gamma}(\eta_i)} = 0, \quad i = (1, N_\Gamma), \tag{17}$$

where $\widehat{(\cdot)}$ indicates in general a to-be-matched scaled quantity of the target full-scale model. Another constraint may be added to prescribe the maximum power coefficient to take place at the same design TSR, i.e., $\lambda_{\max(C_P)} = \lambda_{\max(\widehat{C}_P)}$. Finally, vector $\boldsymbol{c}_a$ specifies additional design inequality constraints, which may include a margin to stall, maximum chord, and others, depending on the application.

Once the new aerodynamic shape is identified, the second step consists in the design of an internal blade structure that can mimic the full-scale aeroelastic behavior while ensuring integrity and satisfying manufacturing and realizability constraints. This approach allows for more freedom than the zooming-down approach; for example, one can use different materials than the ones used for the full-scale design, and nonstructural masses can be added without affecting the matching characteristics of the scaled blade.

The structural design problem can be formally expressed as

$$\min_{\boldsymbol{p}_s} J_s(\boldsymbol{p}_s), \tag{18a}$$

$$\text{subject to} \quad \boldsymbol{m}_s(\boldsymbol{p}_s) = 0, \tag{18b}$$

$$\boldsymbol{c}_s(\boldsymbol{p}_s) \leq 0. \tag{18c}$$

Vector $\boldsymbol{p}_s$ indicates the structural design variables, which include the size of the various blade structural elements (skin, spar caps, shear webs, and leading- and trailing-edge reinforcements), discretized span- and chordwise. Here again, this formulation is very general, and specific goals will lead to different choices of the merit function and of the constraints.

Table 2. Principal characteristics of the full-scale 10 MW wind turbine (Bottasso et al., 2016).

Data	Value	Data	Value
Wind class	IEC 1A	Rated electrical power	10.0 MW
Hub height [H]	119.0 m	Rotor diameter [D]	178.30 m
Cut-in wind speed [V_{in}]	4 m s^{-1}	Cut-out wind speed [V_{out}]	25 m s^{-1}
Rotor cone angle [Ξ]	4.65°	Nacelle uptilt angle [Φ]	5.0°
Rotor solidity [Σ]	4.66 %	Max blade tip speed [$v_{tip_{max}}$]	90.0 m s^{-1}
Blade mass	42 496 kg	Tower mass	617.5 t

Table 3. Spanwise position of the airfoils of the blade of the 10 MW machine.

Airfoil	Thickness	Position	Airfoil	Thickness	Position
Circle	100.0 %	0.0 %	FFA-W3-301	30.1 %	38.76 %
Circle	100.0 %	1.74 %	FFA-W3-241	24.1 %	71.87 %
FFA-W3-480	48.0 %	20.80 %	FFA-W3-241	24.1 %	100.00 %
FFA-W3-360	36.0 %	29.24 %			

For example, assuming the blade to be modeled as a beam, the structural optimization cost can be formulated as

$$J_s = \sum_i^{N_s} \left(\frac{M_p(\eta_i) - \widehat{M}_p(\eta_i)}{\widehat{M}_p(\eta_i)} \right)^2$$
$$+ w_s \sum_i^{N_s} \left(\frac{K_q(\eta_i) - \widehat{K}_q(\eta_i)}{\widehat{K}_q(\eta_i)} \right)^2,$$
$$p \in \mathcal{S}_M, \ q \in \mathcal{S}_K, \tag{19}$$

where w_s is a tuning weight, M_p and K_q are elements of the mass and stiffness matrices, and the sets $\mathcal{S}_M$ and $\mathcal{S}_K$ identify the elements that should be considered within the generally fully populated symmetric mass and stiffness matrices. The first term in the cost aims at the matching of the scaled target mass distribution, while the second aims at the stiffness distribution. Vector $\boldsymbol{m}_s$ indicates the matching equality constraints. These may include the matching of a desired number of natural frequencies $\omega_i = \widehat{\omega}_i$ and the matching of a desired number of mode shapes and/or static deflections $\boldsymbol{u}_j(\eta_i) = \widehat{\boldsymbol{u}}_j(\eta_i)$ at a given number of spanwise stations η_i. Finally, vector $\boldsymbol{c}_s$ specifies the additional design inequality constraints. These constraints express all other necessary and desired conditions that must be satisfied in order for the structural design to be viable and in general include maximum stresses and strains for integrity, maximum tip deflection for safety, buckling, and manufacturing and technological conditions.

It should be noted that the matching of the scaled beam stiffness and mass distributions – if it can be achieved – is an extremely powerful condition. In fact, a geometrically exact nonlinear beam model is fully characterized entirely in terms of its reference curve, stiffness, and mass matrices (Bottasso and Borri, 1998). This means that exactly matching

all of these quantities would ensure the same nonlinear structural dynamic behavior of the full-scale target. As shown later, this is not always possible because of limits due to technological processes, material characteristics, chosen configuration of the scaled model, etc. In this case, there is a partial match between the full-scale and scaled beam models, and the sets $\mathcal{S}_M$ and $\mathcal{S}_K$ include only some elements of the mass and stiffness matrices. When this happens, additional matching constraints can help in ensuring as similar a behavior as possible between the scaled and full-scale structures, for example by including static deflections and/or modal shapes, as shown later.

4 Application and results: subscaling of a 10 MW rotor

The two strategies of straightforward zooming and aerostructural redesign are applied here to the subscaling of a 10 MW machine, developed in Bottasso et al. (2016) as an evolution of the original Danmarks Tekniske Universitet (DTU) 10 MW reference wind turbine (Bak et al., 2013). The main characteristics of the turbine are reported in Table 2. Some of the principal blade characteristics are given in Table 3, which reports the position of the airfoils, whereas Table 4 details the blade structural configuration and Table 5 summarizes the material properties.

Three different subscalings are considered here. The first subscale model, denominated the W model, is based on the German WINSENT test site (ZSW, 2016), which is equipped with two 750 kW turbines with a rotor diameter of 54 m (ZSW, 2017). The reference rotor blades are scaled down to match the span of the WINSENT blades; reblading one of the WINSENT turbines yields a subscale model of the full-scale 10 MW turbine suitable for field testing. The second

Table 4. Main structural characteristics of the blade of the 10 MW machine.

Component	From (% span)	To (% span)	Material type
External shell	0	100	Tx GFRP
Spar caps	1	99.8	Ux GFRP
Shear web	5	99.8	Bx GFRP
Third shear web	22	95	Bx GFRP
TE/LE reinforcements	10	95	Ux GFRP
Root reinforcement	10	99.8	Balsa
Shell and web core	5	99.8	Balsa

Table 5. Mechanical properties of the materials of the blade of the 10 MW machine.

Material type	Longitudinal elasticity modulus [MPa]	Transversal elasticity modulus [MPa]	Density [kg m^{-3}]
Tx GFRP	21 790	14 670	1845
Ux GFRP	41 630	14 930	1940
Bx GFRP	13 920	13 920	1845
Balsa	50	50	110

Table 6. Some key scaling factors for the W, S, and T models.

Quantity	Scaling factor	W	S	T
Length	n_l	1 : 3.30	1 : 6.60	1 : 63.68
Time	$\sqrt{n_l}$	1 : 1.82	1 : 2.57	1 : 7.98
Mass	n_l^3	1 : 36	1 : 288	1 : 258 214
Rotor speed	$\sqrt{n_l}$	1 : 1.82	1 : 2.57	1 : 7.98
Wind speed	$\sqrt{n_l}$	1 : 1.82	1 : 2.57	1 : 7.98
Reynolds number	$n_l^{3/2}$	1 : 6	1 : 16.97	1 : 508
Stiffness	n_l^5	1 : 392	1 : 12 558	1 : 32 360

and limitations of each design strategy for each subscale model.

4.1 Aeroservoelastic and design tools

The aeroservoelastic models are implemented in `Cp-Lambda` (Bottasso et al., 2012). The code is based on a multibody formulation for flexible systems with general topologies described in Cartesian coordinates. A complete library of elements – including rigid bodies, nonlinear flexible elements, joints, actuators, and aerodynamic models – is available, as well as sensor and control elements.

The aerodynamic characteristics of the blade are described through lifting lines, including spanwise chord and twist distribution and aerodynamic coefficients. The code is coupled with aerodynamic models based on the BEM model, formulated according to stream-tube theory with annular and azimuthally variable axial and swirl inductions, unsteady corrections, root and blade tip losses, and a dynamic stall model.

The tower and rotor blades are modeled by nonlinear, geometrically exact beams of arbitrary initially undeformed shapes, which are bending, shear, axial, and torsion deformable. The structural and inertial characteristics of each beam section are computed with `ANBA` (Giavotto et al., 1983), a 2D finite-element cross-sectional model. Finally, full-field turbulent wind grids are computed with `TurbSim` (Jonkman et al., 2009) and used as input flow conditions for the aeroservoelastic simulations.

`Cp-Max` (Bortolotti et al., 2016) is a design framework wrapped around `Cp-Lambda`, which implements optimization algorithms to perform the coupled aerostructural design optimization of the blades and, optionally, of the tower. For the present work, the code was modified to implement also the scaled design matching optimizations defined by Eqs. (15) and (18). All optimization procedures are solved with a sequential quadratic programming algorithm, in which gradients are computed by means of finite differences.

model, denominated the S model, is based on the SWiFT test site, which is equipped with Vestas V27 turbines. Here, the full-scale rotor is scaled down to a diameter of 27 m. Finally, the T model is a wind tunnel model with a rotor diameter of 2.8 m, which is similar to the scaled floating turbine tested in the Nantes wave tank in the INNWIND.EU project (Azcona et al., 2016).

Table 6 reports the different geometric scaling factors and a few additional key quantities of the three subscale models. For all, Froude scaling is used, which sets the timescale factor as previously explained. The application of the scaling laws to the full-scale turbine results in the characteristics listed in Table 7. Independently of the approach chosen to define the internal and external shape, the scaled models must fulfill these conditions to correctly mirror the dynamic behavior of the full-scale wind turbine.

The gravo-aeroservoelastic scaling laws lead to very light and flexible subscale blades. For instance, the standard blades of the V27 weigh 600 kg (Vestas, 1994), which is 4 times more than the gravo-aeroservoelastically scaled blades of the S model. It should, however, be remarked that this ratio would be smaller for a modern blade, since the V27 was designed more than 25 years ago and its blades are heavier than the ones based on contemporary technology.

The following sections detail the design of the external and internal shape of the three subscale blades. Section 4.1 describes the aeroservoelastic and design tools used to this end. Then, Sects. 4.2 and 4.3 discuss, respectively, the strengths

4.2 External shape design

For all three models, the design of the subscale external blade shape aims at replicating the aerodynamic characteristics of

Table 7. Gravo-aeroservoelastic scaling requirements for the W, S, and T models.

Data	Full scale	W	S	T
Diameter [m]	178.3	54.0	27.0	2.8
Hub height [m]	119.0	36.04	18.02	1.87
Total blade mass [kg]	42 496	1180	148	0.16
Rotor speed [rpm]	8.9	16.2	22.9	71.1
TSR for max C_P [–]	7.2	7.2	7.2	7.2
Reynolds number [–]	10^7	1.7×10^6	5.9×10^5	2×10^4
First flapwise frequency [Hz]	0.57	1.04	1.46	4.52
First edgewise frequency [Hz]	0.72	1.31	1.85	5.77

the full-scale rotor, including its wake. As long as the chord-based Reynolds numbers are sufficiently large, a zooming-down approach is clearly the simplest strategy for designing the external shape of a scaled blade.

Airfoil FFA-W3-241 equips the outermost part of the full-scale blade (see Table 3). Its performance at the three typical Reynolds numbers of the full-scale, W, and S models was computed with `ANSYS Fluent` (ANSYS, Inc., 2019). The results are reported in Fig. 1. The performance of the airfoil is clearly affected by the Reynolds number, with a particularly significant drop in efficiency for the lowest Reynolds case. Notwithstanding these Reynolds effects, the zooming-down approach is selected for the W and S models, since the airfoils are still performing well at their corresponding typical subscale Reynolds number. A redesign approach with alternative airfoils was not attempted here, and would probably lead only to marginal improvements of the aerodynamic performance.

On the other hand, for the small geometric scaling factor of the T model, the aerodynamic redesign approach is necessary. In general, smooth airfoils present a large reduction in aerodynamic efficiency below a critical Reynolds number of about 70 000 (Selig et al., 1995). Efficient profiles specifically developed for low-Reynolds-number applications are generally necessary in order to get a good matching of the full-scale aerodynamic performance. As an alternative to the original airfoil, the 14 % thick airfoil RG14 (Selig et al., 1995) is selected, because its aerodynamic characteristics at the scaled Reynolds number are in reasonable agreement with the ones of the original airfoil at its full-scale Reynolds number (Fig. 1). The blade is then completely redesigned, using the RG14 airfoil along its full span.

The blade shape is parameterized by means of chord and twist spanwise distributions. The design problem is formulated as the maximization of the power coefficient at the design TSR λ_d of the full-scale rotor, solving Eq. (15) with the cost given by Eq. (16) for $N_{C_P} = 1$ and $\lambda_1 = \lambda_d$. The nonlinear constraints expressed by Eq. (17) enforce the same spanwise nondimensional circulation distribution of the full-scale blade.

Figure 2 shows the external shapes of the full-scale blade and the three subscale models in terms of chord, relative thickness, twist, and Reynolds number. Clearly, the shape curves for the W and S models overlap with the full-scale ones, because zooming is used in these two cases, as previously explained.

The three subscale models have the same TSR in region II as the full-scale machine and the correspondingly subscaled rated rotor speeds. The rated wind speeds do not exactly match the subscale ones, on account of the differences in the C_P-TSR curves caused by the Reynolds effect.

4.3 Design of the internal structure

The definition of the internal structure has to achieve the following goals: the matching of the full-scale aeroelastic behavior, the integrity of the blade under loading, and the feasibility of the manufacturing process. In the next two sections, the zooming-down and the redesign approaches are applied to the structure of the three subscale blades.

4.3.1 Limits of the zooming-down approach

The straightforward zooming-down approach can be applied to the internal structure of the W- and S-model blades, as their external geometrical shape has also been defined following this approach. The resulting structures satisfy all scaling constraints but present some critical challenges.

First, the thicknesses of some of the components are unrealistically low. The blade root of the W model is, for example, only 20 mm thick and is therefore unable to accommodate the root-bolted connections. Furthermore, the scaling of the outer shell skin leads to a laminate thickness of less than one ply. The third web of the S-model blade is also extremely thin (less than 1 mm) and very close to the trailing edge.

Additionally, the scaled structure requires materials characterized by very peculiar mechanical properties. Indeed, as previously shown, the scaling laws require the modulus of elasticity to obey the relationship $E_M = E_P n_1$ and the material density to be $\rho_{mM} = \rho_{mP}$. For example, the outer shell of the W-model blade requires an elasticity modulus of 6.6 GPa
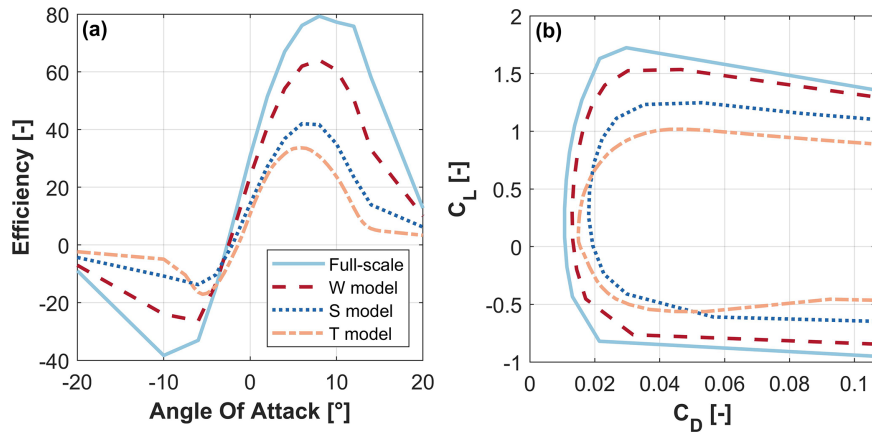
Figure 1. Aerodynamic characteristics of the airfoil at the outermost part of the blades at the corresponding Reynolds number. The full-scale, W, and S models are equipped with the FFA-W3-241 airfoil. The T model is designed with the RG14 airfoil. **(a)** Efficiency, $E = C_{\mathrm{L}}/C_{\mathrm{D}}$, vs. angle of attack; **(b)** polar curves, i.e., C_{L} vs. C_{D}.
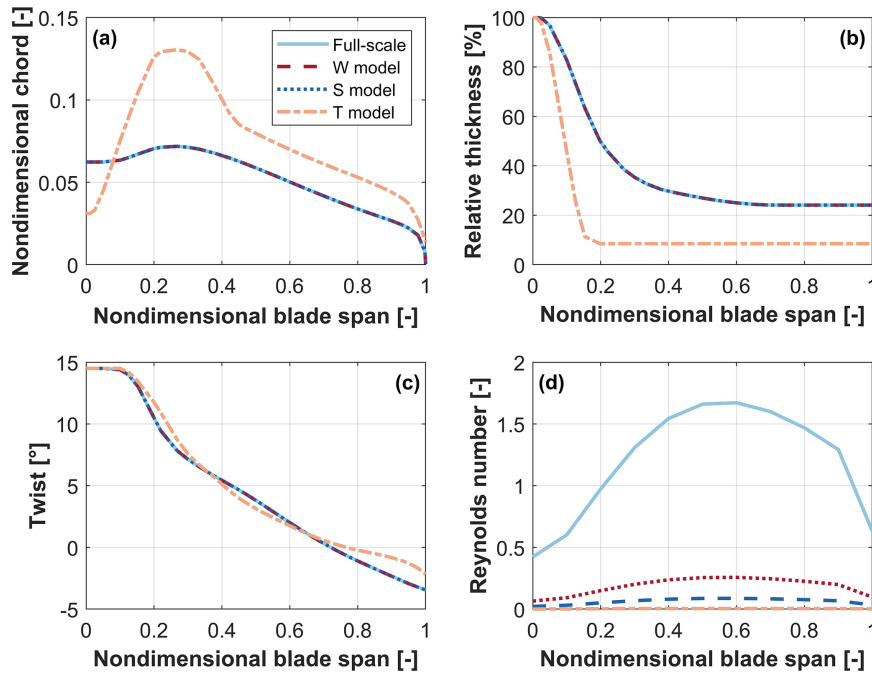
Figure 2. (a) Nondimensional chord, **(b)** relative thickness, **(c)** twist, and **(d)** Reynolds number vs. spanwise position for the full-scale blade and its three subscale models.

and a density of $1845\,\mathrm{kg\,m^{-3}}$, which are not typical values of conventional materials (see Fig. 3). Finally, nonstructural masses – such as glue, paint, and lightning protection – cannot be exactly zoomed down by geometric scaling and need to be treated separately.

One may try to relax some of these hurdles by increasing the necessary component thicknesses and choosing materials with mechanical properties that compensate for this increase. For example, a 3-fold increase of the skin thickness in the W

model would be able to accommodate the root-bolted connection and would satisfy manufacturing tolerances. To meet the mass and inertia constraints, a material should be used that has a lower density, $\rho_{\mathrm{mM}} = \rho_{\mathrm{mP}}/3$, and a lower-elasticity modulus, $E_{\mathrm{M}} = E_{\mathrm{P}}n_{\mathrm{l}}/3$. Figure 3 reports Ashby's diagram of Young's modulus vs. density (Cambridge University Engineering Department, 2003). In this plot, the values corresponding to the outer shell skin materials have been marked with $\times$ symbols. A red symbol indicates the full-scale blade,

a yellow symbol is used for the W model considering the exact zooming-down approach, and a green symbol indicates the solution with a 3-fold thickness increase. It should be noted that, although the properties of the scaled models do correspond to existing materials, these are typically not employed for the manufacturing of blades. Therefore, their actual use for the present application might indeed pose some challenges.

Overall, the zooming-down approach for the structural design is not really straightforward and is significantly more complicated than in the case of the aerodynamic design. An alternative is offered by a complete redesign of the internal structure, which is illustrated in the next section.

4.3.2   Redesign of the W and S models

An alternative to the zooming-down approach is the redesign of the internal structure. This consists of a typical blade design process, subjected not only to additional constraints that enforce the desired scaling relationships but, crucially, also to all other conditions that are necessary to make the design viable. For example, here a lower bound to the thickness of all structural components is set to 1 mm, while a minimum thickness of 60 mm is assumed at the root to accommodate the bolted connection of the W and S models.

Additionally, one has greater freedom in the choice of materials. For the present applications, the glass-fiber-reinforced plastic (GFRP) composites of the full-scale blade appear to be suitable choices also for the W model. On the other hand, these materials are too stiff for the S model, due to its smaller geometric scaling. An alternative was found within the family of thermoplastic materials that have typical stiffness values between 1–3 GPa and densities between 900 and 1400 kg m^{-3} (Brondsted et al., 2005). Although not strictly of interest here, thermoplastics also have interesting advantages over thermosets, such as reduced cycle times, lower capital costs of tooling and equipment, smaller energy consumption during manufacturing, and enhanced recyclability at the end of their life (Murray et al., 2018).

During the design phase of the subscale models, more careful attention can also be paid to the distributions of nonstructural masses. Specifically, masses from shell and sandwich cores must be recomputed for the new scaled structure in order to prevent buckling of the sandwich panels. Additional masses from surface finishing and painting are also recomputed according to the surface of the external shell. In fact, if a zooming-down strategy is chosen for the design of the external geometry, these masses will scale with the length scale factor. Masses from resin uptake in the outer shell and shear webs are recomputed for the scaled structure assuming a constant area density. Indeed, this value does not change from the full scale to the subscale, since it depends on the material and manufacturing process. A different assumption is taken for the masses of bonding plies and adhesive along the shear webs and leading and trailing edge. Since these masses

Table 8. Mechanical properties of the materials used for the W- and S-model blades.

Material type	Longitudinal elasticity modulus [MPa]	Transversal elasticity modulus [MPa]	Density [kg m^{-3}]
Bx GFRP	13 920	13 920	1845
Ux GFRP	42 000	12 300	1940
PMMA	2450	2450	1200
POM	5000	5000	1400
Balsa	50	50	150

are chordwise dependent, the linear density of these materials in the subscale size must be corrected by the length scale factor. Finally, the linear density of the lightning protection system is assumed to be constant for all sizes.

The structural design is formulated as the matching optimization problem expressed by Eq. (18). The cost function given by Eq. (19) considers the sole spanwise matching of the mass distribution, i.e., it neglects inertia terms in $\mathcal{S}_M$ and uses $w_s = 0$. The matching constraints $\boldsymbol{m}_s$ include the lowest three natural frequencies, and the static deflected shape of the outboard 40 % section of the blade. This static condition was chosen to represent the maximum tip displacement resulting from turbulent simulations in power production for the full-scale machine (design load case (DLC) 1.1; see IEC (2005)). Finally, the additional design constraints $\boldsymbol{c}_s$ include stresses, strains, fatigue and technological constraints in the form of bounds on thickness and thickness rate of change of the laminates.

The structural design for the W and S models is based on a typical thin-walled composite configuration, where the design variables are defined as the spanwise thicknesses of the skin, shear webs, spar caps, and leading- and trailing-edge reinforcements. Given the smaller size of the scaled blades, one single shear web is used instead of the three used in the full-scale 10 MW model. Table 8 describes the mechanical properties of the materials used for these two blades, while Table 9 associates the various structural elements with the materials.

For the S model, the thermoplastic materials polymethyl methacrylate (PMMA) and polyoxymethylene (POM) are chosen because of their lower level of stiffness. The use of polymer materials reduces the nonstructural masses, as the adhesive is no longer necessary. Due to the reduced fatigue characteristics of these materials, the blade lifetime is limited to 5 years. This is assumed to be acceptable in the present case, given the research nature of these blades. Constraints on maximum stresses and strains are satisfied with an ample margin for these blades. However, the inclusion of a larger set of DLCs (including extreme events and parked conditions) might create more challenging situations, which could
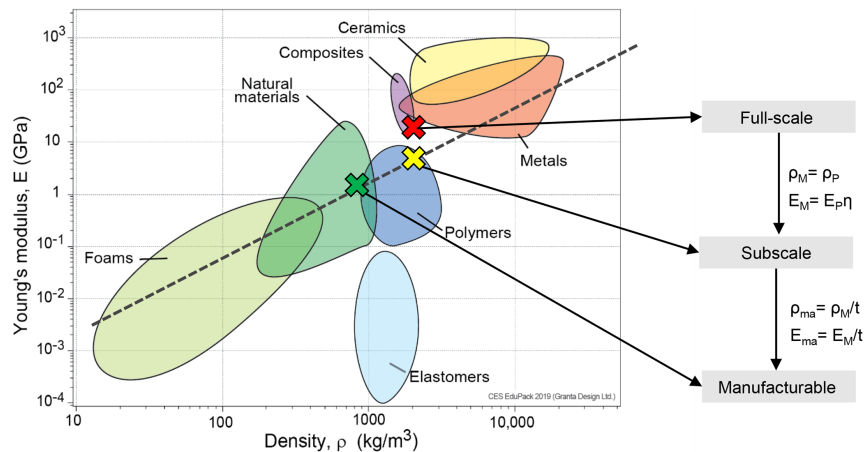
Figure 3. Ashby's diagram of Young's modulus vs. density (Cambridge University Engineering Department, 2003), and the outer shell skin materials for the W model. Chart created using CES EduPack 2019, ANSYS Granta © 2020 Granta Design.
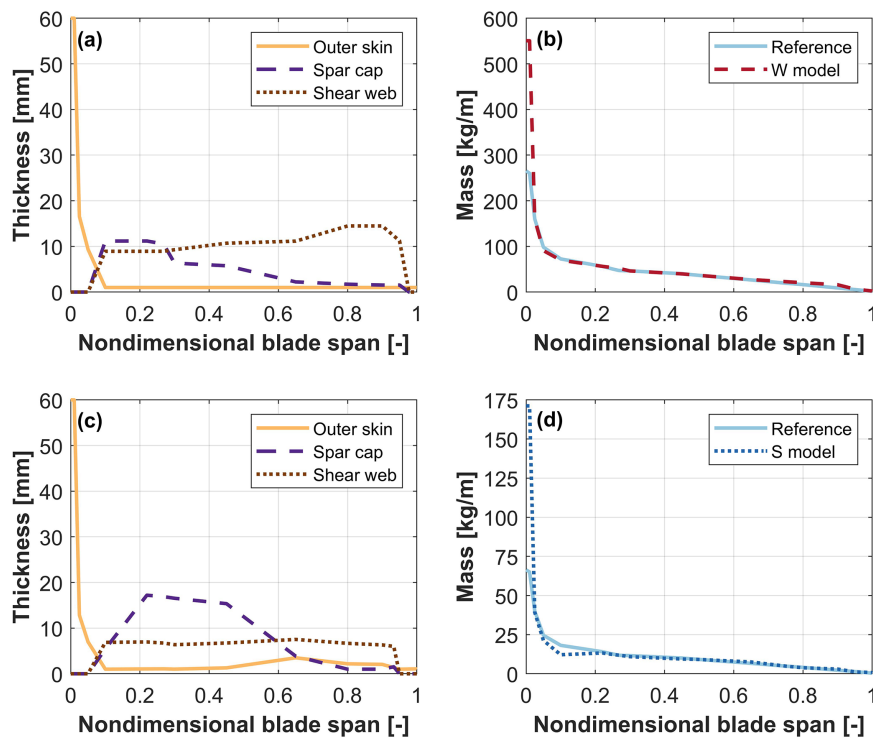

Figure 4. Thickness of the structural components and mass distribution for the W (**a, b**) and S (**c, d**) models. The label "reference" indicates the mass distribution of the full-scale blade, subscaled to the W and S scales.

increase the requirements regarding material strength, possibly eventually leading to the selection of different materials.

Figure 4 reports the internal structure of the W and S models, as well as the overall mass distributions, including realistic nonstructural masses. The scaled mass distribution follows quite closely the reference one along the blade span, with the exception of the root because of the additional thickness that must be ensured to accommodate the bolted connection. The blade satisfies the scaling inertial and elastic constraints within a tolerance of less than 5 %.
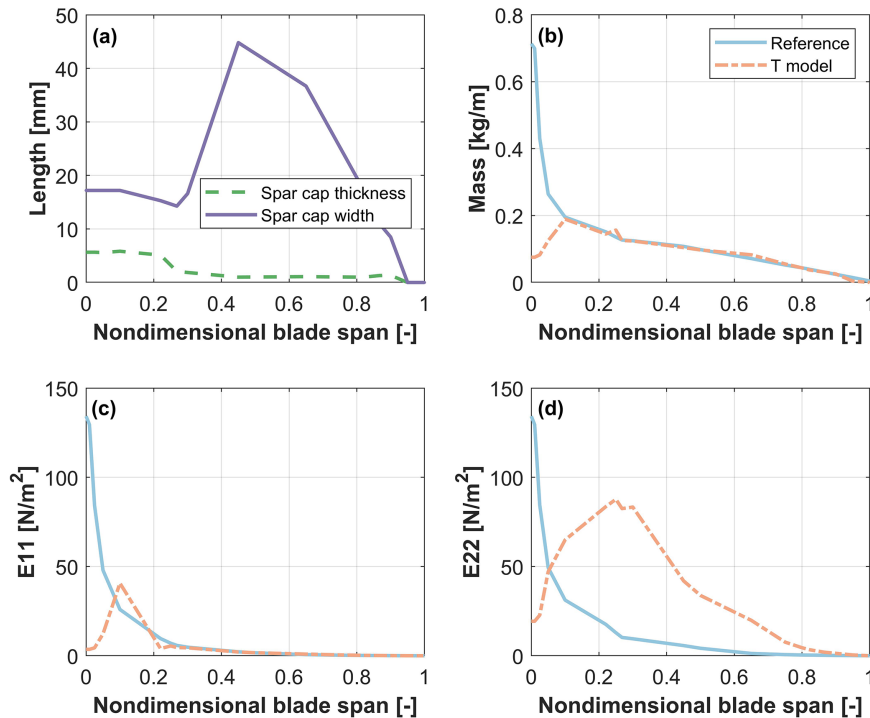
Figure 5. (a) Spar caps thickness and width, **(b)** mass distribution, **(c)** flapwise stiffness distribution, and **(d)** edgewise stiffness distribution for the T model. The label "reference" indicates the characteristics of the full-scale blade, subscaled to the T-model scale.

Table 9. Materials used for the structural components of the W- and S-model blades.

Component	From	To	Material type	
	(% span)	(% span)	W model	S model
External shell	0	100	Bx GFRP	PMMA
Spar caps	10	95	Ux GFRP	POM
Shear web	10	95	Bx GFRP	PMMA
TE/LE reinforcements	10	45	Ux GFRP	PMMA
Shell and web core	10	95	Balsa	Balsa

4.3.3 Redesign of the T model

The very small size of the wind tunnel model blade prevents the use of a typical thin-walled solution. Following Bottasso et al. (2014) and Campagnolo et al. (2014), this scaled blade is not hollow but presents a full cross section obtained by machining a foamy material. Two unidirectional spar caps provide the required flapwise stiffness distribution. The surface smoothness is obtained by a very thin layer of skin made of glue. Although Bottasso et al. (2014) and Campagnolo et al. (2014) considered different scaling laws, their blade design configuration was found to be a suitable choice even in the present gravo-aeroservoelastic scaling exercise. The selection of appropriate materials represents a critical aspect of the problem, and the mechanical properties listed

in the Cambridge University Materials Data Book (Cambridge University Engineering Department, 2003) were used to guide the material selection for the spar caps and core. A rigid polymer foam is chosen as filler, because of its relatively high level of stiffness and lightness. For the spar caps, thermoplastic polymers are again found to be the most suitable solution even though their stiffness-to-density ratio is much lower than materials traditionally used for spar caps. Moreover, the use of thermoplastics allows for alternative and simpler manufacturing processes, leading to a higher flexibility in the spar cap design. From this family of materials, polypropylene is chosen because of its low stiffness modulus. Finally, the external shell is covered by a very thin layer of the epoxy structural adhesive Scotch Weld AF 32 (3M Adhesives Division, 2000).

The design variables are represented by the spanwise thickness and width of the two spars. The design problem is formulated according to the constrained matching optimization expressed by Eq. (18). The cost function of Eq. (19) considers the spanwise mass distribution in $\mathcal{S}_M$ and the flapwise stiffness distribution in $\mathcal{S}_K$. The matching constraints $\boldsymbol{m}_s$ include the lowest three natural frequencies and the flapwise static extreme tip deflection. Both the cost and the constraints only consider the flapwise characteristics of the blade, because the structural configuration consisting of a solid core and two spar caps allows for limited control of the edgewise

characteristics. As a result, the scaled blade presents a higher level of edgewise stiffness than the full-scale reference.

Figure 5 reports the results of the design optimization. The desired matching of mass and flapwise stiffness is achieved, except at blade root. Even though the placement of the first flapwise natural frequency with respect to the rotor speed is ensured, the constraint on the lowest edgewise natural frequency could not be exactly matched due to the large chord. Small disparities in mass distribution introduce a difference of about 1 % in the blade flapping inertia.

5 Performance comparison

In this section, the behavior of the scaled models is compared to the full-scale machine. The main goal here is to assess to what extent the subscale models are capable of successfully mirroring relevant key characteristics and load trends of the full-scale reference.

The same collective-pitch/torque controller governs all machines. The controller uses a look-up table for torque to operate at rated TSR in region II and a proportional–integral–derivative (PID) pitch loop to maintain constant rated power in region III. The PID gains used for the scaled models are obtained by transforming the ones of the full-scale machine using the scaling laws, and the regulation trajectory is adapted to each model to account for differences in the C_P-TSR curves. Notice that the scaling of gains is a conservative approach: in the case of an exact matching at scale of all aeroelastic characteristics of the turbines, the use of a scaled controller will also ensure an identical closed-loop response. However, if the scaled models do not exactly represent the full-scale reference – which is invariably the case in practice – an ad hoc retuned controller (i.e., a controller specifically optimized for the scaled model) will in general have better performance than the one obtained by the scaling of the gains. The choice of gain scaling instead of retuning was made here to consider a worst-case scenario.

5.1 Relevant key indicators

The models are simulated in a power production state at five different wind speeds from cut-in to cut-out. The winds of the scaled simulations are obtained by velocity scaling the turbulent winds used for the full-scale machine (i.e., the integral space and timescales are both correctly scaled). The matching between the scaled and full-scale turbines is assessed with the help of 10 different indicators: AEP; maximum flapwise tip displacement (MFTD); maximum thrust at main shaft (ThS); maximum combined blade root moment (CBRM); maximum flapwise bending root moment (FBRM); maximum edgewise bending root moment (EBRM); and the Weibull-averaged damage equivalent load (DEL) for ThS, CBRM, FBRM, and EBRM.

5.1.1 Utility-scale models

As previously discussed, the design both of the external shape and of the internal structure may induce differences in the behavior of a scaled model with respect to its full-scale reference. To better understand the effects of these differences and their origins, three different sets of results are presented in Fig. 6.

The first plot (a) compares the indicators of the full-scale turbine with the upscaled ones of the W and S models. Both the internal structure and the external shape are obtained by zooming down, and Reynolds effects are accounted for by CFD-computed polars. Although a zoomed-down structure cannot really be a practical solution – as discussed earlier – because of excessively thin structural elements or the need for peculiar material properties, this solution is shown here because it highlights the sole effects of the Reynolds mismatch. In other words, since this is a purely numerical study, the thicknesses and mechanical properties were used exactly as produced by scaling, resulting in a nearly exact satisfaction of the matching of all structural characteristics. Therefore, the differences of the indicators between the full-scale and scaled models shown in this plot can be entirely attributed to Reynolds effects. The full-scale and utility-size models are equipped with airfoil polars at different Reynolds numbers computed with the CFD code `ANSYS Fluent` (ANSYS, Inc., 2019).

The second plot (b) compares the indicators for the W and S models featuring a zoomed-down external shape (which neglects Reynolds effects) and a redesigned internal structure. Although Reynolds effects would, in reality, be present, by neglecting them here – which is again possible because this is a purely numerical study – one can assess from this solution the sole effects of the structural redesign on the matching of the indicators.

Finally, the third and last plot (c) considers the solution obtained by zooming down the aerodynamic shape, considering Reynolds effects and a redesigned internal structure. As argued earlier, this is indeed the solution that is practically realizable, and, therefore, these are the more realistic results of the set considered here. Hence, differences between the full-scale and scaled models are due to mismatches caused by both the Reynolds number and the redesign procedure.

As expected by the size difference, results shown in the first plot suggest a larger effect of the Reynolds number mismatch for the S model than for the W model. This results in a drop in all indicators because of the decreased airfoil efficiency.

The second plot shows a similar matching for both models. Indeed, most of the key loads are matched within 5 % for both the W and the S model. A larger difference between the two models is found for EBRM and DEL EBRM, which are only poorly matched by the W model, whereas they are quite accurate for the S model. The mismatch is due to a slightly higher sectional mass in the last 20 % of the blade
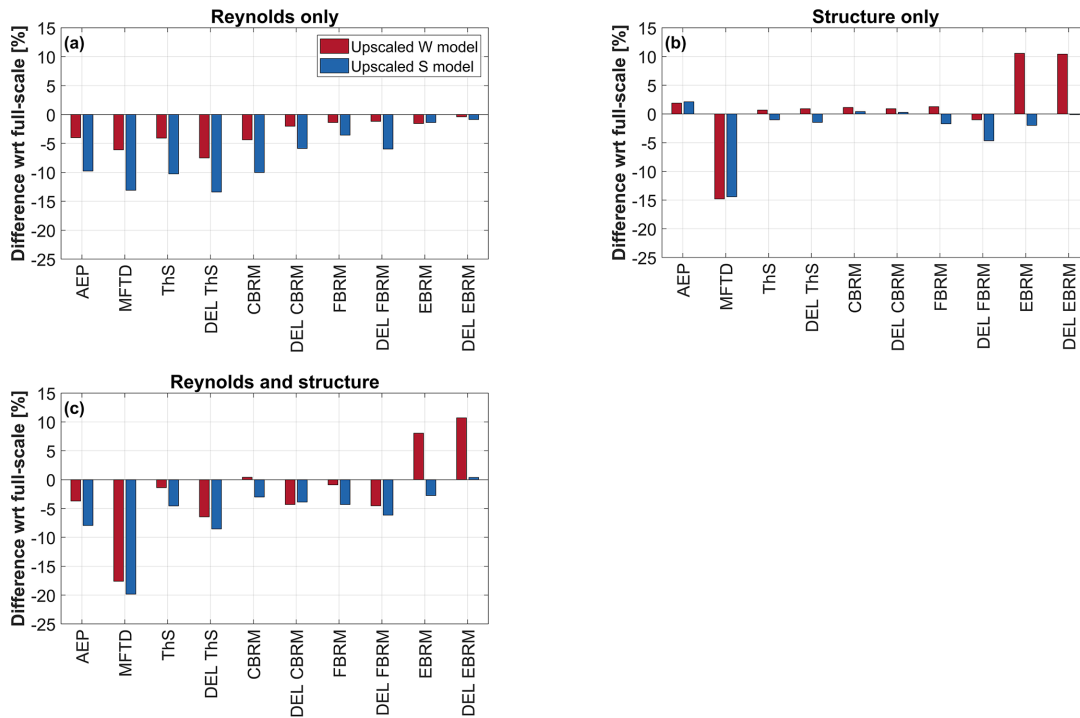
Figure 6. Changes with respect to full scale for several key indicators for the W and S models. **(a)** Effects exclusively due to Reynolds mismatch, **(b)** effects exclusively due to structural redesign, and **(c)** realistic solution considering both the effects of Reynolds mismatch and structural redesign.

of the W model, as shown in Fig. 4. A significant difference with respect to full scale is also observed for the maximum flapwise tip displacement of both the W and S models. This difference is caused by a slightly different dynamic behavior induced by mismatches in the flapwise and torsional stiffness distributions. Even though FBRM matches very well for both the W and S model at the root, these differences lead to a poorer match at sections toward the blade tip, which in the end impacts MFTD.

Overall, both models are capable of matching the key indicators of the full-scale target reasonably well, considering both Reynolds effects and a redesigned structure.

5.1.2 Wind tunnel model

The behavior of the T model is compared with the 10 MW baseline in Fig. 7. The additional indicator, maximum edgewise tip deflection (METD), is considered in this case. The polars for the T model are computed with Xfoil (Drela, 2013).

The comparison shows satisfactory behavior of the wind tunnel model for most key indicators, notwithstanding the very different Reynolds numbers (about 10^7 for the full-scale reference and about 2×10^4 for the T model). As expected, the largest mismatch is found for the maximum edgewise tip displacement. This can be justified by the inability of the
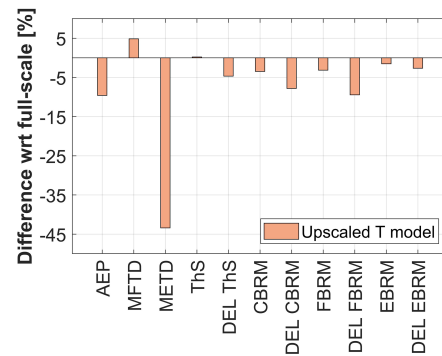
Figure 7. Comparison between full-scale key indicators and the upscaled ones of the T model.

structural design variables (limited to the two caps) in controlling the edgewise stiffness.

5.2 Load trends in waked conditions

Scaled models can also be used to capture trends, instead of absolute values. Indeed, the goal of scaled testing is often to understand the trends generated on some metric by, for example, a control technology or by a particular operating condition or other factors, whereas the exact quantitative assess-
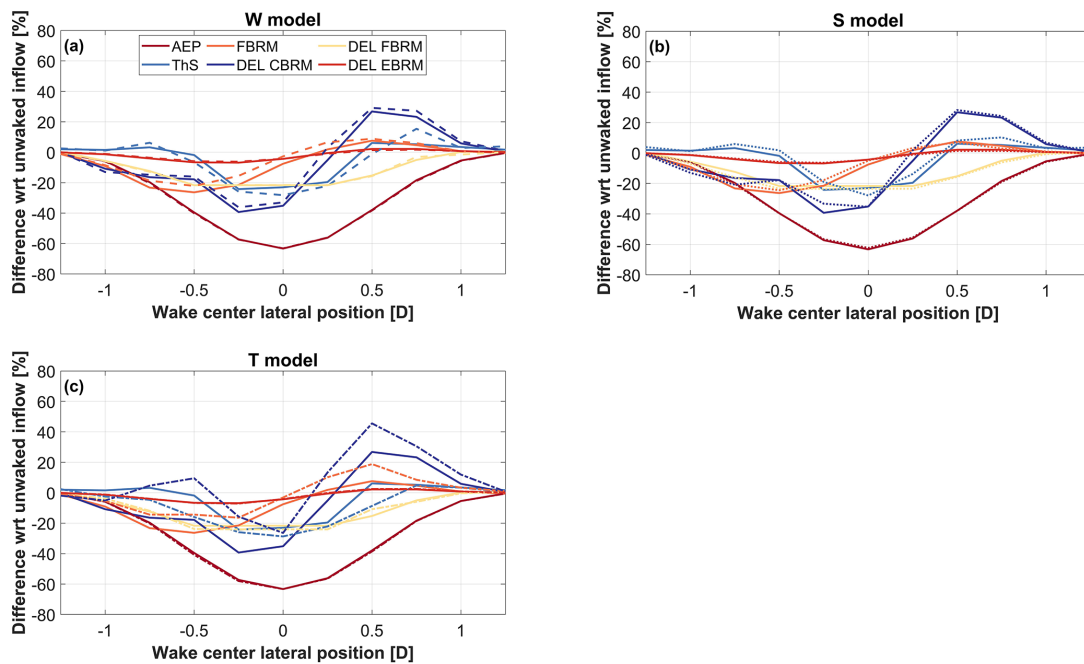
Figure 8. Comparison of key indicators between unwaked and waked inflows for different lateral distances from the wake center. The solid line corresponds to the full-scale model. **(a)** W model (dashed line), **(b)** S model (dotted line), and **(c)** T model (dash-dotted line).

ment of the induced effects must be left to a final full-scale verification.

As an example of the analysis of trends, the scaled models designed here are used to explore changes in loading between unwaked and waked inflow conditions. To this end, the full-scale turbine is simulated with an average inflow velocity of $7\,\mathrm{m\,s^{-1}}$, considering a shear exponent of 0.2 and a turbulence intensity of 8 %. The wake deficit generated by an upstream 10 MW machine is then added to this inflow, in order to simulate a waked condition. The wake is modeled by the superposition of a turbulent wind grid generated with `TurbSim` (Jonkman et al., 2009) and the first-order solution of the deficit of the Larsen model (EWTSII model) (Bottasso et al., 2017). The downstream turbine is located at a longitudinal downstream distance of $4D$ from the upstream machine, and its lateral distance from the wake center is varied from $-1.25D$ (right, looking downwind) to $1.25D$ (left), realizing different degrees of wake–rotor overlap. The scaled models are simulated by velocity-scaling the full-scale inflows. The key indicators considered are AEP; ThS; FBRM; and DELs for CBRM, FBRM, and EBRM.

Figure 8 reports changes in key indicators at several degrees of wake overlap with respect to unwaked inflow conditions. The full-scale machine presents the largest reduction in AEP and ThS in full wake overlap. An asymmetrical load trend of the DELs for FBRM, EBRM, and CBRM is visible when the rotor is operating in partial wake. This behavior is mostly due to the rotor uptilt angle, which introduces

an additional velocity component in the rotor plane. In fact, for a clockwise-rotating (when looking downstream) rotor, this extra velocity component increases the in-plane velocity at the blade sections when the blade is on the right side of the rotor (i.e., during the downstroke; here left and right are defined for an observer looking downstream). Additionally, when a wake impinges on the right side of the rotor, the out-of-plane velocity component decreases, because of the wake deficit. Both of these effects tend to decrease the angle of attack at the blade sections. On the other hand, when a wake impinges on the left portion of the rotor, the effect of the decreased out-of-plane component is in part balanced by the also decreased in-plane component. Because of this different behavior, larger load fluctuations (and hence higher fatigue loads) are observed for right wake impingements than for left ones. A similar effect is caused by the elasticity of the tower: under the push of the thrust, the tower bends backwards, which in turn tilts the rotor upward, adding to the previously described phenomenon. Other minor effects are also due to the elastic deformations caused by gravity, which again contribute to breaking the symmetry of the problem.

Overall, the largest scaled models follow the trends very well, with the S model performing slightly better than the W model. Indeed, the W model is better than the S model when looking at Weibull-averaged quantities (Fig. 6), but the S model presents a slightly superior matching of blade loads at the specific speed at which the load trend study is performed. The trends are also reasonably captured by the

smaller-scale T model, but with significant differences in DEL FBRM. Specifically, there is an overestimation of this quantity around the $-0.5D$ lateral wake center position. A detailed analysis of the results revealed this behavior to be caused by the blade operating at angles of attack close to the stalling point. This indicates another possible limit of models with large-scale factors, whose airfoils may have very different stall and post-stall behavior than their full-scale counterparts.

6 Conclusions

This paper has analyzed the scaling conditions that should be met by a subscale model to match a full-scale reference in terms of its full aeroservoelastic response. The analysis has shown that many relevant key aspects of the steady and unsteady response of a machine, considered as flexible, can indeed be matched. Part of this analysis can also be used to understand expected changes due to upscaling, which can be useful in the design of larger rotors. To the authors' knowledge, this is one of the most comprehensive analyses of the problems of scaling wind turbines presented thus far.

Within this framework, this paper has considered two alternative ways of designing a scaled rotor. The first is based on the idea of exactly zooming down the full-scale reference to obtain the subscale model. An alternative strategy is to completely redesign the rotor, from both an aerodynamic and a structural point of view. This produces a scaled blade that, although possibly very different from the full-scale one, matches some of its key characteristics as closely as possible.

These two alternative strategies have been tested on the gravo-aeroservoelastic scaling of a conceptual 10 MW blade to three different subscale models: two utility-scale ones to be used for the reblading of small existing turbines and one for equipping a very small model turbine to conduct experiments in the controlled environment of a wind tunnel.

The following conclusions can be drawn from the application of the two strategies to these three different scaling problems.

The simplest strategy to design the external shape of utility-scale blades is the straightforward zooming-down approach, as long as the subscale Reynolds number is sufficiently high. This strategy benefits from a simple implementation and leads to an acceptable match of the blade aerodynamic performance. However, when the blade aerodynamic performance is compromised by the Reynolds mismatch – which is the typical case of wind tunnel models – the alternative but more complex strategy of redesigning the aerodynamic shape becomes preferable if not altogether indispensable. Special low-Reynolds-number airfoils may be used to mitigate the effects caused by the reduced Reynolds regime. However, different behavior at and around stall might lead to different loads when operating at large angles of attack.

The straightforward zooming down of the blade internal structure is instead typically very difficult for all scaling ratios. In fact, the need for materials of unusual characteristics and the nonscalability of nonstructural masses unfortunately hinder the applicability of this simple approach. An alternative is found in the structural redesign strategy, which offers more flexibility at the price of increased complexity. Even here, however, the problem is nontrivial. For example, materials may play a critical role, due to the very flexible nature of some of these scaled blades.

The aeroservoelastic analyses conducted herein have shown that, in general, it is not possible to exactly match all the characteristics of a full-scale machine with a subscale model. However, with the proper choices, some key indicators are nicely captured. In addition, changes in operating conditions are represented quite well even at the smaller scale. For example, it was shown that changes in loading from an unwaked to a waked condition are accurately represented by all scaled models, which successfully capture intricate and possibly unexpected couplings with design aspects such as nacelle uptilt and tower deflection. The good performance of the models in capturing such complex effects opens up a range of applications and use cases. For example, with the right design choices, scaled models can be employed to better understand rotor–wake interactions or test sophisticated control strategies at the turbine and/or plant levels.

Further improvements in the performance of the subscale models are certainly possible. Indeed, while some of the limitations result from the choice of quantities to be matched, others can be overcome by technological advances. For instance, improvements in measurement technology can relax the requirements on the scaling of time, allowing for a better match of other quantities. Additionally, advances in material and manufacturing may ease the application of unconventional materials; relax sizing constraints; and lead to more accurate, simpler, faster-to-develop, and cheaper models.

This work has exclusively focused on the wind turbine itself, and the effects of scaling have been quantified for the aerodynamic performance and loading of the rotor. The recent study of Wang et al. (2020) expands this analysis by considering the effects of scaling on wake behavior. Even in that case the conclusion is that properly scaled models can produce very realistic wakes.

Further work should focus on expanding the scope of the scaling analysis, introducing the effect of hydrodynamics. Indeed, as floating wind energy is expected to significantly grow in the coming years, it is becoming increasingly important to better understand which aspects of the aero-hydroservoelastic response of these machines can be matched and how to best design subscale models. This is, however, only part of the problem. Research efforts are also necessary to better understand how to replicate the inflow conditions that full-scale machines face in various types of atmospheric and terrain conditions. This is a challenging task, since it requires a deep understanding of atmospheric

flows, their interaction with the terrain orography and the vegetation, and technology to replicate these flows at scale.

It is the hope of the authors that the results shown in this paper will increase the confidence in scaled testing, in the belief that scaled model have a significant role to play in the advancement of wind energy science.

Appendix A: Nomenclature

a	Axial induction factor
a_s	Speed of sound
c	Chord length
d	Out-of-plane blade section flapping displacement
f	Characteristic frequency
g	Acceleration of gravity
l	Characteristic length
n_l	Geometric scaling factor, i.e., l_M/l_P
n_t	Time scaling factor, i.e., t_M/t_P
n_Ω	Angular velocity scaling factor, i.e., Ω_M/Ω_P
n_v	Wind speed scaling factor, i.e., V_M/V_P
$\boldsymbol{p}$	Vector of design parameters
r	Spanwise coordinate
s	Tip deflection
t	Time
u	Characteristic speed
A	Rotor disk area
A_b	Blade planform area
B	Number of blades
C_D	Drag coefficient
C_L	Lift coefficient
$C_{L,\alpha}$	Slope of the lift curve
C_P	Power coefficient
C_T	Thrust coefficient
E	Young's modulus or airfoil efficiency, i.e., C_L/C_D
EJ	Bending stiffness
Fr	Froude number
I	Rotor polar moment of inertia
I_b	Blade flapping inertia
J	Cost function
K	Stiffness
Lo	Lock number
M	Mass
Ma	Mach number
P	Aerodynamic power
Q	Torque
R	Rotor radius
Re	Reynolds number
Ro	Rossby number
St	Strouhal number
T	Thrust force
U_P	Flow velocity component perpendicular to the rotor disk plane
U_T	Flow velocity tangent to the rotor disk plane
V	Wind speed
W	Flow speed relative to a blade section

β	Blade pitch
ϵ	Strain
θ	Sectional pitch angle
κ	Reduced frequency
λ	Tip-speed ratio
λ_d	Design TSR
μ	Fluid dynamic viscosity
ν	Poisson coefficient
ρ	Air density
ρ_m	Material density
ρ_P	Power density
σ	Stress
τ	Nondimensional time
ω	Natural frequency
Γ	Circulation
$\Delta\theta$	Total blade twist from root to tip
Σ	Rotor solidity
Φ	Rotor uptilt angle
Ξ	Rotor cone angle
Ω	Rotor angular velocity
$(\cdot)_a$	Pertaining to the aerodynamic design
$(\cdot)_s$	Pertaining to the structural design
$(\cdot)_M$	Scaled system
$(\cdot)_P$	Full-scale physical system
$\dot{(\cdot)}$	Derivative with respect to time, i.e., $d\cdot/dt$
$(\cdot)'$	Derivative with respect to nondimensional time, i.e., $d\cdot/d\tau$
$\widetilde{(\cdot)}$	Nondimensional quantity
$\widehat{(\cdot)}$	To-be-matched scaled quantity
AEP	Annual energy production
BEM	Blade element momentum
Bx	Biaxial
CBRM	Combined bending root moment
CFD	Computational fluid dynamics
CFRP	Carbon-fiber-reinforced plastic
DEL	Damage equivalent load
DLC	Design load case
EBRM	Edgewise bending root moment
FBRM	Flapwise bending root moment
GFRP	Glass-fiber-reinforced plastic
LD	Low density
LE	Leading edge
MFTD	Maximum flapwise tip displacement
METD	Maximum edgewise tip displacement
PID	Proportional integral derivative
PMMA	Polymethyl methacrylate
POM	Polyoxymethylene
PP	Polypropylene
SQP	Sequential quadratic programming
ThS	Thrust at main shaft
TSR	Tip-speed ratio
TE	Trailing edge
Tx	Triaxial
Ux	Uniaxial

624

References

Anderson, B., Branlard, E., Vijayakumar, G., and Johnson, N.: Investigation of the nacelle blockage effect for downwind wind turbines, J. Phys. Conf. Ser., 1618, 062062, https://doi.org/10.1088/1742-6596/1618/6/062062, 2020.

ANSYS Fluent: https://www.ansys.com/products/fluids/ansys-fluent (last access: 18 December 2019), 2019.

Armitt, J. and Counihan, J.: The simulation of the atmospheric boundary layer in a wind tunnel, J. Atmos. Environ., 2, 49–61, https://doi.org/10.1016/0004-6981(68)90019-X, 1968.

Azcona, J., Lemmer, F., Matha, D., Amann, F., Bottasso, C. L., Montinari, P., Chassapoyannis, P., Diakakis, K., Spyros, V., Pereira, R., Bredmose, H., Mikkelsen, R., Laugesen, R., and Hansen, A. M.: INNWIND. EU Deliverable D4.24: Results of wave tank tests, http://www.innwind.eu/publications/deliverable-reports (last access: 18 December 2019), 2016.

Bak, C., Zahle, F., Bitsche, R., Kim, T., Yde, A., Natarajan, A., and Hansen, M. H.: INNWIND. EU Deliverable D1.21: Reference Wind Turbine Report, http://www.innwind.eu/publications/deliverable-reports (last access: 18 December 2019), 2013.

Barlow, J. B., Rae, W. H., and Pope, A.: Low-speed wind tunnel testing, 3rd Edn., Wiley, Hoboken, New Jersey, USA, 1999.

Berg, J., Bryant, J., LeBlanc, B., Maniaci, D., Naughton, B., Paquette, J., Resor, B., and White, J.: Scaled Wind Farm Technology Facility Overview, in: 32nd ASME Wind Energy Symposium, AIAA SchiTech Forum, 13–17 January 2014, National Harbor, Maryland, https://doi.org/10.2514/6.2014-1088, 2014.

Bisplinghoff, R. L. and Ashley, H., Principles of Aeroelasticity, Dover Publications, Mineola, New York, USA, 2002.

Bortolotti, P., Bottasso, C. L., and Croce, A.: Combined preliminary-detailed design of wind turbines, Wind Energ. Sci., 1, 71–88, https://doi.org/10.5194/wes-1-71-2016, 2016.

Bottasso, C. L. and Borri, M.: Integrating finite rotations, Comput. Method. Appl. Mech., 164, 307–331, https://doi.org/10.1016/S0045-7825(98)00031-0, 1998.

Bottasso, C. L. and Campagnolo, F.: Wind tunnel testing of wind turbines and farms, Handbook of Wind Energy Aerodynamics, edited by: Stoevesandt, B., Schepers, G., Fuglsang, P., Sun, Y., Springer Nature, Cham, https://doi.org/10.1007/978-3-030-05455-7_54-1, 2021.

Bottasso, C. L., Campagnolo, F., and Croce, A.: Multi-disciplinary constrained optimization of wind turbines, Multibody Syst. Dyn., 27, 21–53, https://doi.org/10.1007/s11044-011-9271-x, 2012.

Bottasso, C. L., Campagnolo, F., and Petrovic, V.: Wind tunnel testing of scaled wind turbine models: Beyond aerodynamics, J. Wind Eng. Ind. Aerodyn., 127, 11–28, https://doi.org/10.1016/j.jweia.2014.01.009, 2014.

Bottasso, C. L., Bortolotti, P., Croce, A., and Gualdoni, F.: Integrated aero-structural optimization of wind turbines, Multibody Syst. Dyn., 4, 317–344, https://doi.org/10.1007/s11044-015-9488-1, 2016.

Bottasso, C. L., Cacciola, S., and Schreiber, J.: Local wind speed estimation, with application to wake impingement detection, Renew. Energ., 116, 155-168, https://doi.org/10.1016/j.renene.2017.09.044, 2017.

Brondsted, P., Lilholt, H., and Lystrup, A.: Composite Materials For Wind Power Turbine Blades, Annu. Rev. Mater. Res., 35, 505–

538, https://doi.org/10.1146/annurev.matsci.35.100303.110641, 2005.

Buckingham, E.: On Physically Similar Systems, Illustrations of the Use of Dimensional Equations, Phys. Rev., 4, 345–376, https://doi.org/10.1103/PhysRev.4.345, 1914.

Burton, T., Jenkins, N., Sharpe, D., and Bossanyi, E.: Wind energy handbook, John Wiley & Sons, West Sussex, UK, 2001.

Busan, R.: Flutter Model Technology, WL-TR-97-3074, Wright-Patterson Air Force Base, OH, USA, 1998.

Cambridge University Engineering Department: Materials Data Book, http://www-mdp.eng.cam.ac.uk/web/library/enginfo/cueddatabooks/materials.pdf (last access: 18 December 2019), 2003.

Campagnolo, F., Bottasso, C. L., and Bettini, P.: Design, manufacturing and characterization of aero-elastically scaled wind turbine blades for testing active and passive load alleviation techniques within a ABL wind tunnel, J. Phys. Conf. Ser., 524, 012061, https://doi.org/10.1088/1742-6596/524/1/012061, 2014.

Chamorro, L. P., Arndt, R. E. A., and Sotiropoulos, F.: Reynolds number dependence of turbulence statistics in the wake of wind turbines, Wind Energy, 15, 733–742, https://doi.org/10.1002/we.501, 2012.

Counihan, J.: An improved method of simulating an atmospheric boundary layer in a wind tunnel, Atmos. Environ., s3, 197–200, https://doi.org/10.1016/0004-6981(69)90008-0, 1969.

Drela, M.: Xfoil 6.99 Documentation, http://web.mit.edu/drela/Public/web/xfoil/ (last access: 18 December 2019), 2017.

Dowler, J. L. and Schmitz, S.: A solution-based stall delay model for horizontal-axis wind turbines, Wind Energy, 18, 1793-1813, https://doi.org/10.1002/we.1791, 2015.

Eggleston, D. M. and Stoddard, F. S.: Wind Turbine Engineering Design, Van Nostrand Reinhold, New York, NY, USA, 1987.

Frederik, J. A., Weber, R., Cacciola, S., Campagnolo, F., Croce, A., Bottasso, C., and van Wingerden, J.-W.: Periodic dynamic induction control of wind farms: proving the potential in simulations and wind tunnel experiments, Wind Energ. Sci., 5, 245–257, https://doi.org/10.5194/wes-5-245-2020, 2020.

General Electric: GE Renewable Energy unveils the first Haliade-X 12 MW, the world's most powerful offshore wind turbine, Press release, available at: https://www.ge.com/news/press-releases/ge-renewable-energy-unveils-first-haliade-x-12-mw-worlds- (last access: 26 April 2021), 2019.

Giavotto, V., Borri, M., Mantegazza, P. and Ghiringhelli, G.: Anisotropic beam theory and applications, Comput. Struct., 16, 403–413, https://doi.org/10.1016/0045-7949(83)90179-7, 1983.

Hansen, M. H., Gaunaa, M., and Madsen, H. A.: A Beddoes-Leishman type dynamic stall model in state-space and indicial formulations, Technical University of Denmark, Riso, Denmark, https://backend.orbit.dtu.dk/ws/portalfiles/portal/7711084/ris_r_1354.pdf (last access: 18 December 2019), 2004.

Hideharu, M.: Realization of a large-scale turbulence field in a small wind tunnel, Fluid Dyn. Res., 8, 1–4, https://doi.org/10.1016/0169-5983(91)90030-M, 1991.

International Electrotechnical Commission: International Electrotechnical Commission, IEC 61400-1 Edn. 3: Wind turbines – Part 1: Design requirements, IEC, Geneva, Switzerland, 2005.

International Renewable Energy Agency: Future of wind: Deployment, investment, technology, grid integration and socio-economic aspects (A Global Energy Transformation paper), Abu Dhabi, 2019.

Jiménez, Á., Crespo, A., and Migoya E.: Application of a LES technique to characterize the wake deflection of a wind turbine in yaw, Wind Energy, 13, 559–572, https://doi.org/10.1002/we.380, 2010.

Jones, R. M.: Buckling of Bars, Plates, and Shells, Bull Ridge Publishing, Virginia, 2006.

Jonkman, J.: TurbSim User's Guide, NREL Report TP-500-36970, NREL, Golden, CO, USA, https://doi.org/10.2172/15020326, 2009.

Kress, C., Chokani, N., and Abhari, R. S.: Downwind wind turbine yaw stability and performance, Renew. Energ., 83, 1157–1165, https://doi.org/10.1016/j.renene.2015.05.040, 2015.

Loth, E., Kaminski, M., Qin, C., Fingersh, L. J., and Griffith, D. T.: Gravo-Aeroelastic Scaling for Extreme-Scale Wind Turbines, in: 35th AIAA Applied Aerodynamics Conference, AIAA AVIATION Forum, Denver, CO, https://doi.org/10.2514/6.2017-4215, 2017.

McAuliffe, B., Larose, G.: Reynolds-number and surface-modeling sensitivities for experimental simulation of flow over complex topography, J. Wind Eng. Ind. Aerod., 104–106, 603–613, https://doi.org/10.1016/j.jweia.2012.03.016, 2012.

Manwell, J. F., McGowan, J. G., and Rogers, A. L.: Wind energy explained: theory, design and application, Second Edition, John Wiley & Sons Publication, West Sussex, United Kingdom, 2009.

Murray, R. E., Jenne, S., Snowberg, D., Berry, D., and Cousins, D.: Techno-Economic Analysis of a Megawatt-Scale Thermoplastic Resin Wind Turbine Blade, Renew. Energ., 131, 111–119, https://doi.org/10.1016/j.renene.2018.07.032, 2018.

Mydlarski, L.: A turbulent quarter century of active grids: from Makita (1991) to the present, Fluid Dyn. Res., 49, 061401, https://doi.org/10.1088/1873-7005/aa7786, 2017.

Pitt, D. M. and Peters, D. A.: Theoretical prediction of dynamic-inflow derivatives, Vertica, 5, 21–34, 1981.

Resor, B. R. and Maniaci, D. C.: Definition of the National Rotor Testbed: An Aeroelastically Relevant Research-Scale Wind Turbine Rotor, in: 32nd ASME Wind Energy Symposium, AIAA SciTech Forum, 13–17 January 2014, National Harbor, MD, https://doi.org/10.2514/6.2014-0357, 2014.

Ricciardi A. P., Canfield, R., Patil, M. J., and Lindsley, N.: Nonlinear aeroelastic scaled-model design, J. Aircraft, 53, 20–32, https://doi.org/10.2514/1.C033171, 2016.

Schmitz, S.: Aerodynamics of Wind Turbines, A Physical Basis for Analysis and Design, John Wiley & Sons Ltd, Hoboken, NJ, USA, 2020.

Selig, M., Guglielmo, J., Broeren, A., and Giguère, P.: Summary of Low-Speed Airfoil Data, SoarTech Publications, Virginia, 1995.

Siemens Gamesa: Powered by change: Siemens Gamesa launches 14 MW offshore direct drive turbine with 222-meter rotor, Press release, available at: https://www.siemensgamesa.com/newsroom/2020/05/200519-siemens-gamesa-turbine-14-222-dd (last access: 26 April 2021), 2020.

Sieros, G., Chaviaropoulos, P., Sorensen, J. D., Bulder, B. H., and Jamieson, P.: Upscaling wind turbines: theoretical and practical aspects and their impact on the cost of energy, Wind Energy, 15, 3–17, https://doi.org/10.1002/we.527, 2012.

Simms, D., Schreck, S., Hand, M., and Fingersh, L. J.: NREL Unsteady Aerodynamics Experiment in the NASA-Ames Wind Tunnel: A Comparison of Predictions to Measurements, available at: http://citeseerx.ist.psu.edu/viewdoc/download?doi=10.1.1.452.974&rep=rep1&type=pdf (last access: 26 April 2021), 2001.

Snel, H., Schepers, J. G., and Siccama, N. B.: Mexico Project: The Database and Results of Data Processing and Interpretation, in: 47th AIAA Aerospace Sciences Meeting Including The New Horizons Forum and Aerospace Exposition, Orlando, FL, https://doi.org/10.2514/6.2009-1217, 2009.

3M Adhesives Division: Scotch-Weld Structural Adhesive Film AF 32, Technical Data Issue No. 3, available at: https://multimedia.3m.com/mws/media/241415O/3mtm-scotch-weldtm-structural-adhesive-film-af-32.pdf (last access: 18 December 2019), 2000.

Vermeer, L. J., Sorensen, J. N., and Crespo, A.: Wind Turbine Wake Aerodynamic, Prog. Aerosp. Sci., 39, 467–510, https://doi.org/10.1016/S0376-0421(03)00078-2, 2003.

Vestas General Specification: Vestas V27–225 kW, 50 Hz Windturbine with Tubular/Lattice Tower, Version 1.2.0.24, 1994.

Wan, Z. and Cesnik, C. E. S.: Geometrically nonlinear aeroelastic scaling for very flexible aircraft, AIAA J., 52, 2251–2260, https://doi.org/10.2514/1.J052855, 2014.

Wang, C., Campagnolo, F., Canet, H., Barreiro, D. J., and Bottasso, C. L.: How realistic are the wakes of scaled wind turbine models?, Wind Energ. Sci. Discuss. [preprint], https://doi.org/10.5194/wes-2020-115, in review, 2020.

ZSW – Zentrum für Solarenergie- und Wasserstoff-Forschung Baden-Württemberg: New WindForS project: Wind Energy Research in the Swabian Alps, available at: https://www.zsw-bw.de/en/newsroom/news/news-detail/news/detail/News/new-windfors-project-wind-energy-research-in-the-swabian-alps.html (last access: 18 December 2019), 2016.

ZSW – Zentrum für Solarenergie- und Wasserstoff-Forschung Baden-Württemberg: ZSW and S&G Engineering Join Forces to Set Up Wind Power Field-Test Site, available at: https://www.zsw-bw.de/en/newsroom/news/news-detail/news/detail/News/zsw-and-sg-engineering-join-forces-to-set-up-wind-power-field-test-site.html (last access: 18 December 2019), 2017.

A.2 Paper II: Gravo-aeroelastic scaling of very large wind turbines to wind tunnel size

Gravo-aeroelastic scaling of very large wind turbines to wind tunnel size

H Canet[1], P Bortolotti[1], CL Bottasso[1,2]

[1] Wind Energy Institute, Technische Universität München, Garching, Germany

[2] Department of Aerospace Science and Technology, Politecnico di Milano, Milano, Italy

E-mail: `carlo.bottasso@tum.de`

Abstract. This work focuses on the design of wind turbine rotors of wind tunnel size that match the aerodynamic (for both rotor and wake) and aeroelastic behavior of multi-MW machines, including gravitational effects. The approach follows the classical definition of length, time and mass scaling ratios to respect nondimensional scaling parameters. The sub-scale model is obtained by a complete aero-structural re-design procedure, considering airfoils with similar polars at sub-scale Reynolds and the use of adequate materials. The approach is applied to the design of a sub-scale wind tunnel rotor that mimics the behavior of a 10 MW wind turbine. Results illustrate the main characteristics of the proposed method as well as its limitations, highlighting the challenges posed by representing a gravo-aeroelastic system at a much reduced scale.

1. Introduction

Significant research efforts are currently being devoted to the development of very large wind turbines. Motivated by the reduction in cost of energy, the size of rotors has indeed dramatically increased in the last decades, and it is expected to grow even more in the next generation of wind turbines. Nonetheless, the design of very large machines remains a challenging activity, especially because of the currently only limited understanding of the aeroelastic and gravitational effects on very flexible rotors and towers. In addition, there is a need for validated numerical models that are capable of simulating such complex systems with the necessary level of confidence. Indeed, high-quality full-scale experimental data is difficult, expensive and sometimes altogether impossible to obtain.

In this scenario, scaled models offer a viable mean to overcome these hurdles. Complementary to full-scale experiments, tests performed on scaled models can provide relevant experimental data, obtained in the controlled environment of a lab, capturing selected aspects of the behavior of the full-scale system. This can be achieved at costs that are orders of magnitude lower than the ones associated with full-scale field testing. In addition, some measurements are possible in a wind tunnel that are not achievable at full-scale with the same level of accuracy or in the same conditions. Of course, these advantages come at a price, as it is typically impossible to match exactly all physical processes that take place at full-scale using a scaled model. Therefore, scaled models have to be designed with specific goals in mind, and they will inevitably suffer from limitations.

Aeroelastic sub-scale models of wind tunnel size have been developed for years, but the scaling of gravitational effects has so far been typically neglected, as the enforcement of other

quantities was prioritized. However, the larger the rotors, the more prevalent the effects of gravity, which should therefore be included in the scaling procedures. This research work aims at closing this gap, proposing an aeroelastic scaling design methodology that includes gravitational effects. A modern automated multi-disciplinary design procedure is used to support and ease the implementation of the proposed scaling approach.

The paper is divided into three main sections. The first is devoted to the description of the theoretical background from which the scaling laws are derived. These conditions are then formulated as design drivers within an aero-structural design procedure, which is described in Sect. 2.2. In the last section, the described approach is applied to design a 2.8 meter sub-scale rotor reproducing the aerodynamic and dynamic behavior of a 10 MW offshore wind turbine.

2. Design methodology

2.1. Scaling laws

The starting point for the formulation of scaling laws lies on seven nondimensional numbers, which are obtained from the application of Buckingham Π Theorem to the equations governing the dynamic behavior of wind turbines [1]. One can classify these quantities into two categories. The first corresponds to the numbers that can be simultaneously enforced in the sub-scale model. These include the tip-speed ratio (TSR, describing the kinematics of the rotor aerodynamics), the nondimensional time, the nondimensional natural frequencies (which determine the ratio of elastic to inertial forces, in relation to the rotor speed), and the Lock number (which sets the relation between aerodynamic and inertial forces). The second category includes instead quantities that cannot be simultaneously guaranteed in the sub-scale model, when testing in air in standard wind tunnels. These include the Reynolds number (representing the ratio of inertial to viscous forces), the Mach number (which describes the flow compressibility), and the Froude number (defined as the ratio of aerodynamic to gravitational forces). For modern very large machines, gravitational loads play an important role, and the correct representation of their effects requires the enforcement of the Froude number in the sub-scale model. This however typically generates a mismatch in the Reynolds and Mach numbers. While the latter may be neglected —at least for today's typical tip speeds—, the former is of much greater importance and leads to marked changes in the aerodynamic performance of the blades.

Enforcing these matching conditions allows for the derivation of the scaling ratios that define the sub-scale characteristics. The length scaling ratio η_l between sub-scale (R_s) and full-scale (R_f) rotor radius is defined as

$$\eta_l = \frac{R_s}{R_f}. \tag{1}$$

Enforcing the Froude number, one obtains the following relation between sub-scale (T_s) and full-scale (T_f) time:

$$\eta_t = \frac{T_s}{T_f} = \sqrt{\eta_l}. \tag{2}$$

Finally, the mass scaling ratio η_m, expressed as sub-scale mass (M_s) over full-scale mass (M_f), is obtained from the matching of the Lock number and writes

$$\eta_m = \frac{M_s}{M_f} = \eta_l{}^3. \tag{3}$$

An overview of these scaling conditions, as well as their implications in the definition of the time and mass scaling ratios, is given in Fig. 1.

Conditions simultaneously matched				Conditions simultaneously not matched		
Dynamic response	Kinematics	Aero/Inertia	Elastic/Inertia	Gravity	Inertia/Viscous	Compressibility
$\tau_s = \tau_f$	$\mathrm{TSR}_s = \mathrm{TSR}_f$	$\mathrm{Lo}_s = \mathrm{Lo}_f$	$\widetilde{\omega}_s = \widetilde{\omega}_f$	$\mathrm{Fr}_s = \mathrm{Fr}_f$	$\mathrm{Re}_s \neq \mathrm{Re}_f$	$\mathrm{Ma}_s \neq \mathrm{Ma}_f$
		$\eta_m = \eta_l^3$	$E_s = E_f \eta_l$	$\eta_t = \sqrt{\eta_l}$		

Figure 1: Scaling laws for very large wind turbines and their implications on the scaling ratios (E indicates Young modulus).

The simplest possible scaling strategy consists in a straightforward zooming-down of the full-scale machine, where all system characteristics are scaled according to the aforementioned scaling ratios [2]. When aiming at a wind tunnel model size, this approach is however typically difficult to implement. First, the effect of the Reynolds mismatch between the two scales would lead to very significant deviations in the aerodynamic performance of the airfoils. Furthermore, zooming down the structural characteristics would imply extremely thin components made of materials with peculiar and possibly unrealistic mechanical properties. Therefore, an alternative approach must be taken, based on a complete aero-structural re-design.

2.2. Aero-structural re-design

An aero-structural re-design approach is here proposed by formulating two separate optimization problems. Both are implemented in the wind turbine design tool `Cp-Max` [3, 4]. This code is wrapped around the high-fidelity aeroservoelastic multibody simulation model `Cp-Lambda` (Code for Performance, Loads, Aeroelasticity by Multi-Body Dynamic Analysis) [5], which performs the necessary aeroelastic calculations. The design tool is coupled to the 2D finite-element cross sectional code `ANBA`, which implements the theory of Giavotto et al. [6]. This tool provides the structural and inertial characteristics of each beam section, serving as input for the multibody model.

The optimization algorithms implemented within `Cp-Max` perform the complete design of a wind turbine, including its control laws. The present sub-scale design activity represents a special application of these general design procedures. In particular, the present case demands the sequential solution of the blade aerodynamic and structural optimization problems, as illustrated in Fig. 2. Both procedures employ a Sequential Quadratic Programming (SQP) optimization algorithm, in which gradients are computed by means of finite differences.

The first design problem focuses on the definition of a scaled shape that mimics the aerodynamic behavior of the full-scale system. This is obtained by ensuring a number of conditions. First, the two rotors should have the same TSR for optimal power coefficient. Second, they should have the same spanwise circulation distribution, which ensures the same shed vorticity in the wake. Third, the airfoils should have the same efficiencies. Unfortunately, this last requirement cannot be met in general, because of the very different sectional Reynolds numbers of the two rotors. To approximate this condition, the scaled rotor is equipped with airfoils that differ from the ones of the full-scale machine, but that have similar (or as similar as possible) polars at their lower operating Reynolds. Based on these requirements, the scaled rotor is designed by optimizing its maximum power coefficient at the desired TSR, while satisfying a target spanwise distribution of the circulation. The resulting shape will be in general quite different from the one of the full-scale rotor, but matches as well as possible its aerodynamic characteristics.

In the second optimization, given the aerodynamic shape defined in the first problem, the blade structure is re-designed to mimic the full-scale aeroelastic behavior, considering available materials and feasible geometries. The structural solution is obtained by designing a blade that

has the same placement of natural frequencies with respect to the rotor speed, as well as the same Lock number of the full-scale one.
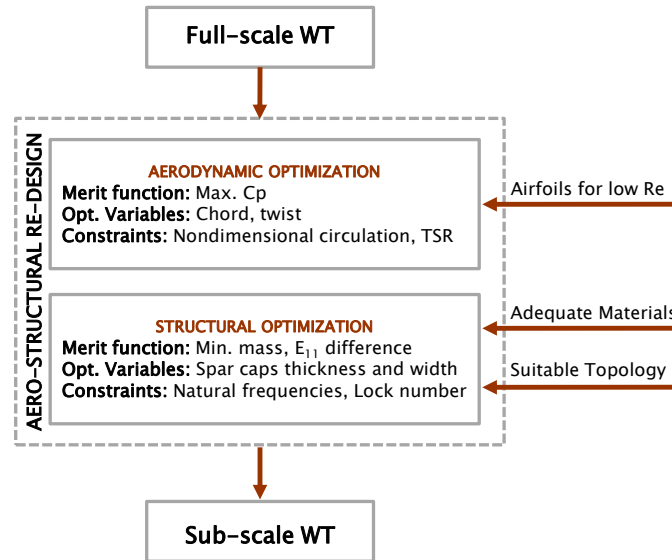
Figure 2: Overview of the proposed aero-structural re-design process.

The structural configuration of the scaled blade can be very different from the one of the full-scale machine. In the present work, we consider a solid blade —in contrast to the typical thin-walled structures used at full-scale—, made with a lightweight foamy material, two spar caps and a thin layer of glue that ensures a smooth finish to the surface. The modeling of the cross sections in `ANBA` is based on quadrilateral planar finite elements, where a meshing procedure implemented in `Matlab` guarantees simultaneously an accurate representation of the geometry and good aspect ratios for the elements. The geometry is parameterized in terms of spanwise shape functions and associated degrees of freedom. In turn, these structural parameters are computed by solving a design problem that minimizes the difference between the scaled and full-scale mass and flapwise stiffness distributions, while satisfying the frequency placement and Lock number constraints.

3. Scaling of a 10 MW rotor to wind tunnel size

The proposed scaling laws and design method are used to develop a sub-scale rotor of 2.8 meters based on the INNWIND.EU 10 MW wind turbine [7]. The length, time and mass scaling ratios for this problem are reported in Table 1, together with the scaling factors for other key quantities. The scaling of all system characteristics only depends on the ratio between the full- and the sub-scale rotor diameters. The re-designed sub-scale machine will have a different external shape and internal configuration, under the enforcement of the scaled parameters reported in Table 2. However, the matching of shape and configuration are irrelevant, as long as the significant scaling conditions are preserved between the two models.

Table 1: Scaling factors derived from the scaling laws.

Quantity	Scaling factor	
Length	n_l	1:63.68
Time	$\sqrt{n_l}$	1:7.98
Mass	$n_l{}^3$	1:258214
Rotor Speed	$\sqrt{n_l}$	1:7.98
Wind Speed	$\sqrt{n_l}$	1:7.98
Reynolds	$n_l{}^{3/2}$	1:508.16
Stiffness	$n_l{}^5$	1:32360

Table 2: Full-scale and sub-scale model characteristics.

Data	Full-scale	Sub-scale
Rotor diameter	178.3 m	2.8 m
Hub height	119 m	1.87 m
Total blade mass	42 t	0.165 kg
TSR for max C_P	7.2	7.2
Rotor speed	8.9 rpm	71.1 rpm
First flapwise frequency	0.57 Hz	4.52 Hz
First edgewise frequency	0.72 Hz	5.77 Hz

3.1. Aerodynamic re-design

The airfoil chosen for the aerodynamic re-design is the RG14 [8], whose shape is compared to the full-scale tip airfoil in Fig. 3a. This airfoil has already been successfully adopted in the context of the INNWIND.EU project [9] to design the rigid rotor of a floating wind turbine. The goal there was to represent the aerodynamic characteristics of the same 10 MW wind turbine considered here.

Although less efficient than the full-scale tip airfoil (Fig. 3a), the RG14 airfoil is found to approximate the polars of the full-scale blade sufficiently well at the low Reynolds generated in the wind tunnel, as shown in Fig. 3c and 3d. The airfoil is used from 20% blade span to the tip. The blade root cylinder smoothly deforms into the RG14 airfoil in the blade inner region, resulting in the relative thickness distribution shown in Fig. 4b.

The blade chord and twist distributions are optimized to reproduce the aerodynamic performance of the full-scale machine as closely as possible. A comparison between the initial and the re-designed blade shapes and nondimensional spanwise circulation distributions are reported in Fig. 4. The enforcement of circulation matching —which is quite good except at 0.22% span— is the active driver for the outer blade shape. In terms of performance, the re-designed blade can only approximate the full-scale one, mostly because of the unavoidable differences in the airfoil behavior at the much reduced Reynolds number.

3.2. Structural re-design

The structural re-design of the blade starts from the work of Campagnolo et al. [10], where an aeroelastically scaled blade for wind tunnel testing was designed and manufactured. For that blade, the time scaling ratio was not driven by the enforcement of the Froude number, but it was based on a trade-off between Reynolds mismatch and an excessive control bandwith. This implied a lower time scaling ratio than the present one, which in turn led to a significantly stiffer blade. In addition, the blade was designed to mirror the full-scale aeroelastic behavior, by achieving a realistic distribution of the inertial and stiffness properties, as well as ensuring the
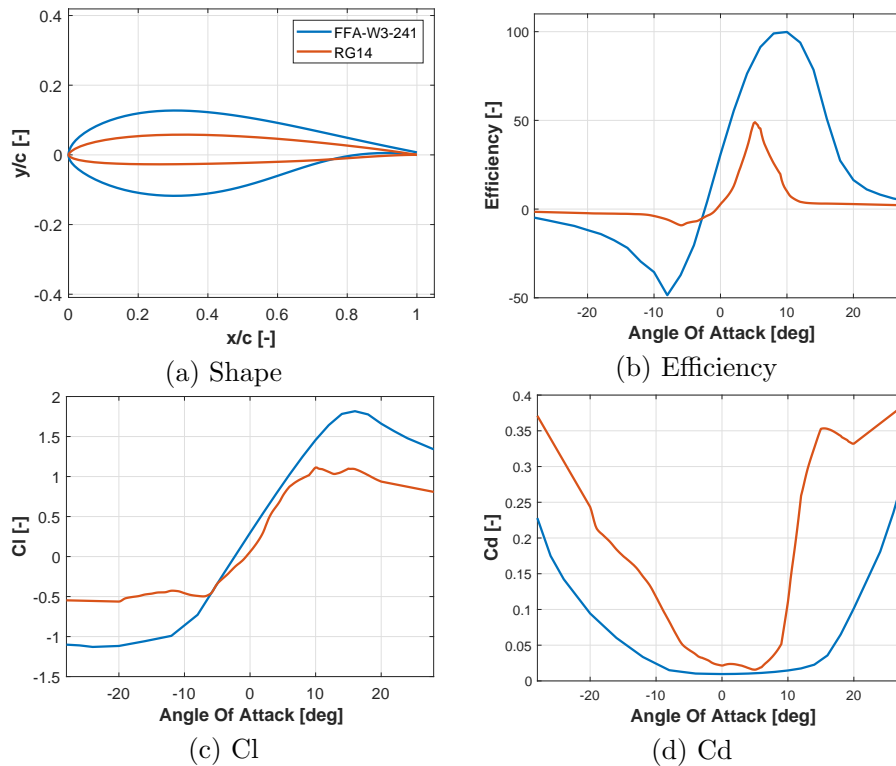
Figure 3: Comparison of aerodynamic characteristics for the full-scale model tip airfoil FFA-W3-241 (Re=1E7) and the low-Reynolds airfoil RG14 (Re=5E4).

same placement of natural frequencies with respect to the rotor speed between the two models. The blade structure adopted a solid sectional layout filled with a foam core made of `Rohacell`, which was machined to provide the outer blade shape. Two unidirectional carbon spar caps provided the required flapwise stiffness distribution. The surface smoothness was obtained by a very thin layer of skin made of glue. The blade re-design was able to replicate the placement of the lowest four rotor natural frequencies and it approximated the mass and flapwise stiffness distributions, but it was stiffer than the full-scale reference in the edgewise direction.

Despite the differences in scaling laws, and thus in desired aeroelastic behavior, the layout developed in Ref. [10] was found to be a suitable solution even in the present case. The selection of materials is a critical aspect of the problem, and the mechanical properties listed in the Cambridge University Materials Data Book [11] are used to guide the material selection process for spar caps and core. A Rigid Polymer Foam (LD) [11] is chosen as filler, because of its relatively high stiffness and lightness. For the spar caps, thermoplastic polymers are found to be the most suitable family of materials. Even though their stiffness to density ratio is much lower than materials traditionally used for spar caps, such as CFRP, they are well suited to this application. Moreover, the use of thermoplastics allows for alternative and easier manufacturing methods, leading to a higher flexibility in the spar cap design. From this family, polypropilene (PP) is chosen because of its low stiffness modulus. Finally, the external shell is covered by a very thin layer of the epoxy structural adhesive `Scotch Weld AF 32` [12].

The structural design procedure implemented in `Cp-Max` [4] and described in Sect. 2.2 is then used to optimize the spar caps thickness and width and ensure the matching of all desired scaling constraints. The problem formulation also includes manufacturability constraints for

(a) Chord

(b) Relative Thickness

(c) Twist
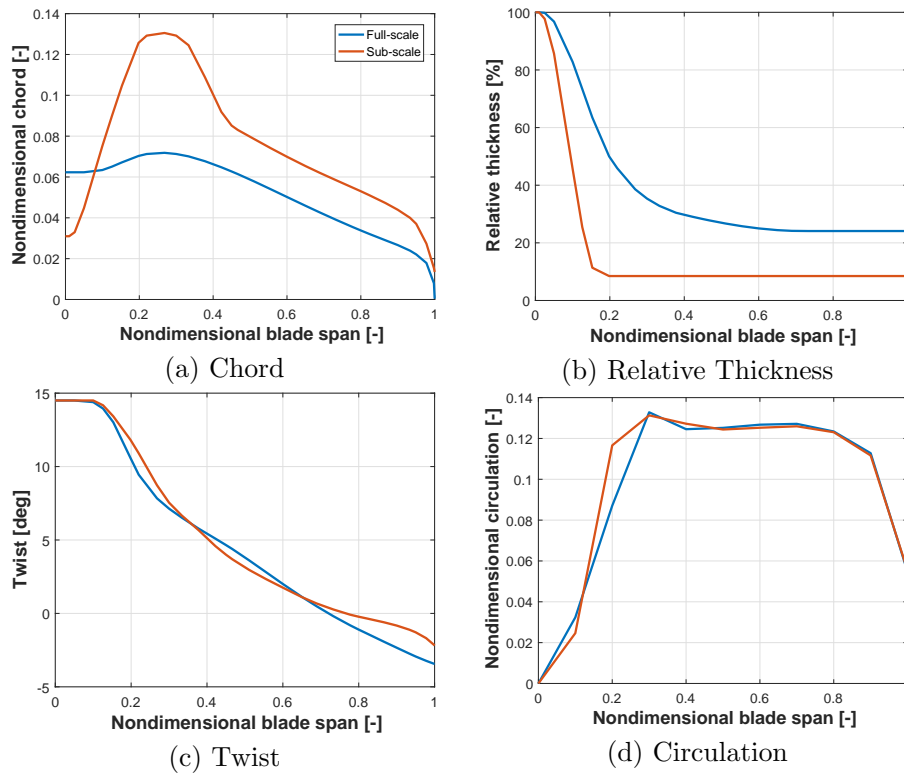
(d) Circulation

Figure 4: Comparisons of external shape and nondimensional circulation in Region 2, for the full- and the sub-scale models.

the components, establishing a 1 mm minimum thickness of the spar caps. The constraint satisfaction tolerance is set at 5%. Figure 5 reports the results of the optimization. The desired matching of mass and flapwise stiffness is achieved, except at blade root. The requirement on edgewise stiffness is instead not met due to the large chord of the sub-scale model. The placement of the first flapwise and edgewise frequencies with respect to the rotor speed is also successfully achieved. However, the corrected placement of higher frequencies is not exactly met. Finally, small disparities in mass distribution introduce a slight mismatch in the Lock number.

4. Conclusions

This work has proposed an approach to develop sub-scale models of wind tunnel size to mimic the gravo-aeroelastic behavior of large wind turbines. The formulation was applied to the design of a 2.8 meter sub-scale model of a 10 MW machine.

The aero-structural re-design approach is able to obtain the desired results, although subject to limitations. Specifically, the replication of the power coefficient vs. TSR behavior is limited by the availability of suitable low-Reynolds airfoils. Furthermore, the structural re-design is constrained by the manufacturing process and by the mechanical properties of existing materials. As a result, only a partial matching of the inertial and elastic behavior can be achieved. More precisely, flapwise stiffness and mass distributions are well matched from 20% of blade span to blade tip, resulting in the correct placement of the lowest two natural frequencies of the blade. These results highlight the challenges posed by representing a gravo-aeroelastic system at a much reduced scale. Although it is clear that the resulting scaled model is unable to exactly replicate the one at full scale, several relevant physical processes are nonetheless well
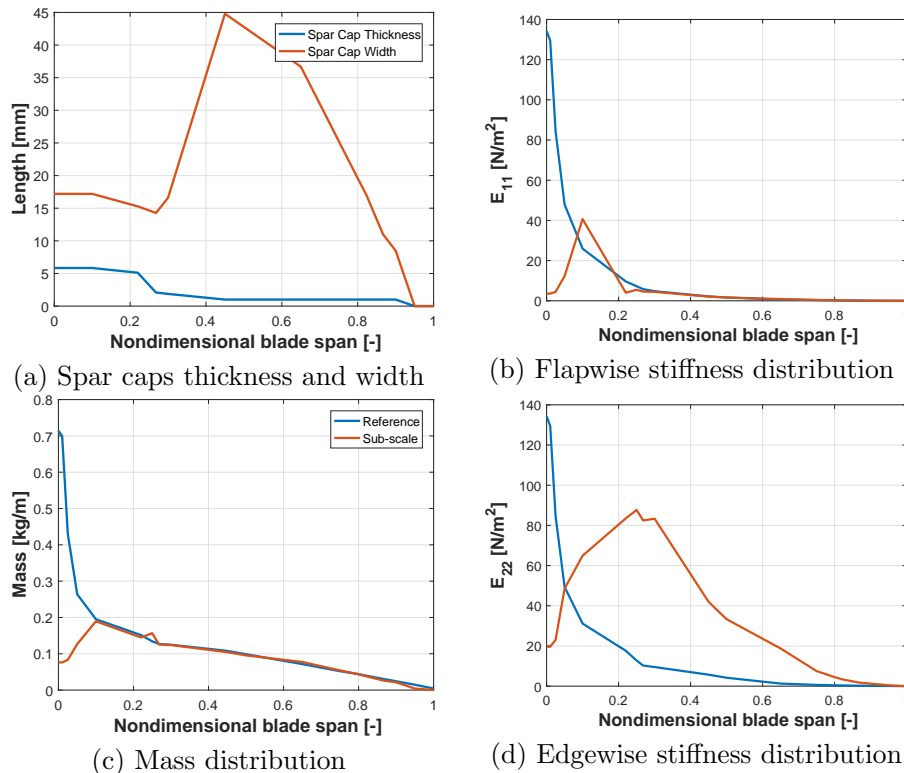
Figure 5: Distribution of spar cap thickness and width along blade span, and comparison between the cross sectional properties of the sub-scale and scaled full-scale model.

represented at the smaller scale. Keeping always well in mind the limits of scaled models, wind tunnel experiments can still play a crucial role in the validation and verification of simulation models, in the understanding of the physics, in the testing of control laws, the exploration of new configurations, and many other relevant activities.

The present research will continue by further investigating the blade structural design, looking in particular at the manufacturing process and the corresponding design limits. Moreover, efforts will be devoted to improve the scaled model edgewise behavior, either by identifying materials with more suitable mechanical properties, or relaxing the aerodynamic constraints.

Acknowledgments

References
[1] Bottasso CL, Campagnolo F and Petrovic V 2014 Wind tunnel testing of scaled wind turbine models: beyond aerodynamics *J. Wind Eng. Ind. Aerodyn.* **127** 1128 doi: 10.1016/j.jweia.2014.01.009
[2] Loth E, Fingersh L, Griffith D, Kaminski M and Qin C 2017 Gravo-Aeroelastically Scaling for Extreme-Scale Wind Turbines *35th AIAA Applied Aerodynamics Conference*, AIAA AVIATION Forum, doi: 10.2514/6.2017-4215
[3] Bottasso CL, Campagnolo F and Croce A 2012 Multi-disciplinary constrained optimization of wind turbines *Multibody Syst. Dyn.* **27** 21-53 doi: 10.1007/s11044-011-9271-x
[4] Bortolotti P, Bottasso CL and Croce A 2016 Combined preliminary-detailed design of wind turbines *Wind Energ. Sci.*, **1** 71-88 doi: 10.5194/wes-1-71-2016

[5] Bottasso CL, Croce A, Savini B, Sirchi W and Trainelli L 2006 Aero-servo-elastic modeling and control of wind turbines using finite-element multibody procedures 2006 *Multibody Syst. Dyn.* **16** 291-308 doi: 10.1007/s11044-006-9027-1

[6] Giavotto V, Borri M, Mantegazza P and Ghiringhelli G 1983 Anisotropic beam theory and applications *Comput. Struct.* **16** 403-13 10.1016/0045-7949(83)90179-7

[7] Bottasso CL, Bortolotti P, Croce A and Gualdoni F 2016 Integrated aero-structural optimization of wind turbines *Multibody Syst. Dyn.* **38** 317-44 doi: 10.1007/s11044-015-9488-1

[8] Selig M, Guglielmo J, Broeren A and Gigure P 1995 *Summary of Low-Speed Airfoil Data* (Virginia: SoarTech Publications)

[9] INNWIND.EU Deliverable 4.24. Results of wave tank tests.

[10] Campagnolo F, Bottasso CL and Bettini P 2014 Design, manufacturing and characterization of aero-elastically scaled wind turbine blades for testing active and passive load alleviation techniques within a ABL wind tunnel *J. Phys.:Conf. Ser.* **524** 012061 doi: 10.1088/1742-6596/524/1/012061

[11] Cambridge University Engineering Department 2003 Materials Data Book

[12] Scotch-Weld: Structural Adhesive Film AF 32. Technical Data, Issue No. 3 doi: https://multimedia.3m.com/mws/media/241415O/3mtm-scotch-weldtm-structural-adhesive-film-af-32.pdf

A.3 Paper III: How realistic are the wakes of scaled wind turbine models?

How realistic are the wakes of scaled wind turbine models?

Chengyu Wang, Filippo Campagnolo, Helena Canet, Daniel J. Barreiro, and Carlo L. Bottasso

Wind Energy Institute, Technische Universität München, 85748 Garching bei München, Germany

Correspondence: Carlo L. Bottasso (carlo.bottasso@tum.de)

Abstract. The aim of this paper is to analyze to which extent wind tunnel experiments can represent the behavior of full-scale wind turbine wakes. The question is relevant because on the one hand scaled models are extensively used for wake and farm control studies, whereas on the other hand not all wake-relevant physical characteristics of a full-scale turbine can be exactly matched by a scaled model. In particular, a detailed scaling analysis reveals that the scaled model accurately represents the principal physical phenomena taking place in the outer shell of the near wake, whereas differences exist in its inner core. A large-eddy simulation actuator-line method is first validated with respect to wind tunnel measurements and then used to perform a thorough comparison of the wake at the two scales. It is concluded that, notwithstanding the existence of some mismatched effects, the scaled wake is remarkably similar to the full-scale one, except in the immediate proximity of the rotor.

1 Introduction

The simulation of wind turbine wakes in wind tunnels has been gaining increasing interest in recent years. In fact, since wakes represent a major form of coupling within a wind plant, understanding their behavior and accurately simulating their effects are today problems of central importance in wind energy science, with direct practical implications on design, operation and maintenance. Recent studies include the analysis of single and multiple interacting wakes – see, for example, the review in Bottasso and Campagnolo (2021) or, among others, Whale et al. (1996), Chamorro and Porté-Agel (2009, 2010), Bartl and Sætran (2016), Bastankhah and Porté-Agel (2016), Tian et al. (2018), Campagnolo et al. (2016), Bottasso et al. (2014a), Campagnolo et al. (2020), Wang et al. (2020c) and references therein.

Wind tunnel testing offers some unique advantages over full-scale field testing.

– The ambient conditions are repeatable and – at least to some extent – controllable.

– Detailed flow measurements are possible with a plethora of devices, from standard pressure and hot-wire probes to particle image velocimetry (PIV) (Meinhart, 1999) and scanning lidars (van Dooren et al., 2017), whereas measurements of comparable accuracy and resolution are today hardly possible at full scale. Additionally, time flows faster in a scaled experiment than at full scale (Bottasso and Campagnolo, 2021; Canet et al., 2021; Campagnolo et al., 2020), which means that a large informational content can be accumulated over relatively short periods of time.

– Models can be designed ad hoc to achieve specific goals and can be extensively instrumented (Bottasso and Campagnolo, 2021), while layouts and scenarios can be readily changed to explore different operating conditions of interest.

– Costs are limited, even for highly sophisticated models, also because there are no energy production losses as it is often the case in the field; additionally, the costs of sophisticated wind tunnel facilities are typically amortized by their use for several different applications over long periods of time.

– Open datasets can be shared within the research community and collaborations are facilitated, since there are no – or few – constraints from intellectual property than when real wind turbine data are used.

Testing in the controlled and repeatable environment of the wind tunnel is today contributing to the understanding of the physical processes at play, generates valuable data for the validation and calibration of mathematical models, and offers opportunities for the verification of control technologies.

However, notwithstanding these and other unique advantages, a major question still hovers over the wind tunnel simulation of wakes: *how faithful are these wakes to the actual ones in the field?* In fact, in private conversations these authors have often been questioned on the actual usefulness of wind tunnel testing, based on a perceived lack of realism of these scaled experiments. Indeed, some skepticism is justified and completely understandable: simulation codes are being calibrated and validated with respect to wind tunnel measurements, and wind farm control techniques are being compared and evaluated in wind tunnel experiments. Therefore, it is important to quantify the level of realism of wind tunnel simulated wakes and to identify with better clarity what aspects faithfully represent the full-scale truth and what aspects do not.

A thorough and complete answer to this question is probably still out of reach today. In fact, detailed inflow and wake measurements of a full-scale turbine would be necessary, with a level of detail comparable to the ones achievable in the tunnel. Lidar technology is making great progress (Zhan, 2020) and might soon deliver suitable datasets. It should be a goal of the scientific and industrial communities to completely open such future datasets to research, which would surely greatly favor the scientific advancement of the field. In the meanwhile, however, some partial answers to the question of wake realism can still be given. This is the main goal of the present paper.

This study considers the Technische Universität München (TUM) G1 scaled wind turbine (Bottasso and Campagnolo, 2021) and a dataset obtained with this machine in the boundary layer wind tunnel of the Politecnico di Milano in Italy. A large-eddy simulation (LES) actuator-line method (ALM) (Wang et al., 2019) is used to simulate the wind tunnel experiments, including the passive generation of a sheared turbulent inflow. The code has been validated with respect to the present and other similar measurements.

Following Bottasso and Campagnolo (2021) and Canet et al. (2021), dimensional analysis and wake physics are used here to review the main factors driving wake behavior. The same analysis also reveals which physical aspects of full-scale wakes cannot be matched at the reduced scale and with the considered experimental setup. A first analysis of scaling was performed by Chamorro et al. (2016), considering the effects caused by the mismatch of the rotor-based Reynolds. Experimental results based on a miniature wind

turbine showed that wake behavior is unaffected by this parameter when it is larger than circa 10^5. However, in reality the behavior of the blades and, as a consequence, of the wake is much more strongly affected by the chord-based Reynolds number, as initially discussed in Bottasso et al. (2014a). In fact, the much lower Reynolds regime of a small-scale model blade compared to a full-scale machine implies very different aerodynamic characteristics of the airfoils, which in turn drive a number of specific design choices of the scaled model (Bottasso and Campagnolo, 2021; Canet et al., 2021). Notwithstanding the differences caused by the chord-based Reynolds number mismatch, it is relatively easy – as shown more in detail later on – to match the main processes taking place in the outer shell of the near wake, as well as the ones that govern its breakdown and the characteristics of the far wake. On the other hand, several mismatched effects do exist in the central core of the near wake. Dimensional analysis also expresses the scaling relationships that allow the mapping of scaled quantities into equivalent full-scale ones, and vice versa.

Based on the understanding provided by dimensional analysis and wake physics, full-scale models are designed in this work to match some of the G1 scaled turbine parameters. Various versions of these models are considered, ranging from a more realistic full-scale turbine – with a larger number of mismatched effects – to less realistic ones that however match a larger set of quantities of the scaled model.

The full-scale models are then simulated with the LES-ALM code, using the same exact numerical methods and algorithmic parameters used for the scaled simulations. These wind turbine models are also exposed to the same identical ambient turbulent inflow used for the scaled model. The underlying assumption is that, since the code was found to be in very good agreement with measurements obtained in the scaled experiments, the same code based on the same numerical setup should deliver results of similar accuracy even at full scale. This assumption cannot be formally proven at this stage, but it seems to be very reasonable, and it is probably the only possible approach that can be pursued in the absence of a detailed full-scale dataset.

Finally, the numerically simulated scaled and full-scale wakes are compared. The analysis considers wind-aligned and misaligned conditions, typical of wake steering control applications, and various metrics, including wake shape, path, speed profile, Reynolds shear stresses, power available and wind direction modification due to the curled wake in misaligned conditions. This detailed comparison is used to quantify the degree of similarity among the different models and across the various metrics. Since the models differ by known mismatched effects, this also helps pinpoint and explain any source of discrepancy.

The paper is organized according to the following plan. Section 2 uses dimensional analysis and wake physics to identify the quantities that can be exactly matched between scaled and full-scale models, the ones that can only be par-

tially matched, the ones that are unmatched, and those that are neglected from the present analysis. Next, Sect. 3 describes the scaled experimental wind turbine and its full-scale counterparts, which include various modifications to highlight the effects of specific mismatches. Section 4 describes the numerical simulation model, including the generation of the turbulent inflow in the wind tunnel. Results and detailed comparisons among the scaled and the full-scale models are reported in Sect. 5. Finally, Sect. 6 summarizes the main findings of this work.

2 Scaling

The matched, partially matched, unmatched and neglected physical effects of the scaled and full-scale models are reviewed next. Quantities referred to the scaled model are indicated with the subscript $(\cdot)_M$, while quantities referred to the full-scale physical system are indicated with the subscript $(\cdot)_P$. Scaling is defined by two parameters (Bottasso and Campagnolo, 2021; Canet et al., 2021): the length scale factor $n_l = l_M / l_P$, where l is a characteristic length (for example the rotor radius R); and the time compression ratio $n_t = t_M / t_P$, where t is time. In the present case $n_l = 1/162.1$ and $n_t = 1/82.5$. A more complete treatment of scaling for wind turbine rotors is given in Bottasso and Campagnolo (2021) and Canet et al. (2021).

2.1 Matched quantities

- *Inflow*. The ambient flow is obtained by simulating the passive generation of turbulence in the wind tunnel, as explained in Sect. 4.2; the developed flow is sampled on a rectangular plane, which becomes the inflow of the scaled turbine simulations. For the full-scale turbine simulations, the sides of the rectangular inflow area are geometrically scaled by n_l, while time is scaled by n_t and speed V as $V_M / V_P = n_l / n_t$, resulting in a flow with exactly the same identical characteristics (e.g., shear, turbulence intensity, integral length scale) at the two scales.

- *Tip speed ratio (TSR)*. The TSR is defined as $\lambda = \Omega R / V$, where Ω is the rotor speed. TSR determines not only the triangle of velocity at the blade sections, but also the pitch of the helical vortex filaments shed by the blade tips.

- *Non-dimensional circulation*. The non-dimensional circulation is defined as $\Gamma(r)/(RV) = 1/2(c(r)/R)C_L(r)(W(r)/V)$, where C_L is the lift coefficient, c the local chord, W the local flow speed relative to the blade section and r is the spanwise blade coordinate (Burton et al., 2011). Each blade sheds trailing vorticity that is proportional to the spatial (spanwise) gradient $d\Gamma / dr$. Therefore, matching the non-dimensional spanwise distribution of Γ (and, hence, also its non-dimensional spanwise gradient) ensures that the two rotors shed the same trailing vorticity.

  The root of the G1 blade is located further away from the rotor axis than a typical full-scale machine, due to the space required for housing the pitch actuation system in the hub. The resulting effects caused on the wake were investigated by developing two different full-scale models: one with the exact same non-dimensional circulation of the G1 and one with more typical full-scale values, as discussed later.

- *Rotor-based Strouhal number*. The rotor-based Strouhal number $St = f D / V$ is matched, where f is a characteristic frequency and $D = 2R$ is the rotor diameter. This definition of the Strouhal number has been recently shown to characterize the enhanced wake recovery obtained by mixing, both in the case of dynamic induction control (Frederik et al., 2020a) and by cyclic pitch excitations (Frederik et al., 2020b).

2.2 Approximatively matched quantities

The following quantities or effects are very nearly, but not exactly, matched.

- *Thrust coefficient*. The thrust coefficient is defined as $C_T = T/(1/2\rho A V^2)$, where T is the thrust force, ρ is air density and $A = \pi R^2$ is the rotor swept area. The thrust characterizes to a large extent the speed deficit in the wake. In misaligned conditions, it is also the principal cause for the lateral deflection of the wake. The thrust coefficient is very nearly matched, whereas the power coefficient is not (as discussed later). In fact, the latter strongly depends on airfoil efficiency, which is affected by the chord-based Reynolds number mismatch between the two models. On the other hand, drag has only a limited effect on thrust, which as a result is very similar in the models at the two scales.

- *Dynamic spanwise vortex shedding*. During transients, spanwise vorticity is shed that is proportional to the temporal gradient of the circulation. To match the spanwise vortex shedding of a rotor, the matching of $(1/RV)d\Gamma/d\tau$ should be ensured (Bottasso and Campagnolo, 2021; Canet et al., 2021), where τ is a non-dimensional time (for example, $\tau = \Omega_r t$, with Ω_r being a reference rotor speed), equal for both the full and scaled models.

  Rewriting the non-dimensional circulation as

  $$\frac{\Gamma}{RV} = \frac{1}{2}\frac{c}{R}C_{L_\alpha}\frac{W}{V}\left(\frac{U_P U_T}{W^2} - \theta\right), \tag{1}$$

  with C_{L_α} being the lift curve slope, the dynamic spanwise vortex shedding condition implies the matching of

the non-dimensional time rates of change of the sectional tangential and perpendicular flow components U_P and U_T, with $W^2 = U_P^2 + U_T^2$, and of the pitch angle θ. The flow speed component tangential to the rotor disk is $U_T = \Omega r + u_T$, where u_T contains terms due to wake swirl and yaw misalignment. The flow speed component perpendicular to the rotor disk is $U_P = (1-a)V + u_P$, where a is the axial induction factor, and u_P is the contribution due to yaw misalignment and vertical shear. A correct similitude of dynamic vortex shedding is ensured if the non-dimensional time derivatives λ', a', u_P', u_T' and θ' are matched, where $(\cdot)' = \mathrm{d} \cdot /\mathrm{d}\tau$.

Matching of λ' is ensured here by the fact that the two rotors operate at the same TSR in the same inflow; additionally, the simulations were conducted by prescribing the rotor rotation (i.e., without a controller in the loop), so that $\Omega' = 0$. The term a' accounts for dynamic changes in the induction, which are due to the speed of actuation (of torque and blade pitch) and the intrinsic dynamics of the wake. The speed of actuation is not relevant in this case, due to the absence of a pitch–torque controller. The intrinsic dynamics of the wake, as modeled by a first-order differential equation (Pitt and Peters, 1981), is also automatically matched thanks to the matching of the design TSR (Bottasso and Campagnolo, 2021; Canet et al., 2021). Finally, u_P' and u_T' are matched because the inflow is the same, with the exception of the contribution of wake swirl, which is not exactly the same because of the different torque coefficient, as noted below.

- *Inflow size.* The cross section of the wind tunnel has a limited size, resulting in the blockage phenomenon, i.e., in an acceleration of the flow between the object being tested and the sides (lateral walls and ceiling) of the tunnel (Chen and Liou, 2011). Although this problem is not strictly related to the scaling laws discussed here, it is still an effect that needs to be accounted for, especially if the ratio of the frontal area of the tested objected and the cross-sectional area of the tunnel is not negligible. Simulations in domains of increasingly larger cross sections were conducted to quantify the blockage affecting the experimental setup considered here.

- *Integral length scale (ILS).* Relative to the size of the TUM G1 turbines, the wind tunnel used in this research (located at Politecnico di Milano, Italy) generates a full-scale ILS of approximately 142 m at hub height, which is respectively about 16 % and 58 % smaller that the lengths specified by the second edition (IEC 61400-1, 1999) and third edition (IEC 61400-1, 2005) of the IEC 61400-1 international standards. To understand the effects of this mismatch on wake behavior, simulations were conducted in turbulent inflows differing only in their integral scales.

2.3 Unmatched quantities

The following quantities cannot be matched based on the current experimental setup and scaling choices.

- *Chord-based Reynolds number.* The chord-based definition of the Reynolds number reads $Re = \rho W c/\mu$, where μ is the fluid viscosity. The Reynolds number mismatch can be computed as $Re_M/Re_P = n_l^2/n_t$, which is equal to $1/318.5$ in the present case. This implies that the blades of the G1 model operate in a very different regime than the ones of the full-scale blade (Lissaman, 1983). To mitigate these effects, the G1 blade has a larger chord than the full-scale one and uses ad hoc low-camber airfoils specifically conceived for low-Reynolds-number flows (Bottasso and Campagnolo, 2021; Selig, 2003). Additionally, note that the scaling relationship of the rotor speed is $\Omega_M/\Omega_P = 1/n_t$. Therefore, by increasing the rotor speed of the model Ω_M (which has the effect of accelerating time by reducing the ratio n_t), one can lower the Reynolds mismatch (Bottasso and Campagnolo, 2021).

- *Power coefficient.* The power coefficient is defined as $C_P = P/(1/2\rho A V^3)$, where P is the aerodynamic power. The power coefficient of the scaled model is lower than the one of the full-scale machine, because of the smaller efficiency of the airfoils at low-Reynolds regimes. Since the torque coefficient is $C_Q = C_P/\lambda$, then also C_Q is unmatched and smaller for the scaled model than for the full-scale one, resulting in reduced wake swirling (Burton et al., 2011).

- *Tower and nacelle vortex shedding.* Bluff bodies periodically release vortices in their wakes (von Karman, 1911), at a characteristic frequency proportional to the Strouhal number. The tower-based Strouhal number $St = fd/V$ is matched when the tower diameter d is geometrically scaled. However, as noted later, the diameter of the G1 tower is larger than the one of the full-scale machine, so that frequency and size of the shed vortices are accordingly affected. An even larger mismatch applies to the nacelle, because of power density and miniaturization constraints.

- *Stall delay due to rotational augmentation.* Matching these effects requires the matching of the blade chord and twist distributions, of the non-dimensional circulation, and of the Rossby number $Ro = \Omega r/(2W)$ (Dowler and Schmitz, 2015; Bottasso and Campagnolo, 2021). While the latter two quantities are indeed matched, the former two are not, in order to mitigate the chord-based Reynolds number mismatch. To quantify the effects of rotational augmentation on wake behavior, two versions of the full-scale turbine were developed, as explained later on.

– *Chord-based Mach number*. The chord-based Mach number is defined as $Ma = W/s$, where s is the speed of sound. Although this flow parameter is not matched, compressibility effects are irrelevant for the full and scaled models considered here, as for virtually all present-day wind turbines.

– *Boundary layer stability and wind veer due to the Coriolis force*. The wind tunnel used in the present research can only generate neutrally stable boundary layers. Although atmospheric stability has a profound effect on wakes (Abkara and Porté-Agel, 2015), this problem has already been studied elsewhere, and it is considered to be out of scope for the present investigation. Similarly, Coriolis effects on the inflow and wake behavior are not represented in a wind tunnel, although they are known to have non-negligible effects on capture, loading and also on wake path (van der Laan and Sørensen, 2007).

2.4 Neglected quantities

The following effects could be matched with a different experimental setup and scaling choices but were neglected in the present work.

– *All gravo-aeroelastic effects*. Since the blades of the G1 turbine are not aeroelastically scaled (and are very stiff), also the full-scale model was simulated without accounting for flexibility. Aeroelasticity could have some effects on near-wake behavior for very flexible rotors but would probably have only a negligible role on the characteristics of the far wake. Therefore, aeroelastic effects were excluded from the scope of the present investigation.

– *Unsteady airfoil aerodynamics*. Unsteady aerodynamics, including linear unsteady corrections (for example, according to Theodorsen's theory; Bisplinghoff and Ashley, 2002), and dynamic stall, was not considered in the present analysis. However, it was verified that the mildly misaligned operating conditions analyzed here would not have triggered dynamic stall, except in a few instances, similarly to what was found in Shipley (1995). Here again, these effects would hardly have any visible effects on far-wake behavior.

2.5 Remarks

Wake stability analysis shows that the vortical structures released by the blade tips and root interact in the near wake (Okulov and Sørensen, 2007).

In the outer shell of the near wake, the mutual interaction of the tip vortices – triggered by turbulent fluctuations – leads to vortex pairing, leapfrogging and eventually to the breakdown of the coherent wake structures (Sørensen, 2011). The scaled and full-scale rotors are exposed to the same inflow

(including the same ambient turbulent fluctuations), the tip vortices have the same geometry (due to a matched design TSR) and strength (due to a matched non-dimensional circulation), and the speed deficit is also essentially the same (because of the very nearly matched thrust coefficient). Hence, it is reasonable to assume a nearly identical near-wake behavior of the external wake shell, given that all main processes are matched between scaled and full-scale models (with the exception of the effects that the unmatched tower may have).

The situation is different in the near-wake inner core. Here the root vortices combine with the effects caused by the presence of the nacelle and tower. In particular, the nacelle has a much larger relative frontal area, creating a different blockage (radial redirection), nacelle wake and vortex shedding. Additionally, in the 20 % inboard portion of the blade, both the circulation and rotational augmentation effects are unmatched. Finally, the mismatch of power induces a mismatch of torque that reduces wake swirl; as shown by blade element momentum (BEM) theory, swirl is mostly concentrated in the inner core of the wake and decays rapidly with radial position (Burton et al., 2011). Hence, the near-wake inner core is expected to behave differently in the scaled and full-scale models. However, some of the results reported here, in addition to evidence from other sources (Wu and Porté-Agel, 2011), indicate that the inner core near wake has only a modest effect on far-wake behavior. For example, it is common practice to simulate far-wake behavior with LES codes without even representing the turbine nacelle and tower (Martínez-Tossas et al., 2015).

As a consequence, thanks to the employed scaling and matching criteria, the far-wake behavior is expected to be extremely similar between the wind-tunnel-generated wake and the full-scale one. The results section will more precisely support this claim.

3 Wind turbine models

3.1 The TUM G1 scaled wind turbine

The TUM G1 is a three-bladed clockwise-rotating (looking downstream) wind turbine, with a rotor diameter D of 1.1 m, a hub height H of 0.825 m, and rated rotor and wind speeds of 850 rpm and 5.75 m s^{-1}, respectively. The G1 was designed based on the following requirements (Bottasso and Campagnolo, 2021):

– a realistic energy conversion process and wake behavior;

– a sizing of the model obtained as a compromise between Reynolds mismatch, miniaturization constraints, limited wind tunnel blockage, and ability to simulate multiple wake interactions within the size of the test chamber;

– active individual pitch, torque, and yaw control in order to test modern control strategies at the turbine and farm levels;

– a comprehensive on-board sensorization.

The turbine has been used for several research projects and numerous wind tunnel test campaigns (Campagnolo et al., 2016, 2020). The main features of the G1 rotor and nacelle are shown in Fig. 1a.

A brushless motor equipped with a precision gearhead and a tachometer is installed in the rear part of the nacelle and generates the resisting torque, which is in turn measured by a torque sensor located behind the two shaft bearings. An optical encoder, located between the slip ring and the rear shaft bearing, measures the rotor azimuth, while two custom-made load cells measure the bending moments at the foot of the tower and on the shaft in front of the aft bearing. Thrust is estimated from the fore–aft bending moment measured by the load cell at the base of the tower, correcting for the drag of the tower and rotor–nacelle assembly.

Each wind turbine model is controlled by its own dedicated real-time modular Bachmann M1 system, implementing supervisory control functions, pitch–torque–yaw control algorithms, and all necessary safety, calibration and data logging functions. Measurements from the sensors and commands to the actuators are transmitted via analogue and digital communication. The Bachmann M1 system is capable of acquiring data with a sample rate of 2.5 kHz, which is used for aerodynamic torque, shaft bending moments and rotor azimuth position. All other measurements on the turbine are acquired with a sample rate of 250 Hz.

3.2 Full-scale wind turbine

A full-scale wind turbine was designed through a backward-engineering approach to match the characteristics of the G1 scaled machine. The DTU 10 MW wind turbine (Bak et al., 2013), shown in Fig. 1b, was used as a starting design for this purpose. This turbine has a rotor diameter of 178 m and a hub height of 119 m, and the modified version used here is termed G178.

The ratio of the rotor diameter D of the G1 and DTU turbines was used to define the geometric scaling factor n_l. The hub height H of the full-scale machine was slightly adjusted to match the ratio D/H of the G1 turbine.

The shape of nacelle and tower were kept the same as the DTU reference, creating a mismatch with the G1 turbine. In fact, the scaled model – due to miniaturization constraints – has a frontal area of the nacelle that is 2.6 times larger than the one of the scaled DTU turbine; similarly, the tower diameter of the G1 turbine is 49 % larger than the scaled one of the DTU machine. This creates a mismatch in the drag of the nacelle and tower, in their local blockage and vortex shedding.

The aerodynamic design of the rotor of the DTU turbine was modified, in order to match the characteristics of the G1 in terms of design TSR and non-dimensional circulation distribution (and, as a consequence, to match also the thrust). Three versions of the rotor were realized. The standard G178 uses the same airfoils of the DTU turbine over the entire blade span, while chord and twist distributions were modified to satisfy the matching criteria. As the root of the G1 blade is located further away from the rotor axis than in the case of the G178, the non-dimensional circulation is matched only between 20 % and 100 % of blade span. To account for the effects of rotational augmentation, the inboard airfoils were corrected for delayed stall according to the model of Snel (1994).

A second rotor was designed to investigate the effects of the mismatched non-dimensional circulation on wake behavior. To this end, the twist angle close to the root was modified to decrease the lift inboard and match the non-dimensional circulation of the G1 turbine even in this part of the blade; all the other parameters of the model were kept the same as in the G178 turbine. This second turbine is termed G178-MC, where MC stands for "matched circulation".

A third version of the rotor was obtained by eliminating from the G178 the rotational augmentation model, to investigate its effects. The resulting rotor is termed in the following G178-nRA, where nRA stands for "no rotational augmentation".

The blades of the reference turbine are equipped with the four airfoils FFA-W3-241, FFA-W3-301, FFA-W3-360 and FFA-W3-480 (Fuglsang et al., 1998), respectively from tip to root. For the operating conditions analyzed in this paper, the chord-based Reynolds of the G1 varies along the blade span within the range 60 000–85 000. Airfoils operating at a Reynolds number below 100 000 experience significant parasitic drag due to the formation of a laminar separation bubble (Winslow et al., 2018), which affects their maximum lift coefficient and lift-to-drag ratio. To limit these effects, the low-Reynolds airfoil RG14 (Lyon and Selig, 1996) is used throughout the whole span of the G1. Trips can be employed for triggering the boundary layer transition and eliminating or reducing the laminar bubble (Selig and McGranahan, 2004). However, tripping is not used on the G1 blades, because it is not effective on these low-camber airfoils (Campagnolo, 2013).

The efficiency $E = C_L/C_D$ vs. non-dimensional span r/R of the reference and scaled blade is shown in Fig. 2 at rated conditions. The airfoil efficiency for the scaled rotor is almost half the one of the full-scale machine in the outer span of the blade; since most of the power is indeed extracted in this region, the reduced efficiency results in a lower power coefficient for the scaled model. The FFA-series airfoil characteristics were computed with Ansys Fluent (ANSYS, 2019), while the RG14 ones were obtained by correcting the baseline values of Lyon and Selig (1996) with rotor
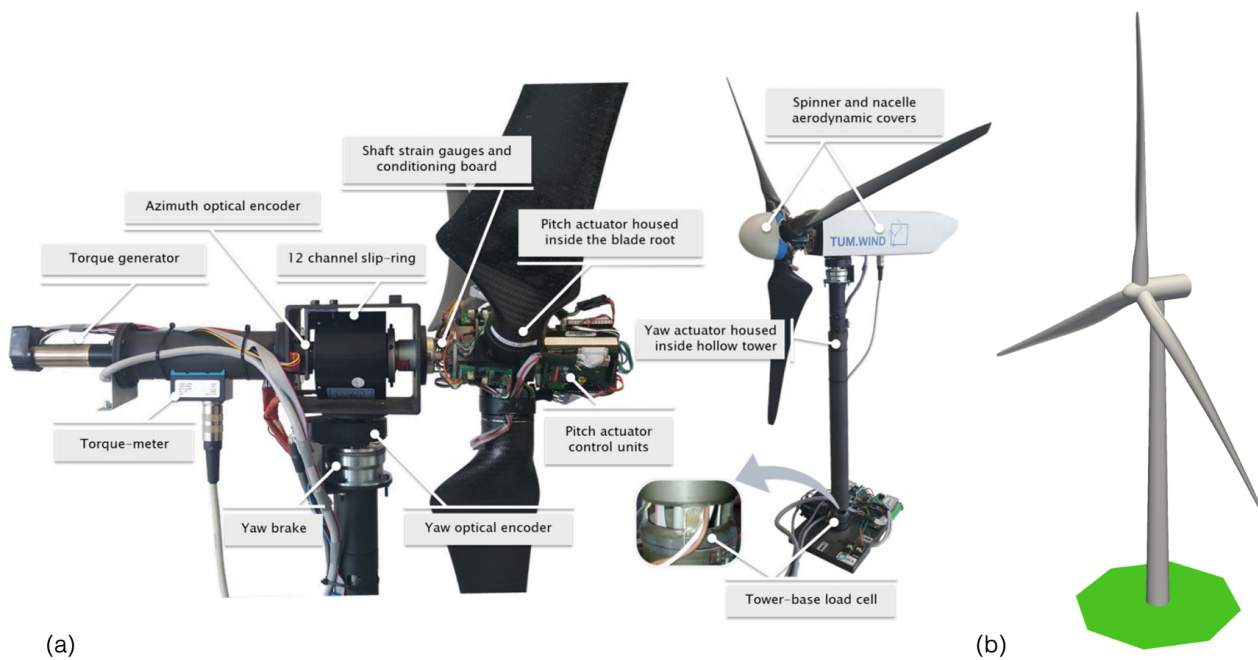
Figure 1. (a) The TUM G1 turbine (Campagnolo et al., 2016). **(b)** The full-scale DTU 10 MW turbine (from Bak et al., 2013).
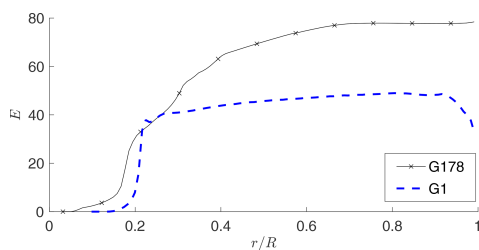

Figure 2. Efficiency E along the blade span r/R for the G178 and G1 turbines at rated TSR.

power and thrust measurements through the tuning approach of Wang et al. (2020a).

Distributions of the twist, chord, lift coefficient and non-dimensional circulation of the G1 and of the full-scale rotors are shown in Fig. 3. Chord distributions are normalized by their respective arithmetic mean c_0 over the span. Lift coefficient and circulation are evaluated at rated conditions using the BEM method implemented in the code FAST 8 (Jonkman and Jonkman, 2018). The lift coefficient of the G1 is significantly smaller than the one of the full-scale turbines, which is a result of its larger rotor solidity. The lower lift is however compensated for by a larger chord and different twist distributions, resulting in a matched non-dimensional circulation from 20 % span to the blade tip for the G178 turbine. For the G178-MC model, the non-dimensional circulation is matched over the whole blade span. The difference in lift and

circulation between G178 and G178-nRA is due to rotational augmentation.

4 Simulation model

4.1 LES-ALM CFD code

Numerical results were obtained with a TUM-modified version of SOWFA (Fleming et al., 2014), more completely described in Wang et al. (2018, 2019). The code has been used extensively to numerically replicate wind tunnel tests conducted with G1 turbines, achieving an excellent correlation with the experimental measurements in a wide range of conditions, including full and partial wake overlaps, wake deflection, static and dynamic induction control, and individual pitch control (for example, see Wang et al., 2019, 2020b, c).

The finite-volume LES solver is based on the standard Boussinesq PISO (Pressure Implicit with Splitting of Operator) incompressible formulation and is implemented in Open-FOAM (Jasak, 2009). Spatial differencing is based on the Gamma method (Jasak et al., 1999), where a higher level of upwinding is used in the near-wake region to enhance stability. Time marching is based on the backward Euler scheme. The pressure equation is solved by the conjugate gradient method, preconditioned by a geometric-algebraic multi-grid, while a bi-conjugate gradient is used for the resolved velocity field, dissipation rate and turbulence kinetic energy, using the diagonal incomplete-LU factorization as preconditioner. The turbulence model is based on Smagorinsky (1963), where the Smagorinsky constant is equal to 0.16.
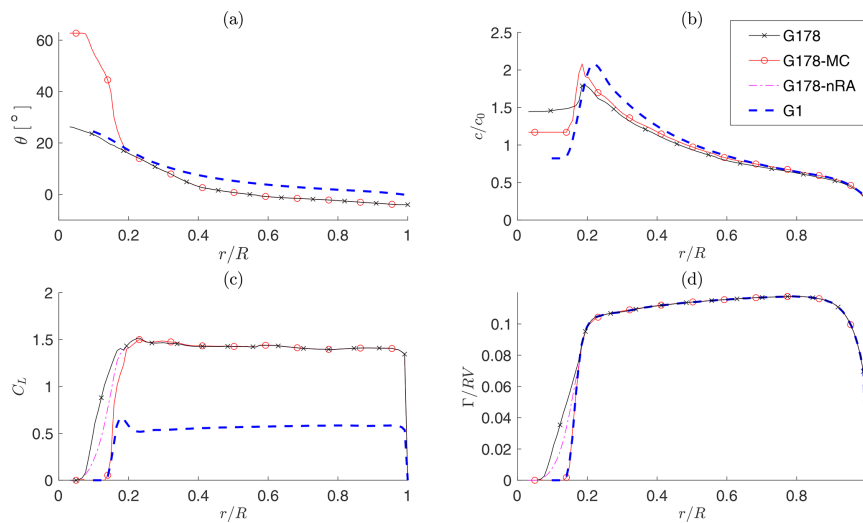
Figure 3. Distributions of twist θ **(a)**, non-dimensional chord c/c_0 **(b)**, lift coefficient C_L **(c)** and non-dimensional circulation Γ/RV **(d)**, for the G1 and for the G178, G178-MC and G178-nRA full-scale turbines.

An actuator-line method (ALM) (Troldborg et al., 2007) is used to represent the effects of the blades, according to the velocity sampling approach of Churchfield et al. (2017). The implementation of the actuator lines is obtained by coupling the computational fluid dynamics (CFD) solver with the aeroservoelastic simulator FAST 8 (Jonkman and Jonkman, 2018). For improved accuracy, the airfoil polars of the G1 are tuned based on experimental operational data (Bottasso et al., 2014b; Wang et al., 2020a). The rotor speed is set to a constant value to precisely match the desired TSR (Wang et al., 2018). Finally, the immersed boundary (IB) formulation method (Mittal and Iaccarino, 2005; Jasak and Rigler, 2014) is employed to model the effects of the turbine nacelle and tower.

Details on the mesh and other algorithmic settings are described in the following sections.

4.2 Turbulent inflow

Experiments with the G1 turbine took place in the large boundary layer test section of the wind tunnel at the Politecnico di Milano, where a turbulent flow is generated passively by the use of spires. Without the spires, the flow at the inlet has a turbulence intensity (TI) of about 1 %–2 % and a small horizontal variability caused by the presence of 14 fans and internal transects upstream of the chamber. The non-uniform blockage caused by the spires decelerates the flow close to the wind tunnel floor, generating an initial vertical shear; furthermore, large vortical structures develop around the edges of the spires, which then break down as the flow evolves moving downstream.

Two setups are considered, with two different TI levels. To mimic a typical medium-turbulence offshore condition, 14 type-B spires were placed side by side 1 m from each other, 1 m downstream of the test chamber inlet. A type-B spire consists of an equilateral trapezoid and a supporting board. The height of the trapezoid is 2.0 m, while the widths of the bottom and top edges are 0.26 and 0.1 m, respectively. The developed turbulent flow where the turbine is located (19.1 m downstream of the inlet) has a vertical shear with a power coefficient equal to 0.12, a small horizontal shear, and hub-height speed and TI of 5.75 m s^{-1} and 5 %, respectively. A second higher-turbulence inflow was generated using nine triangular spires with a height of 2.5 m and a base of 0.8 m, placed at a distance of 1.55 m from each other. In addition, 24 rows of $0.23 \times 0.23 \times 0.1$ m bricks were placed on the ground, with 12 bricks in odd rows and 13 bricks in even ones, resulting in a staggered brick distribution. This second configuration resulted in a vertical shear with a power coefficient equal to 0.19, a small horizontal shear, and hub-height speed and TI of 5.75 m s^{-1} and 14 %, respectively.

The simulations were conducted in two phases: first, developed turbulent flows were obtained by simulating the interaction of the chamber inlet wind with the spires and bricks; next, the results of these precursor simulations were sampled on a plane 3.59 D upstream of the rotor disk and used as inlet for the simulations of the turbine and its wake. For the turbulence-generating precursor simulations, the mesh was obtained with Ansys ICEM, which resulted in a structured body-conforming grid around the spires (Wang et al., 2019), entirely consisting of hexahedral elements. The bricks placed on the floor for the higher turbulence case were modeled by the IB method. All simulations included the floor, side walls and the ceiling of the tunnel. Boundary layers on these surfaces were modeled by wall functions with an average y^+ value of 50, achieved with local mesh refinement. The

chamber cross section has a width of 13.84 m and a height of 3.84 m, resulting in some vertical blockage, whose effects were quantified by running various simulations for increasing values of the chamber height, as reported later.

The grid for the wind turbine simulations uses three zones of increasing density, as shown in Fig. 4, with the smallest cells having a size of 0.015 m (i.e., $1.4 \times 10^{-2} D$). The ALM discretization used 108 points over the blade span, i.e., a spacing equal to $4.7 \times 10^{-3} D$. The simulations were run for 360 rotor revolutions, which were enough for reaching a turbulent steady-state regime.

For the full-scale machine, each inflow was scaled in space and time, as previously explained, resulting in flows with the same identical characteristics at the two scales. Similarly, the same LES and ALM grids were geometrically upscaled and used for the full-scale simulations; this means that also the full-scale simulations have the same slight anisotropic blockage effects of the wind tunnel case.

Figure 5 shows the streamwise velocity $\overline{u}/u_0$, where $\overline{(\cdot)}$ indicates a time-averaged quantity and u_0 the time-constant hub-height wind speed, at the chamber cross section $3.59 D$ in front of the rotor. Figure 5a and c report the results of an experimental mapping of the flow performed with triple hot-wire probes, while Fig. 5b and d report the numerical results; Fig. 5a and b correspond to the medium turbulence case, while Fig. 5c and d correspond to high turbulence. Notice that measurements are available only $0.18 D$ above the floor. A good match between experimental measurements and simulation results can be observed over the whole cross section of the test chamber, including not only the vertical shear but also the slight horizontal non-uniformities. These are made even more clear by Fig. 6, which reports the Reynolds shear stress component $\overline{u'v'}/u_0^2$, where the prime here indicates a fluctuation with respect to the mean.

For the same plane, Fig. 7a shows the mean (i.e., time-averaged) speed profile along a vertical line directly in front of the rotor center, while Fig. 7b reports the TI profile on the same line. Here again, a good match between experimental measurements and simulations can be observed, except in the immediate proximity of the floor.

5 Results

5.1 Code to experiment verification

First, experimental measurements obtained with the G1 are compared with the corresponding numerical simulations. Two operating conditions in the partial load regime (region II) are considered: one aligned with the flow and one with a misalignment angle γ equal to 20°. Table 1 reports the experimental and simulated power and thrust coefficients in the two cases, in medium-TI conditions. Notice that the power coefficient of the G1 is lower than the one of the G178. Using BEM, this difference can be fully explained by the

Table 1. Experimental and simulated power and thrust coefficients for the G1 turbine, in the medium-TI case.

Coefficient	C_P		C_T	
Case	Experiment	Simulation	Experiment	Simulation
$\gamma = 0°$	0.416	0.420	0.881	0.851
$\gamma = 20°$	0.364	0.358	0.810	0.742

lower efficiency of the airfoils of the scaled blade (see Fig. 2), since TSR and circulation are matched.

Figure 8 shows hub-height time-average horizontal profiles of the streamwise velocity and of turbulence intensity (Wang et al., 2019). In the experiments, wake data were measured with triple hot-wire probes at a sampling frequency of 2000 Hz for a duration of 40 s, which corresponds to almost 1 h at full scale. Results are reported for the aligned case at various downstream distances, for both the medium (Fig. 8a) and high (Fig. 8b) TI cases. The downstream distances are different for the two TI cases, because the datasets were obtained in previously performed unrelated experiments. While the match of the wake profile is excellent for all locations, the numerical results slightly overestimate turbulence intensity in the center of the near-wake region. Overall, simulation and experimental results are in very good agreement.

5.2 Scaled to full-scale comparisons

Next, having established a good correspondence between the numerical results and experimental measurements, simulations were conducted with the full-scale turbines to understand the effects of mismatched quantities.

Table 2 shows the turbine power and thrust coefficients for the different cases, considering the G1 and the three G178 turbine models. As expected, the power coefficient of the G1 turbine is lower than the one of all full-scale G178s, because of the reduced efficiency caused by the lower Reynolds number regime. On the other hand, there is a good match of the thrust coefficient, especially for G178; the nRA and MC versions produce a slightly lower lift in the inboard section of the blade and hence have a marginally lower C_T.

Figure 9 gives a qualitative overview of the wakes of the G1 and G178 turbines for the aligned and misaligned cases. The wake deficits are similar, except for the central region of the near wake, as expected. Even this qualitative view shows a significant effect of the much larger nacelle of the G1. This difference however disappears moving downstream, and the far wakes of two turbines appear to be almost identical.

A more quantitative characterization of the differences between the scaled G1 model and the realistic full-scale G178 turbine is given by Fig. 10 (medium TI) and Fig. 11 (high TI), considering the misaligned case. For both figures, panel a shows the mean speed in the longitudinal direction, while panels b and c show the Reynolds stress components $\overline{u'u'}/u_0^2$ and $\overline{u'v'}/u_0^2$, respectively.
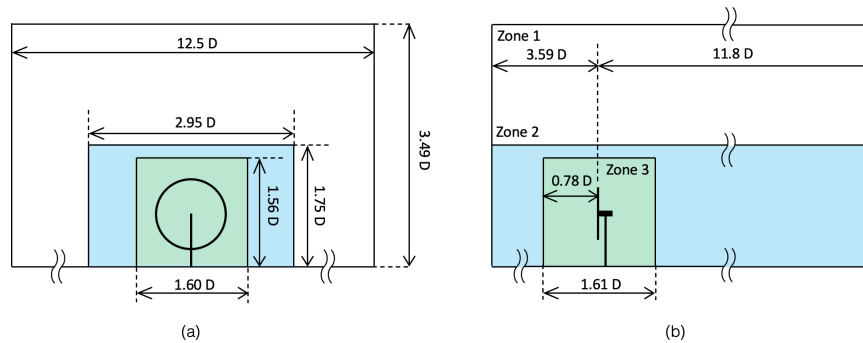
Figure 4. Frontal **(a)** and lateral **(b)** views of the computational domain and refinement zones used for the wind turbine simulations. Precursor simulations were used to generate turbulent inlet conditions at a plane $3.59\,D$ upstream of the rotor disk. The cell size in the three zones is 0.055, 0.027 and $0.014\,D$, respectively.
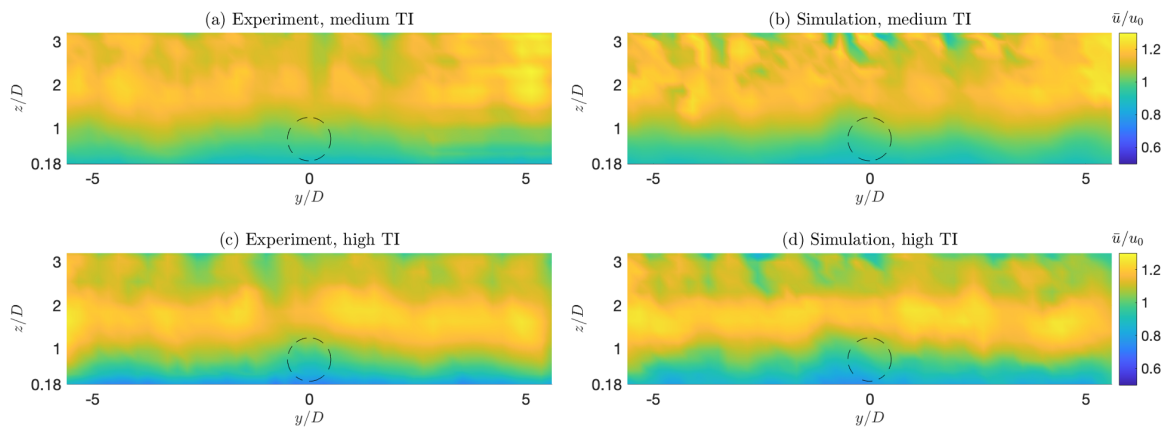

Figure 5. Streamwise velocity distribution on a cross section of the test chamber $3.59\,D$ in front of the rotor. **(a, c)** Experimental measurements; **(b, d)** numerical simulations; **(a, b)** medium-TI case; **(c, d)** high-TI case.

Results indicate an excellent match between the scaled and full-scale wakes, for both TI levels. Some differences only appear in the peaks of $\overline{u'u'}/u_0^2$ immediately downstream of the rotor. However, the velocity profiles are remarkably similar already at $3\,D$, notwithstanding the differences around the hub and the blade inboard sections between the two machines. Similar conclusions are obtained for the aligned case.

5.3 Effects of unmatched inboard circulation and rotational augmentation

The effects of unmatched inboard circulation and rotational augmentation are quantified by computing the differences in $\overline{u}/u_0$, $\overline{u'u'}/u_0^2$ or $\overline{u'v'}/u_0^2$ at various downstream locations. Results are shown in Fig. 12, where differences are computed subtracting the G178 solution from the G178-MC or G178-nRA ones. As indicated by the figure, these effects are extremely small and possibly discernible from numerical noise only in the immediate proximity of the rotor.

5.4 Effect of nacelle size and unmatched C_P on swirl

For the wind-aligned operating condition, Fig. 13 shows the delta wake velocity deficit obtained by subtracting the G178-MC from the G1 solution, looking upstream. Figure 13a represents the near wake $1\,D$ immediately behind the rotor disk plane, while Fig. 13b reports the far wake at $8\,D$. The color field represents the difference in the non-dimensional streamwise velocity deficit component $\Delta(\overline{u} - u_0)/u_0$, whereas the arrows represent differences in the in-plane velocity vectors.

In this case, since the non-dimensional circulation is matched, there are only two factors that could result in nonzero difference fields: the larger relative frontal area of the nacelle (and, similarly, of the tower) of the G1 and its smaller power coefficient caused by the chord-based Reynolds number mismatch. The impacts of these two factors are clearly visible in the near wake, respectively looking at the streamwise and in-plane velocities.

Considering first the streamwise component, the larger blockage of the G1 nacelle creates the negative velocity bubble that is clearly visible at the center of the rotor, which indi-
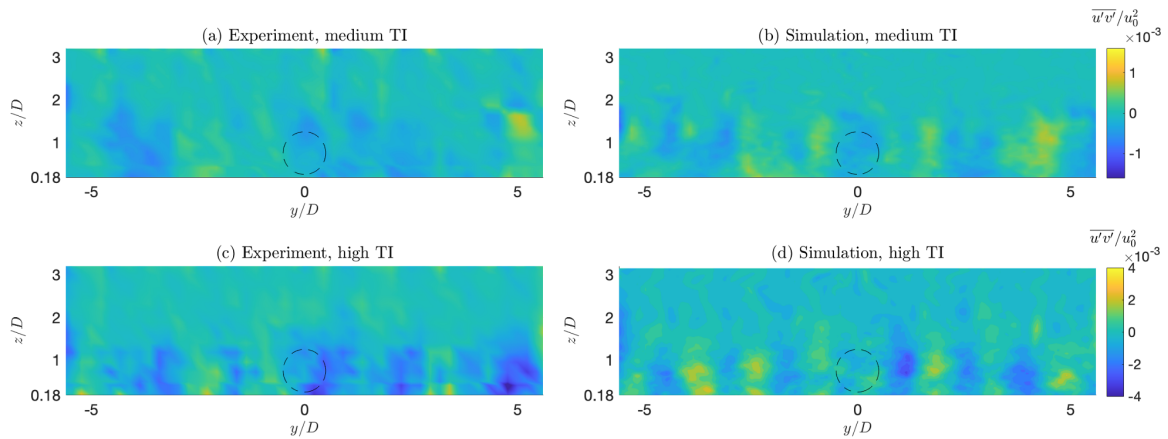
Figure 6. Shear stress distribution on a cross section of the test chamber $3.59\,D$ in front of the rotor. **(a, c)** Experimental measurements; **(b, d)** numerical simulations; **(a, b)** medium-TI case; **(c, d)** high-TI case.
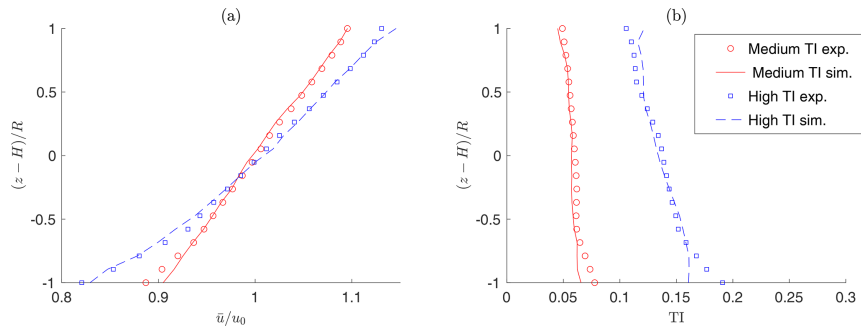
Figure 7. Mean velocity **(a)** and turbulence intensity **(b)** distributions along a vertical line $3.59\,D$ in front of the rotor.

cates a larger deficit behind the G1 than behind the G178-MC in this part of the wake.

The effect of the tower is different from the one of the nacelle and leads to a positive streamwise speed difference instead of a negative one. In fact, while the nacelle is almost a pure blockage in the center of the rotor where wake recovery is the weakest, the presence of the tower wake increases the local turbulence intensity, with the effect of increasing the recovery of the turbine wake. This results in the vertical region of higher streamwise speed that can be seen in the figure in the lower part of the rotor disk. When looking upstream, the rotor spins counterclockwise, whereas the wake rotates clockwise by the principle of action and reaction, and this explains why the region affected by the tower wake is convected towards the negative y direction.

Consider next the in-plane velocities. Compared to the wake of the G178-MC turbine, the wake of the G1 rotates at a slower pace, as indicated by the counterclockwise rotation of the difference field shown in the picture. The slower rotation of the G1 wake is a direct consequence of its smaller power coefficient that, for the same TSR, implies also a reduced torque coefficient. As expected, the mismatch in the

swirl rotation is only concentrated close to the hub and decays quickly with radial position.

As the flow propagates downstream and the wake progressively recovers, differences between the velocity fields decay, and the effects of the mismatches can hardly be seen at $8\,D$. The only difference that can still be appreciated is the effect of the larger tower. This results in some blockage close to the ground that has not yet fully recovered at this distance, resulting in about a 6 % difference in the longitudinal velocity component immediately above the floor and, hence, in a slightly enhanced shear below hub height. Elsewhere, differences between the two fields never exceed 3 %.

5.5 Effect of wind tunnel blockage

Considering the G1 turbine, the wind tunnel test chamber has a height $h_{wt} = 3.49\,D$ and a width $w_{wt} = 12.5\,D$, resulting in a cross-sectional area $A_{wt} = 43.6\,D^2$. Although the resulting area ratio $A/A_{wt} = 0.018$ is relatively small, the non-negligible vertical ratio $D/h_{wt} = 0.286$ can cause some anisotropic blockage. To quantify this effect, numerical simulations were conducted in domains of increasing height
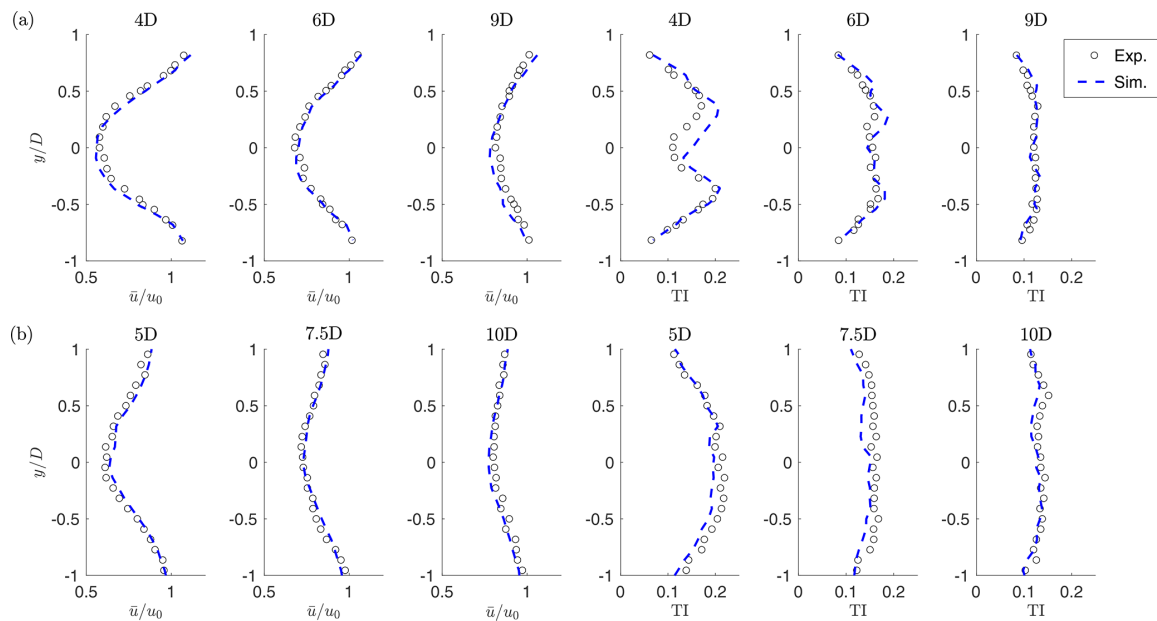
Figure 8. Horizontal hub-height profiles of normalized time-average streamwise velocity and turbulence intensity, for the medium **(a)** and high **(b)** inflow TI cases. Black *o* symbols: experimental results; blue dashed line: G1 simulations.

Table 2. Power and thrust coefficients for the different turbine models in the two considered operating conditions.

Coefficient	C_P				C_T			
Turbine model	G1	G178	G178-nRA	G178-MC	G1	G178	G178-nRA	G178-MC
$\gamma = 0°$	0.420	0.475	0.472	0.470	0.851	0.831	0.827	0.822
$\gamma = 20°$	0.358	0.421	0.418	0.417	0.742	0.731	0.727	0.723

from $1.75\,D$ to $10.47\,D$, as shown in Fig. 14a. The actual wind tunnel height is indicated by a red square mark in the figure.

Figure 14b shows the non-dimensional power increase $\Delta P / P_\infty$ vs. the area ratio A / A_{wt}, where P_∞ is the power for the largest domain – assumed to be blockage-free. Results indicate a power increase caused by blockage of about 1.5 %.

5.6 Wind farm control metrics

The previous analysis has shown that the wake of the G1 turbine has a very close resemblance to the one of the full-scale G178, although some differences are present in the near-wake region. However, it is difficult to appreciate the actual relevance of these differences, and a more practical quantification of the accuracy of the match would be desirable. The G1 turbine is mostly used for studying wake interactions within clusters of turbines and for testing mitigating control strategies. This suggests the use of wind-farm-control-inspired metrics for judging the differences between the scaled and full-scale machines.

The first metric considered here is the available power ratio downstream of the turbine, noted $P_a(x/D)/P_0 = \widehat{u}^3(x/D)/u_0^3$, where P_0 is the power output of the turbine, and $\widehat{u}(x/D)$ is the rotor-effective wind speed at the downstream location x/D. The available power ratio depends on the shape of the wake, its recovery and trajectory. This quantity was computed from the longitudinal flow velocity component in the wake on the area of the rotor disk at various downstream positions directly behind the wind turbine, as shown in Fig. 15.

For the 20° misaligned case, the available power ratio results are reported in Fig. 16a. As shown in the figure, the available power changes moving downstream because the wake expands, recovers and – since the turbine is misaligned with respect to the wind vector – shifts progressively more to the side of the impinged (virtual) rotors. The difference of the available power behind the G1 and G178 turbines is small and decreases quickly moving downstream. The figure also shows the effects of blockage, by reporting the results for the actual wind tunnel size using a solid line and the ones for the
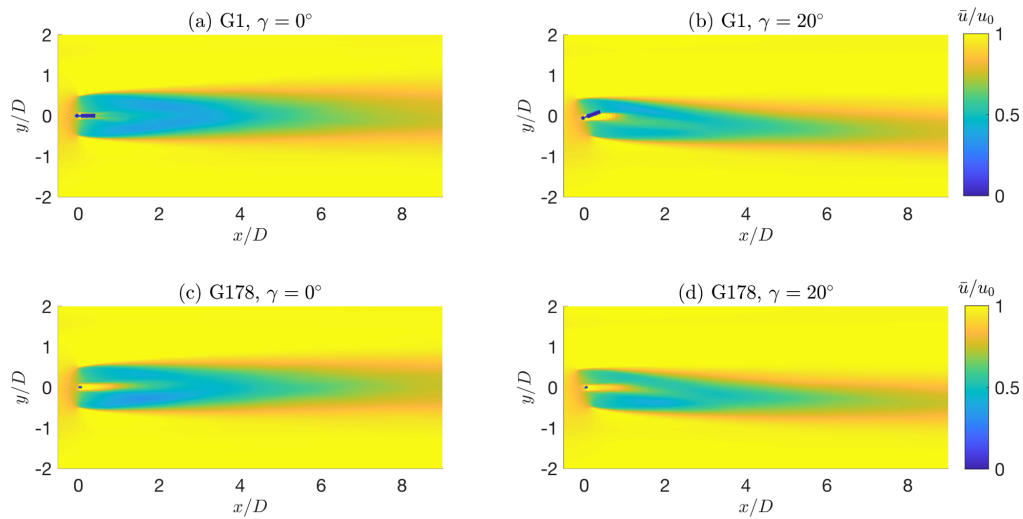
Figure 9. Wakes of the scaled G1 **(a, b)** and full-scale G178 **(c, d)** turbines. **(a, c)** Aligned case; **(b, d)** yaw misaligned case.
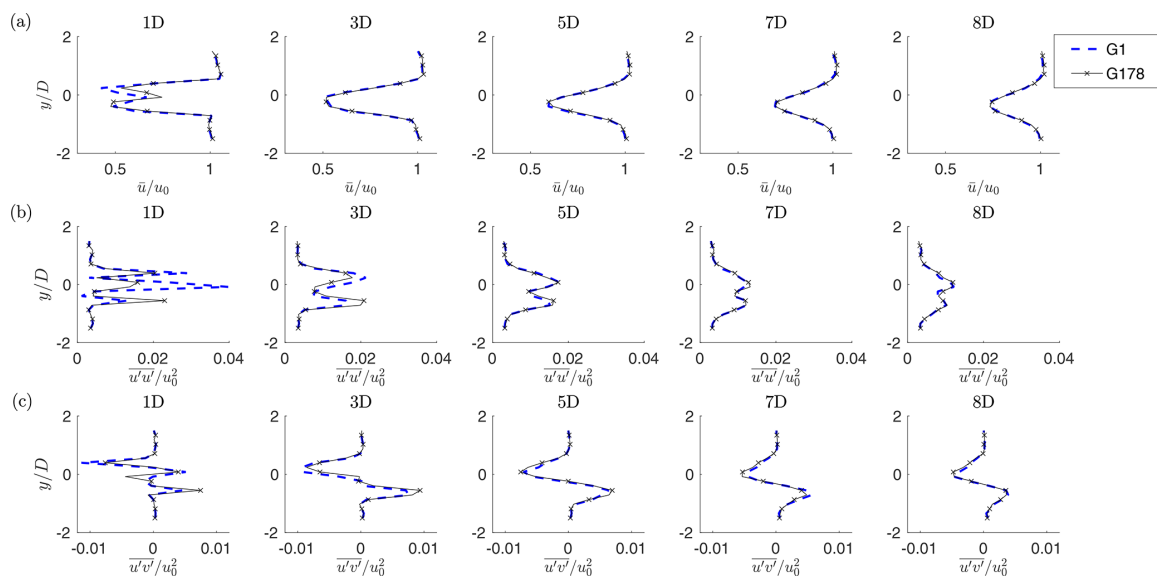
Figure 10. Hub-height profiles of normalized time-average streamwise velocity **(a)**, normal stress **(b)** and shear stress **(c)**, in the misaligned and medium-TI condition.

unrestricted case using a dashed line; here, again, this effect is very modest.

The second metric considered here is the ambient flow rotation in the immediate proximity of a deflected wake. By misaligning a wind turbine rotor with respect to the incoming flow direction, the rotor thrust force is tilted, thereby generating a cross-flow force that laterally deflects the wake. As shown with the help of numerical simulations by Fleming et al. (2018), this cross-flow force induces two counter-rotating vortices that, combining with the wake swirl induced by the rotor torque, lead to a curled wake shape. As ob-served experimentally by Wang et al. (2018), these vortices result in additional lateral flow speed components, which are not limited to the wake itself but extend also outside of it. By this phenomenon, the flow direction within and around a deflected wake is tilted with respect to the upstream undisturbed direction. Therefore, when a turbine is operating within or close to a deflected wake, its own wake undergoes a change in trajectory – termed secondary steering – induced by the locally modified wind direction.

The change in ambient wind direction $\Delta\Gamma$ caused by the curled wake is reported in Fig. 16b as a function of the down-
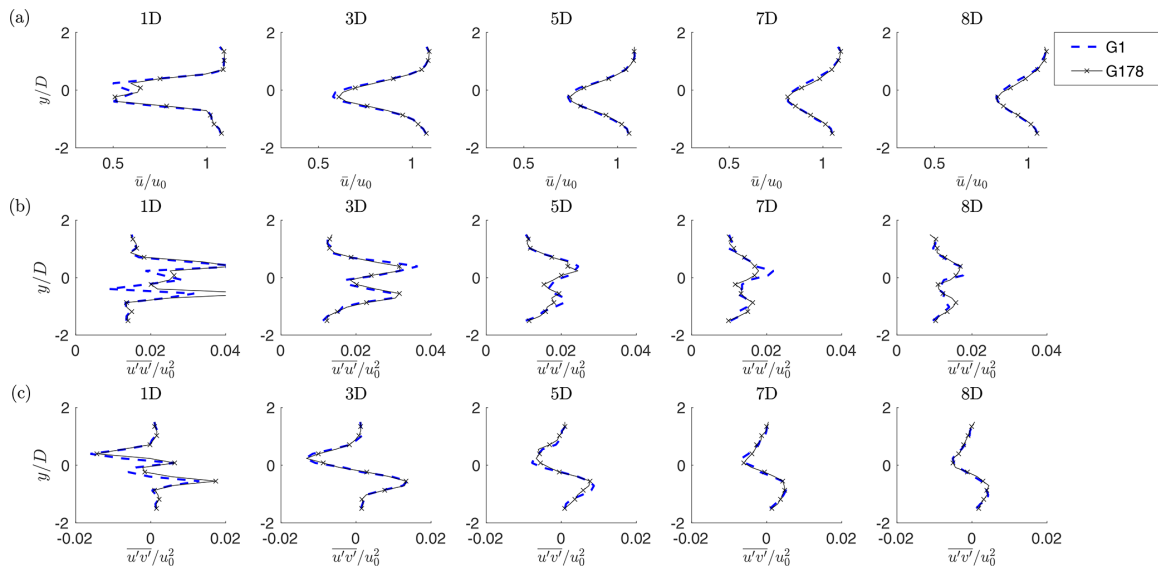
Figure 11. Hub-height profiles of normalized time-average streamwise velocity **(a)** and shear stresses **(b, c)**, in the misaligned and high-TI condition.
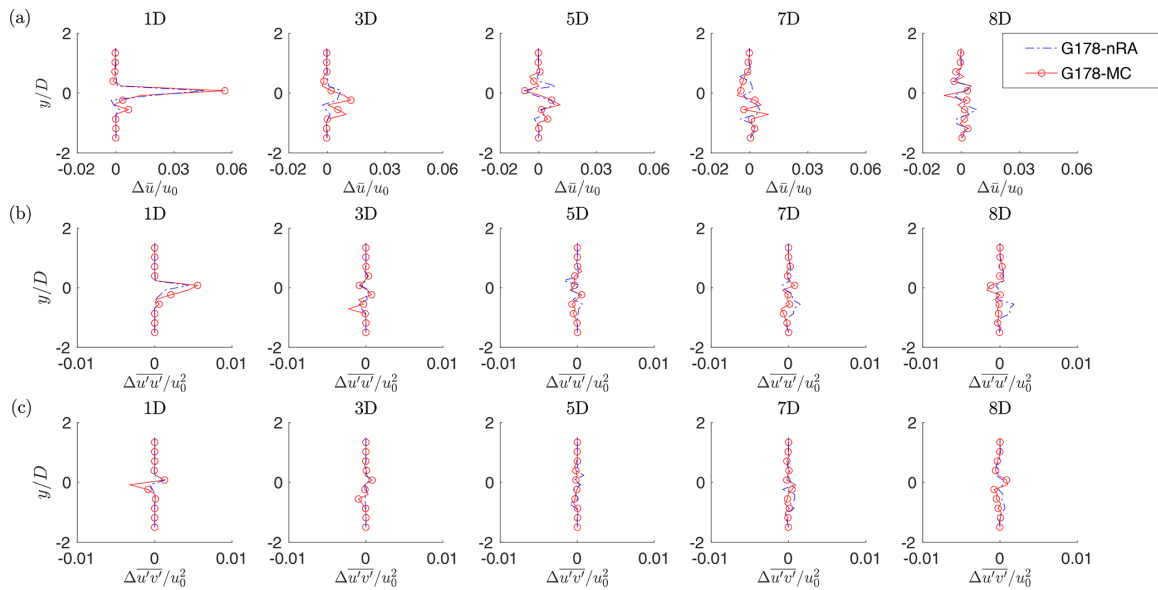
Figure 12. Difference in the profiles of the normalized time-average streamwise velocity **(a)**, normal stress **(b)** and shear stress **(c)** along hub-height horizontal lines, in yaw misaligned and medium-TI conditions. Dash-dotted blue line: effect of rotational augmentation, i.e., G178 results subtracted from G178-nRA results. Red solid line and ° symbols: effect of mismatched circulation close to the root, i.e., G178 results subtracted from G178-MC results.

stream distance x/D; even in this case, the effects of blockage can be appreciated by comparing the solid and dashed lines. The angle $\Delta\Gamma$ was computed from the wake velocity components, averaging over the rotor disk areas already used for the analysis of the available power. Here again the difference in the change in ambient wind direction behind the G1 and G178 turbines is quite small. A non-perfect match is

probably due to the slightly different strength of the central vortex generated in response to the rotor torque. On the other hand, the two counter-rotating vortices caused by the tilted thrust are well matched – given the good correspondence of this force component between the two models.
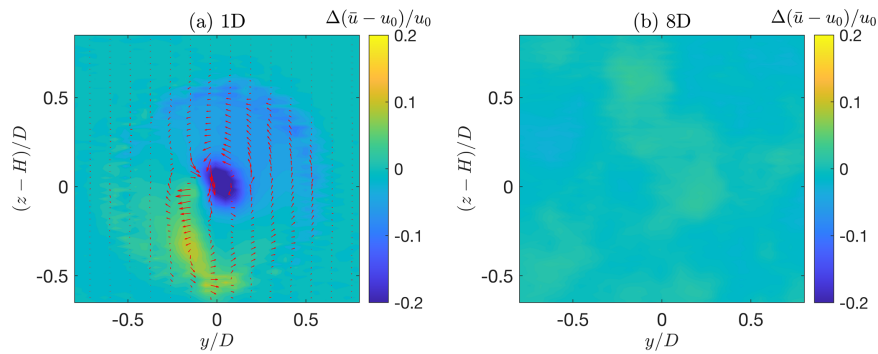
Figure 13. Difference in the wake velocity fields, obtained subtracting the G178-MC solution from the G1 one, looking upstream. Color field: streamwise velocity deficit difference $\Delta(\bar{u}-u_0)/u_0$; arrows: difference in the in-plane velocity vectors. **(a)** Near wake 1 D immediately behind the rotor disk plane. **(b)** Far wake at 8 D.
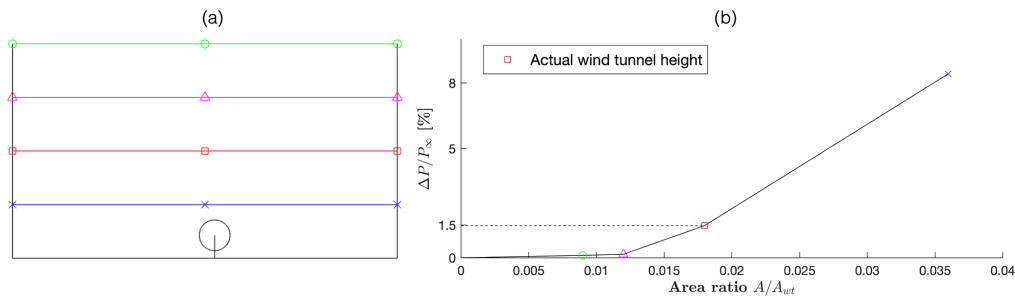
Figure 14. Wind tunnel blockage effect. **(a)** Cross-sectional areas. **(b)** Percent power increase with respect to the unrestricted flow vs. area ratio A/A_{wt}.
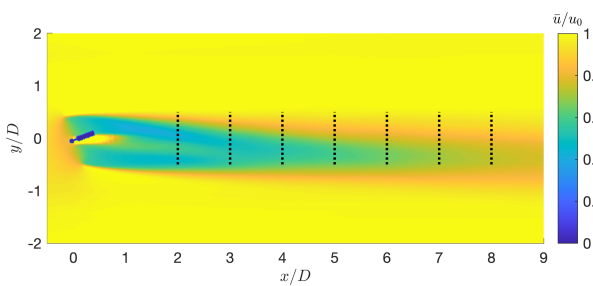
Figure 15. Wake of the G1 turbine for the yaw misaligned case. The black dashed lines indicate the locations of virtual downstream turbines.

5.7 Effect of integral length scale

The ILS of the wind tunnel flow was obtained by first computing the time autocorrelation of the wind speed at one position in front of the turbine and then multiplying the result by the mean wind speed. The length scales obtained from measurements in the wind tunnel and the simulated flow resulted in nearly identical values, as already shown by Wang et al. (2019). A second estimate of the ILS was based on the space autocorrelation between simultaneous values of the simulated wind speed at two points in front of the turbine. For the size of the G1 turbine, this second estimate of the ILS resulted in a full-scale value of approximatively 142 m. On the other hand, the IEC 61400-1 international standards prescribe space-autocorrelation-based lengths of 170 m in the second edition (IEC 61400-1, 1999) and of 340 m in the third edition (IEC 61400-1, 2005). Although the ILS presents a significant natural variability at each location and across different sites (Kelly, 2018), the value achieved in the wind tunnel with the G1 is undoubtedly in the low range of naturally occurring scales.

To understand the effects of the partially mismatched ILS on wake behavior, two turbulent inflows were generated, differing only in this parameter. However, the passive development through spires and bricks of two inflows with different ILS values, but exactly the same TI and vertical shear, is clearly an extremely difficult task. To avoid this complication, the turbulent flow field generator TurbSim (Jonkman, 2009) was used, selecting the Kaimal model and prescribing directly the turbulence scale parameter (see Eq. (23) in Jonkman, 2009). The resulting turbulent wind time histories were specified as Dirichlet inflow conditions for the subsequent LES-ALM simulations.
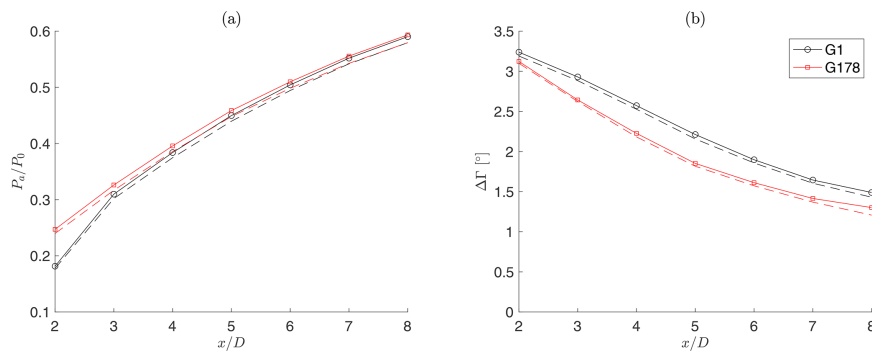
Figure 16. (a) Available power ratio in the wake P_a/P_0 as a function of downstream position x/D. **(b)** Change in wind direction $\Delta\Gamma$ caused by the curled wake as a function of downstream position x/D. Both results are for the 20° misaligned and medium-TI case. Black ° symbols: G1; red □ symbols: G178. Solid lines: actual wind tunnel size; dashed lines: unrestricted case (no blockage).
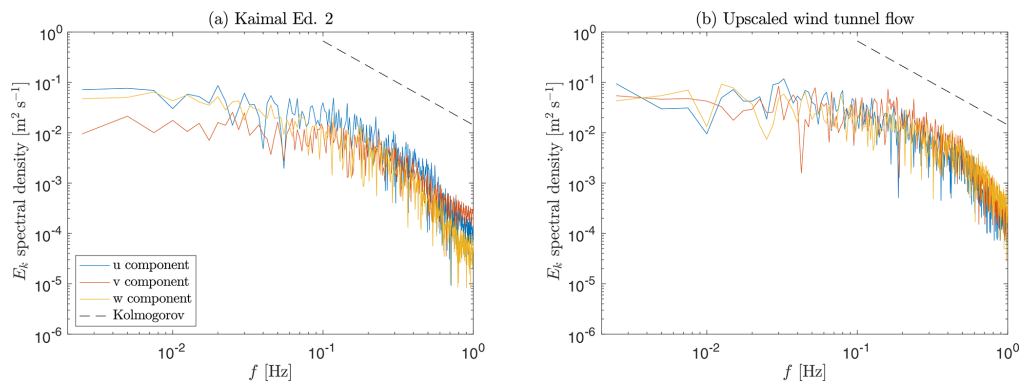
Figure 17. Spectra of turbulent kinetic energy components.

The two resulting developed CFD flows are characterized by an ILS of 176 and 335 m and have a vertical shear exponent equal to 0.18, a hub-height speed of $11.3\,\mathrm{m\,s^{-1}}$ and a TI of 6.0 %. These two different flows were used for conducting dynamic simulations with the G178 turbine in a 20° yaw misaligned condition. Figure 17 shows the spectra of the turbulence kinetic energy components, where the Kaimal second-edition result is reported in Fig. 17a, while the one of the upscaled wind tunnel flow is reported in Fig. 17b. Whereas the streamwise components are very similar, it appears that the upscaled wind tunnel flow is slightly more isotropic than the Kaimal second-edition one.

The ILS indicates the dimension of the largest coherent eddies in the flow. Hence, the main effect of a larger ILS is that of inducing a more pronounced meandering of the wake. To quantify this effect, the instantaneous wake center was computed according to the deficit-weighted center of mass method (España et al., 2011). The standard deviation of the horizontal wake position $5\,D$ downstream of the rotor was found to be equal to $0.089\,D$ for the low-ILS (176 m) case and equal to $0.12\,D$ for the high-ILS (335 m) one, according to expectations.

The effects of a different ILS are much smaller, although still appreciable, when considering mean quantities. Figure 18 reports the profiles of speed and shear stresses at different downstream distances. The mean velocity profile is only very slightly affected, with a maximum change of about only 2 %. A clearer effect is noticeable in the shear stresses at the periphery of the wake.

6 Discussion and conclusions

This paper has analyzed the realism of wind-tunnel-generated wakes with respect to the full-scale case. In the absence of comparable scaled and full-scale experimental measurements, a hybrid experimental-simulation approach was used here for this purpose. A LES-ALM code was first verified with respect to detailed measurements performed in a large boundary layer wind tunnel with the TUM G1 scaled wind turbine. Next, the same code – with the same exact algorithmic settings – was used to simulate different full-scale versions of the scaled turbine. These different full-scale models were designed to highlight the effects of mismatched quantities between the two scales. Clearly, this approach has
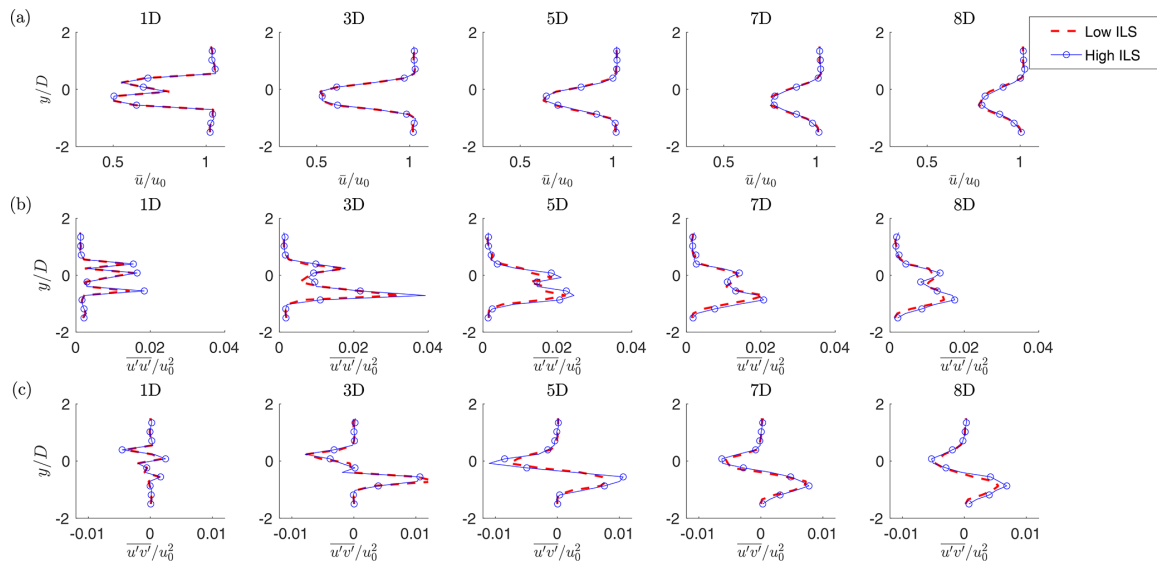
Figure 18. Hub-height profiles of normalized time-average streamwise velocity **(a)** and shear stresses **(b, c)**, for the low- and high-ILS cases in yaw misaligned conditions.

some limits and therefore falls short of providing a comprehensive answer to the realism question. In fact, the comparison is clearly blind to any physical process that is not modeled or that is not accurately resolved by the numerical simulations. Additionally, it is assumed that a numerical model that provides good quality results with respect to reality at the small scale is also capable of delivering accurate answers at the full scale.

Keeping in mind these limits, the following conclusions can be drawn from the present study.

– Overall, the far (above approximatively $4\,D$) wake of the G1 scaled wind turbine is extremely similar to the wake of a corresponding full-scale machine considering all classical mean metrics, i.e., wake deficit, turbulence intensity, shear stresses, wake shape and path, both in aligned and misaligned conditions.

– Small differences of fractions of a degree are present in the local wind direction changes caused by the curled wake, because of a different swirl generated by the smaller aerodynamic torque of the scaled model. The trends in terms of downstream distance and yaw misalignments (not shown here) are however extremely similar.

– The effects of blockage are very limited in the large wind tunnel of the Politecnico di Milano, with differences in power of about 1.5 % and negligible effects on other metrics.

– The effects of rotational augmentation, unmatched inboard non-dimensional circulation and nacelle size are

clearly visible in the inner near-wake region. However, they decay quickly with downstream distance and are typically small enough not to alter the qualitative shape of the speed deficit, turbulence intensity and shear stress distributions in this region of the wake.

– The lower ILS of the flow generated in the wind tunnel at the scale of the G1 has very modest effects on mean wake metrics, although it causes a reduced meandering.

In summary, it appears that the G1 scaled turbine faithfully represents not only the far-wake behavior, but also produces a very realistic near wake. This is obtained by a design of the experimental setup that matches the turbulent inflow, the geometry and strength of the helical tip vortices, and the strength and shape of the speed deficit. These are all the main physical effects dictating the evolution of the near wake. The mismatches that are present in the near-wake inner core (due to a different swirl, inboard non-dimensional circulation, rotational augmentation and a different geometry of the nacelle) do leave a visible mark but overall do not seem to significantly alter the behavior of the wake, as expected. The larger size of the tower leaves a more visible trace further downstream, because it affects the wake recovery by generating a local extra turbulence intensity, in turn altering shear below hub height.

Overall, the realism of both the near and far wake justifies the use of the TUM G1 (and similarly designed) scaled turbines for the study of wake physics and applications in wind farm control and wake mixing.

How would these result change in case of smaller or larger scaled models? For larger models, one would still be able to match all quantities that are matched for the G1, while

improving some of the unmatched quantities described in Sect. 2.3. The out-of-scale nacelle and tower of the G1 are due to miniaturization constraints of the sensors and actuators (Bottasso and Campagnolo, 2021), a problem that would be alleviated with larger models, resulting in a reduced mismatch of the vortex shedding frequency. Similarly, larger blades would reduce the mismatch of the rotation-induced stall delay and of the chord-based Reynolds number. This would lead to a better match of the power coefficient and to improvements of some of the approximately matched quantities, such as the dynamic spanwise vortex shedding and the thrust coefficient. On the other hand, for a same wind tunnel, testing a larger model might increase blockage and the ILS mismatch. Essentially the opposite would happen for smaller models. A large chord-based Reynolds mismatch could be mitigated by increasing the rotor angular velocity, which however leads to higher power and a larger nacelle, and is eventually constrained by compressibility and by the wind tunnel speed through the TSR constraint. Additionally, one may increase solidity, although this moves the optimal TSR away from the reference (Bastankhah and Porté-Agel, 2017; Bottasso and Campagnolo, 2021). Even with very small rotors (Hassanzadeh et al., 2016), it is conceptually possible to match the non-dimensional circulation and thrust coefficient, while only the latter can be matched using porous disks (Xiao et al., 2013; Lignarolo et al., 2016).

The experimental setup used in this study can be further improved, for an even increased realism and expanded capabilities. Regarding the inflow, several facilities have been recently designed or upgraded to generate unstable boundary layers (Chamorro and Porté-Agel, 2010), tornadoes and downbursts (WindEEE, 2020), or for the active generation of turbulent flows (Kröger et al., 2018). Regarding the models, a more realistic geometry and size of the nacelle and tower can be achieved at the price of a further miniaturization. Aeroelastic effects can be included by using ad hoc scaling laws (Canet et al., 2021) to design flexible model rotor blades (Bottasso et al., 2014a; Campagnolo et al., 2014). Advances in 3D printing and component miniaturization will certainly lead to advancements in the design of ever more sophisticated and instrumented models. Regarding measurement technology, a more detailed characterization of salient features of the flow can be obtained by PIV or lidars, for example in support of the study of dynamic stall, vortex and stall-induced vibrations.

Although advancements in the testing of scaled wind turbines come with significant design, manufacturing, measurement and operational challenges, wind tunnel testing remains an extremely useful source of information for scientific discovery, the validation of numerical models and the testing of new ideas. A quantification of the realism of such scaled models is therefore a necessary step in the acceptance of the results that they generate.

References

Abkara, M., and Porté-Agel, F.: Influence of atmospheric stability on wind-turbine wakes: A large-eddy simulation study, Phys. Fluids, 27, 035104 https://doi.org/10.1063/1.4913695, 2015.

ANSYS: Fluent 2019, available at: https://www.ansys.com/products/fluids/ansys-fluent, last access: 18 December 2019.

Bak, C., Zahle, F., Bitsche, R., Kim, T., Yde, A., Henriksen, L. C., Natarajan, A. and Hansen, M.: Description of the DTU 10 MW reference wind turbine, DTU Wind Energy Report-I-0092 5, DTU Wind Energy, Town Kongens, Lyngby, Denmark, 2013.

Bartl, J. and Sætran, L. R: Experimental testing of axial induction based control strategies for wake control and wind farm optimization, J. Phys.: Conf. Ser., 753, 032035, https://doi.org/10.1088/1742-6596/753/3/032035, 2016.

Bastankhah, M. and Porté-Agel, F.: Experimental and theoretical study of wind turbine wakes in yawed conditions, J. Fluid Mech., 806, 506–541, https://doi.org/10.1017/jfm.2016.595, 2016.

Bastankhah, M. and Porté-Agel, F.: A new miniature wind turbine for wind tunnel experiments. Part I: Design and performance, Energies, 10, 908, https://doi.org/10.3390/en10070908, 2017.

Bisplinghoff, R. L. and Ashley, H.: Principles of Aeroelasticity, Dover Publications, Mineola, New York, USA, 2002.

Bottasso, C. L. and Campagnolo, F.: Wind Tunnel Testing of Wind Turbines and Farms, in: Handbook of Wind Energy Aerodynamics, edited by: Stoevesandt, B., Schepers, G., Fuglsang, P., and Yuping, S., Springer, Cham, https://doi.org/10.1007/978-3-030-05455-7_54-1, 2021.

Bottasso, C. L., Campagnolo, F. and Petrović, V.: Wind tunnel testing of scaled wind turbine models: Beyond aerodynamics, J. Wind Eng. Indust. Aerodynam., 127, 11–28, https://doi.org/10.1016/j.jweia.2014.01.009, 2014a.

Bottasso, C. L., Cacciola, S. and Iriarte, X.: Calibration of wind turbine lifting line models from rotor loads, Wind Eng. Indust. Aerodyam., 124, 29–45, https://doi.org/10.1016/j.jweia.2013.11.003, 2014b.

Burton, T., Jenkins, N., Sharpe, D., and Bossanyi, E.: Wind energy handbook, John Wiley & Sons, West Sussex, UK, 2011.

Campagnolo, F.: Wind tunnel testing of scaled wind turbine models: aerodynamics and beyond, PhD Thesis, Politecnico di Milano, Milano, 2013.

Campagnolo, F., Bottasso, C. L., and Bettini, P.: Design, manufacturing and characterization of aero-elastically scaled wind turbine blades for testing active and passive load alleviation techniques within an ABL wind tunnel, J. Phys.: Conf. Ser., 524, 012061, https://doi.org/10.1088/1742-6596/524/1/012061, 2014.

Campagnolo, F., Petrović, V., Schreiber, J., Nanos, E. M., Croce, A., and Bottasso, C. L.: Wind tunnel testing of a closed-loop wake deflection controller for wind farm power maximization, J. Phys.: Conf. Ser., 753, 032006, https://doi.org/10.1088/1742-6596/753/3/032006, 2016.

Campagnolo, F., Weber, R., Schreiber, J., and Bottasso, C. L.: Wind tunnel testing of wake steering with dynamic wind direction changes, Wind Energ. Sci., 5, 1273–1295, https://doi.org/10.5194/wes-5-1273-2020, 2020.

Canet, H., Bortolotti, P., and Bottasso, C. L.: On the scaling of wind turbine rotors, Wind Energ. Sci., 6, 601–626, https://doi.org/10.5194/wes-6-601-2021, 2021.

Chamorro, L. P. and Porté-Agel, F.: A wind-tunnel investigation of wind-turbine wakes: boundary-layer turbulence effects, Bound.-Lay. Meteorol., 132, 129–149, https://doi.org/10.1007/s10546-009-9380-8, 2009.

Chamorro, L. P. and Porté-Agel, F.: Effects of thermal stability and incoming boundary-layer flow characteristics on wind-turbine wakes: a wind-tunnel study, Bound.-Lay. Meteorol., 136, 515–533, https://doi.org/10.1007/s10546-010-9512-1, 2010.

Chamorro, L. P., Arndt, R. E. A., and Sotiropoulos, F.: Reynolds number dependence of turbulence statistics in the wake of wind turbines, Wind Energy, 15, 733–742, https://doi.org/10.1002/we.501, 2012.

Chen, T. Y. and Liou, L. R.: Blockage corrections in wind tunnel tests of small horizontal-axis wind turbines, Exp. Therm. Fluid Sci., 35, 565–569, https://doi.org/10.1016/j.expthermflusci.2010.12.005, 2011.

Churchfield, M. J., Schreck, S., Martínez-Tossas, L. A., Meneveau, C., and Spalart, P. R.: An advanced actuator line method for wind energy applications and beyond, in: 35th Wind Energy Symposium, 9–13 January 2017, Grapevine, Texas, USA, p. 1998, 2017.

Dowler J. L. and Schmitz, S.: A solution-based stall delay model for horizontal-axis wind turbines, Wind Energy, 18, 1793–1813, https://doi.org/10.1002/we.1791, 2015.

España, G., Aubrun, S., Loyer, S., and Devinant, P.: Spatial study of the wake meandering using modelled wind turbines in a wind tunnel, Wind Energy, 14, 923–937, https://doi.org/10.1002/we.515, 2011.

Fleming, P., Annoni, J., Churchfield, M., Martínez-Tossas, L. A., Gruchalla, K., Lawson, M., and Moriarty, P.: A simulation study demonstrating the importance of large-scale trailing vortices in wake steering, Wind Energ. Sci., 3, 243–255, https://doi.org/10.5194/wes-3-243-2018, 2018.

Fleming, P. A., Pieter, M. O., Lee, S., Wingerden, J., Johnson, K., Churchfield, M., Michalakes, J., Spalart, P., and Moriarty, P.: Evaluating techniques for redirecting turbine wakes using SOWFA, Renew. Energy, 70, 211–218, https://doi.org/10.1016/j.renene.2014.02.015, 2014.

Frederik, J. A., Weber, R., Cacciola, S., Campagnolo, F., Croce, A., Bottasso, C. L., and van Wingerden, J. W.: Periodic dynamic induction control of wind farms: proving the potential in simulations and wind tunnel experiments, Wind Energ. Sci., 5, 245–257, https://doi.org/10.5194/wes-5-245-2020, 2020a.

Frederik, J. A., Doekemeijer, B. M., Mulders, S. P., and van Wingerden, J. W.: The helix approach: Using dynamic individual pitch control to enhance wake mixing in wind farms, Wind Energy, 23, 1739–1751, https://doi.org/10.1002/we.2513, 2020b.

Fuglsang, P., Antoniou, I., Dahl, K. S., and Aagaard Madsen, H.: Wind tunnel tests of the FFA-W3-241, FFA-W3-301 and NACA 63-430 airfoils, Risoe-R No. 1041(EN), Forskningscenter Risoe, Risoe, 1998.

Hassanzadeh, A., Naughton, J., Kelley, C. L., and Maniaci, D. C.: Wind turbine blade design for subscale testing, J. Phys.: Conf. Ser., 753, 022048, https://doi.org/10.1088/1742-6596/753/2/022048, 2016.

IEC 61400-1: Wind turbine generator systems – Part 1: Safety requirements, 2nd Edn., International Electrotechnical Commission, Geneva, Switzerland, 1999.

IEC 61400-1: Wind turbines – Part 1: Design requirements, 3rd Edn., International Electrotechnical Commission, Geneva, Switzerland, August 2005.

Jasak, H.: OpenFOAM: open source CFD in research and industry, Int. J. Nav. Arch. Ocean, 1, 89–94, https://doi.org/10.2478/IJNAOE-2013-0011, 2009.

Jasak, H. and Rigler, D.: Finite volume immersed boundary method for turbulent flow simulations, in: 9th OpenFOAM Workshop, 23–26 June 2014, Zagreb, Hrvatska, 2014.

Jasak, H., Weller, H., and Gosman, A.: High resolution NVD differencing scheme for arbitrarily unstructured meshes, Int. J. Numer. Meth. Fluids, 31, 431–449, https://doi.org/10.1002/(SICI)1097-0363(19990930)31:2<431::AID-FLD884>3.0.CO;2-T, 1999.

Jonkman, B. J.: TurbSim User's Guide: Version 1.50, Technical Report NREL/TP-500-46198, available at: https://www.nrel.gov/docs/fy09osti/46198.pdf (last access: 7 June 2021), September 2009.

Jonkman, J. and Jonkman, B. J.: FAST 8, available at: https://www.nrel.gov/wind/nwtc/fastv8.html (last access: 7 June 2021), 2018.

Kelly, M.: From standard wind measurements to spectral characterization: turbulence length scale and distribution, Wind Energ. Sci., 3, 533–543, https://doi.org/10.5194/wes-3-533-2018, 2018.

Kröger, L., Frederik, J., van Wingerden, J.-W., Peinke, J., and Hölling, M.: Generation of user defined turbulent inflow conditions by an active grid for validation experiments, J. Phys.: Conf. Ser., 1037, 052002, https://doi.org/10.1088/1742-6596/1037/5/052002, 2018.

Lignarolo, L. E. M., Ragni, D., Ferreira, C. J., and Van Bussel, G. J. W.: Experimental comparison of a wind-turbine and of an actuator-disc near wake, J. Renew. Sustain. Energ., 8, 023301, https://doi.org/10.1063/1.4941926, 2016.

Lissaman, P. B. S.: Low-Reynolds-number airfoils, Annu. Rev. Fluid Mech., 15, 223–239, https://doi.org/10.1146/annurev.fl.15.010183.001255, 1983.

Lyon, C. and Selig, M. S.: Summary of low speed airfoil data, Soartech Publications, Virginia, USA, 1997.

Martínez-Tossas, L. A., Churchfield, M. J. and Leonardi, S.: Large eddy simulations of the flow past wind turbines: actuator line and disk modeling, Wind Energy, 18, 1047–1060, https://doi.org/10.1002/we.1747, 2015.

Meinhart, C. D., Wereley, S. T., and Santiago, J. G.: PIV measurements of a microchannel flow, Exp. Fluids., 27, 414–419, https://doi.org/10.1007/s003480050366, 1999.

Mittal, R. and Iaccarino, G.: Immersed boundary methods, Annu. Rev. Fluid Mech., 37, 239–261, https://doi.org/10.1146/annurev.fluid.37.061903.175743, 2005.

Okulov, V. L. and Sørensen, J. N.: Stability of helical tip vortices in a rotor far wake, J. Fluid Mech. 576, 1–25, https://doi.org/10.1017/S0022112006004228, 2007.

Pitt, D. M., and Peters, D. A.: Theoretical prediction of dynamic-inflow derivatives, Vertica, 5, 21–34, 1981.

Selig, M.: Low Reynolds number airfoil design lecture notes, in: VKI Lecture Series, available at: https://m-selig.ae.illinois.edu/pubs/Selig-2003-VKI-LRN-Airfoil-Design-Lecture-Series.pdf (last access: 7 June 2021), November 2003.

Selig, M. and McGranahan, B.: Wind tunnel aerodynamic tests of six airfoils for use on small wind turbines, J. Sol. Energ. Eng., 126, 986–1001, https://doi.org/10.1115/1.1793208, 2004.

Shipley, D. E., Miller, M. S., and Robinson, M. C.: Dynamic stall occurrence on a horizontal axis wind turbine blade, in: CONF-950116-8, National Renewable Energy Lab., Golden, CO, USA, 1995.

Smagorinsky, J.: General circulation experiments with the primitive equations: I. The basic experiment, Mon. Weather Rev., 91, 99–164, https://doi.org/10.1175/1520-0493(1963)091<0099:GCEWTP>2.3.CO;2, 1963.

Snel, H., Houwink, R., and Bosschers, J.: Sectional prediction of lift coefficients on rotating wind turbine blades in stall, Netherlands Energy Research Foundation, Petten, the Netherlands, 1994.

Sørensen, J. N.: Instability of helical tip vortices in rotor wakes, J. Fluid Mech., 682, 1–4, https://doi.org/10.1017/jfm.2011.277, 2011.

Tian, W., Ozbay, A. and Hu, H.: An experimental investigation on the wake interferences among wind turbines sited in aligned and staggered wind farms, Wind Energy, 21, 100–114, https://doi.org/10.1002/we.2147, 2018.

Troldborg, N., Sørensen, J. N., and Mikkelsen, R.: Actuator line simulation of wake of wind turbine operating in turbulent inflow, J. Phys.: Conf. Ser., 75, 032031, https://doi.org/10.1088/1742-6596/75/1/012063, 2007.

van der Laan, M. P. and Sørensen, N. N.: Why the Coriolis force turns a wind farm wake to the right in the Northern Hemisphere, J. Phys.: Conf. Ser., 753, 032031, https://doi.org/10.1088/1742-6596/753/3/032031, 2016.

van Dooren, M. F., Campagnolo, F., Sjöholm, M., Angelou, N., and Mikkelsen, T.: Demonstration and uncertainty analysis of synchronised scanning lidar measurements of 2-D velocity fields in a boundary-layer wind tunnel, Wind Energ. Sci., 2, 329–341, https://doi.org/10.5194/wes-2-329-2017, 2017.

von Karman, T.: Über den Mechanismus des Widerstandes, den ein bewegter Körper in einer Flüssigkeit erfärt, 1. Nachrichten von der Gesellschaft der Wissenschaften zu Göttingen, Mathematisch-Physikalische Klasse, Gesellschaft der Wissenschaften zu Göttingen, Gesellschaft der Wissenschaften zu Göttingen, 509–517, 1911.

Xiao, H., Duan, L., Sui, R., and Roesgen, T.: Experimental investigations of turbulent wake behind porous disks, in: 1st Marine Energy Technology Symposium, Washington, DC, USA, April 2013.

Wang, C., Wang, J., Campagnolo, F., Carraón, D. B., and Bottasso, C. L.: Validation of large-eddy simulation of scaled waked wind turbines in different yaw misalignment conditions, J. Phys.: Conf. Ser., 1037, 062007, https://doi.org/10.1088/1742-6596/1037/6/062007, 2018.

Wang, C., Campagnolo, F., and Bottasso, C. L.: Identification of airfoil polars from uncertain experimental measurements, Wind Energ. Sci., 5, 1537–1550, https://doi.org/10.5194/wes-5-1537-2020, 2020a.

Wang, C., Muñoz-Simón, A. Deskos, G., Laizet, S., Palacios, R., Campagnolo, F., and Bottasso, C. L.: Code-to-code-to-experiment validation of LES-ALM wind farm simulators, J. Phys.: Conf. Ser., 1618, 062041, https://doi.org/10.1088/1742-6596/1618/6/062041, 2020b.

Wang, C., Campagnolo, F., Sharma, A., and Bottasso, C. L.: Effects of dynamic induction control on power and loads, by LES-ALM simulations and wind tunnel experiments, J. Phys.: Conf. Ser., 1618, 022036, https://doi.org/10.1088/1742-6596/1618/2/022036, 2020c.

Wang, J., Wang, C., Campagnolo, F., and Bottasso, C. L.: Wake behavior and control: comparison of LES simulations and wind tunnel measurements, Wind Energ. Sci., 4, 71–88, https://doi.org/10.5194/wes-4-71-2019, 2019.

Whale, J., Papadopoulos, K. H., Anderson, C. G., Helmis, C. G., and Skyner, D. J.: A study of the near wake structure of a wind turbine comparing measurements from laboratory and full-scale experiments, Solar Energy, 56, 621–633, https://doi.org/10.1016/0038-092X(96)00019-9, 1996.

WindEEE: The Wind Engineering, Energy and Environment Research Institute, available at: https://www.eng.uwo.ca/windeee/, last access: 13 October 2020.

Winslow, J., Otsuka, H., Govindarajan, B., and Chopra, I.: Basic Understanding of Airfoil Characteristics at Low Reynolds Numbers, J. Aircraft, 55, 1050–1061, https://doi.org/10.2514/1.C034415, 2018.

Wu, Y. and Porté-Agel, F.: Large-eddy simulation of wind-turbine wakes: evaluation of turbine parametrisations, Bound.-Lay. Meteorol., 138, 345–366, https://doi.org/10.1007/s10546-010-9569-x, 2011.

Zhan, L., Letizia, S., and Iungo, G. V.: LiDAR measurements for an onshore wind farm: Wake variability for different incoming wind speeds and atmospheric stability regimes, Wind Energy, 23, 501–527, https://doi.org/10.1002/we.2430, 2020.

A.4 Paper IV: Uncertainty quantification in the aeroservoelastic simulation of wind turbines

WIND
ENERGY
SCIENCE

Open Access

Performance of non-intrusive uncertainty quantification in the aeroservoelastic simulation of wind turbines

Pietro Bortolotti[1], Helena Canet[1], Carlo L. Bottasso[1], and Jaikumar Loganathan[1,2]

[1]Wind Energy Institute, Technische Universität München, 85748 Garching, Germany
[2]GE Global Research, Aero Thermal Lab., Hoodi Village, Bangalore, India

Correspondence: Carlo L. Bottasso (carlo.bottasso@tum.de)

Abstract. The present paper characterizes the performance of non-intrusive uncertainty quantification methods for aeroservoelastic wind turbine analysis. Two different methods are considered, namely non-intrusive polynomial chaos expansion and Kriging. Aleatory uncertainties are associated with the wind inflow characteristics and the blade surface state, on account of soiling and/or erosion, and propagated throughout the aeroservoelastic model of a large conceptual offshore wind turbine.

Results are compared with a brute-force extensive Monte Carlo sampling, which is used as benchmark. Both methods require at least 1 order of magnitude less simulations than Monte Carlo, with a slight advantage of Kriging over polynomial chaos expansion. The analysis of the solution space clearly indicates the effects of uncertainties and their couplings, and highlights some possible shortcomings of current mostly deterministic approaches based on safety factors.

1 Introduction

The analysis and design of complex engineering systems are typically based on sophisticated numerical models. While in the past these have been mostly based on deterministic formulations, more recently probabilistic approaches have been gaining an increased attention because of their ability to account for uncertainties in both the models and their inputs. Although numerous applications of probabilistic methods can be found in many areas of engineering, so far formal uncertainty quantification has been applied to a lesser degree in the wind energy field. In fact, probabilistic approaches have been used to estimate wind turbine extreme loads, as reported by Dimitrov (2016) and Graf et al. (2018) among others, but comprehensive analyses and design procedures that account for uncertainties have been lagging behind. This can probably be attributed to the inherent complexity of the models describing the behavior of wind turbines and the environment in which they operate. Indeed, wind (and water, in the offshore case) excitations are highly unsteady and characterized by complex phenomena. Additionally, comprehensive wind turbine simulation environments are obtained by coupled multi-

physics models, which account for the effects of structural dynamics, aero- and hydrodynamics, closed-loop controls, and their mutual interactions. As a consequence of the inherent complexity and computational cost of the resulting simulation tools, most of the analysis and design methods are currently based on deterministic simulation models and uncertainties are, to a large extent, only indirectly accounted for. For example, instead of computing extreme loads from the tails of probability distributions – which would be the probabilistic approach – artificial deterministic wind time histories are routinely used to generate in a simpler way such limit cases (IEC61400-1, 2005).

The behavior of wind turbines and of the environment in which they operate is profoundly affected by uncertainties. Therefore, time is ripe for investigating rigorous mathematical formulations to evaluate the robustness of designs and to establish confidence levels on outputs of interest. In the literature, already a few authors have taken the first steps in this direction. One of the first wind-energy-related publications in this field is the paper by Witteveen et al. (2007), where an intrusive formulation of polynomial chaos expan-

sion (IPCE) is used to investigate the effects of uncertainties affecting the ONERA dynamic stall model with regard to a 1 MW wind turbine blade. The authors conclude that the model is very sensitive to input uncertainties and that IPCE is able to reconstruct the output statistics with 1 order of magnitude fewer function evaluations than a standard Monte Carlo (MC) approach. In Petrone et al. (2011), the aerodynamic design optimization of a wind turbine blade is presented, where uncertain levels of contamination affect the airfoil polars along the span of the blade. A simplex stochastic collocation (SSC) method is used for the propagation of the uncertainties, and convergence is compared against the standard MC approach. SSC is found to be significantly more efficient than MC, in the sense that it requires a much smaller number of evaluations of the model for convergence. Multi-objective design solutions are also presented in the same work, investigating trade-offs between maximum power coefficient and minimum sound pressure levels. Another approach for the robust design optimization of wind turbine rotor blades is presented by Campobasso et al. (2016), where uncertainties are assumed in the chord and twist distributions as well as in the prescribed pitch angle. Additional recent efforts in this area have been dedicated to the development of novel stochastic models for the aerodynamic analysis of wind turbine blades (Fluck, 2017).

Modern simulation and design frameworks are typically based on validated comprehensive aeroservoelastic models. Drastic rewritings of such complex codes to incorporate stochastic formulations are clearly undesirable. To enable the use of legacy codes as black boxes within a probabilistic approach, studies have been recently focusing on the augmentation of aeroservoelastic solvers with non-intrusive uncertainty propagation methods. In addition to enabling the reuse of existing software, non-intrusiveness also allows one to rapidly reap the benefits of any modeling improvement, as the problem of uncertainty quantification is essentially decoupled from the details of the underlying simulation model. This approach is followed by Abdallah et al. (2015) using MC. The method, however, is non-intrusive but also typically extremely expensive because it performs a straightforward exhaustive sampling of the solution space. More sophisticated spectral methods are used in Matthäus et al. (2016) and Murcia et al. (2017). In these three studies, the impact of uncertainties in the soiling of the airfoils and the wind inflow is estimated in terms of the statistics of rotor performance and extreme loads.

The present study expands and refines the work presented in Matthäus et al. (2016) with the primary goal of identifying the most suitable approaches for the propagation of uncertainties throughout aeroservoelastic wind turbine models. A second goal of this work is that of establishing the performance and convergence properties of such methods for this specific application. The in-depth study of uncertainties and their effects on wind turbines is not amongst the goals of this paper, although it is clearly a long-term objective of

crucial importance. Among the various approaches that are available in the literature (Sudret, 2007), non-intrusive polynomial chaos expansion (NIPCE) and Kriging (Krige, 1951) are considered here because of their generality and typical good performance on a wide range of different applications.

The study is conducted with reference to a conceptual offshore 10 MW wind turbine, which is representative of the most up-to-date technology. The machine is modeled with the code Cp-Lambda (Code for Performance, Loads and Aeroelasticity by Multi-Body Dynamic Analysis), which implements a multibody formulation for flexible systems with general topologies. The element library includes rigid bodies, nonlinear flexible elements, joints, actuators, and aerodynamic models (Bottasso et al., 2006; Bauchau, 2011). Uncertainties are assumed both in the wind characteristics, using actual field measurements, and in the aerodynamic properties of the rotor blades, on account of soiling and erosion. Simulations are performed over a range of wind speeds covering the entire operating regime of the machine. The two considered uncertainty propagation methods are compared in terms of their ability to reconstruct the main statistics of key performance indicators and design drivers, including maximum blade tip deflection, ultimate and fatigue loads at various spots on the machine, and, finally, annual energy production (AEP). An exhaustive sampling by the classical MC approach is used as benchmark to define the convergence and accuracy of the tested methods. The resulting probabilistic simulation framework can quantify the effects of uncertainties for a comprehensive black-box aeroservoelastic simulator, in support of the analysis and design of wind turbines. This work is an intermediate step towards the inclusion of robust design methods in the procedures described in Bortolotti et al. (2016), which are at present purely deterministic (except that for the standard treatment of wind by the use of multiple realizations of turbulent fields; IEC61400-1, 2005).

The paper is structured as follows. Section 2 first discusses sources and models of uncertainty for wind turbine aeroservoelasticity and then briefly presents the two methods considered here for the propagation of such uncertainties. Next, the wind turbine model is presented at the beginning of Sect. 3, followed by a comparison of the convergence trends for the two methods in Sect. 3.2, while an analysis of the results is discussed in Sect. 3.3. Conclusions and recommendations for future work are finally given in Sect. 4.

2 Sources of uncertainty and propagation methods

Uncertainties are commonly categorized into two macro families: aleatory and epistemic uncertainties. The former source of uncertainty emerges from the underlying randomness of a process, as for example described by the probability distribution of the wind speed at a certain site. The latter, on the other hand, originates from a lack of knowledge and data. This work considers the effects of aleatory model parameters

and inputs with established underlying probability distributions.

Wind turbines are subjected to several sources of uncertainty. In addition to the inherently stochastic character of the wind, which varies in time and space for a multitude of reasons, uncertainties are also present in the aerodynamic characteristics of the machine; in the mechanical properties of the materials, structures and foundations; and in the characteristics and performance of many of the subsystems of a wind turbine. Not only the nominal values of all such parameters are uncertain but additional sources of uncertainty are also introduced by manufacturing processes and the status of wear and tear of each individual machine or component. Additionally, one should not forget that measurements are also uncertain (Tarp-Johansen et al., 2002) so an absolute real ground truth can not be established in general.

Due to its preliminary character, this study limits its attention to uncertainties affecting the wind inflow and the aerodynamics of the blades. These are typical and relevant examples of aspects of a turbine model that can often only be described in statistical terms, but also have a profound impact on the behavior and overall performance of the system. It should, however, be remarked that the methods analyzed here are general and in principle applicable to problems other than the ones considered for this work.

2.1 Uncertainty in the characterization of the wind

Wind is a natural phenomenon where air particles move dynamically following three-dimensional paths as a result of a number of driving effects. In general, such a complex process can only be measured and described in terms of its statistics. International standards, such as IEC61400-1 (2005) (International Electrotechnical Commission), represent wind profiles by a combination of deterministic mean parameters – typically mean hub-height speed, shear exponent (SE), and vertical and horizontal inflow angles – and a turbulence model, which, for an assigned mean turbulence intensity (TI), describes the stochastic variability in the flow field. Each realization of the turbulent wind field is associated with a random seed. By combining the mean flow field with the fluctuations produced by the turbulence model, one obtains a representation of the wind field in space and time. Sufficient durations and number of realizations are typically necessary for the statistics of the generated wind fields to reach convergence.

However, effects such as solar irradiation, seasonal and long-term climate changes, vegetation growth, and complex terrain conditions play important roles in increasing uncertainties in the characteristics of the wind (Sathe et al., 2011; Ernst and Seume, 2012). These effects may alter in a significant way the statistics of the wind at a given site. All such effects are difficult to measure and quantify with precision, in turn introducing uncertainties in the assumed wind characteristics used for the simulation and design of wind tur-

bines. This is clearly a problem of crucial importance. In fact, for a given turbine and control system, the assumed wind input plays a fundamental role in determining performance and loading, including lifetime and safety.

This work assumes that both TI and SE are uncertain. However, field data often exhibit a correlation between SE and TI that, according to Dimitrov et al. (2015), can be modeled as

$$SE = SE_{ref} + \frac{TI_{ref} - TI}{TI\, c_{SE}}. \tag{1}$$

In this expression, SE_{ref} is a reference value for the shear exponent, c_{SE} a correction factor that can be generally assumed equal to 4, and TI_{ref} is the value of the turbulence intensity at a wind speed of $15\,m\,s^{-1}$. Here an uncertain multiplicative factor k_{TI} is used to perturb an initial distribution of TI over wind speed; when k_{TI} equals 1, TI at $15\,m\,s^{-1}$ equals TI_{ref}. Therefore, through Eq. (1), k_{TI} also introduces a corresponding uncertainty in SE.

Here and in the following all uncertain parameters are modeled with scaled beta distributions. Such distributions are preferred to other possible choices for two reasons: first, they are highly flexible in shaping the probability density function on account of given statistical data and, secondly, they generate bounded distributions with lower and upper limits. This is a necessary feature when modeling parameters that cannot assume negative values. It should be noted, however, that neither NIPCE nor Kriging are bound to scaled beta distributions, and truncated Gaussian, log-normal, uniform distributions, or others could also be readily used. The parameters of the beta distribution for the uncertain factor k_{TI} are reported in Sect. 3.1.

2.2 Uncertainty in rotor aerodynamic properties

A second important source of uncertainty in wind turbine simulation and design lies in the aerodynamic characteristics of the rotor. Among other effects, the performance of the airfoils – measured in terms of the aerodynamic coefficients of lift, drag, and moment – is considered a possible major source of uncertainty.

The estimation of airfoil aerodynamic coefficients can be obtained by experimental and numerical techniques. Both approaches are challenging and lead to uncertainties of an aleatory and epistemic nature, especially in the stall and post-stall regimes. Although potentially very significant, such uncertainties are not considered further in this work, which focuses instead on blade surface conditions.

During operation, the surface of a blade may be contaminated by the deposition of dust, dirt, insects, and pollen. Additionally, the blade surface can also be altered due to erosion caused by sand and rain. All these effects are typically and particularly prominent at the leading edge, which has a fundamental role in dictating the behavior of airfoils. As a result,
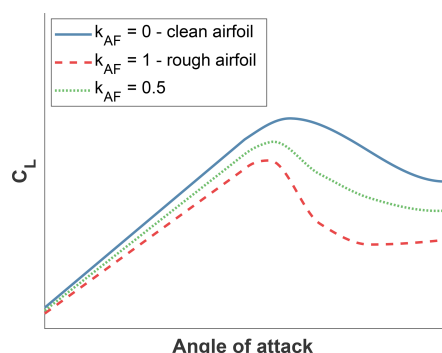
Figure 1. Interpolation of the airfoil aerodynamic coefficients between the fully clean and fully rough conditions.

Table 1. Principal characteristics of the 10 MW AVATAR wind turbine.

Wind turbine model	10 MW offshore
Wind class	IEC 1A
Rated electrical power	10.0 MW
Drivetrain and generator efficiency	94.0 %
Rotor diameter D	205.76 m
Hub height H	127.0 m
Nacelle uptilt angle Φ	5.0°
Rotor cone angle Ξ	2.5°
Cut-in wind speed V_{in}	4 m s^{-1}
Cut-out wind speed V_{out}	25 m s^{-1}
Max tip speed $v_{tip_{max}}$	90 m s^{-1}
Blade mass	52 874 kg
Tower mass	630.0 t

changes in surface conditions during operation may result in significant uncertainties in power capture and loading.

Several studies have quantified the impact of erosion and contamination on aerodynamic performance (Khalfallah and Koliub, 2007; Sareen et al., 2014; Zidane et al., 2016). The exact pattern and location of surface changes during operation is a random process, which is largely governed by local effects, such as the local relative speed of the flow with respect to the blade and the local manufacturing surface quality, e.g., in terms of gel coat thickness and bonding strength (Khalfallah and Koliub, 2007). In the current study, an uncertain level of airfoil profile unevenness is simulated by using the random variable k_{AF}, modeled with a scaled beta probability density function. Variable k_{AF} is assumed to vary within the values of 0 and 1, where 0 corresponds to the nominal (clean) state of an airfoil, while 1 corresponds to a contaminated or fully rough state of operation. The airfoil aerodynamic coefficients between these two states are linearly interpolated for any intermediate value of the random variable, as shown in Fig. 1.

Uncertainties in the actual extension of surface degradation along the span of the blade are modeled by introducing a second parameter, termed extent of spanwise degradation (ESD). Parameter ESD is defined as the nondimensional span length – measured from blade tip – where factor k_{AF} affects the airfoil coefficients. Since surface degradation typically occurs in the outer portion of the blades, ESD is assumed to follow a beta distribution between 0, which corresponds to a fully clean blade, and 0.5, which implies that the outer 50 % of the blade is affected by surface degradation with a severity dictated by k_{AF}.

2.3 Methods for uncertainty propagation

As anticipated in Sect. 1, the current literature offers a vast range of methods for the propagation of uncertainties. A detailed overview of the various formulations can be found in Sudret (2007). Among the many options, based on the results presented in Matthäus et al. (2016), the present study con-

siders the regression-based third-order NIPCE and Universal Kriging (UK), as implemented in DAKOTA (Adas et al., 2015), to propagate the uncertainties discussed in Sect. 2.1 and 2.2.

In Matthäus et al. (2016), the methods of spectral projection and linear regression were tested to determine the polynomial coefficients of NIPCE, the latter typically yielding the best results. In terms of polynomial order, tests were conducted between the first and 16th order. The best results were obtained for the third order, while above this value the solution first stopped improving and then deteriorated. It was also found that Universal Kriging is superior to Ordinary Kriging, mostly due to its better adaptability to a general trend in the response.

3 Application to a 10 MW wind turbine

Here uncertainties in the wind characteristics and in the airfoil polars are propagated throughout the aeroservoelastic model of an offshore wind turbine, with the goal of comparing the performance of the uncertainty quantification methods and of establishing their main convergence characteristics. First, Sect. 3.1 introduces the turbine model together with the assumed uncertainties. Convergence of the statistics is then discussed in Sect. 3.2, while the analysis of the effects of uncertainties on some key outputs is finally presented in Sect. 3.3.

3.1 Wind turbine model and associated uncertainties

The AVATAR wind turbine is considered in this work, as a representative case of a large offshore wind turbine. This conceptual machine was developed by a consortium of academic and industrial partners within the EU project AVATAR (AVATAR Consortium, 2014–2017), and its main characteristics are summarized in Table 1. In this study, the standard configuration defined by the consortium is used, while the

Table 2. Spanwise positions of the airfoils.

Airfoil	Thickness	Position	Airfoil	Thickness	Position
Circle	100.0 %	0.0 %	DU00-W2-350	35.0 %	36.31 %
Circle	100.0 %	0.61 %	DU97-W-300	30.0 %	45.63 %
DU-600	60.0 %	17.00 %	DU91-W2-240	24.0 %	65.00 %
DU00-W2-401	40.1 %	28.47 %	DU91-W2-240	24.0 %	100.00 %

Table 3. Probability density functions for turbulence intensity factor k_{TI}, airfoil roughness k_{AF}, and non-dimensional spanwise extent of erosion ESD.

	α	β	Region
k_{TI}	3.4	6.0	[0.5, 2.0]
k_{AF}	2.0	6.0	[0.0, 1.0]
ESD	2.5	4.0	[0.0, 0.5]

blade inner structure is the one developed at Politecnico di Milano (Croce et al., 2017). Table 2 lists the airfoils used along the span of the blades.

For airfoils DU97-W-300 and DU91-W2-240, which occupy the outermost part of the blade, surface conditions are specified by the two parameters k_{AF} and ESD by interpolating between fully clean and fully rough aerodynamic coefficients. The clean and rough polars of the two airfoils, which are based on the work performed in the AVATAR project (Méndez et al., 2017), are reported in Fig. 2. On the other hand, only clean aerodynamic coefficients are used for the airfoils located closer to the blade root, as surface degradation is less likely to happen in this region.

Uncertainties are considered for k_{TI}, k_{AF}, and ESD. As previously explained, the wind parameter SE is not assumed as an independent uncertain variable, but it obeys the relationship of Eq. (1), assuming SE_{ref} is equal to 0.15 and TI_{ref} is equal to 4.9 % (see Fig. 3). All uncertainties are assumed to follow the beta distributions whose parameters are reported in Table 3. The distribution of turbulence intensity is taken from a measurement campaign conducted in a wind park in the North Sea. The distribution for $k_{TI} = 1$ is reported in Fig. 3.

An extensive MC analysis is first performed to characterize the solution space. The three uncertainties are propagated throughout the aeroservoelastic model in a power production state at 12 different wind speeds from cut-in to cut-out, considering six turbulent seeds. Eight outputs of interest are analyzed, namely maximum blade tip deflection (MTD), ultimate and damage equivalent load (DEL) of the thrust measured at the main shaft (ThS), ultimate and DEL combined blade root moment (CBRM), ultimate and DEL combined tower base moment (CTBM), and finally annual energy production (AEP). MTD and ultimate ThS, CBRM, and CTBM are obtained by computing the maximum overall value across

Table 4. Main statistics of the eight outputs of interest for 1100 MC function evaluations. MTD: maximum tip deflection; ThS: thrust at main shaft; CBRM: combined blade root moment; CTBM: combined tower base moment; DEL: damage equivalent load; AEP: annual energy production.

	Mean	Standard deviation	Coefficient of variation
MTD	6.99 m	0.11 m	1.58 %
ThS	2.08 MN	0.02 MN	1.02 %
DEL ThS	0.34 MN	0.05 MN	13.79 %
CBRM	56.29 MNm	0.63 MNm	1.12 %
DEL CBRM	29.51 MNm	2.61 MNm	8.83 %
CTBM	236.05 MNm	2.20 MNm	0.93 %
DEL CTBM	46.79 MNm	7.82 MNm	16.72 %
AEP	53.7 GWh	0.29 GWh	0.54 %

all time steps and wind speeds. DELs and AEP are instead averaged via the Weibull distribution corresponding to wind class 1A, which is characterized by a shape factor of 2 and an average wind speed at hub height of $10 \, \mathrm{m \, s^{-1}}$ (IEC61400-1, 2005).

The MC analysis was stopped at 1100 evaluations, where the convergence of mean and standard deviations for all quantities consistently returned variations below 1 % of their average values. While convergence is rapidly obtained for the mean values of the eight outputs of interest, standard deviations require a significantly higher number of evaluations to reach convergence. The statistics of the outputs are reported in Table 4.

Here, six seeds were used to limit the computational cost of the MC analysis, following accepted international standards (IEC61400-1, 2005). However, as reported in the literature (Dimitrov et al., 2015; Graf et al., 2018), this number might not always be adequate. This is confirmed also here as the use of only six seeds does not guarantee the full convergence of all quantities, especially in terms of standard deviations, as shown by Fig. 4. While the differences in AEP and DELs are indeed small, this is not true for the ultimate loads. A better understanding of the convergence of results with the number of turbulent realizations should be the subject of future work, as discussed in Sect. 4.
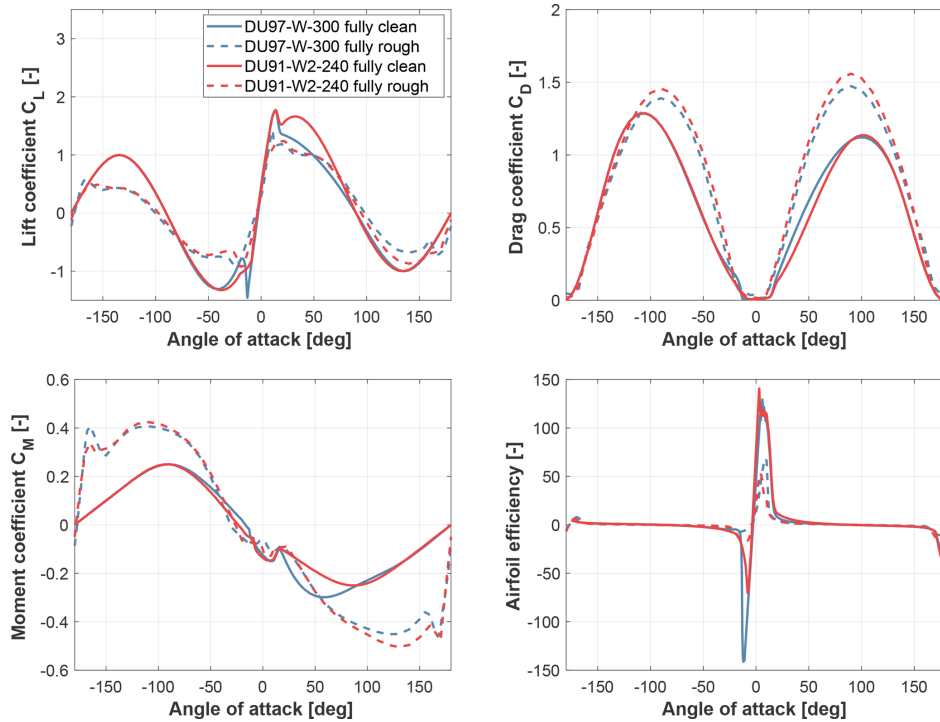
Figure 2. Fully clean and fully rough aerodynamic coefficients C_L, C_D, C_M, and airfoil efficiency vs. angle of attack for airfoils DU97-W-300 and DU91-W2-240.
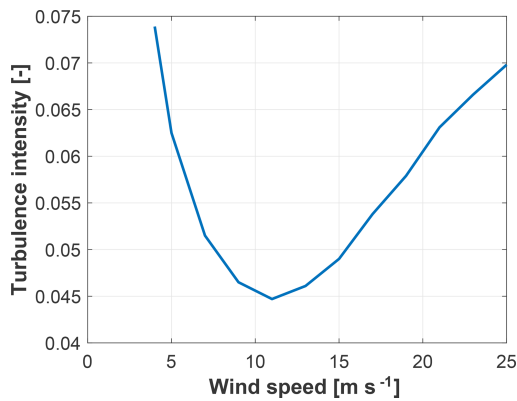

Figure 3. Turbulence intensity distribution for varying wind speed.

3.2 Convergence analysis

The convergence of the uncertainty propagation methods is studied first. The analysis considers mean and standard deviation of AEP, maximum tip displacement, thrust, combined blade root moment, combined tower base moment, and the corresponding damage equivalent loads.

Third-order NIPCE and UK, both as implemented in DAKOTA (Adas et al., 2015), are tested against the MC benchmark presented in Sect. 3.1. To ensure a fair compari-

son, a MC sampling strategy is adopted for both NIPCE and Kriging. The number of training data samples follows the relation $R = r N_t$, where r is the collocation ratio, varying from 0.6 to 8, and N_t is the total number of terms considering a total-order expansion. The collocation ratio is defined as the ratio between the number of function evaluations used to train the model and the total number of terms in the chaos expansion. On the resulting response surface, an extensive MC sampling with 100 000 points is conducted to extract mean and standard deviation.

Both NIPCE and UK appear to be capable of estimating the eight outputs of interest at a much reduced number of function evaluations compared to MC. In addition, UK consistently converges faster than the other two methods, with a reduction of 1–2 orders of magnitude with respect to MC for the estimation of the output mean and standard deviation. The plots reported in Fig. 5 provide a visualization of these results. In the figure, a gray area represents the 95 % confidence intervals for the finite (here equal to 1100) number of sampling points used in the MC analysis. The gray band could be made narrower by increasing the number of samples.

3.3 Effects of uncertainties on outputs of interest

The results obtained by UK with 40 function evaluations are then subjected to a more detailed analysis. Response surfaces
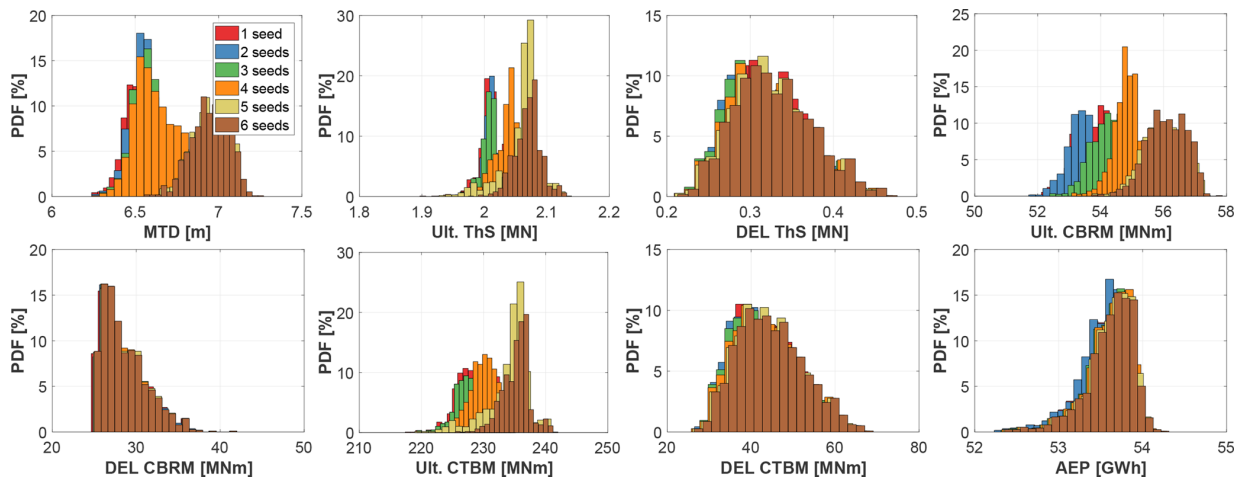
Figure 4. Probability density functions (PDFs) of key output metrics for varying number of seeds. Each case is based on 1100 sampling points.
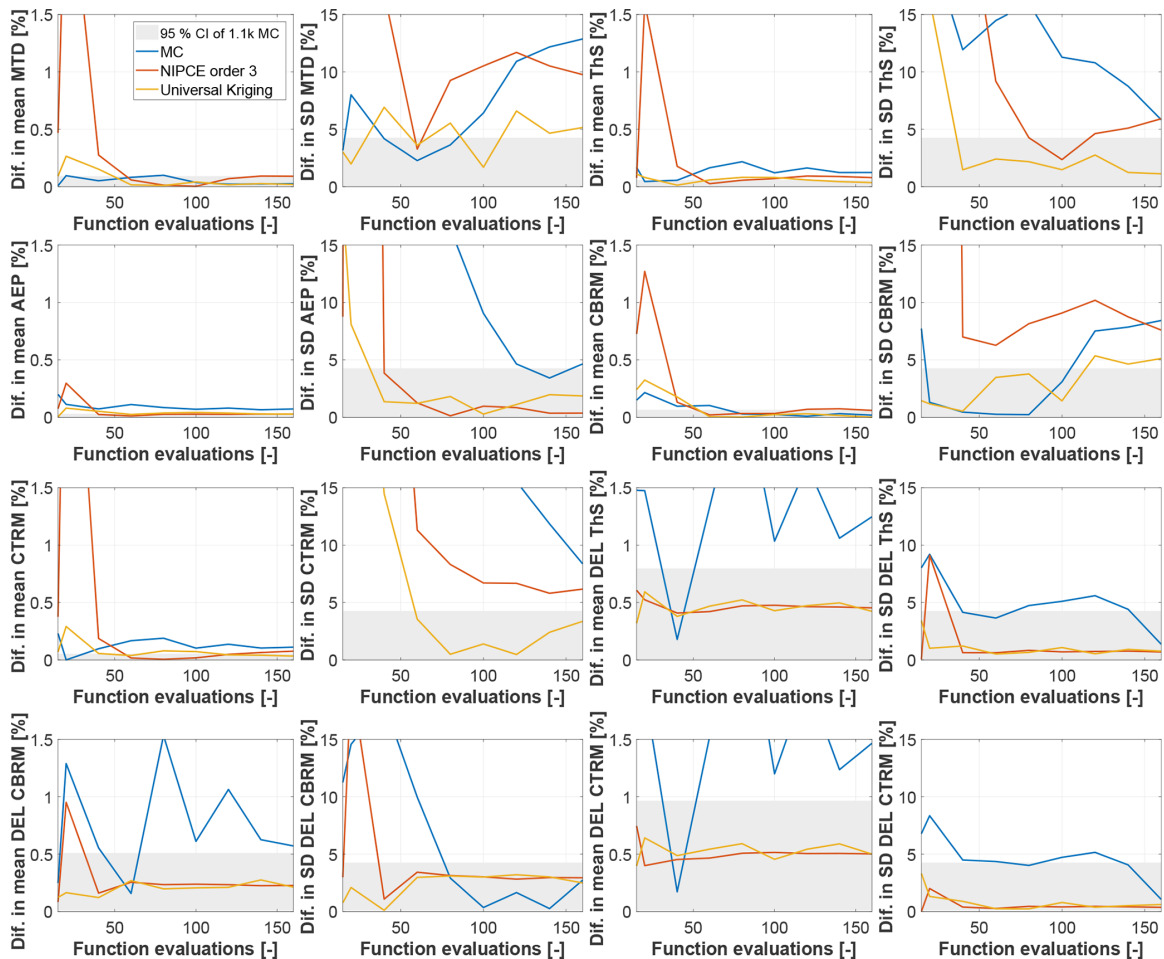

Figure 5. Convergence of mean and standard deviation for key output quantities. The gray area reflects the potential inexactness of the MC benchmark, and it represents the 95 % confidence intervals for 1100 sampling points.
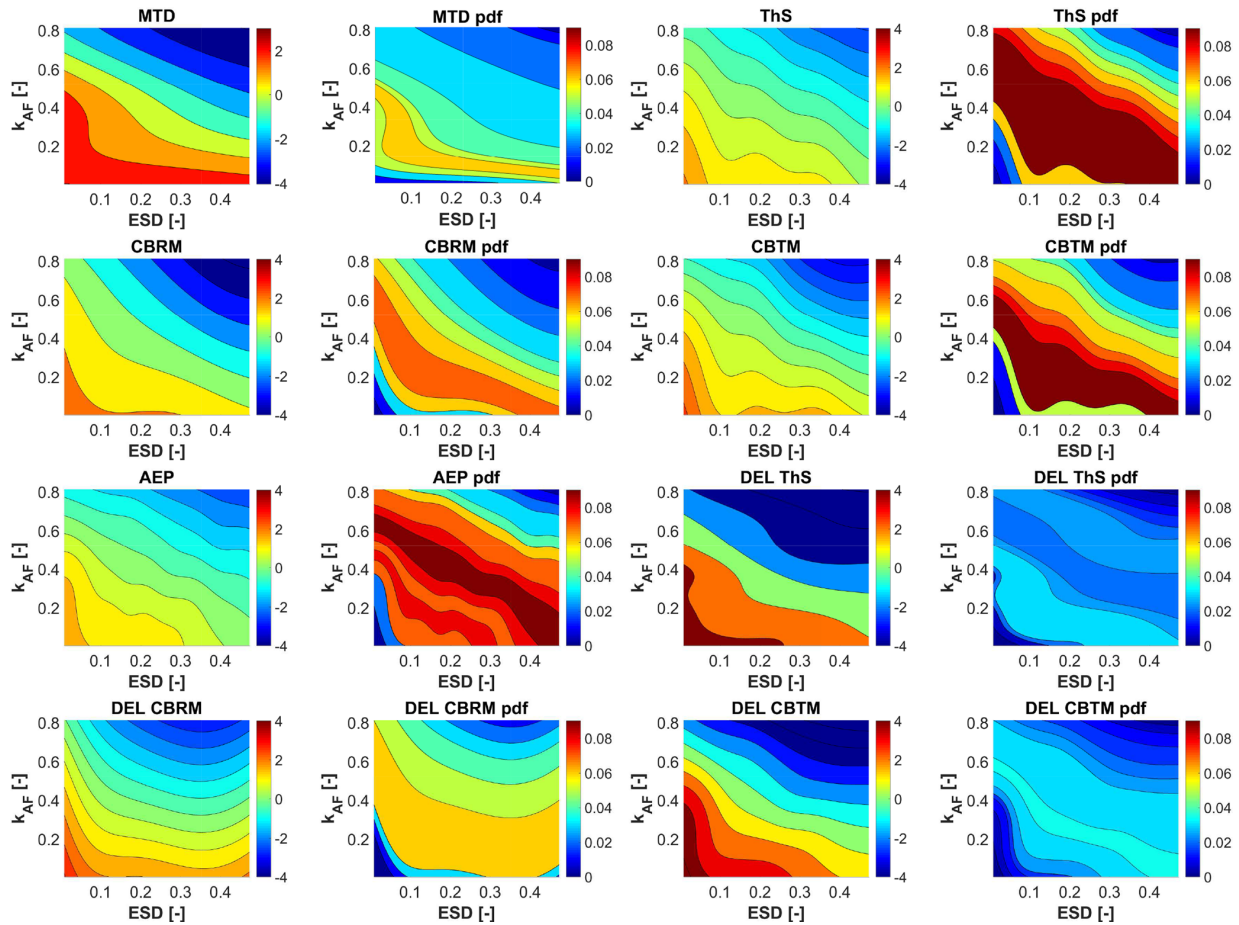
Figure 6. Key outputs (in percent difference with respect to the mean value) and corresponding probability density functions, for k_{TI} equal to one.

for the eight outputs of interest and their corresponding probability density functions are shown in Fig. 6. The plots are generated by first training the UK model with 40 points and then evaluating it with a random sample of 1 million points. Given the three-dimensional nature of the solution space, two-dimensional surfaces are plotted for a constant k_{TI} equal to one.

The contour plots visibly show nonlinearities. Additionally, they also show that the condition corresponding to a fully clean rotor, namely ESD and k_{AF} equal to 0 (bottom left corner of each plot in Fig. 6), generates the highest values for all eight outputs of interest (left plots). However, according to the input distributions of Table 3, these conditions also have a very low probability of occurrence (right plots). For MTD and the three key loads ThS, CBRM, and CTBM, this means that the deterministic simulations prescribed by the standards overestimate the actual output values. Since the variations in the outputs are limited, and typically in the range of ±3 %, these results might appear to suggest that the conventional safety factors equal to 1.2 or 1.3 may be excessive. It is, how-

ever, clear that this analysis is purely limited to the effects of surface roughness and some wind inflow parameters, and a more comprehensive analysis should be conducted before drawing any final conclusion or recommendation. It should also be remarked that the non-intrusive uncertainty propagation methods used here would indeed allow for a more general analysis in a rather straightforward manner.

MTD provides an interesting example. International standards prescribe MTD to be 30 % lower than tower clearance. The top left plots in Fig. 6 show that the largest probability of occurrence corresponds to MTD values that fall within ±1 % of the mean, while very low probabilities are associated with the value of MTD obtained in the deterministic condition prescribed by the standards (k_{AF} and ESD equal to 0). Similarly, a deterministic analysis overestimates AEP by about 3 %, while the uncertainty analysis shows an equal probability within a range of ±1.5 % from the mean value.

In addition, the contour plots of MTD and AEP indicate a fairly linear behavior of the solution space, where the two outputs show a maximum variation along the 45° bisector.

This follows from the fact that, as expected, the rotor is more loaded for clean airfoils and a low extent of erosion (both k_{AF} and ESD equal to zero), generating higher AEP and MTD. These variations are apparently approximately linear and as a result the region of maximum probability aligns with the expected values of k_{AF} and ESD.

4   Conclusions and outlook

This work has reported on the first steps towards the development of a framework for the non-intrusive propagation of uncertainties throughout black-box aeroservoelastic wind turbine models. Non-intrusiveness is key to the reusability of legacy models and for rapidly reaping the benefits of modeling improvements without the need for a extensive rewriting of such complex codes.

NIPCE and UK were applied to a large state-of-the-art conceptual wind turbine, considering power capture, tip deflection, and some typical design-driving loads as performance indicators. Uncertainties were considered for both the wind inflow conditions and the roughness of the blades, on account of soiling and/or erosion. For both methods, comparisons to standard brute-force Monte Carlo predictions indicate a good performance in terms of quality at a significantly lower computational cost. Of the two, UK appears to consistently converge faster than NIPCE.

The analysis of the results indicates nonlinearities and couplings among the various sources of uncertainty. In addition, it was found that the deterministic conditions prescribed by international design standards generate maximum values of loads and power production, which, however, are typically associated with a very low probability of occurrence. Although the results obtained here are not comprehensive enough to draw any significant conclusions, they do suggest that the use of formal mathematical methods of uncertainty propagation may lead to a revision of typical safety factors in the interest of more cost-competitive – but still fully safe – designs.

The present study should be refined in several important aspects. To start, the problem of turbulent realizations deserves specific attention. Here the number of turbulent seeds typically recommended by design standards was used, but appeared not to be always sufficient for guaranteeing convergence of the statistics. If the number of seeds needs to be increased in a substantial manner to ensure convergence, this might require a change in the methodological approach, as the computational cost might become prohibitive. In this sense, the use of surrogate models, instead of the high-fidelity ones used here, might become attractive. An additional problem of interest is the computation of extreme states, which populate the tails of the probability distributions and often act as design drivers. Here, ad hoc sampling strategies have been developed by the statistical research community, and could be applied to the problem at hand

(Graf et al., 2018). Other sophisticated sampling methods, such as Latin hypercube sampling or Hammersley sampling (Hosder et al., 2007; Eldred et al., 2009), have been described in the literature and will be the topic of future studies. Furthermore, additional sources of uncertainty should be investigated. In fact, in principle many parameters and inputs can be assumed to be uncertain. However, comprehensive knowledge of the role played by the various uncertainties and their couplings is still largely missing. A ranking of uncertainties and a deeper understanding of their effects is a very worthwhile endeavor, which might have a significant role in the future design of wind energy systems.

References

Abdallah, I., Natarajan, A., and Sørensen, J. D.: Impact of uncertainty in airfoil characteristics on wind turbine extreme loads, Renew. Energ., 75, 283–300, https://doi.org/10.1016/j.renene.2014.10.009, 2015.

Adams, B. M., Bauman, L. E., Bohnhoff, W. J., Dalbey, K. R., Ebeida, M. S., Eddy, J. P., Eldred, M. S., Hough, P. D., Hu, K. T., Jakeman, J. D., Stephens, J. A., Swiler, L. P., Vigil, D. M., and Wildey, T. M.: Dakota, A Multilevel Parallel Object-Oriented

Framework for Design Optimization, Parameter Estimation, Uncertainty Quantification, and Sensitivity Analysis: Version 6.0 User's Manual, Sandia Technical Report SAND2014-4633, Updated November 2015 (Version 6.3), available at: https://dakota.sandia.gov (last access: December 2018), July 2014.

AVATAR, Advanced Aerodynamic Tools for Large Rotors, available at: http://www.eera-avatar.eu (last access: December 2018), 2014–2017.

Bauchau, O. A.: Flexible Multibody Dynamics, Mechanics and Its Applications, Springer, ISBN: 978-94-007-0335-3, 2011.

Bortolotti, P., Bottasso, C. L., and Croce, A.: Combined preliminary–detailed design of wind turbines, Wind Energ. Sci., 1, 71–88, https://doi.org/10.5194/wes-1-71-2016, 2016.

Bottasso, C. L., Croce, A., Savini, B., Sirchi, W., and Trainelli, L.: Aero-servo-elastic modeling and control of wind turbines using finite-element multibody procedures, Multibody Syst. Dyn., 16, 291–308, https://doi.org/10.1007/s11044-006-9027-1, 2006.

Campobasso, M. S., Minisci, E., and Caboni, M.: Aerodynamic design optimization of wind turbine rotors under geometric uncertainty, Wind Energy, 19, 51–65, https://doi.org/10.1002/we.1820, 2016.

Croce, A., Sartori, L., Riva, R., Spinelli, M., Zahle, F., Barla, A., Milidis, A., Manolas, D., Roman, R. M. S., Pueyo, C. A., and Schwarz, M.: Aerodynamics of Large Rotors, WP4, Deliverable 4.12, Effect of blade flexibility and structural tailoring on loads, available at: http://www.eera-avatar.eu/fileadmin/avatar/user/report-d4-12-update_Oct_6_2017.pdf, August 2017.

Dimitrov, N., Natarajan, A., and Kelly, M.: Model of wind shear conditional on turbulence and its impact on wind turbine loads, Wind Energy, 18, 1917–1931, https://doi.org/10.1002/we.1797, 2015.

Dimitrov, N: Comparative analysis of methods for modelling the short-term probability distribution of extreme wind turbine loads, Wind Energy, 19, 717–737, https://doi.org/10.1002/we.1861, 2016.

Eldred, M. S. and Burkardt, J.: Comparison of non-intrusive polynomial chaos and stochastic collocation methods for uncertainty quantification, Proceedings of 47th AIAA Aerospace Sciences Meeting, https://doi.org/10.2514/6.2009-976, 2009.

Ernst, B. and Seume J. R.: Investigation of site-specific wind field parameters and their effect on loads of offshore wind turbines, Energies, 5, 3835–3855, https://doi.org/10.3390/en5103835, 2012.

Fluck, M.: Stochastic Methods for Unsteady Aerodynamic Analysis of Wings and Wind Turbine Blades, PhD Thesis, University of Victoria, 2017.

Graf, P., Dykes, K., Damiani, R., Jonkman, J., and Veers, P.: Adaptive stratified importance sampling: hybridization of extrapolation and importance sampling Monte Carlo methods for estimation of wind turbine extreme loads, Wind Energ. Sci., 3, 475–487, https://doi.org/10.5194/wes-3-475-2018, 2018.

Hosder, S., Walters, R. W., and Balch, M.: Efficient sampling for non-intrusive polynomial chaos applications with multiple uncertain input variables, Proceedings of 48th AIAA/ASME/ASCE/AHS/ASC Structures, Structural Dynamics, and Materials Conference, https://doi.org/10.2514/6.2007-1939, 2007.

IEC 61400-1, Wind Turbines – Part 1: Design Requirements, 3rd edn., the International Electrotechnical Commission (IEC), International Standard IEC 61400-1, 2005.

Khalfallah, M. G., and Koliub, A. M.: Effect of dust on the performance of wind turbines, Desalination, 209, 209–220, https://doi.org/10.1016/j.desal.2007.04.030, 2007.

Krige, D. G.: A statistical approach to some basic mine valuation problems on the Witwatersrand, Journal of the Chemical, Metallurgical and Mining Society of South Africa, 52, 119–139, 1951.

Matthäus, D., Bortolotti, P., Loganathan, J., and Bottasso, C. L.: Propagation of uncertainties through wind turbine models for robust design optimization, AIAA SciTech Forum, https://doi.org/10.2514/6.2017-1849, 2017.

Méndez, B., Munduate, X., Sørensen, N., García, N. R., Prospathopoulos, J., Papadakis, G., Voutsinas, S., and Ceyham, O.: 2D Airfoil polars for the AVATAR rotor – WP2 Deliverable 2.1, September 2015.

Murcia, J. P., Réthoré, P. E., Dimitrov, N., Natarajan, A., Sørensen, J. D., Graf. P., and Kim, T.: Uncertainty propagation through an aeroelastic wind turbine model using polynomial surrogates, Renew. Energ., 118, 1–13, https://doi.org/10.1016/j.renene.2017.07.070, 2017.

Petrone, G., Nicola, C. D., Quagliarella, D., Witteveen, J., and Iaccarino, G.: Wind turbine performance analysis under uncertainty, Proceedings of 49th AIAA Aerospace Sciences Meeting, https://doi.org/10.2514/6.2011-544, 2011.

Sareen, A., Sapre, C. A., and Selig, M. S.: Effects of leading edge erosion on wind turbine blade performance, Wind Energy, 17, 1531–1542, https://doi.org/10.1002/we.1649, 2014.

Sathe, A., Mann, J., Gottschall, J., and Courtney, M. S.: Can wind Lidars measure turbulence?, J. Atmos. Ocean. Tech., 28, 853–868, https://doi.org/10.1175/JTECH-D-10-05004.1, 2011.

Sudret, B.: Uncertainty Propagation and Sensitivity Analysis in Mechanical Models – Contributions to Structural Reliability and Stochastic Spectral Methods, Rapport d'activité scientifique, Université Blaise Pascal – Clermont II, 2007.

Tarp-Johansen, N., Madsen, H., and Frandsen, S. T.: Partial Safety Factors for Extreme Load Effects, Technical report Risø-R-1319(EN), Risø National Laboratory, Denmark, 2002.

Witteveen, J. A. S., Sarkar, S., and Bijl, H.: Modeling physical uncertainties in dynamic stall induced fluid–structure interaction of turbine blades using arbitrary polynomial chaos, Comput. Struct., 85, 866–878, https://doi.org/10.1016/j.compstruc.2007.01.004, 2007.

Zidane, I. F., Saqr, K. M., Swadener, G., Ma, X., and Shehadeh, M. F.: On the role of surface roughness in the aerodynamic performance and energy conversion of horizontal wind turbine blades: a review, International J. Energy Res., 40, 2054–2077, https://doi.org/10.1002/er.3580, 2016.

A.5 Paper V: Lidar-assisted control in wind turbine design: Where are the potential benefits?

Lidar-assisted control in wind turbine design: Where are the potential benefits?

H Canet[1], S Löw[1], CL Bottasso[1]

[1] Wind Energy Institute, Technical University of Munich, Garching, Germany

E-mail: `carlo.bottasso@tum.de`

Abstract. This study explores the potential benefits of considering Lidar-assisted control (LAC) at the first stages of wind turbine design. The proposed methodology starts with a load analysis of several reference wind turbines to understand which design constraints can be influenced by the use of LAC. The blade and tower of each analyzed model are redesigned considering LAC-induced reductions in key driving quantities. Preliminary results suggest modest reductions in LCOE with potentially significant benefits limited to the tower. The study also discusses the requirements on LAC system purchase and O&M costs, for both onshore and offshore machines, to achieve a reduction in LCOE.

1. Introduction

Turbine-mounted *Light detection and ranging* (Lidar) sensors are able to measure various properties of the incoming wind up to several hundred meters ahead of the wind turbine rotor plane. This preview information has been successfully used to augment conventional feedback controllers with feedforward loops [7], or to replace conventional controllers by advanced predictive ones [13]. These strategies are generically termed *Lidar-assisted control* (LAC).

Multiple studies have concluded that LAC can be used to improve the tracking of C_p, which can lead to an increase of AEP and can reduce fatigue damage and extreme loads in various structural components [7]. These benefits have so far been used to extend the lifetime of existing wind turbines, originally designed to operate with conventional controllers [14].

Even though significant research efforts are currently being devoted to the development of LAC, the benefits of considering LAC within the design of wind turbines are still not fully understood. Within the present work, LAC is considered already at the initial stages of turbine design to fully exploit its potential and reduce Levelized Cost of Energy (LCOE).

This study focuses on two main research questions: first, the paper analyses which key loads can be reduced by a basic LAC implementation and which LCOE reduction can be expected from a LAC-based redesigned turbine. Second, the paper explores the requirements on both the performance and cost of LAC for this device to be economically feasible.

This paper is organized as follows. Sections 2 and 3 are respectively devoted to the description of the approach and the models implemented to answer the two research questions. Section 4 describes the resulting effects of applying LAC at the first stages of design for three different turbines and three different scenarios. Furthermore, the required costs of Lidar are discussed for rendering LAC economically feasible.

2. Approach

The study starts with a load analysis of three reference wind turbines with the goal of understanding the potential reduction margin of their design constraints by the use of LAC. Each model is simulated under a variety of Design Load Cases (DLCs) [12], including power production with normal turbulence (DLC 1.1, DLC 1.2), extreme turbulence (DLC 1.3), loss of electrical network (DLC 2.1) and during extreme operating gusts (DLC 2.3). Also situations where the machine is parked are considered under multiple conditions, such as yaw misalignment (DLC 6.1), grid loss (DLC 6.2) and extreme yaw misalignment (DLC 6.3).

These DLCs are classified into two groups: *modifiable* and *blocking*, according to the influence of the controller on the load envelope. *Modifiable* DLCs are those in which the controller can modify the load envelope. *Blocking* DLCs represent conditions in which the controller performance does not effect the loads, as for example in parked conditions. Table 1 includes a detailed description of the DLCs considered in this study.

The potential load reduction is defined through rankings, where the values of each quantity are ranked in descending order, noting the originating DLC. The value of a key quantity can only be reduced by LAC if the ranking is led by a *modifiable* DLC. Its reduction potential is defined as the difference between its absolute maximum value and the value of the highest ranked *blocking* DLC.

As a second step, a baseline LAC load-reduction model is applied to the resulting loads of all *modifiable* DLCs. This model replaces the simulation of LAC and consists in the application of load-reduction coefficients to the load envelope resulting from aeroelastic simulations with a *non-LAC* controller. Differently performing LAC systems are considered by introducing an optimistic and a pessimistic scenario, defined by a correction factor. This factor multiplies the load-reduction coefficients and is defined as 1.5 for the optimistic scenario, 1 for the baseline scenario and 0.5 for the pessimistic one. The presented method intentionally does not commit to a specific Lidar hardware or controller types, and thus enables a fast preliminary generic assessment for design purposes. Finally, for all three scenarios, the structural redesign of the blades and tower is performed. The resulting changes in the structure are evaluated from an economic point of view through corresponding cost models, according to the wind turbine characteristics.

Table 1: Classification of Design Load Cases (DLC) according to the influence of the controller on the wind turbine load envelope. NTM = Normal Turbulence Model; ETM = Extreme Turbulence Model; EOG = Extreme Operating Gust; EWM = Extreme Wind speed Model

Classification	DLC	Seeds	Design situation	Wind speed	Wind profile	Other condition
Modifiable	1.1	3	Power production	$V_{in}:V_{out}$	NTM	
	1.2	3	Power production	$V_{in}:V_{out}$	NTM	
	1.3	3	Power production	$V_{in}:V_{out}$	ETM	
	2.1	3	Power production	$V_{in}:V_{out}$	NTM	Grid loss
	2.3 V_o	1	Power production	V_{out}	EOG	Grid loss
	2.3 V_r	1	Power production	$V_{rated} \pm 2m/s$	EOG	Grid loss
Blocking	6.1	3	Parked	V_{ref}	EWM 50 year	Yaw mis. $\pm 8°$
	6.2	3	Parked	V_{ref}	EWM 50 year	Grid loss
	6.3	3	Parked	V_{ref}	EWM 1 year	Ext. yaw mis. $\pm 20°$

3. Methodology and models

3.1. Aeroelastic simulation and design procedure

Aeroelastic calculations are performed with the Blade Element Momentum (BEM) based aeroelastic simulator `Cp-Lambda` (Code for Performance, Loads, Aeroelasticity by Multi Body Dynamic Analysis) [6], coupled with a conventional non-LAC controller [13]. This aeroelastic simulator is also the core of the wind turbine design suite, `Cp-Max` [1]. This code can perform the combined preliminary optimization of a wind turbine, including both blade and tower sizing. The optimization of the blade aeroelastic characteristics can be divided into two smaller sub-loops, which size the external aerodynamic shape and the structural components separately. In this work, the aerodynamic shape is kept frozen, and the turbine is redesigned only from the structural point of view. The structural optimization algorithm aims at minimizing blade cost, while guaranteeing its structural integrity and other requirements by enforcing a set of constaints. The optimization variables include the thickness of the structural elements for given blade layout and materials. The inertial and structural characteristics of each blade section are computed with the 2D finite element cross-sectional analysis code ANBA [10].

The tower structural sizing aims at minimizing tower cost, while satisfying a number of constraints to ensure the safety of the machine and other design requirements. The optimization variables include the diameter and thickness of the different tower segments for given material characteristics. The formal description of these algorithms can be found in [4, 1]. Both the blade and tower procedures employ a Sequential Quadratic Programming (SQP) optimization algorithm, in which gradients are computed by means of forward finite differences.

3.2. Baseline LAC load-reduction model

Multiple studies in the literature report the effects of LAC on loads for different controller formulations, such as feedforward, Linear Quadratic Regulator (LQR) or Model Predictive Control (MPC). Within these references, one specific study [7] is chosen to define the load-reduction model employed here. Reference [7] used a simple feedforward Lidar-assisted controller in combination with a conventional feedback controller on a 5 MW turbine.

The work reports reductions on an extensive set of loads for multiple components such as blade, tower and main bearing. Large reduction of fatigue loads resulting from DLC 1.2 for blade, main bearing, tower top and tower base are observed. Extreme loads resulting from DLC 2.3 also significantly benefit from the implementation of LAC. Table 2 reports the considered reduction coefficients for each component and *modifiable* DLC. For simplicity, this model does not include Lidar faults and assumes a Lidar availability of 100%.

DLC 2.1 deserves a specific discussion. Even though it is in principle a *modifiable* DLC, the precise estimation of LAC-induced reductions of extreme loads is difficult in this case. Extreme loads usually result from the wind turbine shut-down manoeuvre after grid disconnection. Since the wind excitation and the time at which grid loss occurs are both random, the state of the turbine at the time the shut-down manoeuvre is initatied is also random. This clearly makes it difficult to reliably estimate the load reduction, unless as specific dedicated simulation is conducted. Since these LAC-induced load reductions are still not fully described in the literature, they are here considered to be negligible.

In terms of Annual Energy Production (AEP), benefits are assumed to be 0.2% below rated speed and nonexistent above rated speed [7].

3.3. Cost models

The economic assessment is performed with different cost models. The SANDIA Blade Cost Model [11] is used to compute the blade cost for both onshore and offshore models. The 2015 NREL Cost Model [16], an updated version of the 2006 model [9], is applied for onshore machines, while the INNWIND Cost Model [8] is used for the study on offshore machines. The outputs

of both models are expressed in 2020€ , correspondingly inflated with the consumer price index and exchange rate. In order to ensure its comparability, LCOE is computed as

$$LCOE = \frac{FCR \cdot ICC}{AEP} + AOE,$$ (1)

where FCR [−] is the Fixed Change Rate, assumed to be 7%, ICC [€] is the Initial Capital Cost, AEP [MWh] is the Annual Energy Production and AOE [€/MWh] are the Annual Operating Expenses.

In addition to the standard turbine costs, the costs for the Lidar system have to be considered. Very conservative cost values for purchase and O&M of the Lidar hardware have been considered, based on the information from two major Lidar manufacturers. It has been assumed that two Lidar scanners have to be purchased over a turbine lifetime of 20 years. This results in additional $100,000$€ of ICC and $2,500$€/year of AOE. Only hardware-related costs have been regarded. Due to lack of information, the costs of development or licensing of Lidar-assisted turbine control software, related commissioning and software maintenance have been neglected.

Table 2: Load reduction coefficients considered in the baseline LAC load-reduction model

BLADE							
	Description	Fx	Fy	Fz	Mx	My	Mz
DLC 1.1 & 1.3	Extreme loads					-2.0%	
	Tip deflection					-2.0%	
DLC 1.2	DEL	-3.8%	-0.1%	-0.25%	-0.4%	-3.8%	-3.5%
DLC 2.3	Extreme loads					-2.9%	
	Tip deflection					-2.9%	
MAIN BEARING							
	Description	Fx	Fy	Fz	Mx	My	Mz
DLC 1.1 & 1.3	Extreme loads						
DLC 1.2	DEL	-10.0%			-1.2%	-0.4%	-1.0%
TOWER TOP (YAW BEARING)							
	Description	Fx	Fy	Fz	Mx	My	Mz
DLC 1.1 & 1.3	Extreme loads						
DLC 1.2	DEL	-12.0%	-0.1%	-2.1%	-2.0%	-1.8%	-0.2%
TOWER BASE							
	Description	Fx	Fy	Fz	Mx	My	Mz
DLC 1.1 & 1.3	Extreme loads					-5.0%	
DLC 1.2	DEL	-3.0%	0.2%	-2.2%	-0.1%	-12.0%	-0.2%
DLC 2.3	Extreme loads					-40.0%	

4. LAC-based effect on LCOE
4.1. Analyzed reference machines
The study is performed on three reference machines of different wind classes: an offshore 10 MW turbine (1A) [6] and two onshore machines: a 2.2 MW (2A) [1] and a 3.4 MW (3A) [2]

turbine. The general characteristics of these turbines, including blade length and tower height, are described in Table 3. A detailed characterization of these machines can be found in the corresponding references.

Table 3: Main characteristics of the reference models included in the study

Turbine	1 [6]	2 [1]	3 [2]
IEC Class & Category	1A	2A	3A
Rated electric power [MW]	10	2.2	3.4
Rotor diameter [m]	178.3	92.4	130.0
Specific power $[W/m^2]$	400.5	298.3	252.4
Hub height [m]	119.0	80.0	110.0
Blade mass [t]	42.5	8.6	16.4
Tower mass [t]	628	125	553

These machines are representative of currently installed wind turbines. The costs of these three machines are compared to the costs of reference projects in the US in terms of capital (CAPEX), operational expenses (OPEX), AEP and LCOE. The first three figures are normalized by rated power. Table 4 shows a good match between the costs of the onshore 2A machine and a generic 2.32 MW turbine of a reference onshore project in the US in 2017 [15]. The costs of the 3A turbine, even if slightly higher for some figures, also follow well the values of the reference turbine. In the second column, the costs of a bottom-fixed offshore 5 MW machine are compared with the 1A machine used in this study. Large differences are found here, for instance in OPEX costs, due to the very different rating of the turbines. In general, the cost distribution presents a similar pattern to the considered reference. The cost breakdown comparison is expressed in 2017 United States Dollars (USD) and CAPEX does not include financial costs. LCOE has been recomputed in all cases as indicated in Eq. (1).

Table 4: Comparison of cost breakdown of the different reference models in 2017 USD

	Onshore			Offshore	
	Stehly et al. [15]	2A	3A	Stehly et al. [15]	1A
Rating [MW]	2.32	2.2	3.4	5	10
CAPEX [USD/kW]	1454	1297	1759	3846	4379
OPEX [USD/kW]	43.6	48.1	51.4	144	225
AEP [MWh/MW]	3633	3520	3866	3741	4500
FCR [%]	7.9	7.9	7.9	7.0	7.0
LCOE [USD/MWh]	43.6	42.9	49.2	110.5	118.1

4.2. Load analysis: Potential reduction margins

The analysis of the load rankings highlights important potential reduction margins that could be exploited by LAC. Figure 1 provides an overview of the ranking position of the first *blocking* DLC for each machine.

Blade tip deflection: As shown in Fig. 1a, this ranking is led by *modifiable* DLCs and reductions are blocked by DLC 2.1 for all machines. More specifically, the reduction margin for turbine 1A is blocked at ranking position 7, for turbine 3A at ranking position 20, and for turbine 2A at ranking position 28. The analysis unveils potential reduction margins of tip displacement between 8% (1A) and 21% (2A). These margins could be exploited in the design of the blade, since maximum tip deflection is typically an important active design driver for the spar caps.

Extreme loads: The analysis of the combined blade root moment ranking (Fig. 1b) leads to similar conclusions. Indeed, DLC 2.1 is here also the first *blocking* DLC to appear for the three turbines, with large potential reduction margins in machines 2A and 3A.

Combined bending moment at tower top (Fig. 1c) shows no potential margin for machine 1A, and reduced margins for turbines 2A and 3A. This potential reduction could relax the buckling constraint. No potential reduction margin is found at tower bottom (Fig. 1d), a load clearly driven by *blocking* cases.

Fatigue: In the case of fatigue, only DLC 1.2 has to be considered according to the standards. Thus, there are no *blocking* DLCs and fatigue reductions from LAC fully translate into relaxed design constraints.

(a) Blade tip deflection

(b) Combined blade root moment (CBRM)

(c) Combined bending moment at tower top (CBMTT)

(d) Combined bending moment at tower bottom (CBMTB)
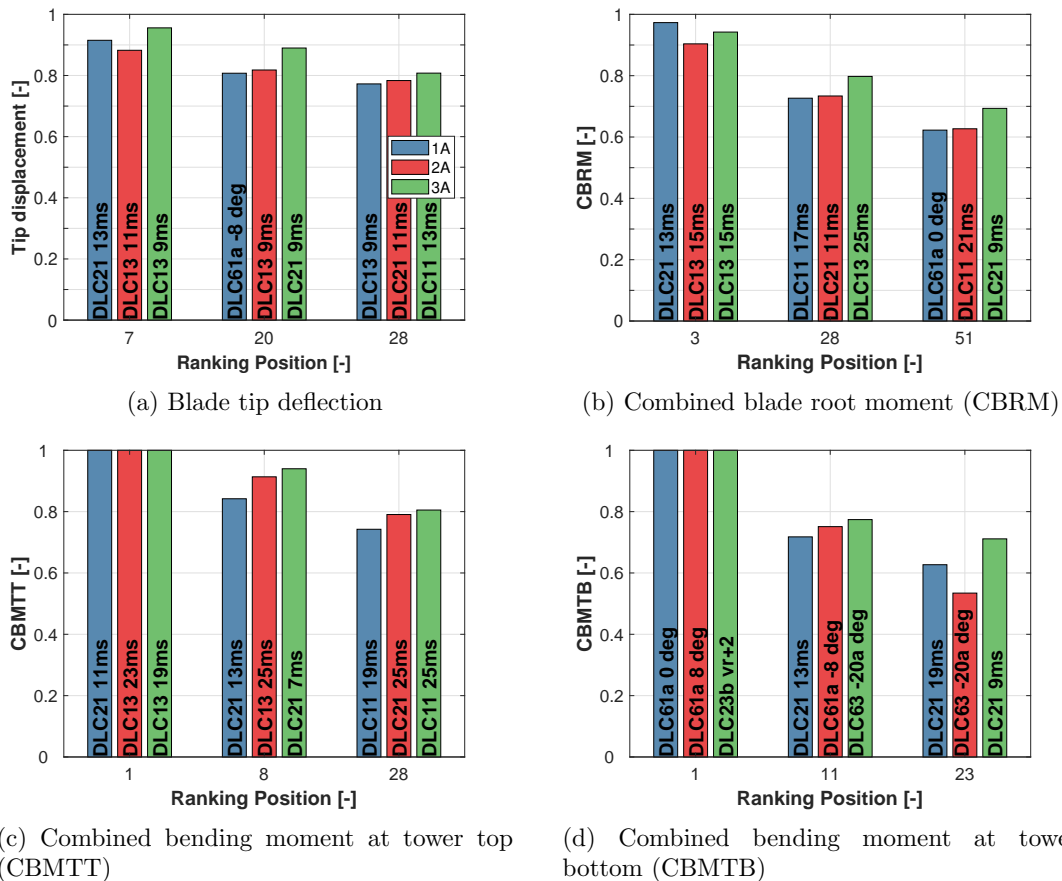
Figure 1: Ranking position of the first appearing *blocking* case for different key quantities and machines. Results are normalized with the maximum load of the respective turbine.

4.3. LAC-induced reductions in blade and tower mass

For the LAC-based redesign of the turbines, the load-reduction coefficients of Table 2 are applied to the loads resulting from initial *non-LAC* runs of all DLCs. Consequently, the design parameters are varied until convergence of the SQP algorithm. This sequence of simulation, application of reduction margins and optimization is repeated until convergence.

The LAC-based redesign leads to large reductions in tower mass and more modest savings in blade mass, as reported in Fig. 2.

Tower: Both the 1A and 3A towers enjoy significant benefits from the large reductions in fatigue and achieve a mass reduction between approximately 17% for the optimistic scenario and approximately 5% for the pessimistic one.

The tower of the 2A machine presents a smaller improvement due to different active design drivers. Indeed, this model presents an increased importance of the buckling constraints when compared to the other turbines. Even though a potential reduction margin of 10% was found in the load analysis for combined bending moment at tower top (Fig. 1c) —a load that may drive the tower buckling behavior— this is not reduced by LAC according to the applied load-reduction model (Table 2), and therefore cannot be exploited.

Blades: Modest reductions are achieved at the blades of all models and for all scenarios, due to the moderate influence of LAC in design-driving constraints. Even though a large potential margin was found for tip deflection, the applied LAC load-reduction model in Table 2 only allows for a reduction of 2%.
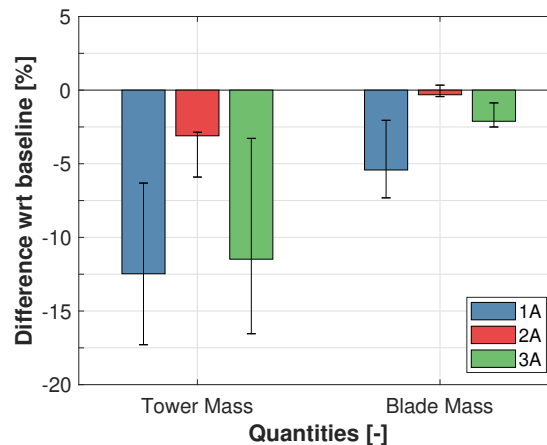
Figure 2: LAC-induced reductions in tower mass and blade mass. The confidence intervals show the values for the optimistic (lower end) and pessimistic scenarios (upper end), introduced by a correction factor.

4.4. LAC-induced reductions in LCOE

LAC-generated improvements not always translate into noticeable LCOE changes. For the 2A turbine, low tower mass reductions in combination with the significant Lidar costs clearly lead to an increase of LCOE. More interesting conclusions are obtained when analyzing the 1A and 3A machines.

While both machines present significant reductions in ICC, a different effect is observed in annual operating expenses (AOE). Indeed, the additional expenses created by maintenance of the Lidar system do not significantly increase the overall AOE for offshore machines, due to the already high O&M expenses. For onshore machines, these costs play a larger role and increase AOE by approximately 2%.the Additionally, AEP is slightly increased for both onshore and offshore

machines. While turbine 1A achieves reductions between 0.5% and 2% in LCOE, for machine 3A a slight decrease of 0.5% is achieved with the best performing scenario.

The reduction in ICC reached by the blade redesign is generally not high enough to compensate for the increase of AOE. Therefore LCOE increases for all onshore machines and slightly decreases for the offshore machine.
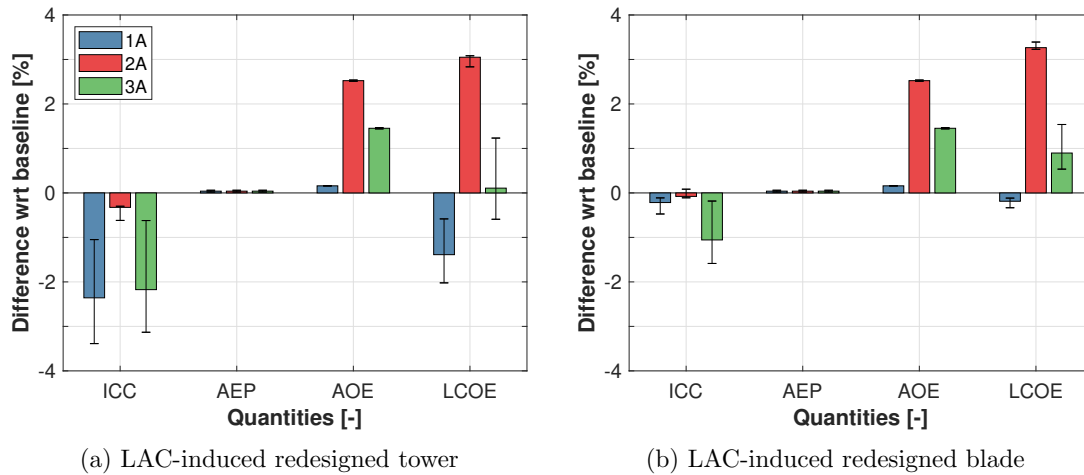

(a) LAC-induced redesigned tower   (b) LAC-induced redesigned blade

Figure 3: LAC-induced reductions in Initial Capital Costs (ICC), Annual Energy Production (AEP), Annual Operating Expenses (AOE) and Levelized Cost Of Energy (LCOE) for tower (left) and blade redesigns (right). The confidence intervals show the values for the optimistic (lower end) and pessimistic scenarios (upper end), introduced by the correction factor.

4.5. Cost sensitivity analysis

Finally, a cost sensitivity analysis is performed to understand how the purchase and maintenance cost of a Lidar system can influence the reduction in LCOE. The analysis is performed on the scenario with baseline LAC load-reduction coefficients.

In the case of the 1A machine (Fig. 4a), LCOE shows little variability when both purchase and maintenance costs are modified. Larger effects are observed for the 3A machine (Fig. 4b). Here an increase or redution of LCOE can be obtained by modifying the LAC system costs. Both machines show modest reductions in LCOE, even with very low LAC costs, implying that a real effect on LCOE can only be achieved by an improved LAC performance in some key loads.

5. Conclusions

This paper has presented a preliminary analysis on the potential benefits of considering LAC at the first stages of wind turbine design. A first load analysis highlights an interesting potential for the blade as well as for fatigue-driven tower designs. For instance, potential reduction margins of up to 20% are observed in tip deflection, as well as in the combined bending moment at tower top. The current LAC systems are only partially exploiting the reduction potential of these loads. Indeed, according to the load-reduction model considered here, blade tip deflection is reduced up to 2% and combined bending moment at tower top is not reduced, leading to negligible benefits for the rotor and buckling-driven towers. Fatigue-driven towers enjoy a more significant effect, since fatigue is greatly reduced by LAC.

In terms of LCOE, the offshore machine shows the largest reductions for all considered systems. This turbine significally benefits from the reduced influence of the additional LAC-based costs, given the already high O&M and ICC figures. In this case, the purchase and O&M costs of
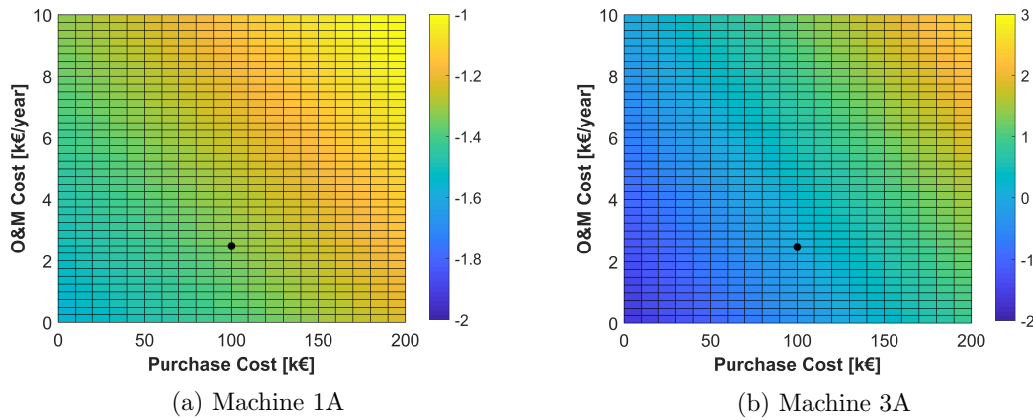
(a) Machine 1A   (b) Machine 3A

Figure 4: Sensitivity analysis of the effect of the purchase and O&M cost of LAC systems on LCOE reduction for the offshore (1A) and onshore (3A) machines. The baseline costs are indicated with a black circle.

Lidar do not play a large role in the overall achieved LCOE reduction. For the onshore machine, the effect on LCOE shows a higher sensitivity to the performance and costs of a LAC system.

This study only partially explores the benefits of introducing LAC in the early stages of wind turbine design. Indeed, even though this study gave some insight into how design differences in the tower can influence the LAC-induced benefits, a deeper analysis of the design drivers should be performed to get a more complete picture. Additionally, the list of analyzed DLCs should be expanded to include other design conditions that occasionally result in design drivers, such as DLC 1.4 (power production with extreme coherent gust with direction change) or DLC 1.5 (power production with extreme wind shear). Further work should also analyze the effects of a reduced Lidar availability, since the current load-reduction model assumes an availability of 100%. Additionally, other applications of LAC should be explored. For instance, LAC-induced lower loading could be exploited to increase hub height and gain power capture. Finally, it should be remarked that the use of a generic load model implies some significant approximations, and more precise conclusions could be obtained with the use of a Lidar simulator and a specific controller implementation.

6. Acknowledgements

7. References
[1] Bortolotti P and Bottasso CL and Croce A 2016 Combined preliminary-detailed design of wind turbines *Wind Energ. Sci.* **1** 71-88 10.5194/wes-1-71-2016
[2] Bortolotti P, Canet H, Dykes K, Merz K, Sethuraman L, Verelst D and Zahle F 2019 IEA Wind TCP Task 37: Systems engineering in wind energy - WP2.1 Reference wind turbines *National Renewable Energy Laboratory technical report* Golden, CO 10.2172/1529216
[3] Bottasso CL, Croce A, Savini B, Sirchi W and Trainelli L 2006 Aero-servo-elastic modeling and control of wind turbines using finite-element multibody procedures. *Multibody Syst. Dyn.* **16** 291-308 10.1007/s11044-006-9027-1
[4] Bottasso CL, Campagnolo F and Croce A 2012 Multi-disciplinary constrained optimization of wind turbines *Multibody Syst. Dyn.* **27** 21-53 10.1007/s11044-011-9271-x

[5] Bottasso CL, Croce A, Nam Y and Riboldi CED 2012 Power curve tracking in the presence of a tip speed constraint *Ren. En.* **40** 1-12 10.1016/j.renene.2011.07.045

[6] Bottasso CL, Bortolotti P, Croce A and Gualdoni F 2016 Integrated aero-structural optimization of wind turbines *Multibody Syst. Dyn.* **38** 317-344 10.1007/s11044-015-9488-1

[7] Bossanyi E, Kumar A and Hugues-Salas O 2014 Wind turbine control applications of turbine-mounted Lidar *J. Phys.: Conf. Ser.* **555** 012011 10.1088/1742-6596/555/1/012011

[8] Chaviaropoulos P, Karga I, Harkness C and Hendriks B 2014 Deliverable 1.23 PI-Based assessment of innovative concepts *INNWIND.EU technical report*

[9] Fingersh L, Hand M and Laxson A 2006 Wind turbine design cost and scaling model *National Renewable Energy Laboratory technical report* Golden, CO NREL/TP-500-40566

[10] Giavotto V, Borri M, Mantegazza P and Ghiringhelli G 1983 Anisotropic beam theory and applications *Comput. Struct.* **16** 403-13 10.1016/0045-7949(83)90179-7

[11] Griffith DT and Johans W 2013 Large blade manufacturing cost studies using the sandia blade manufacturing cost tool and Sandia 100-meter blades *Sandia National Laboratories technical report* Albuquerque, NM SAND2013-2734

[12] International Electrotechnical Commission 2005 IEC 61400-1 Ed.3: Wind turbines - Part 1: Design requirements

[13] Riboldi CED 2012 Advanced control laws for variable-speed wind turbines and supporting enabling technologies *Politecnico di Milano Doctoral dissertation* Milan, Italy

[14] Schlipf D, Fürst H, Raach S and Haizmann F 2018 Systems engineering for Lidar-assisted control: A sequential approach. *J. Phys.: Conf. Ser.* **1102** 012014 10.1088/1742-6596/1102/1/012014

[15] Stehly T, Beiter P, Heimiller D and Scott G 2017 Cost of wind energy review *National Renewable Energy Laboratory technical report* Golden, CO NREL/TP-6A20-72167

[16] WISDEM Repository 2020 github.com/WISDEM

A.6 Paper VI: What are the benefits of lidar-assisted control in the design of a wind turbine?

WIND
ENERGY
SCIENCE

Open Access

What are the benefits of lidar-assisted control in the design of a wind turbine?

Helena Canet, Stefan Loew, and Carlo L. Bottasso

Wind Energy Institute, Technical University of Munich, 85748 Garching bei München, Germany

Correspondence: Carlo L. Bottasso (carlo.bottasso@tum.de)

Abstract. This paper explores the potential benefits brought by the integration of lidar-assisted control (LAC) in the design of a wind turbine. The study identifies which design drivers can be relaxed by LAC, as well as by how much these drivers could be reduced before other conditions become the drivers. A generic LAC load-reduction model is defined and used to redesign the rotor and tower of three representative turbines, differing in terms of wind class, size, and power rating. The load reductions enabled by LAC are used to save mass, increase hub height, or extend lifetime. For the first two strategies, results suggest only modest reductions in the levelized cost of energy, with potential benefits essentially limited to the tower of a large offshore machine. On the other hand, lifetime extension appears to be the most effective way of exploiting the effects of LAC.

1 Introduction

Wind turbines are highly dynamical systems, excited by stochastic and deterministic disturbances from wind. Among their various goals, wind turbine control systems aim at limiting structural loads. In fact, lower ultimate and fatigue loading can be exploited to reduce mass and cost or to design larger and taller turbines that can generate more energy; in turn, all these effects may lead to a reduction of the cost of energy.

Traditional wind turbine controllers rely on feedback measurements to drive blade pitch, generator torque, and yaw. Since they operate based on the response of the system as expressed by live measurements, these controllers are only capable of reacting to wind disturbances that have already impacted the wind turbine. This is an intrinsic limitation of all feedback-based mechanisms: since control actions are based on past measurements, the controller is always "late", in the sense that it reacts to events that are already taking place. To improve on this situation, control systems can be augmented with preview information, which informs the controller on the wind that will affect the turbine in the immediate future.

Wind preview can be obtained from turbine-mounted light detection and ranging (lidar) sensors, which are capable of measuring various properties of the incoming flow field up to

several hundred meters in front of the rotor. Lidar-augmented control strategies are generically termed lidar-assisted control (LAC).

Several LAC formulations have already been investigated, and their performance in terms of power capture and load mitigation are reported in the literature. Bossanyi et al. (2014) describe a standard feedback controller enhanced by a feedforward blade pitch branch enabled by lidar wind preview. Results indicate promising reductions in blade flap and tower fore–aft fatigue damage, without any appreciable loss in power production. Similar benefits are described by other sources such as, for example, Dunne et al. (2011, 2012). Benefits have also been confirmed in the field (Schlipf et al., 2013c), albeit to the present date only on a small research wind turbine. Feedforward torque control strategies have also been investigated; results indicate marginal increments in mean power capture at the expense of high power and torque variations (Bossanyi et al., 2014; Wang et al., 2013; Schlipf et al., 2013). More advanced formulations, such as nonlinear model-predictive controllers (Schlipf et al., 2013b) or flatness-based controllers (Schlipf et al., 2014), have also been enhanced with lidar wind preview information. Promising results were reported in terms of load reductions and power increase, at the expense of a much higher computa-

tional cost, which makes real-time execution more challenging to achieve and test in the field (Scholbrock et al., 2016).

Even though the potential of LAC is widely recognized, the system-level benefits that LAC may possibly bring to the levelized cost of energy (LCOE) are still not fully understood. In general two strategies have been suggested for reducing LCOE by LAC (Schlipf et al., 2018). The first is the *retrofit strategy*, which consists in using lidars to extend the lifetime of a wind turbine that has already been designed and installed. For example, Schlipf et al. (2018) reported the extension of the lifetime of a tower by 15 years. A second strategy is the *integrated approach*, in which LAC is considered as part of the system from its very inception. The idea in this second case is that, by considering LAC within the design process, its full potential can be realized by translating the benefits of load reductions directly into an improved turbine. Indeed, the adoption of a holistic system-level design approach was identified as an opportunity to assess the cost-benefit tradeoffs among turbine, lidar and control system by two IEA Wind Tasks: Task 32 on wind energy lidar systems, and Task 37 on systems engineering for wind energy (Simley et al., 2018, 2020).

This work aims at taking a first step in this direction, providing an initial rough assessment of the potential benefits of considering LAC in the sizing of the two primary components of a wind turbine, namely the rotor and tower. The present work refines and expands the study described in Canet et al. (2020). In a nutshell, this study tries to give a preliminary general answer to the following main research questions:

- To which extent can design-driving constraints be relaxed by LAC?

- What is the best way of reaping the benefits brought by LAC in the design of rotor and tower?

- To make LAC beneficial at the system level, is it necessary to improve its performance or reduce its cost?

The present investigation intentionally does not commit to a specific lidar hardware or control formulation. In fact, the effects of LAC are considered here through a load-reduction model, defined according to the average performance of LAC systems reported in the literature. To understand trends, rather than focusing on a specific case, this baseline average literature-sourced model is expanded to cover an optimistic and a pessimistic scenario, thereby providing a range of possible behaviors. The study is performed on three wind turbines, which differ for wind class, size and power rating. These three reference machines are reasonable representations of current wind turbines available on the market. Clearly, the application of a literature-sourced range of load-reductions to three very different machines cannot give final and precise answers, which would require dedicated turbine and control-specific analyses conducted with coupled LAC-turbine simulations. However, the present approach offers a

way of obtaining an initial preliminary assessment of the potential benefits of adopting LAC, and it helps pinpoint the most promising applications that should be further analyzed.

The paper is organized as follows. Section 2 describes the approach and the models used in the study, while Sect. 3 analyzes the potential benefits of integrating LAC in the design of the tower and rotor of three different reference wind turbines. The study considers mass (and hence cost) reductions of these two components, but also investigates the design of towers that are taller or have a longer lifetime, including the effects of the purchase and maintenance costs of the onboard lidar system. Section 4 closes the paper by reporting and discussing the main conclusions of the study.

2 Approach

Figure 1 presents a graphical depiction of the approach used in the present work. In a first phase, each turbine model is analyzed using a baseline non-LAC controller. This analysis highlights the benefits of reducing some design-driving quantity, and indicates by how much that quantity could be improved before another effect starts driving the design. Based on this information, a second phase of the analysis initially considers each turbine equipped with a LAC controller, and then exploits the obtained load-reduction benefits to perform a structural redesign. Finally, the improved design is subjected to an economic analysis, whose goal is to establish tradeoffs between weight savings made possible by LAC and the additional expenses due to the purchase and operation and maintenance (O&M) costs of the lidar. More details on these analysis processes are provided in the next sections.

2.1 Assessment of potentially exploitable margins

Design-driving quantities are those key indicators that define active constraints, thereby affecting the design solution. Design-driving quantities can be modified by LAC – or, more in general, by any control or technological solution – only to some extent, past which some other effect beyond the reach of LAC becomes the driver, preventing further improvements. The extent by which a design-driving quantity can be affected before another one becomes the driver is called here a *potentially exploitable margin* (PEM). It is an exploitable margin because, if it can be achieved, the design-driving constraints can be relaxed and, therefore, the design can be improved. It is, however, only a potential margin because it represents an upper bound: in fact, a smaller improvement might be actually obtainable by LAC than this maximum limit.

A PEM is clearly a very valuable piece of information: there is no point in using LAC to reduce a certain quantity past the value where the driver switches to some condition that is not controllable by LAC. In fact, any further reduction would be futile, as it would not affect the design-driving constraints and therefore the final design.
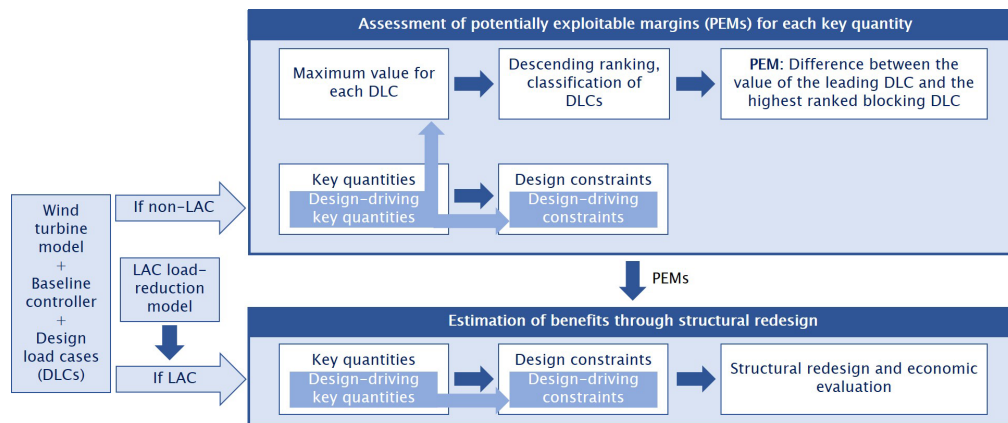
Figure 1. Approach overview.

These considerations clearly do not apply exclusively to LAC but more in general hold for any technology that has the potential to relax the design constraints of a system. Therefore, the analysis of PEMs is an extremely useful exercise, because

– it is able to highlight the possible design benefits brought by the introduction of a new technology and

– it gives a target maximum margin of improvement that that technology should bring.

In the context of the current analysis, the assessment of PEMs is based on key quantities such as ultimate and fatigue loads, and elastic deflections, which result from the aeroservoelastic simulation of a comprehensive set of design load cases (DLCs) run with a non-LAC controller. DLCs represent the different operating conditions that a wind turbine encounters throughout its lifetime, as defined by certification standards (IEC, 2005).

For the purposes of this work, DLCs are classified in two distinct groups: *modifiable* and *blocking*. In modifiable DLCs, the maximum value of each key quantity depends on the controller. For example, this is the case of loads obtained in power production conditions (DLC 1.X). In fact, by modifying the pitch–torque controller of the turbine, the response of the machine changes, and consequently the loads that are produced also change. On the contrary, in blocking DLCs the key quantities are not affected by the controller. For instance, this is the case of loads generated in parked conditions (DLC 6.X). In fact, as the pitch–torque controller is not active when the turbine is parked, it clearly cannot influence the loads that are generated in that condition. Table 1 presents a classification of a selection of DLCs, including a description of the corresponding operating condition.

PEMs are obtained via a two-step procedure.

First, the (active) design constraints that determine the sizing of a given wind turbine component are identified; these are termed *design drivers* or *design-driving constraints*. Design constraints are introduced in the structural design process of a wind turbine component to guarantee structural safety during its lifetime, ensuring that admissible values for stress, strain, and fatigue damage are never exceeded. Additional constraints are enforced to guarantee a safe clearance and to avoid collisions between the blade and tower, to prevent buckling, and to ensure all other desired characteristics from the resulting design (Bottasso and Bortolotti, 2019). These constraints are functions of the key quantities resulting from the various DLCs, augmented by safety factors as prescribed by the norms. Other constraints, such as those enforced to avoid resonant conditions, are not dependent on DLCs.

Second, the maximum value of a key quantity is extracted from each considered DLC. The values are then sorted in descending order and labeled with the indication of the originating DLC. Each DLC is classified as modifiable or blocking. Clearly, the maximum value of a key quantity can only be reduced by LAC if its ranking is led by a modifiable DLC. The PEM is computed for each design-driving key quantity, and it is obtained as the difference between the quantity maximum value and the value of the highest-ranked blocking DLC.

2.2 Estimation of benefits through structural redesign

PEMs can be exploited to improve the structural design of the wind turbine components that are driven by modifiable DLCs. To this end, DLCs should be run again, this time using LAC to yield new reduced values of the key quantities. However, as argued earlier on, instead of focusing on a particular case, it is more interesting to perform an analysis that is less specific and more general in character. To this end, a LAC load-reduction model was used here instead of re-running all DLCs with a given LAC in the loop. The load-reduction model is simply represented by a set of multiplicative co-

Table 1. Classification of a selection of the design load cases into *modifiable* and *blocking* (see text for a definition). NTM: normal turbulence model; ETM: extreme turbulence model; ECD: extreme coherent gust with direction change; EWS: extreme wind shear; EOG: extreme operating gust; EWM: extreme wind speed model.

Classification	DLC	Design situation	Wind speed	Wind profile	Other condition
Modifiable	1.1	Power production	$V_{in} : V_{out}$	NTM	
	1.2	Power production	$V_{in} : V_{out}$	NTM	
	1.3	Power production	$V_{in} : V_{out}$	ETM	
	1.4	Power production	$V_{rated} \pm 2\,\mathrm{ms}^{-1}$	ECD	
	1.5	Power production	$V_{in} : V_{out}$	EWS	
	2.1	Power production	$V_{in} : V_{out}$	NTM	Grid loss
	2.3	Power production	$V_{out}, V_{rated} \pm 2\,\mathrm{ms}^{-1}$	EOG	Grid loss
Blocking	6.1	Parked	V_{ref}	EWM 50 year	Yaw mis. $\pm 8°$
	6.2	Parked	V_{ref}	EWM 50 year	Grid loss
	6.3	Parked	V_{ref}	EWM 1 year	Ext. yaw mis. $\pm 20°$

efficients, which are defined for each key quantity associated with a modifiable DLC. Each coefficient expresses how LAC affects a key quantity with respect to a non-LAC controller; therefore, load reductions correspond to coefficients smaller than one in the model. Clearly, such coefficients depend on a multiplicity of factors, such as the specific control formulation, the tuning of its gains, or the performance of the lidar system. While a specific analysis is crucial when actually designing a wind turbine and its control system, a specific analysis also clearly hinders somehow the generality of the results and conclusions that can be drawn from it. In this spirit, a range of possible performances – in contrast to a case-specific performance – is considered here by defining different load-reduction scenarios. The load-reduction model and additional scenarios are based on results sourced from the literature, as more precisely discussed in Sect. 2.3.

The application of a LAC load-reduction model lowers some of the key quantities, in turn deactivating the associated design-driving constraints. To exploit the slack generated by LAC in the formerly active constraints, a redesign is performed to determine the structure that minimizes a desired figure of merit while guaranteeing structural integrity, in turn reactivating the constraints. After the redesign, an economic evaluation reveals the potential gains in LCOE, as discussed in Sect. 2.4.

2.3 LAC load-reduction model

The load-reduction model is based on a literature survey. The study reported in Bossanyi et al. (2014) was chosen as reference, because it presents a comprehensive list of the effects of LAC for several key quantities of various components. Additionally, that work was based on a rather standard controller, which might be representative of an initial conservative deployment on production machines. The implementation used a simple feedforward collective pitch LAC combined with a conventional feedback controller, applied

to a 5 MW turbine. The paper reports a significant reduction of damage equivalent loads (DELs) resulting from DLC 1.2 for the blades, main bearing, tower top, and tower bottom. Extreme loads resulting from extreme operating gust conditions also experience significant benefits. On the other hand, power capture – and hence annual energy production (AEP) – is largely unaffected by this LAC implementation.

The load-reduction model derived from Bossanyi et al. (2014) is reported in Table 2 for each component and modifiable DLC, in terms of percent changes with respect to a non-LAC controller. In the table, F and M respectively indicate force and moment components, expressed in the (x, y, z) righthanded triad, where x points downstream, y is in the crossflow direction, and z points vertically upwards. Components not reported in the table experience either null or negligible reductions.

The load-reduction model reported in Table 2 prompts a few important remarks.

First, the model only includes DLC 1.1, 1.2, and 1.3, which represent power production cases. In reality, these are not the only DLCs that are modifiable – in the sense that they can be affected by a change in the controller. In fact, additional modifiable DLCs are represented by DLC 1.4 (power production with extreme wind direction), 1.5 (power production with extreme wind shear), 2.1 (power production with control system fault or grid disconnection under normal turbulence conditions), and 2.3 (power production with control system fault or grid disconnection under extreme operating gusts). The first two of these DLCs are not considered in the LAC load-reduction model because they do not typically generate design-driving loads, as further explained in Sect. 3.1. The case of DLC 2.1 and 2.3 is, however, different: here, maximum loads are typically generated during a shutdown, triggered by an extreme ambient condition change, a fault, or a grid disconnection. When this happens, the entity of the generated loads will be largely dictated by the behavior of the shutdown procedure, which here is as-

Table 2. Load-reduction coefficients based on Bossanyi et al. (2014), expressed as percentages with respect to a non-LAC controller.

Blade							
	Key quantity	Fx	Fy	Fz	Mx	My	Mz
DLC 1.2	DEL	−3.8 %	−0.1%	−0.25 %	−0.4 %	−3.8 %	−3.5 %
DLC 1.X	Extreme loads					−2.0 %	
	Tip deflection					−2.0 %	

Main bearing							
	Key quantity	Fx	Fy	Fz	Mx	My	Mz
DLC 1.2	DEL	−10.0 %			−1.2 %	−0.4 %	−1.0 %
DLC 1.X	Extreme loads						

Tower top (yaw bearing)							
	Key quantity	Fx	Fy	Fz	Mx	My	Mz
DLC 1.2	DEL	−12.0 %	−0.1 %	−2.1 %	−2.0 %	−1.8 %	−0.2 %
DLC 1.X	Extreme loads						

Tower bottom							
	Key quantity	Fx	Fy	Fz	Mx	My	Mz
DLC 1.2	DEL	−3.0 %	0.2 %	−2.2 %	−0.1 %	−12.0 %	−0.2 %
DLC 1.X	Extreme loads					−5.0 %	

sumed not to be assisted by a lidar for safety reasons. On the other hand, loads generated during a shutdown might also depend to some extent on the state of the turbine at the time the shutdown was triggered, which does depend on the behavior of the LAC controller. A precise quantification of the effects of LAC on these DLCs would therefore require simulations with LAC in the loop, which are outside of the scope of the present preliminary work.

This point, however, leads to a second, more general, observation: the model in fact includes both DELs and extreme loads, neglecting lidar faults and assuming a lidar availability of 100 %. While faults and availability (as long as it is not excessively low) will not impact DELs significantly, the situation is much more complicated for extreme loads. In fact, the malfunctioning of a lidar might in principle generate increases in ultimate loads, compared to a non-LAC case. A precise analysis of the possible faults and their consequences is clearly not only complex, but also highly case-specific. A mitigation of negative effects caused by faults could be achieved, for example, through triple modular redundancy (Koren and Krishna, 2020), which would, however, clearly affect costs. A comprehensive analysis of these effects is outside of the scope of the present simplified study, and fault-induced increases of ultimate loads are therefore neglected here. Although this is an apparently strong assumption, in the end it does not affect the results of this study. In fact, as shown later, the benefits of the present LAC model on the turbines considered here are confined to fatigue mitigation, and hence only fatigue-driven components do benefit from

LAC in this study. At a more general level, one could wonder whether system-level benefits could be obtained by using LAC also for components driven by ultimate loads. While this remains an open question for now – as the present work is not able to provide definitive answers – it is clear that such an approach drastically raises the bar in terms of the complexity of the analysis and of the implementation, because of its obvious safety-related implications.

Third, differences in the formulation and tuning of a LAC controller will generally imply different reductions of key quantities. To estimate these effects, the results obtained from various authors were compared. The most complete set of results was found for DLC 1.2 in terms of DELs for fore–aft tower bending at tower bottom (FABMTB), flap-wise blade root moment (FBRM), and shaft torsional moment (STM), as reported by Schlipf et al. (2014, 2015), Bottasso et al. (2014), Haizmann et al. (2015), Schlipf (2016), and Sinner et al. (2018). Table 3 reports the outcome of this analysis. There is a significant scatter in the results, especially for DEL FBRM and DEL STM, because of the variety of controller formulations and target wind turbine models. For instance, for DEL STM Schlipf et al. (2014) report a load reduction of 30 % using a flatness-based feedforward controller, while Schlipf (2016) reports an improvement of 6 % when using a feedforward–feedback controller. The lower values reported in Bossanyi et al. (2014) are most likely caused by the utilization of a fairly simple controller.

The scatter shown in Table 3 motivates the definition of two additional sets of coefficients that represent optimistic

Table 3. LAC-enabled load reductions from Bossanyi et al. (2014) compared to other references.

	Bossanyi et al. (2014)	Additional literature
DEL FABMTB	−12 %	−16.4 % ± 9.1 %
DEL FBRM	−3.8 %	−13.4 % ± 6.6 %
DEL STM	−1.2 %	−11.8 % ± 9.3 %

and pessimistic scenarios and provide a more general view of the benefits of LAC. The optimistic scenario is obtained by multiplying the baseline coefficients by a factor of 1.5, whereas the pessimistic one is obtained by using a factor of 0.5. Here again, it is worth remembering that the present study does not target one specific LAC controller but aims at understanding basic trends.

A distinction must be made between the application of load-reduction coefficients to ultimate loads and deflections, which is straightforward (with the caveat of the effects of faults, as previously discussed), and to fatigue loads. The former simply consists in the correction of the key quantities obtained by a non-LAC controller with the corresponding coefficients of the load-reduction model. Combined loads – for example, at tower base or at the main and blade pitch bearings – are computed from the corrected individual load components.

For fatigue damage, the following procedure is used. Site-weighted DELs are computed as

$$\mathrm{DEL} = \sum_{v=V_{\mathrm{in}}}^{v=V_{\mathrm{out}}} f(v) L_{\mathrm{eq}}(v), \tag{1}$$

where $f(v)$ is the Weibull probability density function at a wind speed v, while the damage equivalent load at that same wind speed is expressed as

$$L_{\mathrm{eq}} = \left(\frac{\sum_{i=1}^{n} S_{\mathrm{r},i}^{m}}{N_{\mathrm{eq}}} \right)^{1/m}, \tag{2}$$

where m is the Wöhler coefficient, $S_{\mathrm{r},i}$ is the load range of a cycle i, n is the total number of cycles, and N_{eq} is the equivalent number of cycles (Hendriks and Bulder, 1995).

To compute LAC-reduced DELs, it is assumed that load reductions are independent of wind speed and load range. This way, the Weibull-weighted DEL reductions reported in the literature can be applied directly to the load time histories obtained here with a non-LAC controller by aeroelastic simulations. Clearly this is an approximation, as LAC-enabled reductions generally depend on the wind speed, as reported by several studies (Bottasso et al., 2014; Schlipf et al., 2018, 2013). However, it was verified by aeroelastic analyses that this assumption does not significantly affect the results when the reduction coefficients are small, as those reported in Tables 2 and 3. For example, with reference to Table 3,

considering the DEL FBRM reduction of −3.8 %, the difference in fatigue margin at the blade root between wind-speed-dependent and independent reductions was found to be less than 2 %; for the DEL FABMTB reduction of −12 %, the fatigue margin difference at tower base was found to be approximatively equal to 5 %. Given the character of this study, these differences were deemed to be acceptable and well within the margin of uncertainty of the analysis.

To complete the calculation of LAC-reduced DELs, transient combined loads are computed from the relevant components (for example, combining fore–aft and side–side components at tower base and similarly combining the associated components at the main and pitch bearings) and then processed by rainflow counting to obtain DELs, finally searching for the point in the cross section of interest with the maximum damage. The computation of fatigue margin constraints for the steel tower is performed following the European regulations (EN 1993-1-9, 2006).

2.4 Economic evaluation

During the redesign phase, the components are evaluated from an economic point of view through suitable cost models, based on the characteristics of the wind turbine. The 2015 NREL cost model (NREL, 2020), which is an updated version of the 2006 model (Fingersh et al., 2006), is used for onshore machines, whereas the INNWIND cost model (Chaviaropoulos et al., 2014) is used for offshore turbines. The blade cost for both onshore and offshore models is computed based on the SANDIA cost model (Griffith and Johans, 2013). All cost model estimates are expressed in 2020 Euros (EUR), inflated by the consumer price index and exchange rate. The comparison of the various designs is based on LCOE, which is computed as

$$\mathrm{LCOE} = \frac{\mathrm{FCR} \cdot \mathrm{ICC}}{\mathrm{AEP}} + \mathrm{AOE}, \tag{3}$$

where FCR [–] is the fixed change rate, ICC [EUR] the initial capital cost, AEP [MWh] the annual energy production, and AOE [EUR/MWh] the annual operating expenses.

2.5 Design and simulation environment

Aeroelastic analyses are performed with the blade element momentum (BEM)-based aeroelastic simulator Cp-Lambda (Bottasso et al., 2016), coupled with a conventional non-LAC controller (Riboldi et al., 2012). The aeroelastic simulator Cp-Lambda is also the core of the wind turbine design suite Cp-Max (Bottasso and Bortolotti, 2019; Bortolotti et al., 2016). This code can perform the combined preliminary optimization of a wind turbine, including both rotor and tower sizing.

The optimization of the blade aeroelastic characteristics can be divided into two coupled sub-loops, which size the external aerodynamic shape and the structural components. In

this work, the aerodynamic shape of the blade is kept frozen, and the rotor is redesigned only from the structural point of view. The blade structural optimization algorithm aims at minimizing cost while guaranteeing structural integrity and other requirements by enforcing a set of constraints that include, among others, extreme conditions, fatigue damage, buckling, tower clearance, frequency placement, manufacturability, and transportation. The optimization variables include the thickness of the structural elements (skin, spar caps, shear webs) for given blade layout and materials. The inertial and structural characteristics of each blade section are computed with the 2D finite-element cross-sectional analysis code ANBA (Giavotto et al., 1983).

The structural sizing of the tower aims at minimizing its cost while satisfying constraints from extreme loads, buckling, and fatigue damage, as well as geometric constraints for manufacturing and transportation. The optimization variables include the diameter and thickness of the different tower segments for given material characteristics.

The formal description of the design algorithms can be found in Bottasso et al. (2012) and Bortolotti et al. (2016). Optimization is based on sequential quadratic programming (SQP), where gradients are computed by means of forward finite differences.

3 Results

The potential benefits of adopting LAC in the early stages of the design of the rotor and tower of different wind turbines are analyzed next, following the approach described in Sect. 2.

3.1 Reference machines

Three reference wind turbines are considered: WT1, an offshore class 1A developed in Bottasso et al. (2016) as an evolution of the original DTU 10 MW reference wind turbine (Bak et al., 2013); WT2, an onshore class 2A (Bortolotti et al., 2016); and WT3, an onshore class 3A (Bortolotti et al., 2019). The principal characteristics of these machines are reported in Table 4, while additional details can be found in the corresponding references. These turbines are reasonable representatives of current products available on the market. The three machines have blades made of a glass-reinforced polymer and towers made of thin-walled tubular tapered steel sections.

Table 5 compares the three machines in terms of capital cost (CAPEX), operational expenses (OPEX), AEP, and LCOE with some actual installations in the United States according to Stehly et al. (2017). The cost breakdown is expressed in 2017 United States Dollars (USD), and CAPEX does not include financial costs. The comparison shows a good match between the costs of the onshore 2.2 MW WT2 turbine and the 2017 US land-based 2.32 MW machine. The costs of the 3.4 MW WT3 turbine, even if slightly higher for

Table 4. Principal characteristics of the three reference turbines.

Turbine	WT1	WT2	WT3
IEC class and category	1A	2A	3A
Rated electrical power [MW]	10	2.2	3.4
Type	Offshore	Onshore	Onshore
Rotor diameter [m]	178.3	92.4	130.0
Specific power [W/m^2]	400.5	298.3	252.4
Hub height [m]	119.0	80.0	110.0
Blade mass [t]	42.5	8.6	16.4
Tower mass [t]	628	125	553

some figures, are also in reasonable agreement with the US reference. For the offshore case, a bottom-fixed 5 MW machine is compared to the 10 MW used in the present study. Larger differences are found here, for instance in the OPEX costs, due to the very different rating of the two turbines, although the LCOEs are relatively similar.

3.2 Assessment of potentially exploitable design margins

The present study considers a reduced set of DLCs (IEC, 2005), which are responsible for generating the design drivers of these machines (Bottasso et al., 2016; Bortolotti et al., 2016, 2019). The set includes power production with normal turbulence (DLC 1.1 and DLC 1.2), extreme turbulence (DLC 1.3), loss of electrical network in normal turbulence (DLC 2.1), and with extreme operating gusts (DLC 2.3). Additionally, parked conditions are also considered in yaw misalignment (DLC 6.1), with grid loss (DLC 6.2) and with extreme yaw misalignment (DLC 6.3).

3.2.1 Tower

A first analysis of the design-driving key quantities and constraints of the three towers unveils a significant potential that could be exploited by LAC.

For the design constraint analysis, several cross sections are considered along the tower height, where three local conditions are evaluated: buckling, ultimate strength based on von Mises stresses, and fatigue damage. Additionally, the placement of the first fore–aft and side–side frequencies is constrained to avoid crossing the one per rev at rated rotor speed.

For simplicity of discussion, only results at the tower top and bottom cross sections are shown in Fig. 2, where the constraint margins are displayed. These are formulated as the relative difference between the local conditions and their admissible values. A null value therefore indicates an active constraint, whereas a positive value indicates a slack condition, i.e., a constraint that is satisfied but inactive.

Considering first the tower top section, Fig. 2a shows that at this location the towers of WT1 and WT3 are driven by

Table 5. Cost breakdown of the different reference models expressed in 2017 USD.

Cost [USD/kW]	Onshore			Offshore	
	Stehly et al. (2017)	WT2	WT3	Stehly et al. (2017)	WT1
Rating [MW]	2.32	2.2	3.4	5	10
CAPEX [USD/kW]	1454	1297	1759	3846	4379
OPEX [USD/kW]	43.6	48.1	51.4	144	225
AEP [MWh/MW]	3633	3520	3866	3741	4500
FCR [%]	7.9	7.9	7.9	7.0	7.0
LCOE [USD/MWh]	43.6	42.9	49.2	110.5	118.1
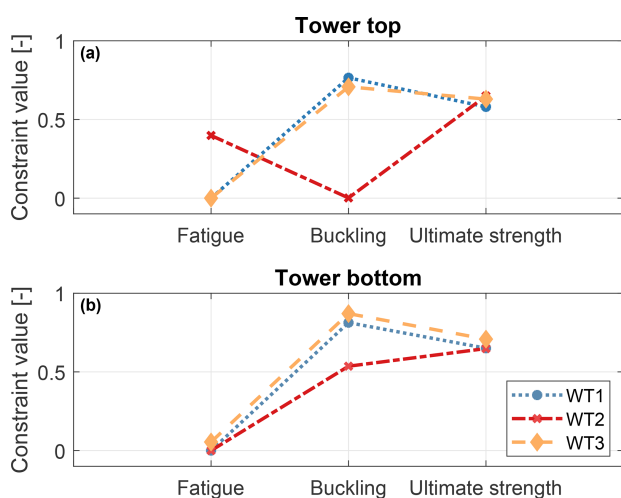
Figure 2. Design constraints at tower top **(a)** and tower bottom **(b)**.

fatigue, whereas buckling and strength are well below their maximum allowed values. The design of this section can therefore benefit from reductions in fatigue damage, which is mostly produced by the modifiable DLC 1.2 (power production in normal turbulence). On the other hand, the upper section of the WT2 tower is driven by buckling, whereas fatigue damage and ultimate strength are inactive. The PEM at this position along the tower is related to the combined bending moment at tower top (CBMTT). The rankings of this key quantity for the three turbines are shown in Fig. 3a. All values are normalized with respect to the leader, and, for clarity, only the leading and first blocking DLCs are shown. The ranking for WT2 is led by DLC 1.3, a modifiable DLC. The first blocking DLC is 2.1, which appears at position 28 in the ranking, leading to a PEM of about 20 %.

Considering the tower bottom cross section, Fig. 2b indicates that all three towers are driven by fatigue. Load rankings for combined bending moment at tower bottom (CBMTB) are reported in Fig. 3b. Results show no potential reduction for the extreme-load constraints, since the load rankings of the WT1 and WT2 towers are led by blocking

DLCs. A PEM of about 21 % is present for the WT3 tower, which, however, cannot be exploited since extreme loads do not drive the design at this section.

3.2.2 Rotor

Rotor design constraints include limits on the placement of the lowest natural frequencies to avoid resonant conditions, as well as a safe clearance with respect to the tower. Additionally, several cross sections are considered along the length of the blade, where upper limits for strains, stresses, and fatigue damage are prescribed on the spar caps, shell, and shear webs. An excerpt from this extensive set of constraints is shown in Fig. 4; the shell, spar cap, and shear web constraints are shown only at the midspan section of the blade, for simplicity of illustration.

The spar caps are the components that play the largest role in dictating the overall blade mass, as they mainly provide the blade flapwise bending stiffness. The design of these elements is driven by the blade-tower clearance constraint, which limits the maximum blade tip displacement (Fig. 4a). On the other hand, stress, strain, and fatigue constraints are all inactive (Fig. 4b). The tip displacement rankings, shown in Fig. 5a, indicate a significant reduction potential for all turbines, since they are all led by modifiable DLCs. This key quantity for all three turbines is first blocked by DLC 2.1, leading to PEMs between 8 % (WT1, ranking position 7) and 21 % (WT2, ranking position 28).

The sizing of the shell is mainly driven by the fatigue damage constraint (Fig. 4c). This is also the main driver in the design of the shear webs, which are elements made of sandwich panels that carry shear. Fatigue damage is driven by the modifiable DLC 1.2. However, here the reduction potential is limited by technological constraints that bound from below the thickness of these elements. The load ranking of the combined blade root moment (CBRM) is shown in Fig. 5b, highlighting potential reductions. Indeed, all turbines are again first blocked by DLC 2.1, with large PEMs for WT2 (25%, ranking position 2) and WT3 (30 %, ranking position 3).
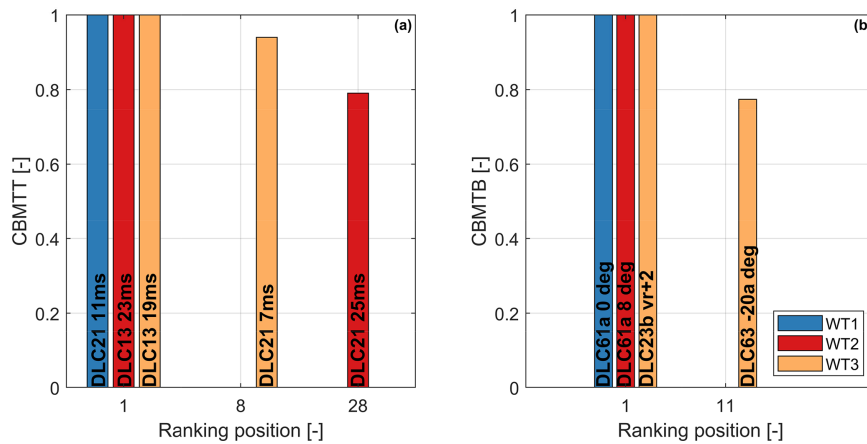
Figure 3. Ranking of normalized combined bending moment at tower top (CBMTT) **(a)** and tower bottom (CBMTB) **(b)**, for the three turbines. Only the leading and first blocking DLCs are shown.
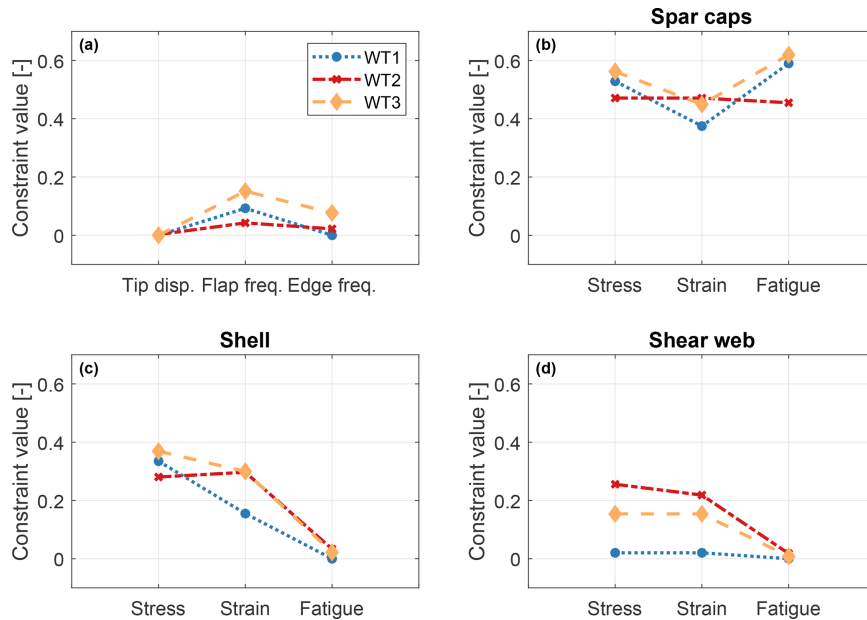

Figure 4. Rotor design constraints for tip displacement and frequency placement **(a)**. For a midspan section of the blade, design constraints at the spar caps **(b)**, shell **(c)**, and shear webs **(d)**.

3.3 Estimated benefits through structural redesign with LAC

This section aims at quantifying the benefits of integrating LAC within the design of the blade and tower of the three reference wind turbines. To this end, the rotor and tower of each turbine are reoptimized, considering loads and elastic deflections as reduced by the coefficients of the load-reduction model (Table 2) and the additional optimistic (values incremented by 50 %) and pessimistic (values reduced by 50 %) scenarios. The economic evaluation is performed as indicated in Sect. 2.4, considering a fixed change rate (FCR) of

7 %. It is further assumed that two lidar scanners have to be purchased over a turbine lifetime of 20 years. This results in an additional EUR 100 000 of ICC. Furthermore, the AOE includes an additional EUR 2500 per year of lidar O&M cost. These costs have been estimated based on input from two major lidar manufacturers and only include hardware-related costs. Due to a lack of information, the costs of development or licensing of LAC control software, related commissioning, and software maintenance have been neglected.
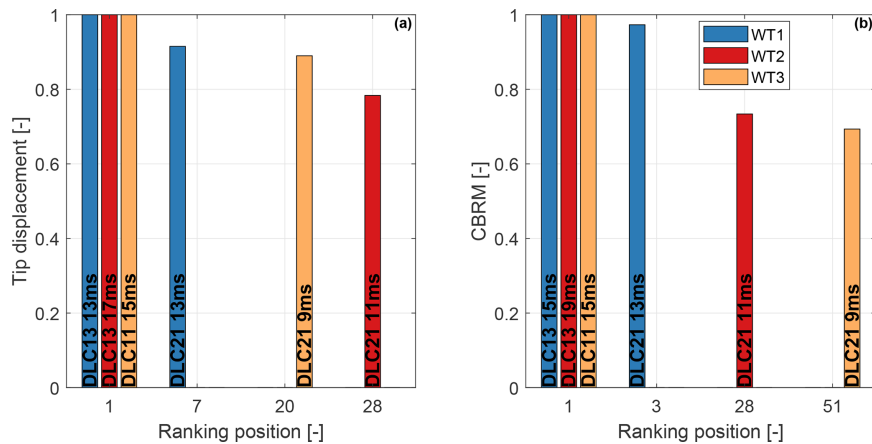
Figure 5. Ranking of normalized blade tip displacement **(a)** and combined blade root moment (CBRM) **(b)** for the three turbines.
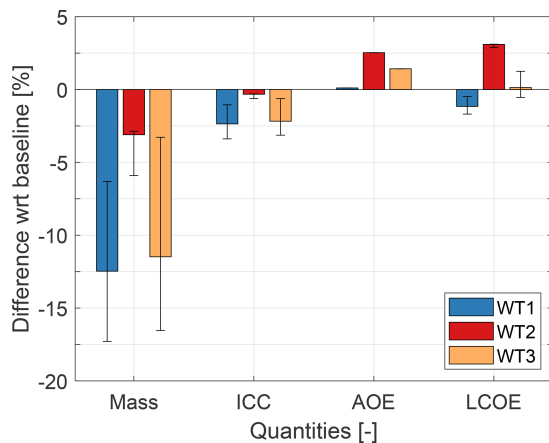
Figure 6. Effects of LAC on the redesign of the tower with respect to the initial baselines. Solid bars: load-reduction model of Table 2; whiskers: range of the pessimistic and optimistic scenarios.

3.3.1 Tower redesign

Figure 6 reports changes in the LAC-based redesigned towers with respect to the initial baselines, when the tower height is held fixed. The solid color bars correspond to the nominal load-reduction model, while whiskers indicate the effects of considering the pessimistic and optimistic scenarios. To ensure direct comparability with the baselines, the redesigned towers are considered to be made of several thin-walled tubular tapered steel sections. Additional geometric constraints to ensure realistic tower shapes are also considered.

Both towers of WT1 and WT3 enjoy significant benefits from large reductions in fatigue damage, which decrease mass between 5 % for the pessimistic scenario and 17 % for the optimistic one. In turn, the lighter weight induces significant reductions in the ICC of both turbines. On the other hand, annual operating expenses (AOE) show a different

behavior. Indeed, the additional expenses generated by the maintenance of a lidar system do not significantly add to the already high O&M costs of the offshore turbine WT1. For the onshore machines WT2 and WT3, where these costs play a larger role, AOE increases by approximately 2 %. For all turbines, AEP is essentially unaffected. In the end, the combination of these various effects produces a reduction in LCOE of about 1.2 % for WT1 and a very slight increase of 0.1 % for this same figure of merit for WT3 (Fig. 6).

The WT2 tower presents a different trend. Indeed, the upper segment of this tower is driven by buckling, and CBMTT presents a significant PEM of about 20 % (see Fig. 3a). However, this PEM cannot be exploited, since the LAC load-reduction model (Table 2) does not affect extreme loads at tower top. As a consequence, the redesign is only capable of a limited mass reduction that, in combination with the significant lidar costs, leads to an increase in LCOE.

3.3.2 Taller tower redesign

Instead of reducing tower mass (and hence cost), LAC-enabled improvements in fatigue damage and ultimate loads can be exploited to design taller towers. In fact, by reaching higher above the ground, the rotor is exposed to faster wind speeds, thus increasing AEP; thanks to LAC, this can be achieved without significantly increasing the cost of the tower. To explore the effects of this concept, towers of increasing heights were designed. The study assumes that LAC performance does not depend on tower height. To ensure direct comparability, the redesigned towers are also considered to be made of several thin-walled tubular tapered steel sections. The corresponding geometrical constraints are therefore also included in the redesign problem.

The study is here performed in two steps. First, the tower structure is sized with a non-LAC controller for a given height. The design objective is minimum mass, constrained to guarantee structural integrity. Next, the resulting tower de-

sign is reoptimized considering the different scenarios of the LAC load-reduction model, exploiting the slack that it generates in some design-driving constraints. The procedure is repeated for increasing tower heights until no further improvements are possible or an upper limit of 15 % height increase with respect to the baseline is reached.

The effects on mass, ICC, AEP, AOE, and LCOE for the three reference machines are reported in Fig. 7.

Different trends are observed for the three turbines. The tower of the offshore machine shows a large potential: for each of the analyzed heights, mass reductions with respect to the non-LAC configuration always translate into decreases in ICC. At the same time AEP increases, whereas AOE remains mostly constant due to the already high O&M costs. LCOE decreases gradually as tower height is increased. However, most of the gains are already achieved for a height increase of 5 %, which is associated with an LCOE decrease of about 1.5 % (Fig. 7e).

An opposite trend is obtained with the tower of WT2: because of its different design drivers, this machine does not benefit from a taller tower, as already noted in Sect. 3.2.1. However, the trend indicates that some LCOE improvements might be possible for very tall towers, which were, however, deemed unrealistic past the upper bound of a 15 % height increase.

Similarly, a taller tower appears not to be very promising even for the onshore fatigue-driven WT3 turbine, although for different reasons. Here, although a 5 % height increase lowers tower mass and ICC and improves AEP by about 2 %, these benefits are offset by an increase in AOE, resulting in marginal – if not completely negligible – benefits in LCOE.

3.3.3 Tower redesign for longer lifetime

Instead of aiming for less expensive or taller towers, as done so far, yet another way to try and exploit the load benefits brought by LAC is to extend the tower lifetime. In this case, the baseline towers are first designed for a 20-year lifetime based on the key quantities resulting from a non-LAC controller. Here again, the towers are redesigned for increasing lifetime in two steps. First, the tower structure is sized with a non-LAC controller for a given lifetime. Next, the resulting tower is reoptimized based on key quantities modified by the LAC load-reduction model (Table 2). WT2 is excluded from this analysis, because of the very limited relevance of fatigue in the sizing of its tower, as shown earlier. To ensure direct comparability with the baseline, the redesigned towers are considered to be made of several thin-walled tubular tapered steel sections, and the corresponding geometrical constraints are included in the sizing.

The tower mass of both WT1 and WT3 increases substantially when sizing for a longer lifetime without using LAC. This negative effect is very nicely counteracted by the use of LAC. Figure 8 reports mass changes generated by LAC for increasing lifetime; all results are computed with

respect to initial non-LAC 20-year baselines. At a lifetime of 40 years, which is double the conventional life duration, the tower mass of WT1 is still 10 % lower than for the non-LAC 20-year case. The effect is similar, although a bit less pronounced, even for WT3: for a lifetime of 40 years with LAC, this tower has in fact nearly the same mass of the 20-year non-LAC design.

It should be remarked that these trends are obtained under the assumption of a 100 % lidar availability; additionally, because of the approximations implicit in the assumed load-reduction model, these results can only be regarded as preliminary rough trends. However, the use of LAC to design towers with longer lifetimes seems to be much more promising than the alternative strategies of aiming for reduced costs or improved AEP by taller towers. Indeed, the trends shown here are in line with the results reported in Schlipf et al. (2018), which estimated a 15-year extended lifetime for a tower without redesign. Additionally, since the tower cost plays a large role in ICC, reductions in LCOE could be expected by the installation of towers with a longer lifetime. Alternatively, the towers could be reused to support more modern rotor-nacelle assemblies, playing the role of long-term support structures that do not necessarily have to be upgraded at the same pace of the rest of the turbine.

3.3.4 Rotor redesign

Only rather modest mass reductions are achieved for the blades of all models and for all scenarios, due to the moderate influence of LAC in design-driving constraints. The situation is more precisely illustrated by Fig. 9, which shows the largest improvements for WT1 and essentially no effect for WT2.

Indeed, the LAC load-reduction model reported in Table 2 shows a larger effect of LAC in fatigue damage mitigation than in the reduction of ultimate loads and deflections. Although shell and shear webs are both driven by fatigue, they are already thin structures with limited reduction potential before technological constraints on their thickness become active. In turn, this leads to the fatigue PEMs not being fully exploited. The design of the spar caps is also not significantly affected by LAC. In principle, a significant PEM is present for tip deflection, but unfortunately here again the LAC load-reduction model has only modest 2 % improvements for this key quantity. Additionally, as previously noted, the exploitation of the reduction of an ultimate condition by LAC raises important issues related to safety and might imply drastically increased costs to ensure redundancy.

For all three turbines, the reduction in ICC generated by the use of LAC in the redesigned rotors is not significant enough to compensate for the increase in AOE. Therefore, LCOE increases for all onshore machines and decreases in a negligible way for the offshore turbine.
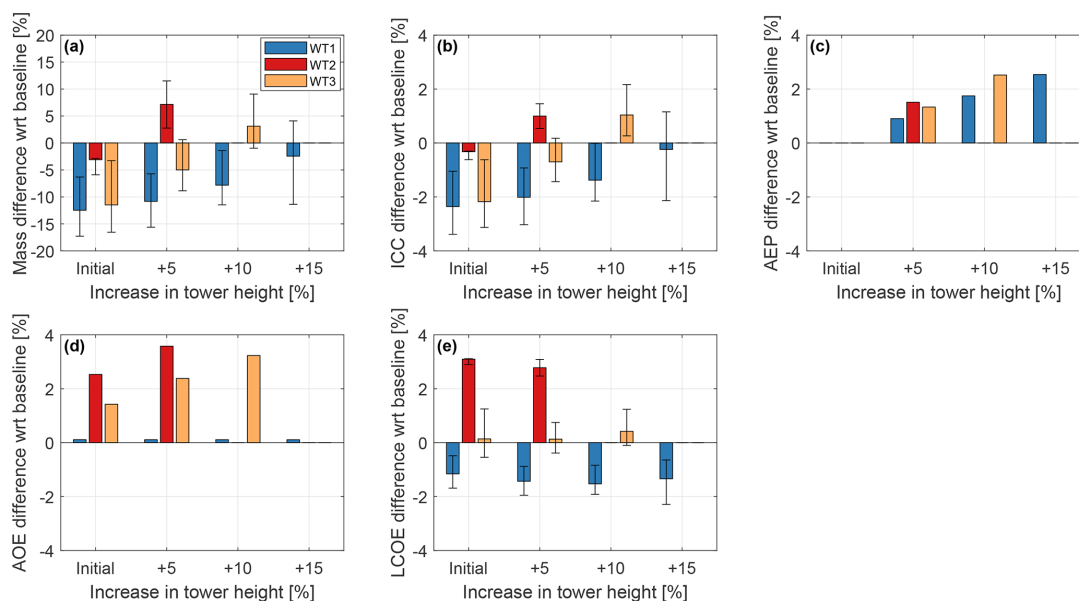
Figure 7. Effects of LAC on the redesign of towers of increasing height with respect to the initial non-LAC baselines. Solid bars: load-reduction model of Table 2; whiskers: range of the pessimistic and optimistic scenarios. The study considers increments of +5 %, 10 %, and 15 % in tower height for WT1; an increment of 5 % in tower height for WT2; and increments of 5 % and 10 % in tower height for WT3.
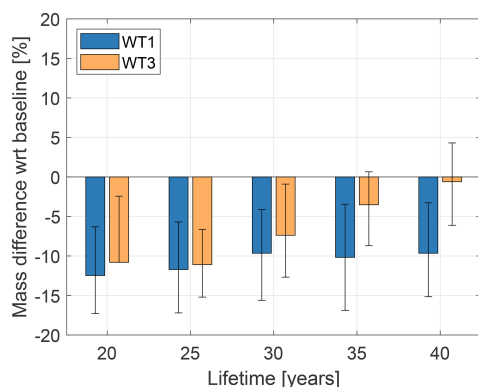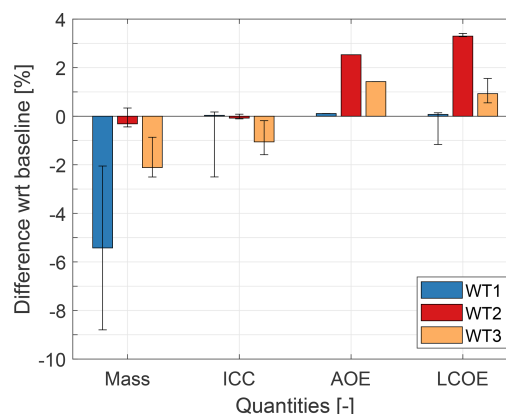

Figure 8. Effects of LAC on the redesign of towers of increasing lifetime with respect to 20-year non-LAC baselines. Solid bars: load-reduction model of Table 2; whiskers: range of the pessimistic and optimistic scenarios.

Figure 9. Effects of LAC on the redesign of the rotor with respect to the initial baselines. Solid bars: load-reduction model of Table 2; whiskers: range of the pessimistic and optimistic scenarios.

3.4 Cost sensitivity analysis

Finally, a sensitivity analysis is performed to understand to what extent the purchase and maintenance costs of a lidar system can influence the reduction in LCOE. Baseline values of EUR 100 000 and EUR 2500 per year, respectively for purchase and maintenance, are gradually modified until reaching the limit of ±100 % variations. It is assumed that lidar-related yearly maintenance costs are constant throughout the wind turbine lifetime and are therefore not affected by external factors, such as the replacement of the lidar system.

Purchase price includes both the cost and the number of lidar systems required throughout the wind turbine lifetime. The analysis considers the nominal LAC load-reduction model of Table 2 applied only to WT1 and WT3, as WT2 did not seem to have any real potential for improvement. Clearly, redundancy to ensure safety would significantly increase all of these costs.

It should be noticed that purchase and maintenance costs are treated here as two independent variables. In reality, purchase price could be correlated with performance, and therefore it might affect load reductions. Additionally, purchase

price could be correlated with maintenance: a higher cost of the lidar could imply a more sophisticated device, which might be more costly to maintain, but it could also be correlated with build quality, which then might be inversely related to maintenance cost. Such considerations would require a sophisticated cost model of the lidar, which was, however, unfortunately not available for this research. The present analysis, being based on the simple change of the two independent quantities, purchase and maintenance costs, could then be interpreted as a price positioning study, where the lidar manufacturer tries to understand the correct price range for the device to make it appealing to customers.

Figure 10a shows that only a modest effect in LCOE can be achieved for WT1 when purchase and maintenance costs are modified. On the other hand, an-order-of-magnitude-larger effect is observed for WT3 (Fig. 10b), where the incidence of the lidar-associated costs is more prominent given the smaller size and rating of this turbine.

Break-even is indicated in both figures as a dotted line, located in the white area that separates reductions (blue) from increments (red) in LCOE. The break-even line is almost perpendicular to the purchase cost axis, implying a large sensitivity of LCOE to this quantity. The figure shows that reductions in purchase costs appear more effective than reductions in O&M costs. This seems to indicate that lidar manufacturers should try to keep the cost of the device as low as possible. The fact that maintenance costs are less relevant might indicate that simple and cheap lidars – although possibly a bit more expensive to maintain – would be more appealing than sophisticated but expensive ones. Cheap single units, as long as availability remains sufficiently high, might also be very interesting from the point of view of redundancy, which might open up the possibility of exploiting ultimate load reductions. However, as noticed earlier, more sophisticated models – capable of capturing the couplings among purchase price, performance (including availability), lifetime, and maintenance – would be necessary to identify economically optimal development strategies for lidar systems.

Overall, results indicate that only modest reductions in LCOE are possible, even with very low LAC-based costs.

4 Conclusions

This paper has presented a preliminary general analysis on the potential benefits of integrating LAC within the design of the rotor and tower of a wind turbine. The design was performed as a constrained optimization based on aeroelastic simulations, conducted in close accordance with international design standards.

The benefits generated by the use of a lidar for controlling a turbine were quantified through a load-reduction model sourced from the literature, considering an average performance of the lidar-assisted controller and additional pes-

simistic and optimistic scenarios. This approach, in contrast to the use of an actual lidar-assisted controller in the loop, was chosen in order to draw conclusions on general trends rather than on the effects of a specific LAC implementation. Realizing that any such redesign exercise is typically highly problem-specific, the study was conducted considering three representative turbines of different class, size, and rating.

Based on the results of this study, the following conclusions can be drawn.

First, a significant improvement potential was observed when the design is driven by fatigue. Indeed, fatigue damage is primarily generated in power production in turbulent wind conditions. Here, the lidar-generated preview of the wind that will shortly affect the rotor is clearly beneficial: as the controller "sees" what will happen, it can anticipate its action. This is in contrast to the case of a pure feedback controller that, since it can only operate in response to a phenomenon that has already taken place, is by definition late in its reaction. In turn, the lidar preview information leads to a general reduction of load fluctuations and hence of fatigue damage.

On the contrary, the improvement potential is only very limited for components driven by ultimate conditions (such as maximum stresses, strains, or blade tip deflection). Indeed, these ultimate conditions cannot always be modified by LAC. In addition, even when LAC plays a role, other factors may have an even larger effect; for example, this is the case of shutdowns, where the pitch-to-feather policy may have a dominant role in dictating the peak response. But even when LAC does improve design-driving ultimate conditions, an even more general question still remains: shall one design a component based on an ultimate condition that was reduced by LAC? If so, what are the extra precautions that should be taken in order to hedge against faults, inaccuracies, misses, or unavailability of the lidar? These issues were not considered here, which is a limitation of the present study. However, it is possible that – at least in some of the cases analyzed in this work – the improvements to ultimate conditions brought by LAC would have to be completely discarded when these additional aspects are considered or where extra costs have to be added, for example, to ensure redundancy by the use of multiple lidars.

It was also found that, for fatigue-driven towers, significant benefits in mass (on average equal to about 12 %, for the cases considered here) can be obtained by the use of a LAC controller. However, these benefits are largely diluted by looking at the more general metric LCOE. In fact, only a large offshore machine showed improvements for this figure of merit: since O&M costs are already high for an offshore turbine, the extra costs due to the lidar play a lesser role. For smaller turbines the situation is different, and the benefits in mass do not repay for the costs of the lidar.

Instead of simply reducing mass, LAC can be used to either increase hub height (which increases power capture in sheared inflow) or to extend lifetime. Both approaches were considered here. The most interesting results were again ob-
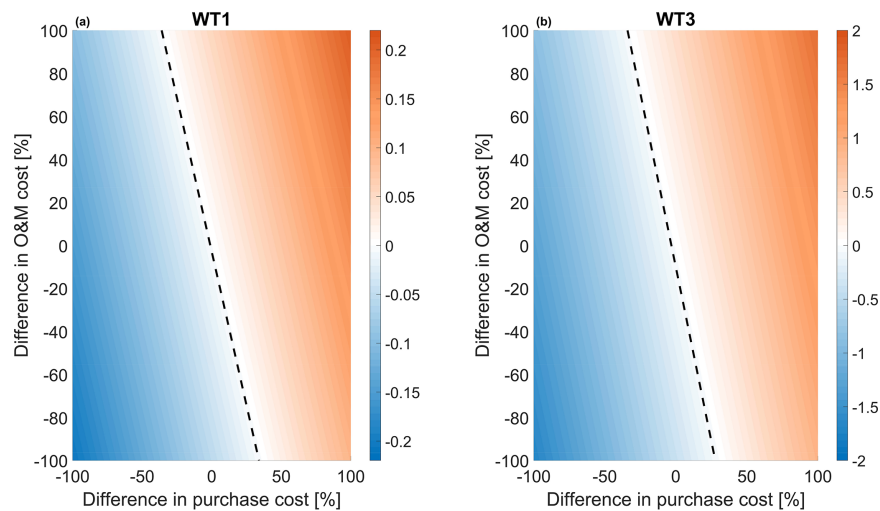
Figure 10. Percent variation of LCOE (shown in the color bars) as a function of purchase and O&M costs of LAC systems for the offshore machine WT1 **(a)** and the onshore machine WT3 **(b)**.

tained for fatigue-driven offshore towers. Indeed, a 15 % taller tower was found to present approximately the same mass of the baseline, but with a 2 % higher AEP. Even more interestingly, a LAC-enabled tower was designed with double the lifetime and 10 % less mass than the baseline.

The situation for the rotor is less promising. In principle, spar caps – which are the main contributors to blade mass – could greatly benefit from LAC when tip deflection is the main driver. Here again lidar preview can clearly help when maximum deflections are triggered by strong wind gusts. On the other hand, stiffness requirements caused by the placement of the flap frequency can substantially reduce this margin of improvement, as this is a blocking effect. Additionally, one would have again to guarantee that the safety-critical tip clearance constraint is always satisfied during operation, which might require redundancy of the lidar or other safety measures. Shear webs and shell are often driven by fatigue, a condition that could in principle be exploited by LAC. However, the improvement potential is limited due to the already limited thickness of these components. In summary, the integration of LAC into the design of the rotor does not seem to lead to significant benefits in terms of LCOE.

Finally, a simple parametric study on the purchase and O&M costs of a lidar system was performed. As previously observed, the study shows that LCOE is largely independent from the LAC purchase and O&M costs in the offshore case. Although a larger effect is visible in the onshore case, improvements in LCOE caused by reductions in the lidar costs are still quite modest. This might indicate that, instead of targeting price reductions, lidar research and development should focus on performance. On the other hand, significant price reductions might allow for redundancy, which in turn

would enable the targeting of drivers based on ultimate conditions.

The present work is based on a number of assumptions, and further work should be performed before more definitive conclusions can be drawn. First, only three turbines were considered; although these machines are reasonable approximations of contemporary products, it is clear that design drivers are typically turbine specific, and a more ample range of cases should be investigated. Additionally, only the conventional configuration of thin-walled steel towers with circular tubular tapered sections was considered. This configuration presents important geometric constraints that impact the benefits of LAC. Second, there was no attempt here to consider lidar availability, faults, and possible redundancy; an analysis of these aspects would help in clarifying whether LAC-enabled reductions in ultimate conditions can indeed be exploited in the structural redesign of the blade and the tower or not. Finally, it should be remarked that the use of a generic load model implies some significant approximations. Although this was done here on purpose with the goal of making the study more general, it is also clear that the performance of different LAC systems can be very different, depending on the lidar characteristics and on the controller formulation and tuning. Therefore, here again, more specific studies based on fully coupled simulations should be performed to further explore the trends reported here and find additional niches of applicability of LAC missed by the present general analysis.

Notwithstanding the limitations of this study, in the end it appears that the answer to the question of whether LAC is beneficial or not might not be so clear-cut, and in reality the situation is much more complex and varied (and also interesting). In hindsight, this is also a useful reminder that

apparently obvious improvements do not always necessarily translate into real system-level benefits. For example, reducing some loads might be irrelevant if the design is driven by other factors or might not pay off if the cost of that reduction neutralizes its benefits. This also stresses once more the central importance of systems engineering and design for the understanding of the true potential of a technology.

References

Bak, C., Zahle, F., Bitsche, R., Kim, T., Yde, A., Henriksen, L. C., Natarajan, A., and Hansen, M. H.: INNWIND. EU Deliverable D1.21: Reference Wind Turbine Report, available at: http://www.innwind.eu/publications/deliverable-reports (last access: 18 December 2019), 2013.

Bortolotti, P., Bottasso, C. L., and Croce, A.: Combined preliminary–detailed design of wind turbines, Wind Energ. Sci., 1, 71–88, https://doi.org/10.5194/wes-1-71-2016, 2016.

Bortolotti, P., Canet, H., Dykes, K., Merz, K., Sethuraman, L., Verelst, D., and Zahle, F.: IEA Wind TCP Task 37: Systems Engineering in Wind Energy – WP2.1 Reference Wind Turbines Technical Report, International Energy Agency, Golden (CO), https://doi.org/10.2172/1529216, 2019.

Bossanyi, E., Kumar, A., and Hugues-Salas, O.: Wind turbine control applications of turbine-mounted lidar, J. Phys. Conf. Ser., 555, 012011, https://doi.org/10.1088/1742-6596/555/1/012011, 2014.

Bottasso, C. L., Campagnolo, F., and Croce, A.: Multi-disciplinary constrained optimization of wind turbines, Multibody Syst. Dyn., 27, 21–53, https://doi.org/10.1007/s11044-011-9271-x, 2012.

Bottasso, C. L., Pizzinelli, P., Riboldi, C. E. D., and Tasca, L.: LiDAR-enabled model predictive control of wind turbines with real-time capabilities, Ren. En., 71, 442–452, https://doi.org/10.1016/j.renene.2014.05.041, 2014.

Bottasso, C. L., Bortolotti, P., Croce, A., and Gualdoni, F.: Integrated aero-structural optimization of wind turbines, Multibody Syst. Dyn., 38, 317–344, https://doi.org/10.1007/s11044-015-9488-1, 2016.

Bottasso, C. L. and Bortolotti, P.: Rotor Design and Analysis, Wind Energy Modeling and Simulation: Turbine and System, edited by: Veers, P., ISBN 978-1785615238, The Institution of Engineering and Technology (IET), London, UK, 2019.

Canet, H., Loew, S., and Bottasso, C. L.: Lidar-assisted control in wind turbine design: Where are the potential benefits?, J. Phys. Conf. Ser., 1618, 042020, https://doi.org/10.1088/1742-6596/1618/4/042020, 2020.

Chaviaropoulos, P., Karga, I., Harkness, C., and Hendriks, B.: Deliverable 1.23 PI-Based assessment of innovative concepts IN-NWIND.EU technical report, available at: http://www.innwind.eu/ (last access: 6 October 2021), 2014.

Dunne, F., Pao, L. Y., Wright, A. D., Jonkman, B., and Kelley, N.: Adding feedforward blade pitch control to standard feedback controllers for load mitigation in wind turbines, Mechatronics, 21, 682–690, https://doi.org/10.1016/j.mechatronics.2011.02.011, 2011.

Dunne, F., Schlipf, D., Pao, L. Y., Wright, A. D., Jonkman, B., Kelley, N., and Simley, E.: Comparison of two independent lidar-based pitch control designs, Proc. AIAA Aerospace Sciences Meeting, Nashville, Tennessee, 9–12 January 2012, https://doi.org/10.2514/6.2012-1151, 2012.

EN 1993-1-9: Eurocode 3: Design of steel structures – Part 1–9: Fatigue, CEN, Brussels, 2006.

Fingersh, L., Hand, M., and Laxson, A.: Wind Turbine Design Cost and Scaling Model, National Renewable Energy Laboratory technical report, Golden, CO, available at: https://www.nrel.gov/docs/fy07osti/40566.pdf (last access: 20 February 2020), 2006.

Giavotto, V., Borri, M., Mantegazza, P., and Ghiringhelli, G.: Anisotropic beam theory and applications, Comput. Struct., 16, 403–413, https://doi.org/10.1016/0045-7949(83)90179-7, 1983.

Griffith, D. T. and Johans, W.: Large blade manufacturing cost studies using the sandia blade manufacturing cost tool and Sandia 100 m blades, Sandia National Laboratories technical report, Albuquerque, NM, available at: https://energy.sandia.gov/wp-content/gallery/uploads/dlm_uploads/SAND_SNLLargeBladeManufacturingCostTrendsAnalysis_SAND2013-2734.pdf (last access: 17 February 2020), 2013.

Haizmann, F., Schlipf, D., Raach, S., Scholbrock, A., Wright, A., Slinger, C., Medley, J., Harris, M., Bossanyi, E., and Cheng, P. W.: Optimization of a feed-forward controller using a CW-lidar system on the CART3, Proceedings of the American Control Conference, Chicago, USA, 1–3 July 2015, https://doi.org/10.18419/opus-3975, 2015.

Hendriks, H. B. and Bulder, B. H.: Fatigue Equivalent Load Cycle Method: A general method to compare the fatigue loading of different load spectrums, Energy Research Centre of the Netherlands technical report, Netherlands, available at: https://publicaties.ecn.nl/PdfFetch.aspx?nr=ECN-C--95-074 (last access: 24 September 2020), 1995.

International Electrotechnical Commission: International Electrotechnical Commission, IEC 61400-1 Ed. 3: Wind turbines – Part 1: Design requirements, IEC, Geneva, Switzerland, 2005.

Koren, I. and Krishna, C. M.: Fault-Tolerant Systems, 2nd Edition, ISBN 978-0-12-818105-8, https://doi.org/10.1016/C2018-0-02160-X, Elsevier, Amsterdam, the Netherlands, 2020.

NREL: WISDEM, v2.1.5, GitHub [code], available at: https://github.com/WISDEM/WISDEM, last access: 8 July 2020.

Riboldi, C. E. D.: Advanced Control Laws for Variable-Speed Wind Turbines and Supporting Enabling Technologies, Ph.D. thesis, Politecnico di Milano, Milan, Italy, 2012.

Schlipf, D., Fleming, P., Kapp, S., Scholbrock, A., Haizmann, F., Belen, F., Wright, A., and Cheng, P. W.: Direct speed control using lidar and turbine data, American Control Conference 2013, Washington, DC, USA, 17–19 June 2013, https://doi.org/10.1109/ACC.2013.6580163, 2013a.

Schlipf, D., Schlipf, D. J., and Kühn, M.: Nonlinear model predictive control of wind turbines using lidar, Wind Energ., 16 1107–1129, 2013b.

Schlipf, D., Fleming, P., Haizmann, F., Scholbrock, A., Hofsäß, M., Wright, A., and Cheng, P. W.: Field Testing of Feedforward Collective Pitch Control on the CART2 Using a Nacelle-Based Lidar Scanner, J. Physics, 555, 012090, https://doi.org/10.1088/1742-6596/555/1/012090, 2013c.

Schlipf, D. and Cheng, P. W.: Flatness-based Feedforward Control of Wind Turbines Using Lidar, IFAC Proceedings Volumes, 47, 5820–5825, https://doi.org/10.3182/20140824-6-ZA-1003.00443, 2014.

Schlipf, D., Simley, E., Lemmer, F., Pao, L., and Cheng, P. W.: Collective pitch feedforward control of floating wind turbines using lidar, Journal of Ocean and Wind Energy, 2, 223–230, https://doi.org/10.17736/jowe.2015.arr04, 2015.

Schlipf, D.: Lidar-Assited Control Concepts for Wind Turbines, Ph.D. Thesis, University of Stuttgart, Dr.Hut editions, Munich, Germany, 2016.

Schlipf, D., Fürst, H., Raach, S., and Haizmann, F.: Systems Engineering for Lidar-Assisted Control: A Sequential Approach, J. Phys. Conf. Ser., 1102, 012014, https://doi.org/10.1088/1742-6596/1102/1/012014, 2018.

Scholbrock, A., Fleming, P., Wright, A., Wang, N., Schlipf, D., and Johnson, K.: Lidar-Enhanced Wind Turbine Control: Past, Present and Future, NREL/CP-5000-65879, NREL, Golden, CO, USA, available at: https://www.nrel.gov/docs/fy16osti/65879.pdf (last access: 6 October 2021), 2016.

Simley, E., Fürst, H., and Schlipf, D.: Optimizing Lidars for Wind Turbine Control Applications – Results from the IEA Wind Task 32 Workshop, Remote Sens., 10, 863, https://doi.org/10.3390/rs10060863, 2018.

Simley, E., Bortolotti, P., Scholbrock, A., Schlipf, D., and Dykes, K.: IEA Wind Task 32 and Task 37: Optimizing Wind Turbines with Lidar-Assisted Control Using Systems Engineering, J. Phys. Conf. Ser., 1618, 042029, https://doi.org/10.1088/1742-6596/1618/4/042029, 2020.

Sinner, M. N. and Pao, L. Y.: A Comparison of individual and collective pitch model predictive controllers for wind turbines, Annual American Control Conference (ACC), Milwaukee, WI, 27–29 June 2018, 1509–1514, https://doi.org/10.23919/ACC.2018.8431598, 2018.

Stehly, T., Beiter, P., Heimiller, D., and Scott, G.: Cost of Wind Energy Review, Tech. Rep. (National Renewable Energy Laboratory), available at: https://www.nrel.gov/docs/fy18osti/72167.pdf (last access: 20 September 2019), 2017.

Wang, N., Johnson, K., and Wright, A.: Comparison of strategies for enhancing energy capture and reducting loads using lidar and feedforward control, IEEE T. Contr. Syst. T., 21, 1129–1142, https://doi.org/10.1109/TCST.2013.2258670, 2013.

A.7 Paper VII: The eco-conscious wind turbine: bringing societal value to design

The eco-conscious wind turbine: bringing societal value to design

Helena Canet[1], Adrien Guilloré[1], and Carlo L. Bottasso[1]

[1]Wind Energy Institute, Technical University of Munich, 85748 Garching bei München, Germany

Correspondence: Carlo L. Bottasso (carlo.bottasso@tum.de)

Abstract.

Wind turbines are designed to minimize the cost of energy, a metric aimed at making wind competitive with other energy-producing technologies. However, now that wind energy is competitive, how can we increase its value for society? And how much would a societal gain cost other stakeholders, such as investors or consumers? This paper tries to answer these questions
5 from the perspective of wind turbine design.

Although wind turbines produce green renewable energy, they also generate various impacts on the environment, as all human endeavours. Among all impacts, the present work adopts the environmental effects produced by a turbine over its entire life cycle, expressed in terms of CO_2-equivalent emissions. A new approach to design is proposed, whereby Pareto fronts of solutions are computed to define optimal trade-offs between economic and environmental goals.

10 The new proposed methodology is demonstrated on the redesign of a baseline 3 MW wind turbine at two locations in Germany, differing for typical wind speeds. Among other results, it is found that, in these conditions, a 1% increase in the cost of energy can buy about a 5% decrease in the environmental impact of the turbine. Additionally, it is also observed that in the specific case of Germany, very low specific-power designs are typically favored, because they produce more energy at low wind speeds, where both the economic and environmental values of wind are higher.

15 Although limited to the sole optimization of wind-generating assets at two different locations, these results suggest the existence of new opportunities for the future development of wind energy where, by shifting the focus slightly away from a purely cost-driven short-term perspective, longer-term benefits for the environment (and, in turn, for society) may be obtained.

1 Introduction

The levelized cost of energy (LCOE) is defined as the net-present cost of an energy-producing technology over its lifetime
20 per MWh supplied. LCOE is the metric that has been traditionally used to evaluate the competitiveness of energy sources. In recent years, the LCOE from wind (and from the sun) has experienced a dramatic decrease (Roser, 2021), which in turn has fueled an astonishing growth of wind energy and great expectations for its further expansion (Veers et al., 2019). About a decade ago, the International Energy Agency (IEA) Wind Task 26, which focuses on the cost of wind energy, identified a key driver for the future development of wind technology: the ability of generating cost parity – without direct policy support –
25 with conventional sources, in a broad range of conditions and locations (Lantz et al., 2012). This indeed has largely happened and the evolution of wind energy technology continues at a fast pace, to the point that even offshore wind is rapidly marching

1

towards subsidy-free competitiveness (Jansen et al., 2020). The decrease in LCOE from wind has been partially driven by technological advancements, which have led to more reliable turbines characterized by higher hub heights and larger rotor diameters and, most importantly, much improved capacity factors. Additionally, economies of scale, increased competitiveness

30 and an improved maturity of the sector have also contributed to the fall of LCOE witnessed in recent years (IRENA, 2021).

LCOE, however, paints only a partial view of a situation that is much more complex and articulated than what appears through cost alone (Joskow, 2011). A more holistic picture of the overall effects of renewable energies in general, and of wind in particular, can only be obtained when looking beyond cost metrics. Indeed, the urgency created by climate change, energy security and independence could not be clearer, as stressed by the headline news coming from all over the world every day.

35 In fact, the future participation of wind power in the energy market and, more broadly, its societal role will not only be shaped by its relative competitiveness, but also by its *value* (Beiter et al., 2021). The word *value* is generally understood in the literature as a synonym for *economic value*, which is a measure of the benefit provided to an actor by some good or service. In reality, in the case of an energy-generating technology, the concept of value is extremely broad. Leaving aside aspects such as energy security and independence, which are of crucial importance but also beyond the scope of the present analysis, it is

40 worth noticing that the value of an energy technology cannot be quantified per se, because it depends on the interactions of that technology with the system in which it operates (Mai et al., 2021). For instance, the total system-value of an asset can be seen as the sum of different system-value components – including energy value, capacity value, ancillary service value and others (Mai et al., 2021). Additionally, due to supply and demand variability, the market price of electricity can vary widely, with high wholesale prices during peak demand times, which however can reach down to even negative values when large amounts of

45 renewable energy are available in the grid. This fact, in addition to transmission and storage constraints, makes the economic value of electricity time- and location-specific (Hirth, 2012).

The importance of value has not gone unnoticed to the recent literature, and a range of options for increasing the economic value of wind energy have been explored. For instance, the geographic location of wind plants – and, more in general, of variable renewable energy plants – and the diversification of the energy mix are two strategies that can be used to this effect

50 (Hirth and Mueller, 2016). Additionally, even the design characteristics of wind-generating assets (which is the focus of the present work) can change when considering value, rather than simply cost. In fact, some wind turbine design parameters – in particular hub height and specific power (i.e. rated power divided by rotor swept area) – can have a significant effect on economic value, as shown by Hirth and Mueller (2016); Lantz et al. (2017); Swisher et al. (2022), among others.

Economic cost and value, however, are actor-centric metrics, which mostly capture the investor point of view and, in turn,

55 also the price eventually paid by the end consumer. Additionally, cost and value are short-term metrics: cost evolves rapidly from year to year, whereas value changes on even much faster time scales of minutes/hours. In this sense, economic cost and value – if used alone – seem to be rather myopic metrics for the design of a wind turbine. Indeed, time is ripe for looking beyond the benefit of the single actor and beyond short-term effects: wind energy should evolve to take into account also its broad and long-term impacts at the societal level. It is a major ambition of this paper to bring this new point of view to the

60 design of wind turbines. Clearly, the same philosophy can also be applied to the design of wind plants and, more in general, to the design of the whole energy system.

2

From this broader perspective, the overarching goal of design becomes the alignment of short-term economic needs with long-term sustainable development goals. In fact, while it is necessary to enhance the economic value of wind energy to increase its competitiveness today, it is also our moral duty to improve the value of this technology for society now and into
65   the future.

How can these broader goals be achieved? What are the new metrics that should be used to capture long-term societal effects? How can value be defined beyond its current economic meaning? How different would new more eco-conscious turbines be from standard LCOE-driven designs? And how much would a societal-level gain cost in terms of LCOE? These are some of the questions that are in need of answers, and that the present paper is trying to address, albeit in a preliminary and certainly
70   yet somehow incomplete form.

There are undoubtedly several different options for including long-term societal effects in the design of wind turbines. This study focuses on the impact exerted by wind technology on the environment in terms of greenhouse gas (GHG) emissions. While GHG emissions clearly do not capture all effects of wind energy, they do provide for a major and quantifiable impact with long-term consequences. As long as they are quantifiable through some appropriate metric, other impacts could be included in
75   a future even more general approach than the one presented here.

At first glance, it might seem unusual to speak about GHG emissions in the context of wind energy. After all, a wind turbine is an eco-friendly machine by definition, which captures kinetic energy from wind to produce electricity without directly releasing pollutants into the environment. Additionally, the deployment of each new wind turbine displaces a certain amount of GHG emissions, because the output of other more polluting energy sources can be correspondingly reduced. However, even wind
80   turbines do have an environmental cost – as indeed all human activities –, and non-negligible amounts of GHGs are emitted throughout the different stages of their life. For example, the production of the large amount of steel needed for the tower, or the extraction of raw materials – such as the rare-earth elements present in the generator –, do have significant environmental impacts; additionally, the end-of-life (EOL) treatments of components with limited recyclability, such as blades largely made of reinforced thermoset polymers, do release polluting emissions into the atmosphere. More in general, all stages of the life-cycle
85   of a turbine, from the extraction of raw materials all the way to the eventual disposal/recycling/repurposing of its components, generate impacts that can be quantified in terms of CO_2-equivalent emissions. Given its importance, it is no surprise that the evaluation of the environmental cost of wind turbines is the subject of various recent studies, including Al-Behadili and El-Osta (2015); Ozoemena et al. (2018), among others. In addition to representing a meaningful metric per se, GHG emissions can also be turned into economic costs by using the societal cost of carbon (SCC), which is an estimate of the net present value
90   of monetized social damages occurring from the emission of an additional metric ton of CO_2 (Gillingham and Stock, 2018; National Academies of Sciences, Engineering and Medicine, 2017). However, care should be exercised when using SCC, as it can take a large range of values, depending on the underlying assumptions and models (IPCC, 2007; Ricke et al., 2018; Kikstra et al., 2021).

While several publications propose metrics that capture the economic profitability of a wind turbine (Ueckerdt et al., 2013;
95   Simpson et al., 2020; Mai et al., 2021), no metrics are yet available to describe the environmental cost and value of wind energy. To address this gap, this work introduces novel eco-conscious metrics that mirror existing economic ones. These metrics are

3

then used within a multi-objective design framework, which sizes some macroscopic parameters of a wind turbine (here rotor diameter and hub height) to find optimal trade-offs between economic and environmental perspectives.

The eco-conscious metrics are defined based on a life-cycle assessment (LCA) method, which has the added benefit of breaking down the contribution to the overall GHG emissions of a wind turbine by its components, materials and technological choices. This way, a ranking of the most harmful aspects of a design is readily obtained, revealing new opportunities and highlighting the most promising pathways for further mitigating GHG emissions beyond what is possible by sizing alone (Guilloré et al., 2022).

The paper is organized as follows. Section 2 defines metrics that quantitatively measure the cost and value of a wind-generating asset, both from the economic and the environmental perspectives. Next, Sect. 3 describes the methods that were used here to estimate the design metrics. In addition to standard energy production, mass, and cost models, this section describes and validates an LCA model whose goal is to estimate the CO_2-equivalent emissions produced during each stage of the life and by each component of a wind turbine. The design approach is also formulated in this same section, in terms of single- and multi-objective constrained optimization problems. The new proposed methodology is exercised in Sect. 4, by redesigning a baseline 3 MW wind turbine at two different locations in Germany, one in the north and the other in the south of the country, characterized by different wind resources. The results are analyzed by looking at the trade-offs between economic and environmental metrics, and at the change in the design characteristics of the optimal turbines with respect to a standard LCOE-driven baseline. Finally, Sect. 5 summarizes the main findings of this study and offers an outlook towards future work.

2 Design metrics from economic and environmental perspectives

This section describes metrics for the preliminary design of an energy-generating unit using three common concepts: cost, value, and net value. In general, *cost* indicates the expense incurred for making a product or service, whereas *value* is a measure of the benefit brought by that good or service. The difference between cost and value is termed *net value*. In the present context, the good or service is the production of energy. The three terms cost, value and net value will be used with two different connotations: *economic*, when relating to money, and *environmental*, when relating to the GHGs emitted in the lifetime of an asset. These metrics are applicable to both single generating units (e.g., a wind turbine) or a plant (e.g., a wind farm), although the present work focuses only on the former case.

2.1 Economic perspective

The economic perspective results from an actor-centric point of view, e.g. the investor or the consumer, where the focus is primarily driven by short-term economic forces, such as revenue or out-of-pocket expenditure.

2.1.1 Levelized Cost of Energy (LCOE)

LCOE is an estimate of the average net-present cost of each unit of energy produced over the lifetime of a generating asset. As such, this metric is widely used to assess the competitiveness of different energy technologies. LCOE is formally defined as the

ratio of the discounted lifetime costs with the discounted generated energy (Aldersey-Williams and Rubert, 2019; Duffy et al., 2020), i.e.

$$\text{130} \quad \text{LCOE}\left[\frac{\text{\euro}}{\text{MWh}}\right] = \frac{\text{Economic costs}}{\text{Energy production}} = \frac{\sum_{y=1}^{Y} \frac{C_y^{\text{CAPEX}} + C_y^{\text{OPEX}}}{(1+d)^y}}{\sum_{y=1}^{Y} \frac{E_y}{(1+d)^y}}, \tag{1}$$

where the subscript $(\cdot)_y$ indicates the y-th year and Y is the lifetime in years, while C^{CAPEX} are the capital costs, C^{OPEX} are the operating and maintenance costs, E is the asset-generated energy, and finally d is the discount rate.

Capital costs include all expenditures incurred to manufacture the asset, while the operating and maintenance costs include all expenditures necessary for running the asset and maintaining it in working conditions (Joskow, 2011; Mai et al., 2021). The discount rate is the interest rate used to determine the present value of future cash flows and, therefore, expresses the time value of money. The discount rate is often affected by significant uncertainties, which in turn may impact LCOE.

2.1.2 Levelized Value of Energy (LVOE)

LVOE is an estimate of the average net-present economic value of each unit of energy produced over the lifetime of a generating asset (Mai et al., 2021). Similarly to LCOE, LVOE is defined as

$$\text{140} \quad \text{LVOE}\left[\frac{\text{\euro}}{\text{MWh}}\right] = \frac{\text{Economic value}}{\text{Energy production}} = \frac{\sum_{y=1}^{Y} \frac{V_y}{(1+d)^y}}{\sum_{y=1}^{Y} \frac{E_y}{(1+d)^y}}. \tag{2}$$

The total revenue V_y generated by the asset in the y-th year is computed as a function of time t as

$$V_y = \int_{t=0}^{T_y} p(t)P(t)\,\mathrm{d}t, \tag{3}$$

where T_y is the year duration, $p(t)$ is the spot market price in €/MWh, and $P(t)$ is the power produced by the unit at time instant t. Alternatively, the same quantity can be estimated as a function of wind speed U as

$$\text{145} \quad V_y = T_y \int_{U_i}^{U_o} p_y(U)P(U)W_y(U)\,\mathrm{d}U, \tag{4}$$

where U_i and U_o are respectively the cut-in and cut-out wind speeds, $P(U)$ is the turbine power curve, while $p_y(U)$ and $W_y(U)$ are respectively the spot market price of energy and the Weibull probability density function at the site where the asset is installed in the year y.

2.1.3 Net Value of Energy (NVOE)

NVOE is defined as the difference between LVOE and LCOE (Mai et al., 2021), i.e.

$$\text{NVOE}\left[\frac{\text{\euro}}{\text{MWh}}\right] = \frac{\text{Economic value} - \text{Economic cost}}{\text{Energy production}} = \text{LVOE} - \text{LCOE}. \tag{5}$$

2.2 Environmental perspective

The environmental perspective results from a societal point of view, in which the goal is no longer to achieve the cheapest energy in the short term, but rather the most sustainable one in the long term. The metrics presented here mirror the ones defined in the previous section. However, instead of considering the economic perspective, these novel metrics focus on the environmental impact and are quantified in terms of CO_2-equivalent emissions.

As money is attributed a time value through the discount rate, even impacts could in principle be discounted, because emissions produced/displaced today might have a different effect from the ones of tomorrow. Indeed, time horizons are included in the estimation of the Global Warming Potential (GWP) that is used to convert the effects of different gases into equivalent CO_2 climate impacts (IPCC, 2007). However, discount rates for CO_2-equivalent emissions are at present not available, and would probably be subjected to high uncertainties; therefore, discount rates were not considered in the definition of the environmental-based metrics.

2.2.1 Impact of Energy (IOE)

IOE represents an estimate of the average environmental cost of each unit of energy produced over the lifetime of a generating asset:

$$\text{IOE} \left[\frac{\text{kg CO}_2\text{eq}}{\text{MWh}} \right] = \frac{\text{Environmental cost}}{\text{Energy production}} = \frac{\sum_{m=1}^{M} Q_m}{\sum_{y=1}^{Y} E_y}, \qquad (6)$$

where Q_m is the CO_2-equivalent GHG emissions during life stage m, and M is the total number of life stages of the asset, from the extraction of the raw materials all the way to EOL treatments. IOE is the environmental counterpart of LCOE, with the difference that decommissioning and EOL costs are generally not considered in the definition of the latter. Similar definitions of IOE have been given elsewhere using different names, as for example *Carbon Footprint* (Hauschild et al., 2018), *Emission Factor* (Koffi et al., 2017), *CO₂ Intensity* (Tremeac and Meunier, 2009), and *Global Warming Potential* (Ozoemena et al., 2018).

2.2.2 Environmental Value of Energy (EVOE)

EVOE is the counterpart of LVOE, and it is defined as the average environmental value per unit of energy generated by an asset over its lifetime:

$$\text{EVOE} \left[\frac{\text{kg CO}_2\text{eq}}{\text{MWh}} \right] = \frac{\text{Environmental value}}{\text{Energy production}} = \frac{\sum_{y=1}^{Y} V_y^{\text{env}}}{\sum_{y=1}^{Y} E_y}. \qquad (7)$$

The environmental value is quantified here in terms of the CO_2-equivalent emissions that are displaced in the grid by the energy-producing asset. At time t, the energy mix is characterized by G_t generating technologies, each producing a certain power $P_g(t)$. The activation of a renewable generating unit that produces a power output $P(t)$ displaces some output $P_g^{\text{dis}}(t)$ of the g-th generating technology, such that $P(t) = \sum_{g=1}^{G_t} P_g^{\text{dis}}(t)$. Despite the activation of a renewable generating unit, the

time-dependent total power in the grid remains the same, as it is driven by demand. As a consequence, an environmental value V_y^{env} is generated over the time duration T_y, which is equal to the amount of displaced emissions, i.e.

$$V_y^{\text{env}} = \int_{t=0}^{T_y} \sum_{g=1}^{G_t} f_g(t) P_g^{\text{dis}}(t) \, \mathrm{d}t. \tag{8}$$

The emission factor f_g quantifies the environmental impact of each generating technology in the mix. This quantity depends on time, because it is related to the operational conditions of the generating technology. For instance, operating a fossil-fueled plant at partial load has an efficiency penalty that increases the fuel consumption and the GHG emissions per unit of generated energy (Silver-Evans et al., 2012; Thomson et al., 2017). For simplicity, here each given technology g is associated with an average time-independent emission factor defined as

$$f_g = \frac{Q_g}{E_g}, \tag{9}$$

where Q_g indicates the average CO_2-equivalent GHG emissions caused by the production of an amount of energy E_g.

The actual displacement of grid emissions is a complex time-dependent phenomenon (Hawkes, 2010; Thomson et al., 2017; Boeing et al., 2019). In fact, the only emissions that will be displaced are the ones of generators operating on the margin, i.e. the last generators needed to meet demand at a given time that are capable of rapidly adapting their power generation in response to a change in demand (Silver-Evans et al., 2012; Seckinger, 2021). Therefore, the actual displacement of grid emissions is determined by these marginal generators, which in turn depend on time-variable factors such as power demand, resource availability (e.g., wind speed and solar irradiation), or availability of other generation technologies. For simplicity, here it is assumed that all generating technologies are displaced equally, i.e. $P_g^{\text{dis}}(t)/P_g(t) = P(t)/\sum_{g=1}^{G_t} P_g(t)$, for each generating technology g at each time t. This is a conservative approach that is generally used to estimate emission displacements, and which has been shown to underestimate the real displacement potential of wind energy (Hawkes, 2010; Silver-Evans et al., 2012; Thomson et al., 2017). Under this hypothesis, the environmental value writes

$$V_y^{\text{env}} = \int_{t=0}^{T_y} \frac{\sum_{g=1}^{G_t} f_g P_g(t)}{\sum_{g=1}^{G_t} P_g(t)} P(t) \, \mathrm{d}t = \int_{t=0}^{T_y} f_{\text{grid}}(t) P(t) \, \mathrm{d}t. \tag{10}$$

The expression on the right hand side of the equation considers the whole grid as one aggregated generating unit, characterized by one equivalent time-dependent system-average emission factor $f_{\text{grid}}(t)$, which reflects the composition of the energy mix at each time instant (Thomson et al., 2017; Seckinger, 2021).

As for economic value V_y, also environmental value V_y^{env} can be estimated as a function of wind speed, instead of time, by the following expression

$$V_y^{\text{env}} = T_y \int_{U_i}^{U_o} f_{\text{grid}}(U) P(U) W_y(U) \, \mathrm{d}U. \tag{11}$$

7

2.2.3 Net Environmental Value of Energy (NEVOE)

NEVOE is the counterpart of the economic metric NVOE, and it is defined as the difference between the environmental value of energy and the impact of energy, i.e.

$$\text{NEVOE} \left[\frac{\text{kg CO}_2\text{eq}}{\text{MWh}} \right] = \frac{\text{Environmental value} - \text{Environmental cost}}{\text{Energy production}} = \text{EVOE} - \text{IOE}. \tag{12}$$

2.2.4 Future economic Societal Savings (FSS)

FSS estimates the future societal savings enabled by the displacement of GHG emissions, and writes

$$\text{FSS} \left[\frac{\text{\euro}}{\text{MWh}} \right] = \text{SCC} \cdot \text{NEVOE}. \tag{13}$$

The societal cost of carbon (SCC) is the present discounted monetary value of the future damage caused to the environment by one metric ton increase in CO_2-equivalent emissions (National Academies of Sciences, Engineering and Medicine, 2017). The quantification of SCC is clearly not a straightforward task. Indeed, the literature reports a large range of values (Ricke et al., 2018; Kikstra et al., 2021), mostly due to different assumptions on climate sensitivity, economic and non-economic impacts, and response lags, among others (IPCC, 2007). Additionally, NEVOE depends on EVOE that, as previously argued, is based on the simplifying assumption that all generation technologies are equally displaced by wind power; since this is hardly exactly true in practice, further uncertainties are introduced in the estimation of FSS.

3 Methods

This section describes the eco-conscious design of wind turbines, formulated as a constrained multi-objective optimization problem based on a number of interconnected underlying models. Figure 1 shows a schematic representation of the workflow and of its main components.

3.1 Energy model

The energy E_y produced by a wind turbine at a specific location in the year y is computed as

$$E_y = f_a f_p f_w T_y \int\limits_{U_i}^{U_o} P(U) W_y(U) \, \mathrm{d}U. \tag{14}$$

Three correction coefficients are included in the formula. The availability factor f_a accounts for failures, maintenance, and curtailment time, and it is set to the typical value of 0.98 (Vestas, 2011, 2013a, b; Pfaffel et al., 2017). The performance factor f_p considers different sources of losses due to turbulence, gusts, wakes, blade soiling/erosion, etc., and is set to the value of 0.65, which is the lower limit of the range indicated in Lantz et al. (2017). The wind factor f_w accounts for possible deviations of the wind resource from the Weibull distribution, for example due to yearly variability (Lantz et al., 2017). Since the present analysis is based on actual historical data, which already includes any variability of the resource, f_w is set to the value of one.
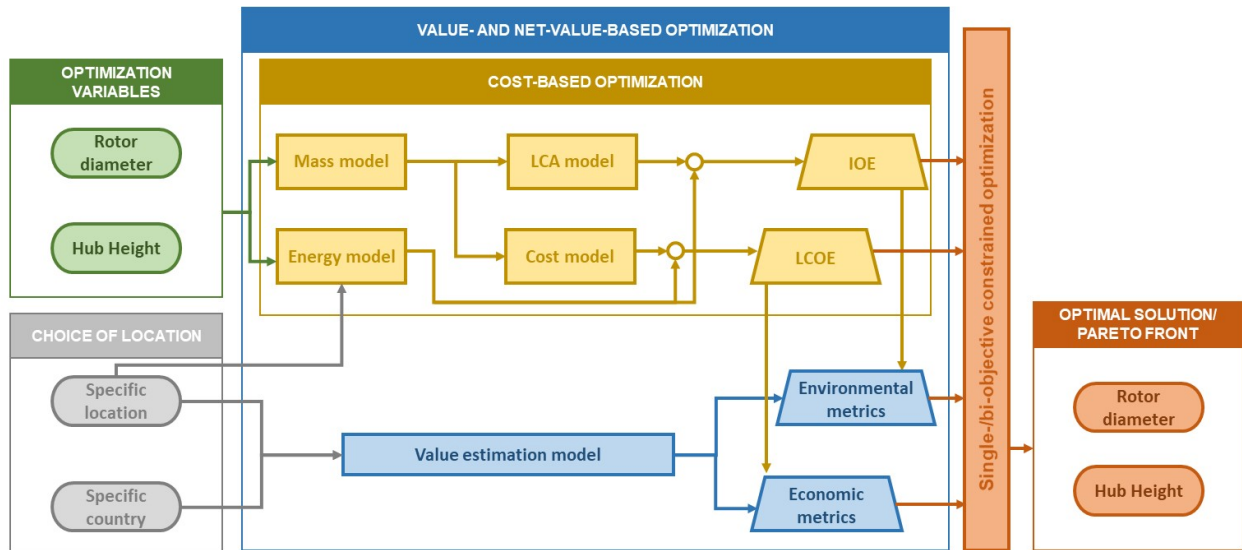
Figure 1. Schematic illustration of the workflow for the eco-conscious multi-objective design optimization of wind turbines. Rounded squares represent variables, squares are models and trapezoids are merit functions.

3.2 Mass model

The mass estimation model is composed of three sub-models. The mass of the various turbine components is based on the 2017 NREL mass model (NREL, 2021), which is an updated version of the 2006 cost and scaling model (Fingersh et al., 2006). Based on the mass of the single components, a material breakdown model defines a bill of materials. This model is based on information sourced from several references (Rydh et al., 2004; Vestas, 2011, 2013a, b; Demir and Taskin, 2013; Haapala and Prempreeda, 2014; Ozoemena et al., 2018), and includes 15 different material types: glass fiber, carbon fiber, epoxy resin, sandwich foam, alloyed steel, unalloyed steel, galvanized steel, copper, aluminium, PVC and other plastics, paint and coating, Neodymium permanent magnet (NdFeB), electronics, and concrete. Finally, a waste factor model estimates the quantity of material that is wasted during the different stages of the component lifetime. Waste factors for fiberglass, epoxy resin, foam, rubber, paint and coating are modeled according to Bortolotti et al. (2019), while a factor of 5% is considered for the other materials.

The use of mass and scaling models is one of the various approximations of the present approach. More precise estimates of masses and bills of materials would clearly be possible by using detailed sizing procedures (Bortolotti et al., 2016; NREL, 2021). This level of complication and computational cost was however not deemed necessary for capturing general trends, which is the main goal here.

3.3 LCA model

LCA is a normed scientific methodology to exhaustively assess the environmental impacts of a product or a service, over its entire lifetime from cradle to grave. Here LCA is performed by an in-house-developed literature-sourced model that follows the environmental management standards of the International Organization for Standardization (ISO), according to ISO 14040 and ISO 14044 (Wolf et al., 2012; Hauschild et al., 2018).

The objective of the LCA model is to assess the complete life-cycle GHG emissions associated with the production of one functional unit, which in this case is 1 kWh of electricity. Emissions are broken down in terms of life-cycle stages, components and materials. Only climate-change-related environmental impacts are considered, and other effects such as human toxicity, eco-toxicity, acidification or resource depletion are excluded.

The model is formulated in a parametric way, i.e it is not specific to a given wind turbine model, and it is generally applicable to contemporary onshore variable-speed horizontal-axis technology. It is assumed that the turbine is installed in Europe between 2015 and 2025, and has a lifetime of 20 years. The machine is composed by rotor, nacelle, drivetrain, tower and foundations, and the elements within these components (e.g., the generator); connection to the grid, storage or other equipment and devices are outside of the scope of this model.

The processes involved in each one of the life-cycle stages are modeled based on typical scenarios from Rydh et al. (2004); Vestas (2011, 2013a, b); Demir and Taskin (2013); Haapala and Prempreeda (2014); Ozoemena et al. (2018), among others. Emission factors are based on Ecoinvent IPCC 2013 (Myhre et al., 2013; Ecoinvent, 2019; Bourgault, 2019).

This LCA method considers the atmospheric emissions of all gases that are recognized to have a greenhouse effect, including CO_2, CH_4, N_2O and fluorinated gases. For each one of these gases, the mass of CO_2 that would have the same greenhouse effect is defined and used as a measure of impact (Myhre et al., 2013; Bourgault, 2019).

3.3.1 Life-cycle stages

This section briefly defines the life-stages considered in the present work, and the assumptions taken in each of them. For further details, the reader is referred to Guilloré et al. (2022).

– Life-cycle stage 1: Raw material extraction and processing. This stage accounts for the environmental impact upstream of the purchasing of a unit of ready-to-use material for manufacturing. Raw material extraction and processing emissions are modelled according to Ecoinvent (2019).

– Life-cycle stage 2: Transportation of raw materials to manufacturing sites. This stage considers both direct emissions caused by the burning of transportation fuel, and indirect emissions produced in the life-cycle of the fuel from well to tank. Indirect emissions from the production of the transportation technology itself are also included. Based on Vestas (2011, 2013a, b), it is assumed that all materials are transported over a distance of 600 km to the manufacturing site, except for concrete, which is only transported over a distance of 50 km. Emission factors for transportation are considered

from Ecoinvent (2019), assuming that materials are transported by freights and lorries heavier than 32 t, with EURO4 exhaust emissions (Spielmann et al., 2007).

– Life-cycle stage 3: Wind turbine component manufacturing. This stage considers the environmental impact of the energy consumed for the transformation of the materials into wind turbine components. The upstream environmental impact of the energy consumed – which is generally electricity from the grid, whose impact depends on the specific electricity mix – is also considered. Manufacturing emissions are obtained from several sources (Song et al., 2009; Hill and Norton, 2018; Ecoinvent, 2019).

– Life-cycle stage 4: Transportation of the components to the wind plant site. For this stage, the same assumptions on transportation vehicles of the life-cycle stage 2 are taken, adding ship transport. Assumptions on transportation distances are modeled according to Vestas (2011, 2013a, b).

– Life-cycle stage 5: Assembly and installation of the wind turbine. This life-cycle stage considers the direct and indirect emissions from the assembly and installation of the different wind turbine components. It is assumed that a hydraulic crane is required for 16 hours of work (Rydh et al., 2004; Ozoemena et al., 2018).

– Life-cycle stage 6: Operation and maintenance (O&M). This stage considers different impacts related to operation and maintenance, and is defined according to Rydh et al. (2004); Vestas (2011, 2013a, b); Demir and Taskin (2013); Haapala and Prempreeda (2014); Ozoemena et al. (2018). The GHG emitted during O&M are determined as the sum of the emissions related to the turbine lubricant oil change, to the use of an inspection van and maintenance crane, and related to the replacement of components, as detailed next.

  – Lubricant Oil. The oil employed for the regular change of gearbox oil and lubricant is considered. Assumptions are taken according to Rydh et al. (2004), Haapala and Prempreeda (2014) and Ozoemena et al. (2018).

  – Inspection van. It is assumed that a roundtrip from the maintenance base is required every 6 months (Ozoemena et al., 2018) with a diesel passenger car of emission category EURO4 (Spielmann et al., 2007).

  – Maintenance Crane. It is considered that heavy crane machinery is required for a total of 8 hours over the turbine lifetime (Ozoemena et al., 2018).

  – Replacements of components. All components may be subjected to failures, and generally several parts need to be replaced over the lifetime of a wind turbine. Failure rates are modeled according to Tremeac and Meunier (2009); Demir and Taskin (2013); Haapala and Prempreeda (2014); Ozoemena et al. (2018). Life-cycle stages 1 to 5 are used to estimate the emissions resulting from the spare components that need to be replaced. Additionally, the impact of the transport of the replacement components to the site is doubled, to account for the trip back with the defect replaced components.

11

– Life-cycle stage 7: Decommission and transportation of parts. This life-cycle stage considers 16 hours of crane work, as described in Rydh et al. (2004) and Ozoemena et al. (2018). The same assumptions taken for life-cycle stage 4 are used also here to estimate the emissions caused by the transportation of the parts to their EOL treatment centers.

– Life-cycle stage 8: EOL treatment. The EOL scenario is a key stage in the life-cycle of a wind turbine. Three treatments are considered in this work: recycling, incineration, and landfilling. In accordance with ISO 14044 (Wolf et al., 2012; Hauschild et al., 2018), the approach of closed-loop material cycle is considered, where full credit is given to the emissions of life-cycle stage 1 linked to the recycled materials. Recycled materials are therefore considered to have a negative impact, and thus represent environmental benefits. Metals – steel, copper, and aluminium – have high recyclability rates, as shown in Fig. 2 (Tremeac and Meunier, 2009; Vestas, 2011, 2013a, b; Haapala and Prempreeda, 2014; Schmid, 2020). On the other hand, there is no mature technology yet for the recycling of thermoset glass-fiber reinforced polymers (GFRP), which are currently incinerated or landfilled (Schmid, 2020; Beauson et al., 2022), depending on the legislation of the country. A representative scenario of 50% incineration and 50% landfilling is assumed here, as described in Vestas (2011, 2013a, b). The overall EOL impact is the sum of the recycling, incineration and landfilling environmental impacts. This quantity can either be positive or negative, depending on whether or not the recycling benefits outweigh the incineration and landfilling environmental impacts.
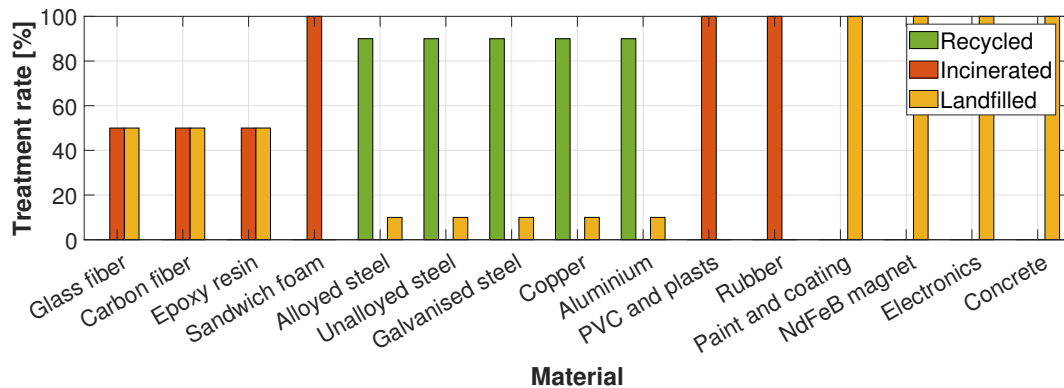
Figure 2. EOL treatment rates (by mass) for various materials types.

3.3.2 Validation of the LCA model

The LCA model was validated against results published by Schleisner (2000); Tremeac and Meunier (2009); Vestas (2011, 2013a, b); Al-Behadili and El-Osta (2015); Ozoemena et al. (2018), as shown in Fig. 3.

In general, there is a good match between previous studies and the present model. Differences arise due to non identical hypotheses and assumptions, for instance in life-cycle scenarios, bill of materials, or energy production. Indeed, several pub-
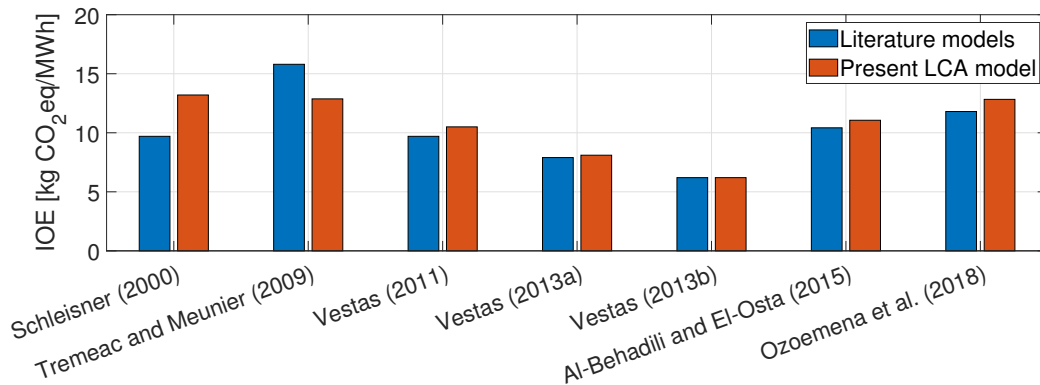
Figure 3. Comparison of the environmental impact obtained with the present LCA model and with results sourced from the literature.

lications do not thoroughly detail the assumptions taken, or the processes considered in the different life-stage cycles, which hinders an exact comparison.

3.4 Cost model

Costs are based on the 2015 NREL cost model (NREL, 2021), converted to 2017 € values. The model estimates the initial capital costs and O&M costs. Initial capital costs include rotor, nacelle, drivetrain, tower and foundations, as well as balance of station (BOS) costs, including transportation, assembly and installation. Additional BOS-related costs such as engineering, permitting, and grid connection are excluded, as their environmental impact is not considered in the present LCA model. Annual operating expenses include O&M costs, whereas land lease costs are not considered.

3.5 Value estimation model

This model estimates the economic and environmental value of a wind turbine, for a specific location and a specific time frame, as illustrated in Fig. 4.

The estimation of economic value is based on historical data, using Eq. (4). Time series of spot market price were correlated with time series of wind speed at a specific location and hub height, resulting in the price-wind model $p_y(U)$. Similarly, the environmental value was estimated with Eq. (11), where the grid average emission factor $f_{\text{grid}}(U)$ was computed based on the energy mix time history of the country, or region, where the turbine is located. The average emission factor of each generation technology in the mix was obtained from Ecoinvent (2019), and only considers operational emissions (Thomson et al., 2017; Boeing et al., 2019). Wind speed time histories were adjusted to the turbine hub height based on the site mean shear, and used to estimate the Weibull distribution, spot market price, and grid-average emission factor.
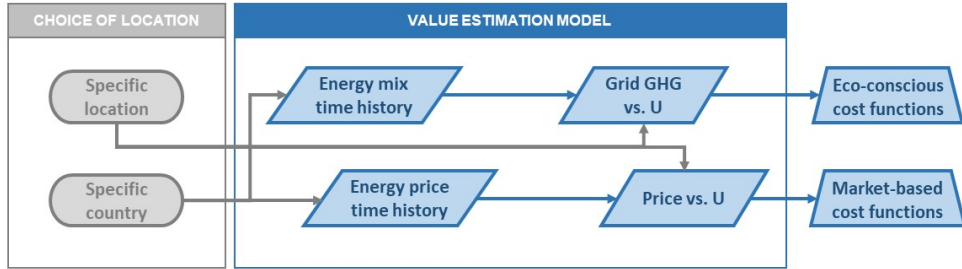
13

Figure 4. Workflow of the value estimation model of Fig. 1. Rounded squares represent variables, squares are models, rhombuses are data, and trapezoids are merit functions.

3.6 Optimal design problems

In this work two different design problems are considered, based on either a single- or a two- objective constrained optimization. In both cases, the problem is formulated as:

$$\min_{\mathbf{p}} \quad J(\mathbf{p}), \tag{15a}$$

$$\text{such that:} \quad \mathbf{c}(\mathbf{p}) \leq 0, \tag{15b}$$

where J is the cost function, chosen among the design metrics of Sect. 2, $\mathbf{p} = (D, H)$ are the design variables, with D the rotor diameter and H the hub height. Finally, $\mathbf{c}$ are inequality constraints that enforce desired design conditions.

The single-objective optimization problem is solved with a sequential quadratic programming algorithm, in which gradients are computed by means of finite differences (Mathworks, 2019). The multi-objective optimization problem is solved with a non-dominating sorting genetic algorithm (NSGA-II) (Seshadri, 2020).

This simplified design problem is termed *preliminary*, in the sense that it only determines macroscopic parameters of the machine. Based on the results of this preliminary sizing, standard detailed design procedures should be used to dimension all components and systems.

4 Case study: cost-driven and eco-conscious designs of a wind turbine for Germany

Trade-offs were investigated between an economic and an environmental point of view, by analyzing the characteristics of the resulting optimal turbines with respect to a standard LCOE-driven baseline assumed as reference. The study was performed with the methods described in the previous sections, where the cost model was tuned to represent the situation in Germany according to Deutsche WindGuard (2018) and Duffy et al. (2020).

4.1 Baseline description

The baseline is chosen to represent a recent LCOE-driven industrial product, and corresponds to a wind class IIA machine with a rated power of 3 MW, a rotor diameter of 115.7 m, a hub height of 92 m, and a lifetime of 20 years. These characteristics make the baseline loosely resemble one of the several E-115/3.0 MW models (Enercon, 2021) that, according to Deutsche WindGuard (2018), was the most installed turbine in Germany in 2016, 2017 and 2018 – the years considered in this study. This wind turbine has an IOE of 11.83 kg CO_2eq/MWh and an LCOE of 35.6 €/MWh, according to the models of §3.4. Given the typical large uncertainties in the discount rate, $d = 0$ was assumed in Eq. (1).

Figure 5 shows a breakdown of the environmental cost of the wind turbine by its principal components. The figure reports both absolute emissions per unit of component mass (green bars), as well as relative emissions with respect to the overall impact produced by the wind turbine (blue bars). Tower and foundations play the largest role in the overall IOE, each one accounting for about 20% of the total. The high environmental impact of the foundations is due to the significant amount of concrete that they require, and the negative effects caused by landfilling at the end of life. The tower, on the other hand, is made of steel, a material with a high recyclability rate (see Fig. 2). Notwithstanding the resulting emissions credits at the end of life, the tower still has a significant environmental impact because of its very large mass. Blades also present a large environmental impact, because of their reduced recyclability. Electronics have the highest impact per unit of material, but a small overall contribution due to their reduced mass.
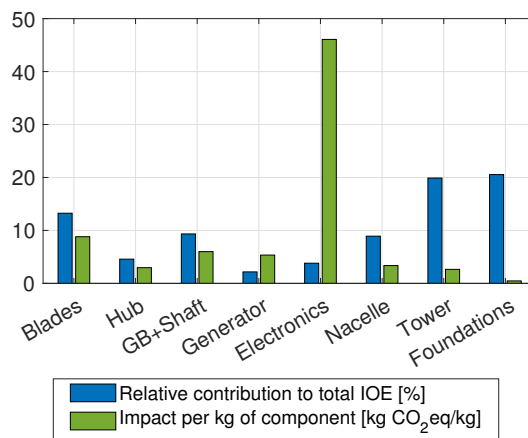

Figure 5. Environmental impact of the life-cycle of each component of the baseline wind turbine, expressed in terms of absolute emissions per unit of component mass (green bars), and relative percent emissions with respect to the overall impact of the machine (blue bars).

15

4.2 Cost-driven design

The baseline turbine was then optimized from an economic-environmental cost perspective. Only hub height and rotor diameter are free design variables, whereas rated power is held fixed to the baseline value. The bi-objective design problem is expressed by Eq. (15), where J considers economic cost by LCOE and environmental cost by IOE. The design constraints of Eq. (15b) are set to express conditions on height/diameter ratio and on the specific power of the turbine:

$$0.5 < \frac{H}{D} < 1, \tag{16a}$$

$$100\,\text{MWm}^{-2} < \frac{P_r}{A} < 350\,\text{MWm}^{-2}, \tag{16b}$$

where P_r is the rated power, and $A = \pi D^2/4$ is the rotor swept area. These same inequality constrains were used also in all the following design problems.

Figure 6a shows the resulting Pareto front of optimal non-dominating solutions. The corresponding optimal rotor diameters and hub heights of the Pareto front designs are shown in Fig. 6b.
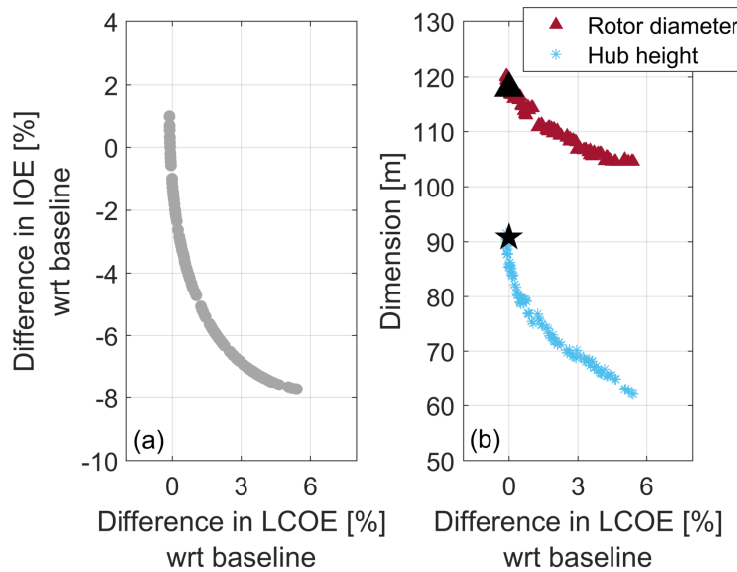
Figure 6. Pareto front of IOE vs. LCOE **(a)**. Rotor diameter and hub height of the Pareto optimal designs **(b)**. Differences are expressed with respect to the baseline configuration, whose dimensions are given by black ▲ (diameter) and ★ (hub height) symbols.

Results indicate that a decrease in IOE can be achieved by reducing the overall size of the turbine, both in terms of rotor diameter and hub height; since rated power is held fixed, the resulting turbines have an increased specific power P_r/A. A maximum reduction in IOE of about 8% is achieved at the expense of an increase of about 5% in LCOE.

However, what is more interesting to observe is that the curve is very steep close to the point of minimum LCOE. This means that a significant reduction in IOE can be achieved with marginal increments in LCOE. For instance, a turbine with a 110 m diameter and a 75 m hub height presents an LCOE that is only 1% higher than the baseline, while at the same time achieving

400 an IOE reduction of about 5%. This result is achieved by the design of smaller rotors and shorter towers that, although imply a somewhat reduced power capture, have lower environmental costs.

4.3 Value-driven design

The previous section showed that, from a cost perspective, there is room to reduce the impact on the environment if one is willing to accept some increase in the cost of energy from wind. However, cost by itself does not capture the full complexity

405 of the problem, and further insight can be obtained by including also value in the analysis.

To this end, the turbine was optimized considering economic and environmental value, instead of cost. Two different locations in Germany were selected: one in the north of the country (labelled LN in the following), characterized by very good wind conditions, and a second one in the south (labelled LS), with lower average wind speeds. The site wind characteristics are more precisely shown by the two Weibull distributions reported in Fig. 7 (NEWA, 2021).
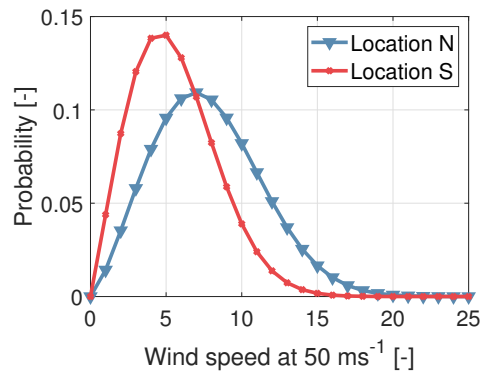

Figure 7. Weibull distributions at the northern and southern German locations, at 50 m height above ground.

410 The economic and environmental values were estimated with the model described in §3.5. Day-ahead spot market price and energy mix time series were collected from the SMARD database (SMARD, 2020), and completed with wind speed time series obtained from NEWA (2021), considering the years 2016, 2017 and 2018. All quantities were sorted into 50 wind speed bins, each containing the same number of data points. The resulting interpolating curves were extrapolated above the last bin upper boundary all the way to cut-out wind speed.

415 Figure 8 and 9 respectively show the histograms of spot market price and grid GHG emissions vs. wind speed at 50 m height at the LN and LS sites, for the three considered years. For both locations, the spot market price and grid GHG emissions exhibit a decreasing trend with respect to wind speed. In fact, at low wind speeds there is a large amount of energy from coal-fired power stations in the energy mix, pushing both the price and grid GHG emissions up. With higher wind speeds, the amount of

17

wind energy in the grid increases, so that more expensive and polluting energy sources are displaced. This is clearly a partial
420 view of the behavior of a very complex system, which does not only depend on wind speed.
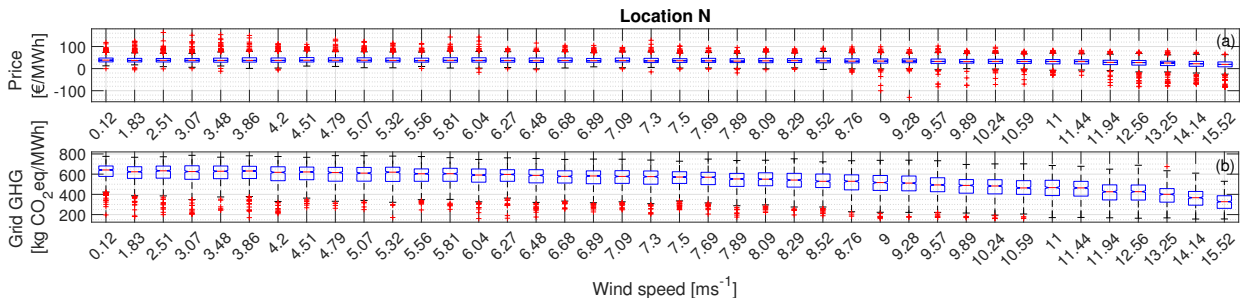

Figure 8. Spot market price **(a)** and grid GHG emissions **(b)** vs. wind speed at 50 m for LN (site in the north of Germany).
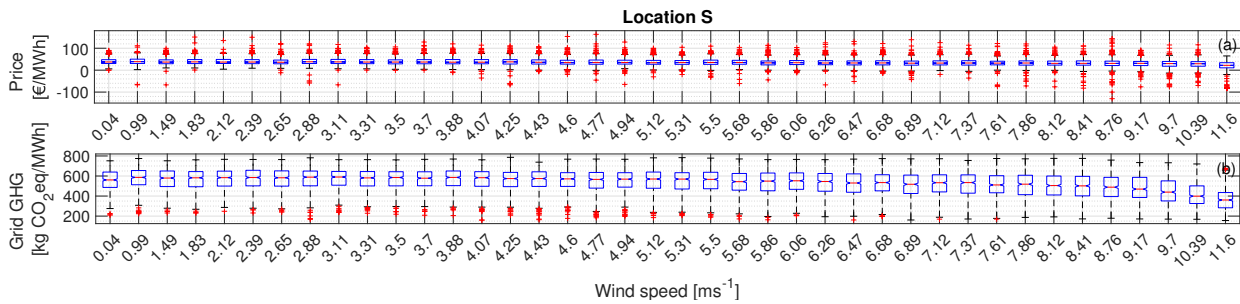

Figure 9. Spot market price **(a)** and grid GHG emissions **(b)** vs. wind speed at 50 m for LS (site in the south of Germany).

4.3.1 Single-objective optimization

First, a single-objective optimization was run for each metric at the two locations in order to analyze the behavior of the optimal turbine design characteristics. The resulting diameters are shown in Fig. 10a, while the hub heights are given in Fig. 10b. The figures of merit are organized from left to right as follows: the first two are cost-based metrics (LCOE and IOE), the next two
425 are value-based metrics (LVOE and EVOE), and finally the last two are net-value-based metrics that consider both cost and value (NVOE and NEVOE).

Analyzing first the cost-based perspective, results indicate that, as already observed in §4.2, a turbine designed for minimum IOE has a smaller rotor and a shorter tower than a turbine designed for minimum LCOE, on account of their large environmental impact. For both metrics, the southern location LS requires a turbine with a larger rotor and a taller tower than the northern
430 location, due to lower typical wind speeds.

From a value point of view, no differences in rotor diameter and hub height are found between the economic (LVOE) and the environmental (EVOE) perspectives. In fact, for both metrics, the optimal rotor and hub height are as large as possible, hitting the lower bound for specific power. This can be explained by noticing that, since low wind speeds are associated with larger
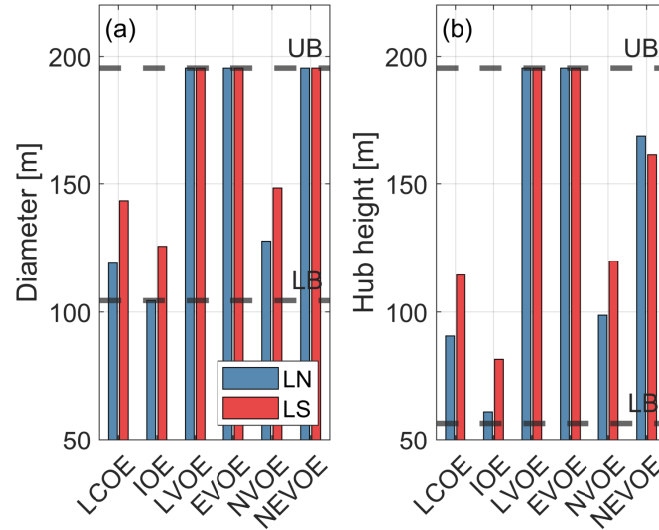
18

Figure 10. Optimal diameters **(a)** and hub heights **(b)** for each single objective function, for the two locations. Cost-based metrics: LCOE, IOE; value-based metrics: LVOE, EVOE; net-value-based metrics: NVOE, NEVOE.

economic and environmental values (see Figs. 8 and 9), optimal economic/environmental value-driven designs tend to produce
435   as much as possible at low wind speeds. This can be achieved by minimizing the extent of the partial load region (region II), which is obtained by reducing the rated wind speed $V_r = \sqrt[3]{2P_r/\rho A C_{P_{\max}}}$, where ρ is the air density and $C_{P_{\max}}$ the maximum power coefficient of the rotor. A shown by the formula, since $C_{P_{\max}}$ is limited by physics, for given ambient conditions ρ, V_r decreases for smaller specific powers P_r/A. These results are in line with similar studies that have shown how low specific power turbines have a higher economic value (Hirth and Mueller, 2016; Swisher et al., 2022).

440   Finally, both NVOE and NEVOE – which consider both cost and value – lead to configurations that can be interpreted as compromises between the cost and value perspective. For NVOE, as economic value has the same order of magnitude as economic cost, the solution presents a rotor diameter and hub height that fall in between the cost- and value-based solutions. On the other hand, for NEVOE the environmental value is one order of magnitude larger than the environmental cost, and this drives the rotor size, which even in this case hits the lower limit for specific power. The introduction of cost, however, penalizes
445   the hub height, which is reduced with respect to the value-based solution because of the large influence of the tower.

4.3.2   Bi-objective optimization

Next, trade-offs between the economic and environmental net value were analyzed through a Pareto front, computed solving the bi-objective optimization problem expressed by Eq. (15). The LCOE-driven designs obtained in the previous section and displayed in Fig. 10 are used here as baselines for each location.

19

450　　For the two sites LN and LS, Fig. 11a shows the Pareto front NEVOE vs. NVOE, while Fig. 11b reports the change in rotor diameter and hub height with respect to the baselines, as functions of NVOE. As already observed in Fig. 6, even in this case results indicate that it is possible to increase the environmental net value (NEVOE) without significantly decreasing the economic net value (NVOE). For example, accepting a decrease in NVOE of 1 €/MWh buys half of all possible improvement in NEVOE, for both locations. This is achieved with larger diameters (i.e., smaller specific powers), and taller hub heights.

455　　Another interesting observation is that both locations present the same Pareto front shape. While LN has a better economical performance than LS (as expected, because of the better wind resource), both locations appear to have a similar net value from an environmental point of view.
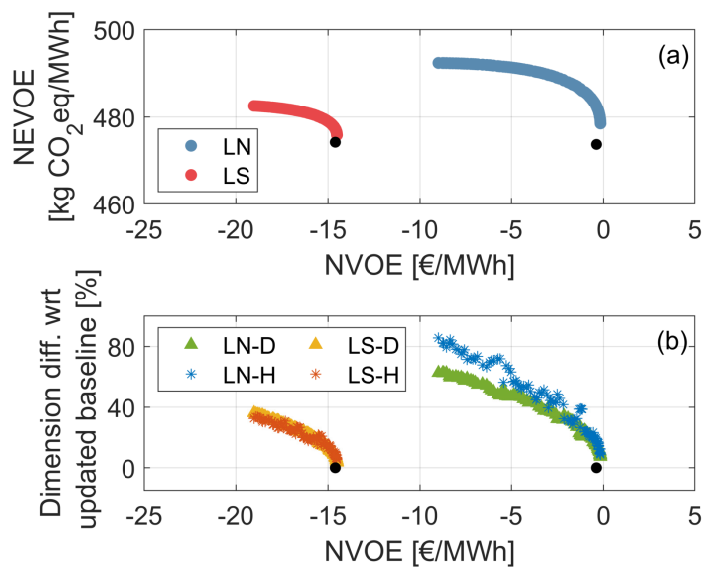

Figure 11. Pareto front between a net environmental value point of view (NEVOE) and a net economic value point of view (NVOE) **(a)**. Optimal diameters and hub heights for the solutions of the Pareto front, expressed as percent changes with respect to the corresponding LCOE-driven baseline of each location **(b)**

Finally, environmental net value was used to estimate future economic societal savings, multiplying NEVOE by SCC, as described in §2.2.4. An SCC of 1 €/kg CO_2eq was considered in this work. However, as previously noted, SCC can take widely

460　　different values depending on the assumptions and models considered (IPCC, 2007). Although this makes the resulting FSS values affected by high uncertainty, the analysis is still useful because it may reveal interesting trends.

　　Figure 12 presents the designs that result from trading LCOE – the metric currently used to asses the competitiveness of an energy-producing technology – with FSS – the metric proposed here to estimate the future societal savings obtained by deploying an energy-producing technology.
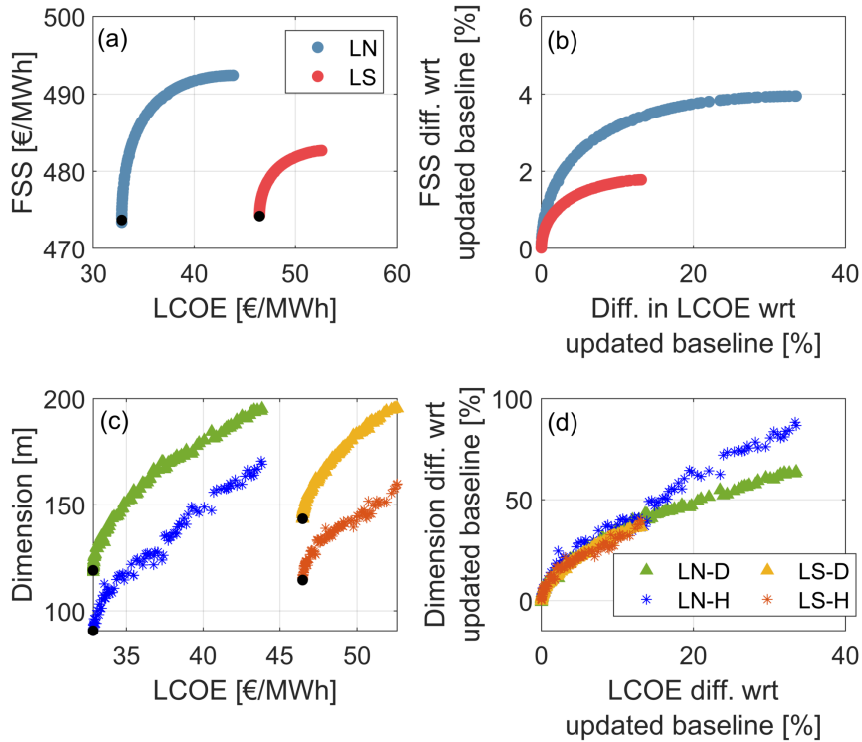
Figure 12. Pareto front between FSS and LCOE, in absolute values **(a)**, and relative to the LCOE-driven baseline of each location **(b)**. Optimal diameters and hub heights of the Pareto solutions in absolute values **(c)**, and relative to the corresponding LCOE-driven baseline of each location**(d)**.

The Pareto front is displayed in absolute quantities in Fig. 12a, and relative to the LCOE-driven baselines in Fig. 12b. Similary, the solutions of the Pareto front are displayed in absolute quantities in Fig. 12c, and relative to the baseline configurations in Fig. 12d. The values shown here should be treated only as rough estimates because of the many simplifications and assumptions. Nonetheless, some interesting trends seem to emerge.

First, as expected, the current LCOE-driven designs (which capture the individual point of the view of the investor and consumer) are not optimal from the societal point of view. This means that, to improve the societal metric, an individual would have to accept an increase in out-of-pocket expenditure.

Second, the largest opportunities appear to be close to the LCOE optima, where the curves are very steep. This means that even marginal increases in cost can have an impact on the societal savings. However, away from the LCOE optima, the curves level off, meaning that optimal societal savings would require significant increases in cost, which would probably not be acceptable by consumers.

Third, the general trend of the Pareto solutions is similar at both sites. Hence, even at sites characterized by poor wind resources, there is room for improving the societal value of wind energy.

Fourth, although better wind resources at the northern Germany site are associated with lower costs, the societal savings are similar at both locations. This is an interesting finding, because it implies that the installation of each new wind turbine is of a similar environmental and societal value, independently of the characteristics of the site. However, since sites with worse wind resources are penalized by a higher LCOE, policies may be needed that – by taking a long-term view on future economic societal savings – increase in the short-term the competitiveness of wind turbines at these locations.

5   Conclusions

This paper has explored the idea of enhancing the inherent societal value of wind turbines by changing the way they are designed. While societal value is clearly a very broad concept, the focus here is on the societal benefits brought by the displacement of environmental emissions made possible by the generation of renewable energy from wind.

The paper first defined metrics that quantify the societal value of wind turbines based on two concepts: *environmental cost* and *environmental value*. The former expresses the GHG emissions generated throughout the entire lifetime of a wind turbine, while the latter quantifies the displacement of GHG emissions from the grid caused by the deployment of a wind turbine; in both cases, these quantities are computed per unit of generated energy. These metrics are defined mirroring already existing economic metrics, based on the familiar concepts of economic cost and value.

Next, a toolchain was described, which implements a complete LCA model capable of estimating the emissions of a wind turbine throughout its lifetime, broken down in life-cycle stages, components and materials. Using the LCA model, together with energy and mass models, a simplified design problem was formulated, which can determine the optimal geometric characteristics of a wind turbine (in terms of its rotor diameter and hub height) for a given rated power. The resulting preliminary design gives only the overall dimensions of the turbine, and would have to be followed by a detailed design of its aerodynamics, structures, systems and control laws. The design problem can be formulated either as a single or a multi(bi)-objective minimization. The classical standard approach of designing wind turbines by minimizing LCOE is included in the formulation as a special case.

A 3 MW wind turbine, representative of the LCOE-driven machines currently installed in Germany, was chosen as a baseline reference to study the effects of considering various possible economic and/or environmental metrics in the preliminary sizing problem.

The environmental assessment of the baseline highlighted the large contribution of the foundations – made of concrete –, and of the tower – made of highly-recyclable steel – to the total life-cycle emissions of the wind turbine. These components have low emission factors – i.e., a low environmental cost per unit of mass – but require large quantities of material. Electronic components, on the other hand, have a modest overall contribution even if they have very high emission factors. Clearly, the overall environmental cost of a wind turbine depends on the technological solutions chosen for its main components. Indeed, choices at all stages of the life-cycle – from the processes used to mine or produce the materials to EOL decisions –

have implications on both the economic and environmental costs, as the two aspects are intimately connected. Understanding
510   the environmental cost of each material, each component and each life-cycle stage is critical for identifying alternatives that
minimize both forms of cost.

The baseline turbine was then redesigned using a bi-objective optimization for LCOE and IOE, obtaining a Pareto front of
optimal non-dominating solutions. This family of solutions can be interpreted as the cost-optimal designs that trade the point
of view of the individual (LCOE) with the point of view of society (IOE). It is one of the main findings of this work that the
515   Pareto front is very steep around the LCOE-optimal designs. For the case considered here, it appears that an LCOE increase
of only 1% can buy an IOE decreases of 5%. In other words, it pays off to be altruistic, and a large societal impact can be
achieved if consumers are willing to pay a bit more for the energy that they consume.

Finally, the effects of value and net value were considered, again looking at both the economic and environmental points of
view. Value-based metrics are location- and time-dependent quantities, and therefore tightly linked to the site where the wind
520   turbine is installed. Two locations were considered: one in the north of Germany with better wind resources, and one in the
south of the country, where typical wind speeds are lower. Results show that, for the years considered here, spot market price
and grid GHG emissions are generally higher at low wind speeds for both sites, as generally expected.

A Pareto front of optimal solutions was generated that trades-off economic net value – i.e. the difference between economic
value and cost –, and environmental net value – similarly defined, but considering emissions. Results indicate that, here again,
525   the curves are very steep close to the net-value economic optima. Therefore, even from this point of view altruism pays off,
and significant net value environmental gains can be achieved with rather small losses in net economic value.

Unsurprisingly, economic net values were found to be profoundly different at the two locations, the better wind resources in
the north being associated with much lower values of NVOE. However, interestingly, the environmental net values at the two
locations were found to be very similar. This result points to the fact that wind turbines have similar beneficial effects no matter
530   where they are installed, with little sensitivity to the local wind resources. Therefore, wind energy is a sensible choice also for
places with modest wind conditions, as for example the south of Germany. Clearly, these results should be further explored
considering transmission constraints.

Additionally, it was found that environmental value is one order of magnitude larger than environmental cost, whereas
economic value and cost are of the same order of magnitude. Consequently, the economic net value is more sensitive than the
535   environmental one to the characteristics of the location.

Finally, future societal savings were estimated by using the societal cost of carbon, which quantifies the present cost of
future damage caused by the emission of one additional unit of CO_2eq. Similar conclusions as the ones discussed earlier can
be drawn from these results.

This study shows that, in general, low specific power turbines present higher economic and environmental values, at the
540   expense of a higher cost of energy. This is due to the fact that, with the present technology, the larger energy captured by
a bigger rotor does not generally compensate its larger cost. However, the present findings highlight that the benefits of low
specific power turbines go well beyond what is quantified through LCOE alone, which, in hindsight, appears to be a rather
myopic and incomplete metric. Indeed, several studies have shown that low specific power turbines bring benefits beyond

economic value: for instance they can better utilize the transmission system, reduce forecasting errors, and could lead to cheaper financing (Hirth and Mueller, 2016; Swisher et al., 2022).

The present work and its findings are affected by several limitations.

First, the LCA, mass, and cost models are based on general trends of current wind turbines. Clearly, low specific power machines push the boundaries of these models. More accurate estimates could be obtained by using detailed design procedures that, from the rough sizing produced by the present approach, yield refined designs.

Additionally, the trends shown here are only valid for Germany in the years considered. Clearly, both economic and environmental value depend on the time-specific composition of the energy mix, whose behavior is very complex and depends on more variables than just wind speed, as it was assumed here for simplicity. The assumptions taken in this work are clearly oversimplifications that try to produce initial rough preliminary trends. Future work should couple the present models with more sophisticated descriptions of the energy mix, able to capture their present and future composition. In fact, understanding how the economic and environmental value of wind energy will develop in the next years is yet another crucial element that deserves further work. Indeed, as wind penetration is set to increase, the economic value of wind energy is expected to decrease, an effect called "self-cannibalization". However, predicting the impact of an increase in wind energy is not straightforward, as the final effects depend on the emission factors of the generating technologies in the energy mix. The impact on displaced GHG is even more complex to estimate, as it depends on the emission factors of the generating technologies operating on the margin, which are not only strongly country-specific, but also time-dependent. Here again, these effects can only be properly captured by using more sophisticated models, including an electricity market model.

Notwithstanding these limitations, it was one major ambition of this paper to bring the inherent societal value of wind turbines under the spotlight. While this study only focused on the changes in overall dimensions (and, in turn, specific power) of the machine, the potential for further improvements is much larger that what would appear by this simple analysis alone. In fact, the same metrics developed here can also be employed to guide the choice of technologies and the detailed design of the various components of a wind turbine. In addition, beyond the single wind turbine case analyzed here, this new eco-conscious design philosophy can be used to design a whole wind plant.

575 **Nomenclature**

A	Rotor swept area
C	Cost
D	Rotor diameter
E	Energy
H	Hub height
J	Cost function
P	Power
T	Duration
Q	Emissions
U	Wind speed
V	Value
W	Weibull distribution
$\mathbf{c}$	Constraints
d	Discount rate
f	Factor
p	Spot market price
$\mathbf{p}$	Design parameters
t	Time
CO_2eq	Equivalent grams of CO_2 with the same global warming potential of a given gas
$(\cdot)_y$	Relative to year y
EOL	End of life
EVOE	Environmental value of energy
FSS	Future societal savings
GFRP	Glass-fiber reinforced plastic
GHG	Greenhouse gas, i.e. CO_2, CH_4, NO_2, F-gases, among others
IOE	Impact of energy
LCA	Life-cycle assessment
LCOE	Levelized cost of energy
LVOE	Levelized value of energy

580

585

590

595

600

605 NEVOE Net environmental value of energy

NVOE Net value of energy

SCC Societal cost of carbon

References

610   Al-Behadili S.H. and El-Osta W.: Life Cycle Assessment of Dernah (Libya) wind farm, Ren. Energy, 83, 1227-1233, https://doi.org/10.1016/j.renene.2015.05.041, 2015.

Aldersey-Williams J. and Rubert T.: A theoretical justification and critical assessment, Energy Policy, 124, 169-179, https://doi.org/10.1016/j.enpol.2018.10.004, 2019.

Beauson J., Laurent A. and Pagh Jensen J.: The complex end-of-life of wind turbine blades: A review of the European context, Renewable
615   and Sustainable Energy Reviews, 155, 111847, doi.org/10.1016/j.rser.2021.111847, 2022.

Beiter P., Cooperman A., Lantz E., Stehly T., Shields M., Wiser R., Telsnig T., Kitzing L., Berkhout V., Kikuchi Y.: Wind power costs driven by innovation and experience with further reductions on the horizon, WIREs Energy and Environment, 10 (5), https://doi.org/10.1002/wene.398, 2021.

Bortolotti P., Bottasso C.L, Croce A.: Combined preliminary-detailed design of wind turbines, Wind Energy Science, 1, 71-88,
620   https://doi.org/10.5194/wes-1-71-2016, 2016.

Bortolotti P., Berry D., Murray R., Gaertner E., Jenne D., Damiani R., Barter, G.E. and Dykes, K.: A Detailed Wind Turbine Blade Cost Model, NREL Report TP-5000-73585, NREL, Golden, CO, USA, https://dx.doi.org/10.2172/1529217, 2019.

Boeing F. and Regett A.: Hourly CO2 Emission Factors and Marginal Costs of Energy Carriers in Future Multi-Energy Systems, Energies, 12, 2260, https://doi.org/10.3390/en12122260, 2019.

625   Bourgault G.: Implementation of impact assessment methods in the ecoinvent database version 3.6, Ecoinvent, Swiss Center for Life Cycle Inventories, Tech. Report, 2019.

Deutsche Bundesnetzagentur: SMARD Strommarktdaten platform, smard.de/home, 2020.

Deutsche WindGuard: Wissenschaftlicher Bericht: Vorbereitung und Begleitung bei der Erstellung eines Erfahrungsbericht gemäß §97 Erneuerbare-Energien Gesetz. Teilvorhaben II e): Wind an Land, Technical Report, 2019.

630   Demir N., Taskin A.: Life cycle assessment of wind turbines in Pinarbasi-Kayseri, Journal of Cleaner Production, 54, 253-263, 10.1016/j.jclepro.2013.04.016, 2013.

Duffy A., Hand M., Wiser R., Lantz E., Dalla Riva A., Berkhout V. Stenkvist M., Weir D. and Lacal-Arántegui R.: Land-based wind energy cost trends in Germany, Denmark, Ireland, Norway, Sweden and the United States, Applied Energy, 277, 114777, 10.1016/j.apenergy.2020.114777, 2020.

635   Enercon: E-115 EP-3, produkte/ep-3/e-115-ep3/ (last access: 24 November 2021), 2021.

Fingersh L., Hand M., Laxson A.: Wind Turbine Design Cost and Scaling Model, NREL Report NREL/TP-500-40566, https://www.nrel.gov/docs/fy07osti/40566.pdf, 2006.

Gillingham K. and Stock J.H.: The Cost of Reducing Greenhouse Gas Emissions, Journal of Economic Perspectives, 32(4), 53-72, doi.org/10.1257/jep.32.4.53, 2018.

640   Guilloré A., Canet H., Bottasso C.L.: Life-Cycle Environmental Impact of Wind Turbines: What are the Possible Improvement Pathways?, J.Phys. Conf.Ser., to appear.,2022.

Haapala K. and Prempreeda P.: Comparative life cycle assessment of 2.0 MW wind turbines, Int. J. of Sustainable Manufacturing, 3, 170-185, 10.1504/IJSM.2014.062496, 2014.

Hauschild M.Z., Rosenbaum R.K. and Olsen S.I.: Life Cycle Assessment, Theory and Practice, Springer, doi.org/10.1007/978-3-319-56475-
645   3, 2018.

Hawkes A.D.: Estimating marginal CO2 emissions rates for national electricity systems, Energy Policy, 38, 5977-5987, https://doi.org/10.1016/j.enpol.2010.05.053, 2014.

Hill C. and Norton A.: LCA database of environmental impacts to inform material selection process, Damage Controlled Composite Materials (DACOMAT) Deliverable 6.1, 2018.

650 Hirth L.: Integration costs and the value of wind power. Thoughts on a valuation framework for variable renewable electricity sources, USAEE Working Paper, 12-150 doi.org/10.2139/ssrn.2187632, 2012.

Hirth L. and Müller S.: System-friendly wind power: How advanced wind turbine design can increase the economic value of electricity generated through wind power, Energy Economics, 56, 51-63 10.1016/j.eneco.2016.02.016, 2016.

International Panel on Climate Change: Climate Change 2007: Impacts, Adaptation and Vulnerability. Contribution of Working Group II to
655 the Fourth Assessment Report of the Intergovernmental Panel on Climate Change, M.L. Parry, O.F. Canziani, J.P. Palutikof, P.J. van der Linden and C.E. Hanson, Eds., Cambridge University Press, Cambridge, UK, 2007.

International Renewable Energy Agency: Renewable Power Generation Costs in 2020, Abhu Dhabi, 2021.

Jansen M., Staffell I., Kitzing L., Quoilin S., Wiggelinkhuizen E., Bulder B., Riepin I. and Müsgens F.: Offshore wind competitiveness in mature markets without subsidy, Nature Energy, 5, 614-622, https://doi.org/10.1038/s41560-020-0661-2, 2020.

660 Joskow P.: Comparing the costs of intermittent and dispatchable electricity generation technologies, Am. Econ. Rev. Pap. Proc., 100 (3), 238-241, 10.1257/aer.101.3.238, 2011.

Kikstra J.S., Waidelich P., Rising J., Yumahev D., Hope C. and Brierley C.M.: The social cost of carbon dioxide under climate-economy feedbacks and temperature variability, Environ. Res. Lett., 16, 094037, https://doi.org/10.1088/1748-9326/ac1d0b, 2021.

Koffi B., Cerutti A.K., Duerr M., Iancu A., Kona A. and Janssens-Maenhout G.: Covenant of Mayors for Climate and Energy: Default
665 emission factors for local emission inventories, Technical Report EU 28718 EN, Publications Office of the European Union, Luxembourg, 10.2760/290197, 2017.

Lantz E., Wiser R. and Hand M.: IEA Wind Task 26 - The Past and Future Cost of Wind Energy, technical report NREL/TP-6A20-53510, NREL, Golden, CO, USA, https://www.nrel.gov/docs/fy12osti/53510.pdf, 2012.

Lantz, E., Dalla Riva A., Hethey J., Vitina A.: Impacts of Wind Turbine Technology on the System Value of Wind in Europe, technical report
670 NREL/TP-6A20-70337, NREL, Golden, CO, USA, nrel.gov/docs/fy18osti/70337.pdf, 2017.

Mai, T., Mowers, M. and Eurek, K.: Competitiveness Metrics for Electricity System Technologies, technical report NREL/TP-6A20-72549, NREL, Golden, CO, USA, https://www.osti.gov/biblio/1765599, 2021.

MATLAB 2019a; Fmincon, The MathWorks,Inc., Natick, Massachusetts, United States, https://www.mathworks.com/help/optim/ug/fmincon.html, 2019.

675 Myhre G., Shindell G. Breon F.-M., Collins W., Fuglestvedt J., Huang F., Koch D., Lamarque J.-F., Lee D., Mendoza B., Nakajima T., Robock A., Stephens G., Takemura T. and Zhang H.: Anthropogenic and Natural Radiative Forcing, Cambridge University Press, book section 8, p. 659-740, 2013.

National Academies of Sciences, Engineering and Medicine: Valuing Climate Damages: Updating Estimation of the Social Cost of Carbon Dioxide, The National Academies Press, Washington DC, https://doi.org/10.17226/24651, 2017.

680 New European Wind Atlas (NEWA): Map Interface for the NEWA, Mesoscale Data Download, neweuropeanwindatlas.eu, (last access: 24 November 2021), 2021.

NREL: WISDEM v3.2.0, https://github.com/WISDEM/WISDEM, 2021.

Ozoemena M., Cheung W., Hasan R.: Comparative LCA of technology improvement opportunities for a 1.5 MW wind turbine in the context of an onshore wind farm, Clean Technologies and Environmental Policy, 20, 173-190, 10.1007/s10098-017-1466-2, 2018.

685 Pfaffel S., Faulstich S. and Rohrig K.:Performance and Reliability of Wind Turbines: A Review, Energies, 10, 1904, https://doi.org/10.3390/en10111904, 2017.

Ricke K., Drouet L., Caldeira K. and Tavoni M.: Country-level social cost of carbon, Nature Clim. Change, 8, 895-900, doi.org/10.1038/s41558-018-0282-y, 2018.

Roser M.: Why did renewables become so cheap so fast?, Our World in Data, https://ourworldindata.org/cheap-renewables-growth(last

690 access: 29 Dec. 2021), 2021.

Rydh C., Jonsson M. and Lindahl P.: Replacement of Old Wind Turbines Assessed from Energy, Environmental and Economic Perspectives, Technical report NEI-SE-544, Kalmar, Sweden, https://www.osti.gov/etdeweb/biblio/20534695, 2004.

Schleisner L.: Life cycle assessment of a wind farm and related externalities, Ren. Energy, 20(3), 279-288, 10.1016/S0960-1481(99)00123-8, 2000.

695 Schmid M., Gonzalez Ramon N., Direckx A. and Wegman T.: Accelerating Wind Turbine Blade Circularity, Wind Europe Report, https://windeurope.org/intelligence-platform/product/accelerating-wind-turbine-blade-circularity/ , 2020.

Seckinger N. and Radgen P.: Dynamic Prospective Average and Marginal GHG Emission Factors – Scenario-Based Method for the German Power System until 2050, Energies, 14, 2527, 10.3390/en14092527, 2021.

Seshadri, Aravind: NSGA-II: A multi-objective optimization algorithm, MATLAB Central File Exchange,

700 https://www.mathworks.com/matlabcentral/fileexchange/10429-nsga-ii-a-multi-objective-optimization-algorithm, last access: September 14, 2020.

Silver-Evans K., Azevedeo I.L. and Morgan M.G.: Marginal Emissions for the U.S. Electricity, Environmental Science & Technology, 46, 9, 4742-4748, doi.org/10.1021/es300145v, 2012.

Simpson J., Loth E. and Dykes K.: Cost of Valued Energy for design of renewable energy systems, Renewable Energy, 153, 290-300,

705 doi.org/10.1016/j.renene.2020.01.131, 2020.

Song Y., Youn J. and Gutowski T.: Life-cycle energy analysis of fiber-reinforced composites, Composites Part A: Applied Science and Manufacturing, 40, 1257-1265, 2009.

Spielmann M., Bauer C., Dones R. and Tuchschmid M.:Transport Services in Ecoinvent, ecoinvent report No. 14, Swiss Center for Life Cycle Inventories, https://db.ecoinvent.org/reports/14_transport.pdf, 2007.

710 Swisher P., Murcia Leon J.P., Gea Bermúdez J., Koivisto M.J., Madsen H.A., Münster M.: Competitiveness of a low specific power, low cut-out wind speed wind turbine in North and Central Europe towards 2050. Applied Energy, 306, 118043, https://doi.org/10.1016/j.apenergy.2021.118043, 2022.

Swiss Center for Life Cycle Inventories: Ecoinvent version 3.6, https://v36.ecoquery.ecoinvent.org (last access: October 2020), 2020.

Thomson R.C., Harrison G.P. and Chick J.P.: Marginal greenhouse gas emissions displacement of wind power in Great Britain, Energy

715 Policy, 101, 201-210, 10.1016/j.enpol.2016.11.012, 2017.

Tremeac B. and Meunier F.: Life cycle analysis of 4.5MW and 250W wind turbines, Renewable and Sustainable Energy Reviews, 13, 2104-2110,/10.1016/j.rser.2009.01.001, 2009.

Ueckerdt F., Hirth L.,Luderer G., Edenhofer O.: System LCOE: What are the costs of variable renewables?, Energy, 63, 61-75, 10.1016/j.energy.2013.10.072., 2013.

720 Veers P., Dykes K., Lantz E., Barth S., Bottasso C.L., Carlson O., Clifton A., Green J., Green,P., Holttinen H., Laird D., Lehtomäki V., Lundquist J.K., Manwell J., Marquis M., Meneveau C., Moriarty P., Munduate X., Muskulus M., Naughton J., Pao L., Paquette J., Peinke J., Robertson A., Sanz Rodrigo J., Sempreviva A.M., Smith J.C., Tuohy A., Wiser R.: Grand challenges in the science of wind energy, Science, 366(6464), 10.1126/science.aau2027, 2019.

Vestas: Life Cycle Assessment of Electricity Production from a V90-2.0 MW Gridstreamer Wind Plant, Technical report, Aahrus, Denmark, 725 December 2011.

Vestas: Life Cycle Assessment of Electricity Production from an onshore V100-2.6 MW Wind Plant, Technical report, Aahrus, Denmark, October 2013.

Vestas: Life Cycle Assessment of Electricity Production from an onshore V90-3.0 MW Wind Plant, Technical report, Aahrus, Denmark, October 2013.

730 Wiser R., Mills A., Seel J., Levin T. and Botterud A.: Impacts of Variable Renewable Energy on Bulk Power System Assets, Pricing and Costs, Technical report LBNL-2001082, Lawrence Berkeley National Laboratory, Berkeley, CA, USA, 2017.

Wolf M.A., Pant R., Chomkhamsri K., Sala S., Pennington D.: The International Reference Life Cycle Data System (ILCD) Handbook - Towards more sustainable production and consumption for a resource-efficient Europe, Technical report, Joint Research Center, European Commission, 2012.